Title
Mechanisms of Synaptic Neuromodulation in Prefrontal Cortex

Author
Burke, Kenneth John

Publication Date
2018

Peer reviewed|Thesis/dissertation

Mechanisms of Synaptic Neuromodulation in Prefrontal Cortex

by

Kenneth John Burke Jr.

DISSERTATION

Submitted in partial satisfaction of the requirements for the degree of

DOCTOR OF PHILOSOPHY

in

Neuroscience

in the

GRADUATE DIVISION

of the

UNIVERSITY OF CALIFORNIA, SAN FRANCISCO

DEDICATIONS AND ACKNOWLEDGEMENTS

I have been remarkably lucky to have so many people in my life to help me cross the finish line with this PhD. But first I would like to dedicate this thesis to future graduate students. I offer you the following mantra to remember when things get tough, in the hopes that it will be as grounding for you as it was for me.

Success in science is due in equal parts to wisdom, perseverance, and luck.

First, wisdom. Developing a successful research project requires more than a mere theoretical understanding of one's field. It also requires a certain intuition for the current scientific zeitgeist, developed only with years of first-hand experience. My thesis mentor, Dr. Kevin Bender, exemplified this wisdom spectacularly as he guided me through the strange world of synaptic electrophysiology. I hope I caught some of this wisdom during my PhD.

Second, perseverance. Yes, perseverance is about putting in those long and strange hours. But graduate school can also be an exceptionally emotionally trying experience. It requires a passionate resolve that you must find in yourself to withstand the inevitable failures. It is also a commitment to caring for yourself and your loved ones, to continuing to fully live your life throughout graduate school. A healthy life outside of the lab will make you a more creative and resilient scientist.

Lastly, luck. So much in life's trajectory can feel random, and yet I have never met a researcher who's never felt a little ego hit that comes with a failed experiment or an invalidated hypothesis. I could tell you, intrepid young scientist, that you need to divorce your ideas from your ego, but of course you won't heed that advice (no one does). Instead, let me simply suggest that you get very good at being very wrong. Practice getting tied up in an idea, and then mooring yourself back to reality. Practice persevering through a bad luck streak. Practice learning the difference between bad luck and bad ideas. And most of all, practice grace in the face of the profound ignorance that comes with any meaningful scientific endeavor.

Now on to the tangible dedications. First, my thesis mentor Dr. Kevin Bender. I joined Kevin's lab early on in his career as a young professor. While I certainly respect Kevin's experimental aptitude, it was only after joining the lab and seeing the team that he built that I fully understood the vision he had for the future of his field. Kevin is the kind of scientist who wants to know, above all else, that the work done in his laboratory is grounded in careful experimental execution and attention to detail. I couldn't be more proud to be a part of that scientific tradition.

The team Kevin built in his laboratory has also been instrumental to my success in completing this thesis, including Gina, Roy, Alayna, Caroline, Becky, Jiggy, Perry and Anna. This team has been like a family to me over the last six years. As with family, I've shared so much with all of them: celebration, arguments, disappointment, resolve and support. I owe much of my success to being surrounded by such brilliant and compassionate humans.

The team Kevin has built in his laboratory is also reflective of UCSF Neuroscience at large. The graduate program here is filled with talented scientists at every career stage who are deeply invested in graduate student success, and it shows in their mentorship and willingness to accept criticism. The professors on my thesis committee, Drs. Roger Nicoll, Vikaas Sohal and Anatol Kreitzer have provided instrumental advice in keeping my thesis research focused and on track for success. But there are plenty of other scientists outside of my committee who were also invested in my success, especially Professors Dorit Ron, Howard Fields, Alexandra Nelson and Massimo Scanziani, as well as members of the Scanziani, Sohal and Nelson laboratories, especially Sarah Robinson-Schwartz, Guy Bouvier and Ally Girasole. Finally, I would like to acknowledge my network of friends in San Francisco who have made my time in this city so unforgettable: Anthony, Davide, Malay, David, Michael, Kati, and Anna. This list is certainly not comprehensive, another sign of good fortune.

Of course, I would have never made it to graduate school in the first place if it weren't for my family, who instilled in me the importance of an education and who supported my move to California: my parents, Donna and Ken Sr., and my brother Christopher, who I left behind in Rhode Island to pursue this degree. In particular I would like to acknowledge my late grandfather, William Renzulli. His emphasis on education for his family was evident in his words as well as his deeds; when my family suffered financial hardship in my first year of college, it was support from my entire family that kept me in school. It was also my grandfather's diagnosis of Parkinson's disease that led me to the field of neuroscience to begin with. In the end, Grandpa gave me so many

precious gifts by leading me to higher education and to the field of neuroscience, and this thesis is very much a product of these gifts.

Finally, I would like to that my partner, Drew Wenzel, and his parents Ruth and Dick, and sister Shelley. Moving across the country and starting a new life was terrifying, but I was lucky to find these amazing people and to build a sense of community with them. Drew and I have started to build a family here in San Francisco. He has been my confidant, my advocate, my inspiration. He's supported me through the long hours, the experiments gone awry, the paper writing and rewriting. And through the example of his own passionate dedication to his work, he's also led me to become a better man than I thought I ever could be.

AUTHOR CONTRIBUTIONS

Chapter 1 of this dissertation was written by Kenneth Burke.

Chapter 2 of this dissertation is reproduced in its entirety with permission from:

> Burke, K.J., Keeshen, C.M., and Bender, K.J. (2018). Two Forms of Synaptic Depression Produced by Differential Neuromodulation of Presynaptic Calcium Channels. Neuron 99, 969–984.e7.

Experimental design: Burke and Bender; Experimental execution: Burke, Keeshen and Bender; Data analysis: Burke, Keeshen and Bender; Funding acquisition: Bender; Project administration: Burke and Bender; Supervision: Bender; Visualization: Burke, Keeshen and Bender; Writing: Burke and Bender.

Chapter 3 of this dissertation was written by Kenneth Burke, with sections related to the algorithm application to a mouse model of autism reproduced in part and adapted with permission from:

> Spratt, P., Ben-Shalom, R., Keeshen, C., Burke, K., Clarkson, R., Sanders, S., and Bender, K. (2018). The autism-associated gene *Scn2a* plays an essential role in synaptic stability and learning. BioRxiv 366781.

Algorithm design by Kenneth Burke. Experiments in figures 2-5 were generated by Kenneth Burke. Experiments with *Scn2a* model of autism (including figures 1, 6 and 7) performed by P. S., R. B., K. Burke and K. Bender.

Chapter 4 of this dissertation is reproduced in its entirety with permission from:

Unger, E.K., Burke, K.J., Yang, C.F., Bender, K.J., Fuller, P.M., Shah, N.M., and Shah, N.M. (2015). Medial amygdalar aromatase neurons regulate aggression in both sexes. Cell Rep. 10, 453–462.

EKU and NMS designed the experiments. EKU and KJB Jr performed the experiments. PMF and CFY provided viral reagents. EKU, KJB Jr, KJB, and NMS analyzed the data. EKU and NMS wrote the paper.

Chapter 5 of this dissertation is reproduced in its entirety with permission from:

Yang, T., Yang, C.F., Chizari, M.D., Maheswaranathan, N., Burke, K.J., Borius, M., Inoue, S., Chiang, M.C., Bender, K.J., Ganguli, S., et al. (2017). Social Control of Hypothalamus-Mediated Male Aggression. Neuron 95, 955–970.e4.

T.Y., C.F.Y., M.D.C., and N.M.S. designed the experiments. T.Y., C.F.Y., M.D.C., M.B., S.I., and M.C.C. conducted all experiments except the electrophysiological experiments, which were conducted by K.J.B., Jr. and K.J.B. T.Y., C.F.Y., K.J.B., Jr., K.J.B., and N.M.S. analyzed the findings. T.Y., N.M., S.G., and N.M.S. designed and discussed modeling strategies in light of the findings, and N.M. implemented the subsequent modeling studies. T.Y. and N.M.S. wrote the manuscript.

Chapter 6 was written by Kenneth Burke.

Mechanisms of Synaptic Neuromodulation in Prefrontal Cortex

Kenneth John Burke Jr.

ABSTRACT

Neuromodulation encompasses a large array of mechanisms that regulate the excitability and dynamics of neuronal circuits. Activation of neuromodulatory receptors can regulate intrinsic neuronal excitability, synaptic transmission, activity-dependent neuroplasticity, homeostasis, gene transcription and other cell biological functions. These pathways are engaged both in healthy animals and during disease, and have been exploited by bioengineers to develop new experimental tools for controlling neuronal subpopulations *in vivo*. In this dissertation, we will describe several efforts to understand neuromodulation at multiple levels of analysis, from synapses to circuits. First, we will dissect the mechanisms underlying the regulation of vesicle release in prefrontal cortex by the neuromodulators dopamine and GABA. Then, we will develop an analytical pipeline for studying synaptic inputs in noisy electrophysiological recordings and apply this system to study how synapses are modulated by pathological conditions in a mouse model of autism. Finally, we validate a technique that allows for experimenter-controlled neuromodulation of genetically-identified cell populations and use it to study how the amygdala and hypothalamus regulate aggressive and mating behaviors in both sexes. Taken together, this dissertation sheds light on the physiological mechanisms, functional implications and technical applications of neuronal modulation in the mouse brain.

TABLE OF CONTENTS

LIST OF TABLES

LIST OF FIGURES

CHAPTER 1

INTRODUCTION

1.1 OVERVIEW OF DISSERTATION

The content of this dissertation covers several research endeavors that span multiple subfields in neuroscience, including synaptic electrophysiology, computational modelling, two-photon calcium imaging, mouse models of neuropsychiatric disease and behavioral assays of innate social behaviors. The theme of neuromodulation serves as a connecting thread across these disparate projects, tying together the effects of neuronal modulation at the level of the synapse, neuronal microcircuit, and animal behavior in health and disease.

In Chapter 2, we study the effects of two neuromodulators, dopamine and GABA, on synaptic transmission in mouse prefrontal cortex. We show that both dopamine and GABA suppress the probability of vesicle release at glutamatergic synapses by suppressing presynaptic calcium channel activity. We then go on to show that these two neuromodulators suppress presynaptic calcium channels in biophysically-distinct ways, with different functional consequences for release dynamics. Using a combination of electrophysiology, two-photon calcium imaging and computational modelling, we propose a simple model whereby dopamine and GABA modulate the gain and frequency-dependent filtering of the synaptic transfer function, respectively.

In Chapter 3, we improve modern analytical techniques to detect synaptic activity in electrophysiological recordings. Building upon the techniques established by Pernía-

Andrade et al., we build an analytical pipeline that overcomes several technical obstacles in the use of deconvolution for synaptic event detection. We then apply this approach to demonstrate that mutation of the autism-associated gene *Scn2a* leads to a selective decrease in spontaneous excitatory synaptic activity in mouse prefrontal cortex.

In Chapter 4, we study how neurons expressing the enzyme aromatase in the medial amygdala regulate aggression. We found that these neurons are critical for aggression against other males in male mice, as well as maternal aggression in females. This finding suggests that these neurons control aggression generally, regardless of the sexual dimorphism in how the aggressive behavior is manifested.

In Chapter 5, we study how progesterone receptor expressing neurons in the ventromedial hypothalamus contribute to male territorial aggression. We find that these neurons drive aggression in solitary males in the absence of normal environmental and internal cues, but *not* in socially-housed males under specific circumstances. These data demonstrate that the behavioral response is a nonlinear function of environmental cues, physiological cues and the activity of this neuronal subpopulation.

Finally, in Chapter 6 I provide concluding remarks and an overview of promising future directions.

1.2 INTRODUCTION

1.2.1 The Neurophysiology of Synaptic Transmission

Presynaptic neurons transmit electrical signals across the synapse through a series of biochemical intermediate steps. This process includes the invasion of the action potential into the presynaptic active zone, the opening of voltage-gated calcium

channels (CaVs), the binding of calcium ions to vesicle release machinery, and finally the exocytosis of neurotransmitter vesicles. Notably, many of these steps are fundamentally stochastic, nonlinear or regulated by neuromodulators, which leads to a dynamic and nonlinear transfer function between the rate of presynaptic action potentials and the rate of transmitter release. Furthermore, both the function and physiology of this process vary significantly between synapses in the brain, ranging from reliable and frequency-invariant transmission in the cerebellum (Turecek et al., 2017) to noisy cortical synapses with strong, target-specific temporal filtering properties (Abbott and Regehr, 2004; Branco and Staras, 2009; Markram et al., 1998). This complexity has historically hindered efforts to develop a comprehensive theory that links axon neurophysiology to a quantitative description of synaptic transfer functions and their neuromodulation.

1.2.2 Neuromodulation and Paradigm Shift in Theories of Synaptic Transmission

Theoretical analysis of synaptic transmission and small neuronal circuits is often simplified into a mathematical framework whereby neurons transmit discrete packets of information to each other through weighted electrical potentials at the synapse (Hennig, 2013; London et al., 2002; Silver, 2010). One example with significant historical consequences dates to 1943, when Warren McCulloch and Walter Pitts first described how highly complex patterns of activity can arise in the brain when modelling neurons and their synaptic contacts in terms of propositional logic (McCulloch and Pitts, 1943). These “McCulloch-Pitts neurons” were the intellectual precursors to so-called artificial neural networks, with clear influence on the nascent field of artificial intelligence that persists to this day (Abraham, 2002). Other models of neuronal activity that abstracted

away biophysical details to different extents have yielded similarly significant fruits to the field of neuroscience (Bialek, 2012; Rall, 1964). However, it was quickly appreciated that many simplified models of this sort ignored the contribution of important neurotransmitters to neuronal circuit dynamics when their behavior was not well-described by simple electrical currents.

As early as the late 1970's, it was apparent that while some neurotransmitters do generate rapid electrical potentials at the synapse, many others generate more qualitative or modulatory effects (Marder, 2012). These "neuromodulators" were shown to initiate biochemical signaling cascades in the postsynaptic cell, leading to the regulation of synaptic strength, postsynaptic voltage-dependent currents and gene transcription (Huang and Thathiah, 2015). Some of these neuromodulators were also shown to act at a large distance from any synapse, apparently activating many postsynaptic cells through diffusion (Jan and Jan, 1982). This stood in stark contrast to the simple "wiring diagram" model of the brain, whereby neurons transmit information at anatomically well-defined synapses. Soon afterwards, researchers began to discover that signaling by these neuromodulators was also critical for both normal and pathological behavior in multiple animal species (Arnsten and Goldman-Rakic, 1985; Brozoski et al., 1979; Kim et al., 2017).

The revelation that neuromodulators were critical for normal animal behavior while simultaneously violating many simplifying assumptions about the nature of synaptic transmission spurred a significant body of research into the biophysical mechanisms that underlie neuromodulation. This response was, indubitably, in part a continuation of the effort to establish a comprehensive and quantitative theory that links the complex

physiology of neurotransmission to the computational function of neuronal circuits. Chapter 2 of this dissertation can be viewed as an extension of this intellectual effort, by connecting a rigorous description of biophysical mechanisms of dopamine neuromodulation to its functional consequences to synaptic transmission in prefrontal cortex.

1.2.3 Detection of Synaptic Activity and Application to Neuropsychiatric Disorders

One major experimental technique to study the physiology of synaptic transmission has historically been the whole-cell patch-clamp recording. This approach is often coupled with stimulation of presynaptic inputs, either through paired whole-cell recordings from neurons with synaptic connections or through extracellular stimulation of putative presynaptic axons. However, many cells have long and thin dendrites with high electrical impedance that attenuate and filter synaptic signals as they travel to the site of the recording electrode. Especially when combined with non-biological sources of noise, small synaptic events can thus be difficult to detect. This problem, known as the “space-clamp problem”, is particularly severe for spiny neurons such as the cortical pyramidal neuron, which show very strong electrical attenuation of signals and poor penetration of holding currents in voltage-clamp (Bar-Yehuda and Korngreen, 2008; Beaulieu-Laroche and Harnett, 2018; Williams and Wozny, 2011). This complicates the ability of neurophysiologists to study synaptic activity and dynamics, and the modulation or dysregulation thereof, using patch-clamp recordings, and illustrates the need for better experimental and analytical tools to accurately measure synaptic activity.

Importantly, the dysregulation of synaptic connectivity and function has been implicated in the pathophysiology of several neuropsychiatric diseases, including autism and schizophrenia (Arnsten et al., 2012; De Rubeis et al., 2014; Sanders et al., 2015). In Chapter 3 of this dissertation, we will describe a novel synaptic activity detection algorithm, discuss its advantages and limitations (including how to overcome some of these limitations), and apply it to study how neuronal synapses in prefrontal cortex are modulated in the context of an autism-associated genetic mutation.

1.2.4 Neural Circuits Underlying Aggression and Mating

The development of innate, sexually dimorphic social behaviors, including aggression and mating, is a critical component of ethologically-relevant behavioral neuroscience (Bayless and Shah, 2016). The neural circuits underlying these behaviors include several neuronal subpopulations that are identifiable based on both brain region and gene expression patterns. Recent technological advances have allowed for the experimental manipulation of these subpopulations, which has significantly advanced our understanding of how activity in these neural "circuit nodes" contribute to social behavior. In Chapters 4 and 5 of this dissertation, we will use these techniques to modulate neuronal subpopulations in the amygdala and hypothalamus *in vivo* and study their influence on aggression and mating behaviors in both sexes.

1.3 REFERENCES

Abbott, L.F., and Regehr, W.G. (2004). Synaptic computation. Nature 431, 796–803.

Abraham, T.H. (2002). (Physio)logical circuits: the intellectual origins of the McCulloch-Pitts neural networks. J. Hist. Behav. Sci. 38, 3–25.

Arnsten, A.F., and Goldman-Rakic, P.S. (1985). Catecholamines and cognitive decline in aged nonhuman primates. Ann. N. Y. Acad. Sci. 444, 218–234.

Arnsten, A.F.T., Wang, M.J., and Paspalas, C.D. (2012). Neuromodulation of thought: flexibilities and vulnerabilities in prefrontal cortical network synapses. Neuron 76, 223–239.

Bar-Yehuda, D., and Korngreen, A. (2008). Space-Clamp Problems When Voltage Clamping Neurons Expressing Voltage-Gated Conductances. J. Neurophysiol. 99, 1127–1136.

Bayless, D.W., and Shah, N.M. (2016). Genetic dissection of neural circuits underlying sexually dimorphic social behaviours. Philos. Trans. R. Soc. B Biol. Sci. 371.

Beaulieu-Laroche, L., and Harnett, M.T. (2018). Dendritic Spines Prevent Synaptic Voltage Clamp. Neuron 97, 75–82.e3.

Bialek, W. (2012). Biophysics: Searching for Principles (Princeton University Press).

Branco, T., and Staras, K. (2009). The probability of neurotransmitter release: variability and feedback control at single synapses. Nat. Rev. Neurosci. 10, 373–383.

Brozoski, T.J., Brown, R.M., Rosvold, H.E., and Goldman, P.S. (1979). Cognitive deficit caused by regional depletion of dopamine in prefrontal cortex of rhesus monkey. Science 205, 929–932.

Hennig, M.H. (2013). Theoretical models of synaptic short term plasticity. Front. Comput. Neurosci. 7, 45.

Huang, Y., and Thathiah, A. (2015). Regulation of neuronal communication by G protein-coupled receptors. FEBS Lett. 589, 1607–1619.

Jan, L.Y., and Jan, Y.N. (1982). Peptidergic transmission in sympathetic ganglia of the frog. J. Physiol. 327, 219–246.

Kim, S.M., Su, C.-Y., and Wang, J.W. (2017). Neuromodulation of Innate Behaviors in Drosophila. Annu. Rev. Neurosci. 40, 327–348.

London, M., Schreibman, A., Häusser, M., Larkum, M.E., and Segev, I. (2002). The information efficacy of a synapse. Nat. Neurosci. 5, 332–340.

Marder, E. (2012). Neuromodulation of neuronal circuits: back to the future. Neuron 76, 1–11.

Markram, H., Wang, Y., and Tsodyks, M. (1998). Differential signaling via the same axon of neocortical pyramidal neurons. Proc. Natl. Acad. Sci. U. S. A. 95, 5323–5328.

McCulloch, W.S., and Pitts, W. (1943). A logical calculus of the ideas immanent in nervous activity. Bull. Math. Biophys. 5, 115–133.

Pernía-Andrade, A.J., Goswami, S.P., Stickler, Y., Fröbe, U., Schlögl, A., and Jonas, P. (2012). A Deconvolution-Based Method with High Sensitivity and Temporal Resolution for Detection of Spontaneous Synaptic Currents In Vitro and In Vivo. Biophys. J. 103, 1429–1439.

Rall, W. (1964). Theoretical Significance of Dendritic Trees for Neuronal Input-Output Relations. In Neural Theory and Modeling, (Stanford University Press), p.

De Rubeis, S., He, X., Goldberg, A.P., Poultney, C.S., Samocha, K., Cicek, A.E., Kou, Y., Liu, L., Fromer, M., Walker, S., et al. (2014). Synaptic, transcriptional and chromatin genes disrupted in autism. Nature 515, 209–215.

Sanders, S.J., He, X., Willsey, A.J., Ercan-Sencicek, A.G., Samocha, K.E., Cicek, A.E., Murtha, M.T., Bal, V.H., Bishop, S.L., Dong, S., et al. (2015). Insights into Autism Spectrum Disorder Genomic Architecture and Biology from 71 Risk Loci. Neuron 87, 1215–1233.

Silver, R.A. (2010). Neuronal arithmetic. Nat. Rev. Neurosci. 11, 474–489.

Turecek, J., Jackman, S.L., and Regehr, W.G. (2017). Synaptotagmin 7 confers frequency invariance onto specialized depressing synapses. Nature 551, 503.

Williams, S.R., and Wozny, C. (2011). Errors in the measurement of voltage-activated ion channels in cell-attached patch-clamp recordings. Nat. Commun. 2, 242.

CHAPTER 2

Two Forms of Synaptic Depression Produced by Differential Neuromodulation of Presynaptic Calcium Channels

---

2.1 ABSTRACT

Neuromodulators are important regulators of synaptic transmission throughout the brain. At the presynaptic terminal, neuromodulation of calcium channels (CaVs) can affect transmission not only by changing neurotransmitter release probability, but also by shaping short-term plasticity (STP). Indeed, changes in STP are often considered a requirement for defining a presynaptic site of action. Nevertheless, some synapses exhibit non-canonical forms of neuromodulation, where release probability is altered without a corresponding change in STP. Here, we identify biophysical mechanisms whereby both canonical and non-canonical presynaptic neuromodulation can occur at the same synapse. At a subset of glutamatergic terminals in prefrontal cortex, GABAB and D1/D5 dopamine receptors suppress release probability with and without canonical increases in short-term facilitation by modulating different aspects of presynaptic calcium channel function. These findings establish a framework whereby signaling from multiple neuromodulators can converge on presynaptic CaVs to differentially tune release dynamics at the same synapse.

2.2 INTRODUCTION

Neuromodulators regulate synaptic transmission through a wide array of biophysical mechanisms (Chalifoux and Carter, 2011; Seamans and Yang, 2004; Tritsch

and Sabatini, 2012). In presynaptic boutons, neuromodulators can affect the function of voltage-gated calcium channels, which in turn alters the probability of vesicle release (P_R) (Branco and Staras, 2009). Due to complex interactions between calcium influx and vesicle release machinery in the presynaptic active zone, changes in P_R typically do not result in a simple change in gain (i.e. a linear scaling of synaptic strength). Canonically, presynaptic modulators change the relative strength of subsequent closely-timed synaptic events, a phenomenon termed short-term plasticity (STP) (Kamiya and Zucker, 1994; Zucker and Regehr, 2002; Hennig, 2013; Jackman and Regehr, 2017). However, exceptions to this rule have been observed for a variety of neuromodulators and synapses. In these instances, presynaptic modulation suppresses release probability without canonical changes in STP (Gao *et al*., 2001; Seamans *et al.*, 2001; Delaney *et al.*, 2007; Li *et al.*, 2012; Holmes *et al.*, 2017; Tejeda *et al.*, 2017). Moreover, modulation with and without parallel changes in STP has been observed at a single synapse in response to two different neuromodulators (Hefft *et al.*, 2002; Delaney *et al.,* 2007; Li *et al.*, 2012; Tejeda *et al.*, 2017). Why this occurs at some synapses, and why different neuromodulators evoke different forms of presynaptic suppression, is unclear.

In prefrontal cortex (PFC), there is evidence that GABA and dopamine may differentially regulate glutamatergic transmission by activating presynaptic $GABA_B$ receptors ($GABA_BR$) and D1/D5 family dopamine receptors (D1R). At these synapses, $GABA_BR$ activation acts as a canonical presynaptic neuromodulator, robustly reducing P_R for single presynaptic action potentials (APs) but facilitating later events in a high frequency burst of APs (Chalifoux and Carter, 2011). As such, $GABA_BR$ activation is thought to impose a high-pass filter on these synapses (Abbott and Regehr, 2004). How

dopamine regulates the same synapses is less clear. Dopamine modestly suppresses glutamatergic excitatory postsynaptic currents when EPSCs are evoked by local electrical stimulation (Seamans et al., 2001; Urban et al., 2002). By contrast, EPSCs between synaptically-coupled pairs of glutamatergic neurons are more strongly suppressed, suggesting that dopamine may suppress presynaptic release in an input-specific manner (Gao *et al.*, 2001; Gao and Goldman-Rakic, 2002; Gao *et al*, 2003; but see Urban *et al.*, 2002). Although other lines of evidence suggest a presynaptic site of action, this modulation occurs without a change in STP (Gao *et al*., 2001; Seamans *et al.*, 2001). Thus, in contrast to $GABA_B$, dopamine may act non-canonically to regulate presynaptic gain. This may be important for the hypothesized role of D1R in suppressing background noise during working memory tasks *in vivo* (Vijayraghavan et al., 2007).

Using a combination of pharmacology, 2-photon calcium imaging, and computational modeling, we found that activation of either D1R or $GABA_BR$ suppressed P_R, but with differential effects on short-term dynamics. We examined D1R modulation at a variety of glutamatergic inputs to PFC and found that D1R suppressed glutamatergic transmission at only a subset of inputs, but did so with no increase in short-term facilitation. At synapses where D1R-mediated suppression was present, $GABA_BR$ activation also suppressed vesicular release probability, but with canonical increases in short-term facilitation. At these synapses, we show that release is likely mediated by a very small number of CaVs, and that these CaVs are the targets of both D1R and $GABA_BR$ signaling. Interestingly, D1R and $GABA_BR$ regulate different biophysical properties of presynaptic CaVs, which alone were sufficient to account for the differences in STP. Thus, the interplay between CaV function and vesicle release machinery, combined with

the precise mechanism by which CaVs are regulated, can bias how neuromodulators regulate synaptic transmission.

2.3 RESULTS

2.3.1 Dopaminergic modulation of glutamatergic inputs to PFC

To test the sensitivity of specific PFC excitatory inputs to dopaminergic modulation, we made whole-cell recordings from pyramidal cells in layer 5b of PFC and evoked EPSCs either via local electrical stimulation (eEPSC), which recruits an unknown population of inputs, or via optogenetic recruitment of anatomically-specified inputs (oEPSC, Fig. 1A, B). Stimuli were delivered every 15 seconds and resulting EPSCs were monitored in cells voltage-clamped to -80 mV. EPSCs were almost entirely blocked by the AMPA/kainate antagonist NBQX (10 μM; residual current=1.4±0.8% of baseline, n=11). Following a stable baseline, D1Rs were activated by application of the D1-selective agonist SKF 83822 (20 μM, with 1 μM of the D2-family antagonist sulpiride present throughout recording). Consistent with previous findings (Seamans et al., 2001), eEPSCs evoked by local electrical stimulation were only modestly suppressed (Fig. 1C, E; Norm Amp: 0.88±0.05 of baseline, n=16, $p<0.05$, rank-sum test). This suggests that dopamine either has minimal effects on all glutamatergic inputs to these neurons, or perhaps selective effects depending on the input source.

To distinguish between these possibilities, we injected a virus encoding channelrhodopsin2 (ChR2) into six major glutamatergic input sources to mPFC (Figs. 1B, S1; either AAV5-CaMKIIα-ChR2-EYFP or AAV5-Ef1α-DIO-ChR2-EYFP, see Methods). Injections were made in PFC, both ipsilateral and contralateral to the recording site (iPFC,

cPFC); ipsilateral ventral hippocampus (vHPC); contralateral orbitofrontal cortex (cOFC); ipsilateral mediodorsal thalamus (MDT); or ipsilateral amygdala (Amyg). In contrast to local electrical stimulation, optically-evoked oEPSCs were modulated by SKF in only 3 of 6 inputs (Fig. 1D, F, G): iPFC, cPFC and vHPC (iPFC, Norm Amp: 0.62±0.05, n=13, p<0.01; cPFC: 0.64±0.04, n=18, p<0.01; vHPC: 0.66±0.04, n=18, p<0.01; rank-sum test), and were blocked by the D1 antagonist SCH 23390 (10 μM SCH; Norm Amp: 0.96±0.04, n=6, p<0.01 vs. SKF alone, rank-sum test; Fig. 1H). Inputs from cOFC, MDT, and Amyg were insensitive to D1 agonist application (cOFC, Norm Amp: 1.03±0.04, n=8, p=0.47; MDT:=1.04±0.04, n=6, p=0.37; Amyg: 1.01±0.08, n=8, p=0.93, rank-sum test). Taken together, these data suggest that D1Rs suppress a subset of glutamatergic inputs into PFC that is defined, at least in part, by anatomical source.

The pattern of modulation observed above can be explained most easily by input-specific, presynaptic actions of D1Rs. To identify the locus of dopaminergic modulation, we first examined the paired pulse ratio (PPR) and coefficient of variation (CV) of oEPSCs in modulated pathways. At many synapses, reductions in release probability (P_R) are accompanied by an increase in PPR and a decrease in CV^{-2}, whereas changes in postsynaptic charge transfer per vesicle lead to reductions in EPSC amplitude with no change in PPR or CV^{-2} (Clements, 1990; Kamiya and Zucker, 1994; Quastel, 1997; Sigworth, 1980). We first validated that PPR and CV accurately reflect changes to pre- and postsynaptic aspects of transmission by altering extracellular calcium (Ca) concentration, which changes P_R, or by applying subsaturating concentrations of the AMPA/kainate receptor antagonist NBQX, which attenuates EPSC amplitude without altering P_R. These manipulations were calibrated to suppress the amplitude of the first

oEPSC to a similar extent as observed after D1R activation. Neither PPR nor CV^{-2} was affected by NBQX application (40 nM), consistent with its postsynaptic actions (Norm Amp: 0.70±0.04, p<0.001, Norm PPR: 0.99±0.04, p=0.86, Norm CV^{-2}: 0.98±0.05, p=0.72; n=8, rank-sum test). In contrast, both PPR and CV^{-2} co-varied with EPSC amplitude when extracellular calcium concentration was changed (Fig. 2A-C, ΔCa^{2+}; relative to 1.3 mM $CaCl_2$. All data normalized to baseline. 2.0 mM, Amp: 1.43±0.07, PPR: 0.82±0.03, CV^{-2}: 3.00±0.82, n=9 ; 0.9 mM, Amp: 0.77±0.06, PPR=1.11±0.05, CV^{-2}=0.43±0.09, n=10; 0.75 mM, Amp: 0.49±0.06, PPR=1.30±0.07, CV^{-2}=0.53±0.07, n=9; PPR vs Ca^{2+}, chi-square statistic=18.19, p<0.001, Kruskal-Wallis ; CV^{-2} vs Ca^{2+}, chi-square statistic=18.22, p<0.001, Kruskal-Wallis). Furthermore, baseline paired-pulse facilitation was comparable between the electrical and optical stimulation methods (for oEPSC, PPR=1.38, 1.08 – 1.70 for median, 25^{th} – 75^{th} percentile, n=98 cells; for eEPSC, PPR=1.57, 1.27 – 1.83 for median, 25^{th} – 75^{th} percentile, n=16; p=0.12, rank-sum test). Taken together, this indicates that PPR and CV^{-2} can distinguish between canonical pre- and postsynaptic manipulations at these synapses.

To examine how PPR is affected by D1Rs, oEPSCs were evoked in each dopamine-sensitive pathway. Comparable levels of paired pulse facilitation were observed at baseline for iPFC, cPFC, and vHPC inputs (1.31±0.09, 1.31±0.08, 1.10±0.08, respectively; 50 ms interstimulus interval). Interestingly, PPR was not increased after D1-dependent modulation of iPFC, cPFC, or vHPC inputs (Fig. 2A-C, SKF, for iPFC, cPFC and vHPC, respectively: Norm PPR: 0.96±0.07, 1.01±0.04, 0.93±0.07; n=13, 18, 18; p=0.60, 0.83, 0.20, rank-sum test with Holm-Sidak correction vs PPR=1.00; chi-square statistic=1.57, p=0.67, Kruskal-Wallis), a result consistent with previous studies in PFC

(Gao *et al*., 2001; Seamans *et al.*, 2001). In contrast, CV^{-2} was reduced at both prefrontal inputs, and trended towards a decrease for ventral hippocampal inputs (iPFC, cPFC and vHPC, respectively: Norm CV^{-2}=0.58±0.07, 0.61±0.09, 0.82±0.10; p=0.0001, =0.0003, =0.107).

Given the disagreement between PPR and CV results, we next sought to isolate pre- and postsynaptic components of synaptic transmission. To examine presynaptic release probability, we used optical quantal analysis (OQA), where transmission success and failures can be monitored at single synapses via NMDA receptor-mediated spine Ca influx (Mainen *et al.*, 1999; Oertner *et al.*, 2002; Higley *et al.*, 2009; Little and Carter, 2012). Pyramidal cells were voltage-clamped to 0 mV to inactivate calcium channels, and spines responsive to ChR2 stimuli were identified using Fluo-5F (Figure 2D-F). Release probability across all tested spines was 0.28±0.03 at baseline (range=0.10–0.40, n=11 spines, 30 trials each). After pharmacological activation of D1Rs, release probability was significantly reduced (Figure 2E-F, success threshold=2 S.D. of noise; baseline P_R =0.27±0.04, post-SKF P_R =0.13±0.04, n=7, p<0.05, signed-rank test). Release probability was unaltered in time-locked controls (baseline P_R=0.28±0.04, post-vehicle P_R=0.30±0.04, n=4, p>0.99, signed-rank test). Data were consistent when using different noise thresholds to define success and failure trials (see Methods; success threshold=1 S.D. of noise; SKF - baseline P_R =0.33±0.06, post-SKF P_R =0.16±0.04, n=7, p<0.05, Vehicle - baseline P_R =0.28±0.04, post-vehicle P_R =0.35±0.06, n=4, p=0.375; success threshold=3 S.D. of noise; SKF - baseline P_R=0.21±0.05, post-SKF P_R=0.09±0.03, n=7, p<0.05, Vehicle - baseline P_R =0.25±0.02, post-vehicle P_R =0.24±0.03, n=4, p>0.99). These data indicate that D1Rs suppress release probability at individual PFC synapses.

To isolate potential postsynaptic modulation by D1Rs, we bypassed transmitter release and instead uncaged glutamate on single spines. Uncaging pulses were delivered in a pair, with increased intensity on the second pulse to mimic paired pulse facilitation observed using ChR2 stimulation. No change in uEPSC amplitude or PPR was noted (Fig. S4. Norm. uEPSC amplitude=1.01±0.11, 0.97±0.06, n=8, 11 for SKF and vehicle, respectively; p=0.62, Mann-Whitney U test, SKF vs. vehicle; Unnormalized PPR=1.45±0.21, 1.41±0.16, 1.41±0.10, 1.40±0.07, n=8, 8, 11 ,11 for SKF baseline, post-SKF, vehicle baseline and post-vehicle, respectively; p=0.87, Mann-Whitney U test for SKF baseline vs vehicle baseline; p>0.99,=0.86, Wilcoxon signed rank test for baseline PPR vs post condition for SKF and vehicle, respectively).

D1 receptors are more commonly expressed in thin-tufted layer 5 pyramidal cells in PFC, which have intrinsic cell properties that can be distinguished from neighboring cell classes (Gee *et al.*, 2012; Seong and Carter, 2012; Clarkson *et al.*, 2017). To determine whether postsynaptic cell type contributes to D1-dependent modulation of oEPSCs, we divided the dataset from Fig. 1 not by projection source, but by postsynaptic cell class and found that D1R-dependent modulation was present in putative D1-expressing and D1-lacking cell classes (Fig. S2C, D). Taken together with OQA and uncaging experiments, these data indicate that D1R suppression of long-range EPSCs is due to presynaptic suppression of release probability, despite the fact that this modulation does not increase PPR.

How might D1Rs suppress release probability without increasing paired-pulse facilitation? D1Rs have been observed to regulate the high voltage-activated CaVs that underlie transmitter release (Surmeier *et al.*, 1995; Zhang *et al.*, 2002; Seamans and Yang,

2004). To test whether D1Rs regulate presynaptic calcium influx, we imaged calcium in axonal boutons that originated from different long-range inputs using 2-photon laser scanning microscopy. We used a similar viral strategy as with ChR2, injecting both AAV5-hSyn-DIO-gCaMP6f and AAV5-Ef1α-Cre into the same brain regions as studied above in animals from a Cre-dependent tdTomato reporter line (Ai14; Fig. 3A). In a subset of experiments, we confirmed that gCaMP6f responses were AP-mediated by visually ensuring that responses to a prolonged train of stimuli (50x 50Hz, Fig. 3A) were blocked by 1 μM tetrodotoxin (n=6 boutons, 3 slices). When assessing D1R modulation, stimuli were limited to 3x 50Hz, as this produced reliable gCaMP signals that were restricted to individual boutons (Fig. S5, gCaMP full-width half-max 1.70±0.16 μm before stimulus vs. 1.68±0.16 μm after stimulus, n=8, p=0.88, rank-sum test). Consistent with oEPSC results, D1R activation strongly suppressed action-potential evoked calcium influx in axonal boutons from cPFC and vHPC, but not cOFC, MDT or Amyg (Fig. 3B, C; Norm Peak ΔF/F=0.57±0.07, 0.71±0.08, 1.04±0.09, 1.01±0.11, 0.99±0.07; n=13, 12, 14, 13, 10; p<0.001, =0.003, =0.64, =0.96, =0.72, respectively; rank-sum test with Holm-Sidak correction), and modulation was blocked by SCH 23390 (10 μM; Fig. 3D; for SKF, Vehicle, and SKF+SCH, respectively: Norm Peak ΔF/F=0.57±0.07, 1.04±0.05, 1.03±0.08; n=13, 7, 14; chi-square statistic=14.80, p<0.001, Kruskal-Wallis; SKF vs. Vehicle p<0.001, SKF vs. SKF+SCH p<0.001, rank-sum test with Holm-Sidak correction). Note that iPFC boutons were not measured with this approach, as boutons could not be resolved within the dense fluorescence of the injection site. Instead, modulation at iPFC boutons was assessed by imaging axon calcium influx with synthetic indicators during whole-cell recordings (see Fig. 4). Overall, these data suggest that D1Rs suppress specific PFC

glutamatergic inputs by a non-canonical presynaptic mechanism that reduces vesicle release probability without increasing paired-pulse facilitation.

2.3.2 Canonical and non-canonical presynaptic modulation at PFC glutamatergic inputs

Is dopamine unique in its ability to regulate release probability without altering short-term plasticity, or do other presynaptic neuromodulators have similar effects at these synapses? To address this question, we compared the effects of D1R to $GABA_BR$ activation, which is known to suppress release though $G_{\beta\gamma}$-dependent modulation of presynaptic CaVs (Chalifoux and Carter, 2011; Otis and Trussell, 1996; Park and Dunlap, 1998; Takahashi et al., 1998). The $GABA_BR$ agonist baclofen (350 nM) suppressed oEPSCs from cPFC inputs to a slightly larger extent than SKF (Fig. 4A, B; Norm oEPSC Amp: 0.46±0.05, n=7, $p<0.001$, rank-sum test with Holm-Sidak correction; compare to Fig. 1G, H); however, CV^{-2} and PPR decreased and increased, respectively, to an extent that mimicked the reduced extracellular calcium condition (Fig. 4B; Norm CV^{-2}: 0.39±0.08, $p<0.001$; Norm PPR: 1.27±0.10, $p=0.03$, rank-sum test with Holm-Sidak correction; see also Fig. S3). These data indicate that $GABA_BR$-mediated suppression of presynaptic release leads to canonical increases in PPR, suggesting that neuromodulation by $GABA_BR$ and D1R may occur through different signaling mechanisms.

Previous work has shown that D1Rs, as opposed to $G_{\beta\gamma}$-dependent $GABA_BRs$, regulate $Ca_V2.1$ and $Ca_V2.2$ calcium channels through a protein kinase A-dependent (PKA) pathway (Surmeier et al., 1995; Zhang et al., 2002). To test this, as well as to

measure neuromodulatory effects in iPFC axons, we made whole-cell recordings from layer 5 pyramidal cells and imaged AP-evoked bouton calcium transients with Fluo-5F. Calcium transients were suppressed by SKF and baclofen to similar degrees (Figure 4C-D; Norm Peak ΔF/F=1.00±0.03, 0.56±0.06, 0.59±0.05; n=6 each for vehicle, SKF, and baclofen, respectively) and calcium transients were suppressed by both D1R and $GABA_BR$ at individual boutons with serial application of both agonists (Norm Peak ΔF/F=0.62±0.03, 0.44±0.05 for SKF and SKF+baclofen, respectively; n=7, $p<0.05$, signed-rank test). D1-dependent modulation was blocked by the PKA inhibitor H89 (Figure 4C-D; Norm ΔF/F=0.98±0.02, n=8), whereas $GABA_BR$-dependent modulation was not (Norm ΔF/F=0.66±0.05, n=7; chi-square statistic=24.1, $p<0.001$, Kruskal-Wallis; SKF vs. SKF+H89 $p<0.001$, SKF vs. Vehicle $p=0.002$, Baclofen vs. Baclofen+H89 $p=0.366$, Baclofen vs. Vehicle $p=0.002$, Baclofen+H89 vs Vehicle $p=0.001$, rank-sum test with Holm-Sidak correction).

We next tested whether the distinct signaling pathways of D1R and $GABA_BR$ result in regulation of different presynaptic CaV subtypes. Application of ω-conotoxin-MVIIC (1 μM) blocked oEPSCs by 98.3±0.6% (n=5, data not shown), indicating that release is mediated by $Ca_V2.1$ and $Ca_V2.2$ channels at this synapse. To determine whether D1R and $GABA_BR$ selectively regulate one of these channel types, we applied $Ca_V2.1$ and $Ca_V2.2$-specific antagonists ω-agatoxin-TK (AgaTx, 150 nM) or ω-conotoxin-GVIA (CTx, 3 μM, Bender and Trussell, 2009), followed by either SKF or baclofen. Though both AgaTx and CTx suppressed calcium transients, neither occluded modulatory effects of D1R or $GABA_BR$. (Figure 4E-F; Norm ΔF/F=0.75±0.06, 0.47±0.06 for AgaTx and AgaTx+SKF, respectively, n=7, $p<0.05$; Norm ΔF/F=0.64±0.08, 0.44±0.08 for AgaTx and

AgaTx+Bac, respectively, n=6, $p<0.05$; Norm $\Delta F/F=0.82\pm0.04$, 0.57 ± 0.06 for CTx and CTx+SKF, respectively, n=6, $p<0.05$; Norm $\Delta F/F=0.80\pm0.06$, 0.48 ± 0.07 for CTx and CTx+Bac, respectively, n=7, $p<0.05$, signed-rank test for all comparisons). Thus, these data indicate that D1Rs and $GABA_BRs$ both suppress excitatory transmission through reduction of presynaptic AP-evoked calcium influx through $Ca_V2.1$ and $Ca_V2.2$ channels, although they act via different signaling cascades.

Given that D1R suppression can occur in conjunction with $GABA_BR$ suppression within the same bouton, it is possible that they regulate different biophysical properties of presynaptic CaVs. We reasoned that differential CaV modulation could account for differences in how D1Rs and $GABA_BRs$ regulate vesicle release. Interestingly, a similar dissociation between regulation of P_R and short-term dynamics has been observed at hippocampal Schaffer collateral synapses. At this synapse, it has been proposed that vesicle release is mediated by a small number of CaVs (i.e. nanodomain release configuration, Scimemi and Diamond, 2012). In such a configuration, reductions in the amount of calcium fluxed by single CaVs during an AP (i_{CaV}) can suppress calcium influx, reduce initial P_R, and increase PPR through an accumulation of calcium bound to vesicular release machinery (Jackman and Regehr, 2017; Zucker and Regehr, 2002). By contrast, reductions in the probability a CaV opens in response to an AP (p_{open}) could have multiple effects. If many CaVs contribute to vesicle release (i.e. microdomain release configuration), then a reduction in p_{open} should simply reduce the total calcium current (I_{CaV}) and have similar effects on P_R and PPR as reductions in calcium current per channel (e.g. single-channel current, i_{CaV}). However, if very few CaVs contribute to vesicle release, then the likelihood of local calcium influx failures on individual trials ($I_{CaV} = 0$)

becomes non-negligible, and on these trials a reduction in P_R may be followed by a lack of facilitation due to the absence of calcium accumulation at calcium sensors that mediate release.

Due to differences in dissociation rate, the divalent channel antagonists manganese (Mn) and cadmium (Cd) can differentially suppress i_{CaV} or p_{open}, respectively. Mn, which can bind and dissociate from a CaV many times within the timecourse of an AP, functionally reduces i_{CaV}, similar to lowering extracellular Ca. In contrast, Cd dissociation rates are an order of magnitude slower than an AP (0.02 ms^{-1}, Thévenod and Jones, 1992). At subsaturating concentrations, individual CaVs will likely be completely blocked or not blocked by Cd during the timecourse of a single AP. As such, Cd reduces p_{open}. At Schaffer collateral synapses, Mn and Cd both reduced EPSC amplitude, but PPR increased only with Mn (Scimemi and Diamond, 2012), suggesting that these synapses operate in the nanodomain configuration. To test whether long-range inputs into PFC also show different responses to reductions in i_{CaV} or p_{open}, we suppressed CaVs using Mn or Cd at cPFC inputs (Fig. 5). As with Schaffer collaterals, we observed a dose-dependent effect of Mn on both reducing oEPSC amplitude and increasing PPR (Fig. 5A, B; n=8; [Mn^{2+}]=50, 100, 200 μM, Norm Amp.=0.87±0.03, 0.71±0.05, 0.47±0.05, Norm PPR=1.09±0.03, 1.13±0.06, 1.28±0.07). By contrast, we observed a dose dependent effect of Cd on decreasing oEPSC amplitude, but no corresponding increase in PPR (Fig. 5C, D; n=7; [Cd^{2+}]=2, 5, 7.5, 10 μM, Norm Amp.=0.94±0.03, 0.69±0.04, 0.41±0.03, 0.30±0.03, Norm PPR=0.98±0.04, 0.94±0.06, 0.94±0.06, 0.88±0.07). The relationship between PPR and oEPSC amplitude was remarkably similar for Mn and $GABA_BR$ activation, and for Cd and D1R activation (Fig.

5E). Further, both Mn and Cd reduced CV^{-2}, consistent with D1R and $GABA_BR$ activation (Fig. 5F; Mn Norm CV^{-2}=0.70±0.16, 0.53±0.19, 0.41±0.14; Cd Norm CV^{-2}=0.84±0.19, 0.58±0.09, 0.42±0.15, 0.33±0.12).

2.3.3 Differential modulation of CaVs by D1Rs and $GABA_BRs$ account for differences in short-term plasticity

Based on these results, we hypothesized that D1Rs and $GABA_BRs$ could have distinct effects on short-term facilitation if D1Rs mimics Cd and $GABA_BRs$ mimics Mn. This could occur through several biophysical mechanisms. For example, $GABA_BR$-induced changes in channel gating, perhaps by depolarizing the voltage dependence of activation or increasing the reluctance of channel opening, could reduce the channel open duration during an AP (Huynh et al., 2015; Mintz and Bean, 1993; Patil et al., 1996). This would be functionally equivalent to Mn application, as it would produce a partial suppression of calcium influx per channel. By contrast, D1R-dependent modulation that reduces the likelihood that a CaV opens at all in response to an AP would mimic Cd, as it would produce all-or-none suppression of calcium influx per channel.

To test the hypothesis that D1Rs and $GABA_BRs$ differentially regulate the way CaVs respond to AP stimuli, we applied optical fluctuation analysis (OFA) to PFC bouton calcium signals (Carter and Jahr, 2016; Svoboda and Sabatini, 2000). We made whole-cell recordings and visualized AP-evoked calcium signals in axonal boutons (Fig. 6A, B). Boutons were always imaged in serial pairs to ensure that trial-to-trial variability was uncorrelated and thus unlikely to be the result of AP conduction failures (Fig. S6A, B). Both the mean amplitude, $\Delta\langle F\rangle$, and variance, σ_F^2, were measured immediately following

the AP to limit signal contamination from sources other than the bouton CaVs (Fig. 6C). The variance predicted by dark noise and shot noise alone was subtracted from the measured variance to obtain variance related to CaV activity (Fig. 6D).

Analysis of the resulting calcium transients is mathematically similar to EPSC nonstationary fluctuation analysis, but applied to imaging data instead of electrophysiological data (Quastel, 1997; Sigworth, 1980; Svoboda and Sabatini, 2000). Calcium influx in a bouton can be modeled as a binomial process arising from *N* CaVs, each with single-channel current *i* and open probability *p*, and quantitative predictions can be made for how trial-to-trial variability is affected given changes to *N*, *i*, or *p*. Within this framework, the mean-normalized variance should not change when reducing the single-channel current *i*, but it should increase with reductions in *N* and *p*. Importantly, the variance should increase more for reductions in *p* than for similar reductions in *N*, especially in boutons where CaV open probability per AP is high (Fig. S6C; Yasuda et al., 2003). Lastly, because we used propagating APs as our stimulus, *i* and *p* reflect the single-channel calcium charge transfer and overall channel open probability per AP, respectively.

In time-locked control conditions, AP-evoked bouton calcium transients were stable for >100 trials (Fig. 6E). All subsequent pharmacological experiments were therefore limited to a maximum of 100 trials. Baseline and post-drug measurements of 40-50 trials were separated by ~10 minutes to allow for drug equilibration. Both D1R and $GABA_BR$ activation suppressed presynaptic calcium influx (Fig. 6F, G), but decreases in CV_{CaV}^{-2} were observed primarily with D1R, not $GABA_BR$, activation (Fig. 6H-K; for D1R and $GABA_BR$, respectively: n=6, 6; Norm. CV_{CaV}^{-2} =0.18±0.07, 0.94±0.05; Norm. Peak

∆G/R=0.56±0.06, 0.59±0.05; chi-square statistic=23.88, p<0.001, Kruskal-Wallis; SKF vs. Baclofen p<0.001, rank-sum test with Holm-Sidak correction). Like $GABA_BRs$, reducing extracellular calcium suppressed calcium signals with little change in CV_{CaV}^{-2} (Fig. 6L; n=6; ΔCV_{CaV}^{-2}=0.95±0.05; Norm. $\langle \Delta F \rangle$=0.39±0.05; ΔCa^{2+} vs. Baclofen p=0.92, rank-sum test with Holm-Sidak correction). Thus, these data indicate that $GABA_BRs$ limit calcium influx from individual CaVs per AP, whereas D1Rs decrease the average number of CaVs that open in response to an AP, which could be due to a change in *N* or *p*.

To determine whether D1Rs reduce CaV number or open probability, we compared D1R effects to application of a subsaturating dose of ω-conotoxin MVIIC (35 nM). Because the dissociation rate of ω-conotoxin MVIIC is substantially slower than the timecourse of these experiments (McDonough et al., 1996), it should act as an irreversible CaV antagonist and effectively reduce *N*. Indeed, CV_{CaV}^{-2} decreased linearly with calcium response amplitude after conotoxin application (Fig. 6L; n=7; Norm. CV_{CaV}^{-2}=0.57±0.05; Norm. $\langle \Delta F \rangle$=0.60±0.05). This contrasts with D1R results where CV_{CaV}^{-2} reduced more quickly than $\langle \Delta F \rangle$ (conotoxin vs. SKF p<0.001, rank-sum test with Holm-Sidak correction), suggesting that D1Rs do not reduce the number of channels at the bouton.

Because D1Rs suppressed CV_{CaV}^{-2} more strongly than predicted by reductions in *N*, we next asked whether D1R suppression was consistent with a reduction in *p*. In cases where *p* is modulated, the steepness of the change in CV_{CaV}^{-2} depends strongly on the baseline open probability; thus, one can fit observed changes in CV_{CaV}^{-2} and $\langle \Delta F \rangle$ to a nonlinear function parameterized by different estimates of baseline CaV open probability

(Fig. S6C). The observed changes in CV_{CaV}^{-2} and $\langle \Delta F \rangle$ after D1R activation agreed well with a baseline open probability of 0.83 (95% confidence interval=0.73–0.93), consistent with more direct measures of *p* at other terminals (Borst and Sakmann, 1998; Li *et al.*, 2007). Taken together, these data indicate that D1Rs and $GABA_BRs$ suppress presynaptic CaV p_{open} and i_{CaV}, respectively (Fig. 6L).

To determine whether the different biophysical mechanisms of CaV modulation predicted by OFA are sufficient to explain the differing effects of D1Rs and $GABA_BRs$ on short-term plasticity, we developed a reduced synaptic model (Fig. 7A; Table S1). We simulated 50 synapses onto a single postsynaptic neuron, where each presynaptic terminal contained a constant number of CaVs. Channel activity was simulated as a simple binomial process to adapt OFA data directly into the model, and vesicle release probability was calculated as a Hill function of the calcium concentration per bouton (Stanley, 2016; Zucker and Regehr, 2002). Note that the resulting total number of vesicles was convolved with an AMPA-like sum of exponential waveforms for visualization, but analysis of EPSC amplitude and PPR was based solely on mean quantal content (see Methods).

We began by assuming that vesicle release was driven by only one CaV per synapse with an open probability of 0.83 per AP (derived from OFA analysis, Fig. 6L; Bucurenciu *et al.*, 2008; Scimemi and Diamond, 2012; Stanley, 2016). Given this open probability, four different calcium transients were observed with differing probabilities in response to paired-pulse stimulation (Fig. 7A, four rows). In most cases, both APs resulted in a CaV opening (69% of trials), but in some cases the CaV opened in response to only the first or second AP (14% each), or to neither (3%). This is a direct result of the

CaV openings being independent across channels and trials. These probabilities, when translated into release via the Hill function (S=0.25, cooperativity=3.72, Scimemi and Diamond, 2012) and aggregated across all 50 simulated synapses, resulted in modest paired-pulse facilitation of quantal content (model PPR=1.14, compared to measured oEPSC PPR of 1.31±0.09, 1.31±0.08, 1.10±0.08 for iPFC, cPFC and vHPC, respectively).

Given these baseline conditions, we next altered either the CaV single-channel current (*i*) or open probability (*p*) per AP to an extent that matched the D1R and $GABA_BR$ OFA data (0.6 of baseline for either model parameter, Fig. 7B, C; compared to peak ΔG/R amplitude reduction to 0.56±0.06 and 0.59±0.05 of baseline for D1R and $GABA_BR$, Fig. 6L). Modulation of *i* strongly reduced P_R due to the Hill function nonlinearity described above. As such, differences in residual calcium levels after the first AP nonlinearly enhanced P_R on the second AP, and PPR was increased. By contrast, when only one CaV contributed to release per synapse, modulation of *p* did not change calcium transient amplitude ratios or residual calcium; instead, modulation of *p* decreased the likelihood of two APs both eliciting successful calcium influx and increased the likelihood that calcium influx would occur on only the first AP, only the second AP, or not at all. Thus, when aggregated across all synapses and trials, the net EPSC amplitude was reduced without increasing PPR. In fact, more dramatic reductions in *p* led to a small decrease in PPR. This is because our simulations were tuned to evoke modest PPF at baseline, matching empirical observations (Fig. 2), and as *p* decreased, the likelihood of successful calcium influx for both APs (and thus, facilitation) approached zero. As a result, the net EPSC will be weighted more heavily towards calcium influx failures and PPR will trend towards 1, which would appear as a decrease when normalized to

facilitation at baseline (Fig. 5C-E). This result did not depend on the exact values chosen for the calcium concentration decay time constant or interval between APs and was also observed when synapses had a distribution of channel numbers and calcium decay time constants (Fig. S7A-C).

Synaptic facilitation can occur through multiple mechanisms, including slow clearance of calcium from the presynaptic terminal (i.e. the residual calcium hypothesis, Jackman and Regehr, 2017), saturation of endogenous calcium buffers (i.e., the buffer hypothesis, Blatow et al., 2003; Rozov et al., 2001), or interactions with a high affinity calcium sensor that has calcium dissociation kinetics that are slower than the paired-pulse interval (e.g., synaptotagmin7, bound calcium hypothesis, Jackman *et al.*, 2016). While the simulations described above use residual calcium as a mechanism for facilitation in a highly-reduced manner, similar results were obtained with a model that incorporates three additional, more realistic features (Fig. S7D-I). First, rather than simulating the bouton as a point, the linearized buffer approximation ("LBA", Naraghi and Neher, 1997; Neher, 1998) was used to approximate calcium concentration as a function of distance from the CaV. Then, calcium-dependent short-term facilitation was generated by scaling release probability by a second, higher-affinity Hill function with calcium affinity and cooperativity derived from synaptotagmin7 (see Methods and Table S1). Last, a simple model of vesicle depletion and replenishment was added, which is critical to generate calcium-dependent short-term facilitation in this form of model (Scimemi and Diamond, 2012). Paralleling results from our simpler model, the same basic pattern of canonical and noncanonical modulation with changes in i and p was observed when only a few CaVs were responsible for release, especially for CaV-vesicle

distances that reflect tight diffusional coupling (<25 nm, Bucurenciu et al., 2010; Nakamura et al., 2018; Scimemi and Diamond, 2012; Fig. S7D-H). This is likely because noncanonical short-term plasticity due to suppression of *p* occurs upstream of release machinery and calcium diffusion dynamics, and because the "paired-pulse facilitation" of intracellular calcium also trends towards 1 in these conditions. To further illustrate this point, we built a linear phenomenological model of short-term facilitation (Fig. S7J-L; Betz, 1970; Varela *et al.*, 1997; Markram *et al.*, 1998). This model makes no assumptions about the cellular mechanisms that support facilitation; its only requirement is that facilitation is calcium-dependent. Even here, we observed the same differences in PPR modulation by changes in *i* and *p*. Thus, these models can account for different mechanisms by which facilitation could occur, including buffer saturation or a high affinity calcium sensor with slow kinetics, provided that facilitation depends on residual calcium in some way.

This PPR dependence on *i* but not *p* was consistent across a range of parameter reductions (Fig. 7D-E). As expected, reductions in quantal size $q_{vesicle}$ did not alter PPR, and the insensitivity of PPR to reductions in *p* was diminished as the number of CaVs driving release per synapse increased (Fig. 7F-H). PPR invariance was observed only when few channels (1-3), either uniformly or randomly distributed across boutons, contributed to release (Fig. 7D,F-H, Fig. S7C,F,I,L). Importantly, this model also reproduced our finding that CV analysis indicated a presynaptic site of action for all tested presynaptic configurations but not the postsynaptic modulation of $q_{vesicle}$ (Fig. 7I). Taken together with OFA results, these data indicate that the different effects of D1Rs

and $GABA_BRs$ on short-term facilitation can, in principle, be explained by differential modulation of presynaptic CaVs.

2.3.4 Non-canonical presynaptic modulation strongly suppresses ongoing activity

Given these differences in short-term plasticity, we next sought to determine how ongoing activity was shaped by these two neuromodulators. We stimulated cPFC inputs expressing ChR2 with trains of 10 light pulses at either a regular frequency of 20, 10, or 5 Hz, or at a combination of these three frequencies (Fig. 8A-F). We found that stimulation of D1Rs consistently suppressed the entire sequence of all ten oEPSCs (Fig. 8A), and often suppressed oEPSCs that occurred at the end of the train to the greatest extent (Fig. 8B,E). But due to increased PPR, $GABA_BR$ suppression of oEPSCs was clearer at the beginning of trains, with little difference in oEPSC amplitude towards the end (Fig. 8C-E). This pattern was observed across multiple frequencies as well as with stimulation of variable intervals (Fig. S8A). We quantified the "charge ratio", ΔR_Q, which measures the suppression of trains of oEPSCs normalized to the suppression of the first oEPSC. When $\Delta R_Q < 1$ or $\Delta R_Q > 1$, the entire sequence of stimuli was suppressed more or less than the initial stimulus, respectively. Indeed, D1Rs and $GABA_BRs$ showed significantly different values of ΔR_Q across multiple frequencies (Fig. 8F, ΔR_Q : SKF, n=7, 20 Hz=0.73±0.08, 10 Hz=0.71±0.05, 5 Hz=0.70±0.08, Mixed Int.=0.71±0.05 ; ΔR_Q : Baclofen, n=7, 20 Hz=1.38±0.06, 10 Hz=1.33±0.12, 5 Hz=1.14±0.08, Mixed Int.=1.34±0.08 ; chi-square statistic=40.48, $p<0.001$, Kruskal-Wallis ; SKF vs Baclofen, 20 Hz $p<0.001$, 10 Hz $p<0.001$, 5 Hz $p=0.002$, Mixed Intervals $p<0.001$, rank-sum test

with Holm-Sidak correction). These data suggest that $GABA_BRs$ act as a high-pass filter on synaptic transmission whereas D1Rs act to suppress synaptic transmission independent of event timing.

We next sought to test whether these differences in short-term plasticity translate to differences in AP generation in more realistic, *in-vivo*-like conditions. We performed current-clamp experiments where we injected a noisy current waveform stimulus that was comprised of randomly-generated simulated EPSCs and IPSCs in order to depolarize the postsynaptic cell and generate APs. We also stimulated the cell with a train of LED pulses with shuffled intervals, ranging from 1 Hz to 20 Hz in frequency, to activate long-range ChR2-expressing cPFC inputs (Figure 8G). Stimulation of these inputs by the LED generated short-latency APs (Figure 8H-I). Importantly, due in part to the injected noisy current waveform, LED stimulation did not generate APs on every trial. This allowed us to apply D1R or $GABA_BR$ agonists and test whether these neuromodulators suppress ChR2-mediated spiking in different ways depending on ChR2 stimulation frequency. At the slowest frequency of 1Hz, LED-evoked spiking was suppressed significantly by both D1R and $GABA_BR$ agonists (norm. spike frequency within 12 ms of LED=0.43±0.07, 0.38±0.05 for SKF and baclofen, respectively). However, as the input LED frequency increased, $GABA_BR$-mediated suppression weakened significantly, whereas D1R-mediated suppression remained similar across all frequencies (Figs. 8I-J, S8B; norm. frequency after SKF=0.43±0.07, 0.55±0.07, 0.49±0.09, 0.50±0.20, for 1, 5, 10 and 20Hz, respectively, n=6, chi-square statistic=1.25, p=0.74, Kruskal-Wallis; norm. frequency after baclofen=0.38±0.05, 0.82±0.06, 0.74±0.06, 0.82±0.04, for 1, 5, 10 and 20Hz, respectively, n=8, chi-square

statistic=16.08, $p<0.05$, Kruskal-Wallis; $p<0.05$ for baclofen 1 Hz vs all other frequencies, rank-sum test with Holm-Sidak correction). Thus, these data indicate that GABA and dopamine have differential effects on synaptic integration, with GABA facilitating the transmission of inputs that occur in high-frequency bursts and dopamine suppressing transmission in a frequency-independent manner.

2.4 DISCUSSION

2.4.1 Overview

We demonstrate here that activation of the D1 dopamine receptor suppresses a subset of excitatory long-range and local inputs in prefrontal cortex. By reducing presynaptic CaV open probability, D1R can suppress vesicle release probability without a parallel increase in short-term facilitation. This non-canonical presynaptic neuromodulation suppresses AP generation across multiple stimulation frequencies and is well-explained by a simple synapse model where vesicle release is mediated by a small number of CaVs.

These results provide mechanistic insight into how modulation of specific biophysical properties of presynaptic CaVs can result in surprisingly large differences in synaptic transmission and short-term plasticity. These data address a longstanding puzzle related to prefrontal dopaminergic modulation by explaining how a neuromodulator can have little effect on paired-pulse facilitation despite a presynaptic site of action (Gao *et al*., 2001; Seamans *et al.*, 2001; Gao and Goldman-Rakic, 2002; Seamans and Yang, 2004). In addition to prefrontal cortical synapses, the mechanisms identified here may account for similar observations made in a diverse set of synapses

and neuromodulatory systems (Behr et al., 2000; Delaney et al., 2007; Holmes et al., 2017; Li et al., 2012; Tejeda et al., 2017). In future work, it will be critical to understand the role that distinct canonical and non-canonical presynaptic modulatory pathways play in information transfer in neuronal networks.

2.4.2 CaV-Vesicle Coupling and Presynaptic Neuromodulation

The facilitation-independent form of presynaptic modulation described here requires that release is mediated by nanodomain coupling between only a few CaVs per vesicle (Fig. 7; Scimemi and Diamond, 2012). This configuration is similar to other synapses, including the mature calyx of Held (Fedchyshyn and Wang, 2005), auditory ribbon synapses (Goutman and Glowatzki, 2007), hippocampal basket cell boutons, (Bucurenciu *et al.*, 2010) and Schaffer collaterals (Scimemi and Diamond, 2012). In the nanodomain configuration, the overall calcium concentration that triggers release is strongly influenced by the stochastic opening of individual CaVs and as such, slow CaV antagonists like cadmium suppress release without increasing PPR (Fig. 5; Hefft et al., 2002; Hjelmstad, 2004; Scimemi and Diamond, 2012). By contrast, when release is mediated by calcium microdomains, the overall calcium concentration is less influenced by single-channel stochasticity. At microdomain synapses, including the immature calyx of Held (Fedchyshyn and Wang, 2005), cadmium suppresses release while also increasing PPR (Otis and Trussell, 1996). We explored this difference between nanodomains and microdomains in our reduced model by examining how changing the number of functional CaVs per synapse affects the response of the model synapse to modulation of i_{CaV} or p_{open} (Fig. 7). Indeed, we observed that reductions in CaV p_{open}

preserved paired-pulse facilitation in the nanodomain-like configuration, but increased facilitation in the microdomain-like configuration. These differences have been proposed previously (Eggermann et al., 2012) and may account for why D1Rs suppress release with and without changes in PPR at different synapses (e.g., Wang *et al.*, 2012).

Presynaptic gain modulation has been observed with several synapses and neuromodulators. At hippocampal Schaffer collaterals, where release is driven by few CaVs, reducing CaV p_{open} with cadmium does not increase PPR (Scimemi and Diamond, 2012). At the perforant pathway synapse in subiculum, D1R also suppresses presynaptic gain (Behr et al., 2000). In the nucleus accumbens, excitatory inputs from amygdala, but not ventral hippocampus, display PPR-independent P_R suppression (Tejeda *et al.*, 2017). At this synapse, both kappa-opioid receptors (KORs) and $GABA_BR$ suppress P_R; however, KORs do not change PPR whereas $GABA_BRs$ increase PPR. Presynaptic gain modulation at other synapses, including KOR suppression in the bed nucleus of the stria terminalis and noradrenergic suppression in central amygdala, has been attributed to a reduction in the number of presynaptic release sites (Delaney *et al.*, 2007; Li *et al.*, 2012; but see Saviane and Silver, 2006). Taken together, the prevalence of neuromodulators that suppress release without increasing PPR throughout the brain suggests that presynaptic gain modulation may be a more common phenomenon than previously appreciated.

2.4.3 Possible mechanisms of CaV modulation

Both D1Rs and $GABA_BRs$ are known to modulate high voltage activated (HVA) CaVs (Surmeier *et al.*, 1995; Zhang *et al.*, 2002; Kisilevsky *et al.*, 2008; Chalifoux and

Carter, 2011). Our imaging and pharmacological experiments suggest that $GABA_BRs$ and D1Rs modulate AP-evoked calcium influx in a graded or all-or-none manner, respectively, at individual presynaptic CaVs. Multiple biophysical mechanisms could underlie these observations. $GABA_BRs$ could modify AP waveform by recruiting inward rectifying potassium channels or modulating other potassium channels, though the former has not been observed in PFC pyramidal cell axons (Xia et al., 2014). Alternatively, partial reductions in the current fluxed by single CaVs per AP could result from a $GABA_BR$-induced reduction in channel conductance, delayed time to first opening, or depolarized shift in voltage-dependent activation. The latter two possibilities seem most likely, as $GABA_BRs$ have been shown to interact directly with CaVs via $G_{\beta\gamma}$ subunits to either induce a rightward shift in activation or delay the time of first opening via the induction of a "reluctant state" (Huynh et al., 2015; Mintz and Bean, 1993; Patil et al., 1996), whereas $GABA_BR$-mediated changes in channel conductance have not been reported. The PKA-independence of CaV modulation by $GABA_BRs$ observed in the current study suggests that a similar $G_{\beta\gamma}$ mechanism may be present at prefrontal synapses.

D1R modulation was PKA dependent, similar to previous reports in basal ganglia (Surmeier *et al.*, 1995; Zhang *et al.*, 2002), and produced all-or-none reductions in AP-evoked CaV opening. This could be instantiated biophysically through alterations in gating modes, perhaps through modulation of beta subunits that increase channel opening latency to an extent that exceeds the duration of the AP (Luvisetto et al., 2004). Alternatively, hyperpolarized shifts in steady-state inactivation could reduce the number of channels available for activation by an AP. Such modulatory effects have been observed with D3 dopamine receptor-dependent regulation of $Ca_V3.2$ channels at the

axon initial segment (Bender *et al.*, 2010; Yang *et al.*, 2016; Clarkson *et al.*, 2017). Ca_V2 channels could be modified by similar mechanisms, especially during AP trains (Patil et al., 1998). Overall, these data suggest that further investigation into the signaling pathways and biophysics of CaV channel modulation by dopamine and other metabotropic receptors will yield greater insight into the diversity of synaptic neuromodulation in the axon.

2.4.4 Functional implications

Regulating synaptic gain is an important mechanism for shaping information transfer throughout the brain. Traditionally, gain modulation has been thought to occur at the postsynaptic site, either through changes in neurotransmitter receptor number, modulation of cable properties, or recruitment of inhibition (Silver, 2010). Because these mechanisms target the postsynaptic membrane, they often modulate overall neuronal excitability and are not input-specific. By contrast, neuromodulation of release probability is intrinsically input-specific. Canonically, neuromodulation of release probability has nonlinear and frequency-dependent effects on synaptic transmission (e.g. parallel changes in facilitation and/or depression, see $GABA_BR$ in Fig. 8). Thus, the ability of D1R to non-canonically suppress P_R at the presynaptic axon without increasing paired-pulse facilitation represents a novel mechanism for input-specific synaptic gain modulation.

Why do D1Rs suppress synaptic gain, rather than impose a canonical high-pass filter? Cortical neuronal activity is often characterized by sparse and irregular firing patterns (Barth and Poulet, 2012; Boudewijns et al., 2013), with high-frequency bursts encoding

behaviorally-relevant events (Burgos-Robles et al., 2007; Holmes et al., 2012; Laviolette et al., 2005). Canonical presynaptic neuromodulators like $GABA_B$Rs that suppress only low-frequency input are thought to be capable of enhancing the signal-to-noise ratio of these bursts. Conversely, D1R modulation may serve to suppress specific inputs into PFC, independent of input frequency. One major function of dopamine during working memory is to improve the saliency of task-related signals, largely by suppressing activity unrelated to the task at hand in a PKA-dependent manner (Arnsten et al., 1994; Brozoski et al., 1979; Vijayraghavan et al., 2007). Dopamine, by suppressing glutamatergic activity without altering short-term dynamics, may contribute to this noise suppression. Moreover, we now know that interactions between MDT and PFC are critical for working memory and attentional control (Bolkan et al., 2017; Schmitt et al., 2017). One interesting possibility, highlighted by the input-specific modulation shown here, is that D1Rs functionally enhance the signal-to-noise ratio on MDT inputs by suppressing many other inputs. Thus, the gain modulation employed by dopamine may confer advantages to information processing in PFC, especially during working memory.

2.5 METHODS

2.5.1 Experimental Model and Subject Details

All procedures were performed in accordance with UCSF IACUC guidelines. C57B6 wild type mice or Ai14 reporter mice (Jackson Laboratory, stock no. 007914) aged postnatal day (P) 50-80 were used for all experiments, with the exception of optical fluctuation experiments (Fig. 7) where animals from the age range P35-45 were used. No significant differences based on sex were observed, and data were pooled between sexes.

2.5.2 Viral Injections

Subjects were injected with virus at P26-35. Prior to viral injection, mice were anesthetized by isofluorane and head-fixed in a stereotaxic frame. For channelrhodopsin stimulation experiments, subjects were then unilaterally injected with 300-500 nL of AAV5-CamKIIα-hChR2(H134R)-eYFP ("CaMKII-ChR2") virus into prefrontal cortex (cPFC, from bregma: A/P +1.70, M/L +0.35, D/V -2.60 mm), mediodorsal thalamus (MD-Thal, from bregma: A/P -1.70, M/L -0.30, D/V -3.45), ventral hippocampus (vHPC, from bregma: A/P -3.30, M/L -3.20, D/V -4.00), orbitofrontal cortex (cOFC, from bregma: A/P +2.2, M/L +1.0, D/V -2.75) and amygdala (Amyg, from bregma: A/P -1.6, M/L -2.75, D/V -5.00). For sparse transfection of local recurrent PFC connections (iPFC), the same coordinates as cPFC were used but instead a virus cocktail was injected including AAV5-EF1α-Cre-IRES-mCherry and AAV5-EF1α-DIO-hChR2(H134R)-eYFP ("Cre-mCherry" and "DIO-ChR2", ratios between 1:10 – 1:20). For gCaMP experiments, the same injection coordinates and volumes were used in Ai14 heterozygous animals with a viral

cocktail that contained a 1:1 ratio of AAV5-hSyn-Flex-gCaMP6f-WPRE-SV40 and Cre-mCherry. Experiments were then performed approximately 4-8 weeks after injection (4-5 weeks cPFC/iPFC/cOFC, 5-6 MD-Thal/Amyg, 6-8 vHPC) to allow sufficient expression and trafficking. Acute slices were prepared from the majority of subjects. Additional subjects were perfused transcardially with 4% paraformaldehyde in phosphate buffered saline (PBS) and coronal sections were prepared (40 μm thickness). Tissue was rinsed with PBS 3 times over the course of 10 min, and then blocked in a solution of PBS with 10% normal goat serum (NGS, Jackson ImmunoResearch) and 0.2% Triton-X in PBS (PBS-T) for one hour. Tissue was then incubated in a solution of 2% NGS and 0.1% PBS-T containing an antibody conjugated to a 488 fluorophore (Invitrogen) to amplify the signal from stereotaxic injections of YFP-expressing viruses. This solution was incubated overnight at 4°C, rinsed with PBS 5 times over the course of 20 minutes, and mounted on slides with ProLong Gold Antifade with DAPI (Life Technologies). Images were obtained using a high speed wide-field microscope (Nikon Ti, with Andor Zyla 5.5 sCMOS) with a 10x/0.45 or 20x/0.75 Plan Apo objectives. Data were post-processed to stitch images and for brightness and contrast in FIJI.

2.5.3 Slice Preparation and Whole-Cell Recordings

Acute coronal slices of prefrontal cortex (225-300 μm) as well as the injection site if a virus was used (for post-hoc confirmation) were cut in high-sucrose solution, bubbled with 5% CO_2 / 95% O_2 and maintained at 4°C. Cutting solution contained (in mM): 87 mM NaCl, 25 mM $NaHCO_3$, 25 mM glucose, 75 mM sucrose, 2.5 mM KCl, 1.25 mM NaH_2PO_4, 0.5 mM $CaCl_2$ and 7 mM $MgCl_2$. Following cutting, slices were incubated in

artificial cerebrospinal fluid (aCSF, see below) for 30 min at 33°C, then at room temperature until recording. Pyramidal cells were visualized with Dodt contrast and two-photon microscopy. Single neurons were identified for electrical recording based on laminar position and teardrop somatic morphology. External aCSF recording solution contained (in mM): 125 NaCl, 2.5 KCl, 1 $MgCl_2$, 25 $NaHCO_3$, 1.25 NaH_2PO_4, 25 glucose; bubbled with 5% CO_2 / 95% O_2; 30-33°C. The day of the experiment, 1.3 mM $CaCl_2$ and 1 µM sulpiride (D2/3/4 antagonist, Tocris) were added to the aCSF from stock solutions. Recordings were performed in voltage-clamp with glass patch electrodes (2-4 MΩ tip resistance) and internal solution containing (in mM): 113 K-Gluconate, 9 HEPES, 4.5 $MgCl_2$, 0.1 EGTA, 14 $Tris_2$-phosphocreatine, 4 Na2-ATP, 0.3 tris-GTP; ~290 mOsm, pH: 7.2-7.25. Cells were compensated for whole-cell capacitance and series resistance (50%) and voltage-clamped at -80 mV (corrected for 12 mV junction potential) unless otherwise stated. For cesium-based imaging experiments (Figure 2D-F, OQA), internal solution contained (in mM): 110 $CsMeSO_3$, 40 HEPES, 1 KCl, 4 NaCl, 4 Mg-ATP, 10 Na-phosphocreatine, 0.4 Na_2-GTP, 0.25 Fluo-5F, 0.02 Alexa-594; ~290 mOsm, pH: 7.2-7.25, data corrected for 11 mV junction. Electrophysiological data were acquired at 20 kHz and filtered at 3 kHz using a Multiclamp 700A or 700B amplifier (Molecular Devices) and a custom data acquisition program in Igor Pro (Wavemetrics).

2.5.4 Synaptic Stimulation Experiments and Pharmacology

For channelrhodopsin stimulation experiments (Figs. 1, 2, 4, 5, 8, S1, S2), pairs of blue light stimulation (472 nm LED through 40x objective, 2 x 1ms at 20 Hz, or more complex patterns in Fig. 8) or stimulation via theta stimulating electrode (2 x 200 µs at

20 Hz, Fig. 1C, E) occurred at regular 15s intervals to avoid induction of plasticity. Theta simulating electrodes were placed ~100-150 μm lateral to the recording electrode, within layer 5. Light power or electrode amperage were adjusted for each cell to minimize polysynaptic responses, but generally ranged from 0.5 to 2 mW/mm^2 and 0.01-0.2 mA, respectively. Pyramidal cell subtype was identified based on intrinsic excitability during the first two minutes of recording, as described previously (Fig. S2, Clarkson et al. 2017). The following criteria were used to exclude cells from data analysis: 1) total temperature range of >1.0°C within one experiment, 2) series resistance (Rs) of > 20 MΩ or change in Rs of > 20%, 3) holding current (I_{hold}) < -100 pA, or change in I_{hold} > ±50pA, 4) change in input resistance (R_{in}) > 25%, 5) violation of any of these criteria sooner than 5 minutes after the last measurement timepoint.

Baseline data began 10 minutes post-break in (about 7-8 minutes after start of light stimulation) and lasted for at least 10 minutes. If a stable baseline EPSC trace was observed, SKF-83822 (D1/D5 agonist, Tocris) was dissolved to 10 mM in ethanol vehicle then immediately (<1 minute) diluted in aCSF (20 μM) and applied to the slice for 10 minutes, followed by washout into baseline aCSF. Similar approaches were applied for other pharmacological manipulations, including (*R*)-Baclofen, NBQX, manganese and cadmium, as well as changing extracellular calcium concentration, (distilled H_2O was used as vehicle for all drugs besides SKF, see Results for concentrations). For PKA blockade experiments (Fig. 4), the PKA antagonist H89 was present in all recording solutions (10 μM) as well as the incubation chamber for at least 30 minutes prior to recording. The D1R antagonist SCH was similarly present in all recording solutions for D1R blockade experiments (Figs. 1, 3). For agatoxin TK, ω-conotoxin GVIA and ω-

conotoxin MVIIC (Figs. 4, 6), aCSF was recirculated with the addition of 0.1 mg/ml bovine serum albumin. All drugs were obtained from Tocris Bioscience, with the exception of calcium channel peptide antagonists (agatoxin and ω-conotoxin GVIA and MVIIC) and bovine serum albumin, which were obtained from Peptides International and Sigma-Aldrich, respectively.

2.5.5 Imaging Experiments

For gCaMP experiments, external aCSF also included 50 μM picrotoxin, 10 μM NBQX or DNQX and 10 μM (*R*)-CPP to block GABA-A, AMPA, and NMDA receptors, respectively. AP-evoked bouton gCaMP transients were evoked by a theta-barrel electrode positioned >100 μm from imaged boutons. Boutons were identified via two-photon microscopy (910 nm) based on the string-of-pearls morphology in the red channel (tdTomato / mCherry expression) and sensitivity of green channel fluorescence to extracellular stimulation (gCaMP expression). A train of three extracellular stimulations (200 μs at 20 ms interval) was delivered to evoke bouton-restricted, tetrodotoxin-sensitive gCaMP signals. Approximately 20-30 trials were obtained, followed by application of drug (as with ChR2 stimulation experiments) and another 20-30 trials. Data are displayed as ΔF/F, or as peak ΔF/F normalized to the baseline mean peak ΔF/F.

For imaging of local PFC boutons, K-Gluconate internal solution was used as in ChR2 stimulation experiments, except EGTA was replaced with 250 μM Fluo-5F and 20 μM Alexa 594. Axons were traced to find an offshoot that contained the string-of-pearls morphology, and calcium influx was elicited via precisely-timed single action potentials

generated by short current injections at the soma (2-2.5 nA x 2ms). The same inclusion criteria applied to ChR2 stimulation experiments were applied here, except the holding-current criterion was modified for current-clamp (exclude if membrane voltage (V_m) > -63 mV or changed by > ±5 mV). Data were always obtained simultaneously from two neighboring boutons to determine whether variability correlated across boutons (see "Optical Fluctuation Analysis").

For imaging of postsynaptic spines during uncaging experiments (Fig. S4) slices were perfused with 3 mM MNI-caged-L-glutamate, and 20 μM Alexa 488 was added to the internal solution. Neurons were imaged at 810 nm and MNI-glutamate was uncaged at 720 nm (1 ms pulses, 5-8 mW at focal point). Spines on the basal dendrites within 15 μm of the slice surface were chosen for uncaging. EPSC amplitudes were calculated from the average of 5-10 trials before and 10 minutes after SKF or vehicle application. Paired pulses with modest facilitation were obtained by increasing the laser intensity by 40% on the second pulse.

For imaging of postsynaptic spines during Optical Quantal Analysis experiments (Fig. 2D-F), cells were filled with Cs internal solution containing 250 μM Fluo-5F and 20 μM Alexa 594. Experiments were done in the presence of 10 μM NBQX and 10 μM D-Serine. Neurons were voltage-clamped at 0 mV and trains of 5x LED pulses were delivered to the slice in frame-scan mode at 0.06 Hz to locate spines with detectable Ca transients. Due to changes in microscope configuration to allow for simultaneous LED stimulation and imaging, fluorescence was collected on substage detectors only. To avoid damage to our GaAsP PMTs from the LED, a fast physical shutter was inserted in the detection path between the substage periscope and PMT beamsplitter cube housing

(Sutter IQ35). Success trials (Fig. 2E-F) were defined when peak ΔF/F exceeded 1, 2 or 3 standard deviations of baseline ΔF/F noise within 10 ms of shutter reopening.

2.5.6 Optical Fluctuation Analysis

Optical fluctuation analysis models calcium influx as a binomial process arising from *N* CaVs, each with single-channel current *i* and open probability *p*. This process is similar to nonstationary fluctuation analysis of electrophysiological recordings, but modified to account for added sources of variability in imaging data that do not reflect variance in channel opening, including dark noise and shot noise. Because variances add linearly, the variance predicted by dark noise and shot noise alone can be subtracted from the measured variance to obtain variance related to CaV activity (Fig. 6D):

$$\sigma_{CaV}^2 = \sigma_F^2 - \sigma_d^2 - \sigma_s^2 \qquad (1a)$$

where dark noise, σ_d^2 , is the product of the width of the bouton in pixels, N_p , and the estimated dark noise per pixel, $\sigma_{d,p}^2$:

$$\sigma_d^2 = N_p \, \sigma_{d,p}^2 \qquad (1b)$$

and shot noise, σ_s^2, is the product of the mean change in peak fluorescence, $\langle \Delta F \rangle$, and the intensity per photon (in arbitrary units), q:

$$\sigma_s^2 = q \, \langle \Delta F \rangle \qquad (1c)$$

The dark-noise parameter, $\sigma_{d,p}^2$, was measured in every experiment during the initial 50 ms of each trial (see Fig. 6B) by measuring the variance at each pixel over multiple trials and averaging this variance across pixels. The shot-noise parameter q was

estimated by imaging a pipette filled with fluorescein with varying laser intensities and fitting the observed variance to the line:

$$\sigma_F^2 = q\,\langle F\rangle + \sigma_d^2 \qquad (1d)$$

Once q and $\sigma_{d,p}^2$ are measured, the inverse-square of the CaV-related coefficient of variation can then be estimated as:

$$CV_{CaV}^{-2} = \frac{\langle \Delta F\rangle^2}{\sigma_{CaV}^2} \qquad (2)$$

One can make quantitative predictions as to how this variance should vary with $\langle F\rangle$ under different conditions. Specifically, CV_{CaV}^{-2} should either reduce linearly, not change, or reduce quickly (nonlinearly, as a "linear rational function") with reductions in *N*, *i* or *p*, respectively:

$$for\ \Delta N = R \ \rightarrow\ \Delta CV_{CaV}^{-2} = R \qquad (3)$$

$$for\ \Delta i = R \ \rightarrow\ \Delta CV_{CaV}^{-2} = 1 \qquad (4)$$

$$for\ \Delta p = R \ \rightarrow\ \Delta CV_{CaV}^{-2} = \frac{R(1-k)}{1-kR} \qquad (5)$$

where $R = \langle F_{post}\rangle/\langle F_{baseline}\rangle$ and $k = p_{baseline}$.

To ensure that variance was related to fluctuations in CaV activity, care was taken to minimize other sources of variance, including optical drift. Data were excluded if: 1) the timing of the action potential peak changed by>0.1 ms), 2) trial-by-trial variability in peak ΔG/R after the AP was correlated when monitored between two simultaneously-imaged boutons in series, or 3) failures were observed in both boutons within the same trial, as these effects could result from AP conduction failures rather than independent CaV opening failures. Furthermore, time-locked vehicle controls showed no rundown of more than 5% up to 100 trials, after which spontaneous rundown of peak ΔG/R was

occasionally observed; therefore, all OFA experiments were limited to a maximum of 100 trials, and variance was estimated with trial-to-trial correction for drift:

$$\sigma_F^2 = \frac{1}{2(n-1)} \sum_{i=1}^{n-1} (\Delta F_{i+1} - \Delta F_i)^2 \quad (6)$$

where n is the number of trials. This is equivalent to the standard measurement of variance as the sum of squared difference from the mean for an experiment without systematic drift, but has the advantage of minimizing unwanted increases in variance due to runup or rundown.

2.5.7 Computational Modeling

All modeling was performed in Python 3.5 (Numpy version 1.11). Images in Figure 7 were generated using Matplotlib version 2.0. See Supplemental Table 1 for a comprehensive list of model parameters in all models. Models were subjected to continuous integration testing using pytest via Travis CI (https://travis-ci.org/kenburke/synapseModel) to ensure successful execution across a wide range of combinations of parameter values, including rejection of invalid parameters (e.g. negative channel open probabilities or trial numbers).

We first designed a reduced computational model of synaptic transmission in order to directly incorporate the binomial parameters obtained from optical fluctuation analysis. We simulated 50 presynaptic axons, where calcium influx in response to each simulated action potential was modeled as the result of a binomial process resulting from *N* CaVs, each with independent probability *p* of increasing the calcium concentration instantaneously by amount *i* (in arbitrary units). Calcium concentration decayed with a

single-exponential timecourse (time constant=50 ms, fit alongside Hill function to produce modest paired-pulse facilitation, Brenowitz and Regehr, 2007). We simulated the stochastic opening of single CaVs using a Monte Carlo method by generating an array of random uniformly distributed numbers in the range $[0, 1)$ and testing whether the generated numbers were less than the open probability *p* on any given trial. Total calcium concentration was then calculated as the sum of all successful CaV openings (*i* current each) and residual calcium present from previous APs.

Vesicle release probability P_R was then calculated per synapse as a Hill function of the calcium concentration (when zero CaVs opened in response to a stimulus, P_R was set to zero to prevent release purely due to residual calcium). The maximum release probability per vesicle was a parameter that we hand-tuned in order to obtain realistic values of release probability (see Table S1, "vesicle_prox"). Individual release events were then modeled using a Monte Carlo method akin to CaV channel openings. Total quantal content was calculated as the total number of successful vesicle release events across synapses for a single trial. Quantal content was convolved with an AMPA-like waveform (kinetics adapted from Jonas *et al.*, 1993) for visualization purposes only, as we wanted to avoid the contribution of postsynaptic filtering in our estimation of neurotransmitter release statistics.

This process was repeated 10,000 times for each parameter set tested. Modulation of individual model parameters (e.g. i_{CaV} or p_{open}) repeated this array of 10,000 simulations for a range of parameter values, scaling the parameter from 20% to 100% of its baseline value in 5% increments. In order to make fair comparisons between presynaptic configurations with differing numbers of CaVs driving release, we held

constant the expected average calcium influx (the product $N_{CaV} \cdot i_{CaV} \cdot p_{open}$). This was achieved by multiplying the number of CaVs and dividing the single-channel current by the same parameter, "num_cav_ratio" (see Supplemental Table 1). PPR and CV^{-2} were calculated using the quantal content rather than the peak AMPA current for computational efficiency because they were mathematically equivalent. Simulation runs were then saved in a .pkl format for subsequent reference and replication.

In a second simulation, we modeled the diffusion of calcium from CaVs to vesicles explicitly using the "linearized buffer approximation" (Naraghi and Neher, 1997; Neher, 1998):

$$[Ca^{2+}] = \frac{i_{CaV}}{4\pi F D_{Ca} r} exp\left(\frac{-r}{\lambda}\right) \quad (7a)$$

where $i_{CaV} = 0.13\, pA$ (Li et al., 2007; Scimemi and Diamond, 2012), F is the Faraday constant, D_{Ca} is the diffusion coefficient of free calcium (220 $\mu m^2/s$, Allbritton et al., 1992), r is the distance between the vesicle and the calcium influx, and λ is the characteristic length constant:

$$\lambda = \sqrt{\frac{D_{Ca}}{K_{on}[B]_{free}}} \quad (7b)$$

where K_{on} is the rate of calcium binding to free buffer (Klingauf and Neher, 1997) and $[B]_{free}$ is the concentration of free buffer:

$$[B]_{free} = \frac{[B]_{total} K_D}{K_D + [Ca]_{basal}} \quad (7c)$$

where $[B]_{total}$ is the total concentration of endogenous buffer, K_D is the buffer dissociation constant and $[Ca^{2+}]_{basal}$ is the basal free calcium concentration. Taken together, these three equations allowed us to calculate the initial calcium concentration

as a function of distance from the point of calcium influx (assuming rapid equilibration at short distances). The calcium concentration then decayed exponentially, independent of distance, with a time constant of 40 ms to mimic slower timescale extrusion mechanisms (Brenowitz and Regehr, 2007).

The second feature we added to this model was two Hill functions with realistic parameters for calcium affinity and cooperativity to mediate vesicle release and facilitation. The Hill parameters for both functions were adapted from electrophysiological as well as biochemical measurements of affinity and cooperativity for synaptotagmin1 and synaptotagmin7 (Brandt et al., 2012; Scimemi and Diamond, 2012; Sugita et al., 2002). The initial release probability $p_{release}$ was calculated by the first, lower affinity Hill function using instantaneous initial calcium concentration immediately following the AP, which was then facilitated based on the residual calcium concentration preceding the AP via the second Hill function:

$$p_{release} = Hill_{release}([Ca]) \cdot \left(1 + Hill_{facil}([Ca])\right) \qquad (8a)$$

where

$$Hill([Ca]) = \frac{S \cdot [Ca]^N}{EC_{50}^N + [Ca]^N} \qquad (8b)$$

and S, N, and EC_{50} are parameters for maximum value, cooperativity and half-maximal effective concentration, respectively. The values for cooperativity and half-maximal effective concentration were obtained from the literature (see Table S1), and the maximum value parameter S for the release and facilitation Hill functions was tuned to reproduce a realistic baseline release probability (based on OQA data, Fig. 2) and modest baseline paired-pulse facilitation, respectively.

In the initial reduced model, the increase in PPR with reductions in i_{CaV} was the result of both release events being calculated with a single Hill function. With the addition of a second, higher affinity Hill function to mediate facilitation, it was necessary to incorporate vesicle depletion and replenishment parameters to account for the increases in paired-pulse facilitation observed with reductions in i_{CaV} (Abbott et al., 1997; Scimemi and Diamond, 2012; Tsodyks and Markram, 1997). Each "synapse" was paired with one vesicle (because synapses are independent in this model, one could equivalently conceptualize them as independent pairs of release sites and CaV clusters). At the beginning of each trial, it was assumed that all vesicles were replenished and available for release by defining a binary variable $pool\_size$. After calculating calcium influx and stochastic release for the first AP, the variable $pool\_size$ was set to zero at synapses where release was successful. On the second AP, all synapses where $pool\_size = 0$ were randomly "replenished" (i.e. $pool\_size$ set to 1) with a time-dependent probability:

$$Pr_{recov} = 1 - exp\left(\frac{-t}{\tau_{recov}}\right) \quad (9a)$$

where t is the time elapsed since the previous AP (i.e. the inter-stimulus interval), and τ_{recov} is the replenishment time constant. After determining if each empty release site was replenished, the release probability for the second AP was calculated as

$$p_{corrected} = pool\_size \cdot p_{release} \quad (9b)$$

where $p_{release}$ is the output of Eq. 8a.

In the reduced model of Figure 7, when increasing the number of CaVs per synapse we reduced the single channel current in order to maintain constant the expected calcium concentration per synapse. Because we used realistic values for CaV

single-channel current in the diffusion model, when increasing the number of channels per synapse we instead kept single-channel current constant and simply increased the CaV-vesicle distance to keep the expected value of the calcium concentration constant at each synapse (Fig. S7F,I). Without this adjustment, release probability would quickly saturate due to the Hill Function nonlinearity with the addition of even one CaV (data not shown, but see Fig. S7G). The following values for CaV-vesicle distance were used for synapses with the corresponding number of CaVs:

Number CaVs	***CaV-Vesicle Distance (nanometers)***
1	15
2	23.3
3	29.2
5	37.6
10	50.7
50	86.2

Table 2.1: Simulated distances between vesicle and calcium channel cluster
For the diffusion model of presynaptic release, we varied the number of calcium channels with the distance between the channel cluster and the vesicle to hold approximately constant the expected value of the calcium concentration at the vesicle.

In some simulations, facilitation was modelled phenomenologically (Figure S6). In these simulations, we began with the reduced model from Figure 7, but rather than modeling exponential decay of calcium concentration, the vesicle release probability

was calculated directly from the calcium influx per AP. The release probability for the second AP was then scaled according to the following formula:

$$p_{release} = p_{initial}\left(1 + ks(1 - p_{initial})\right) \quad (10a)$$

where $p_{initial}$ is the initial release probability calculated from the Hill function of the calcium concentration, k is the facilitation parameter ("phenom_param", Table S1) and:

$$s = \begin{cases} 1, & \geq 1\ CaV\ opening\ previous\ AP \\ 0, & otherwise \end{cases} \quad (10b)$$

2.5.8 Short-Term Dynamics in Voltage- and Current-clamp

Evaluation of short-term plasticity for longer trains of stimuli and across different frequencies was achieved using the same preparation as earlier ChR2 stimulation experiments but with custom stimulation patterns (Fig. 8). In order to quantify the relative suppression of ongoing activity relative to single EPSCs, we quantified the charge ratio:

$$R_Q = \frac{Q_T}{Amp_1} \quad (11a)$$

where

$$Q_T = \frac{Total\ Charge_{post}}{Total\ Charge_{baseline}} \quad (11b)$$

$$Amp_1 = \frac{First\ Amplitude_{post}}{First\ Amplitude_{baseline}} \quad (11c)$$

For current-clamp experiments (Fig 8), EPSP amplitude was monitored by stimulating once 250 ms before the onset of injected noisy current waveforms. In each cell, rheobase was estimated by injecting one-second long square pulses of current in 25 pA increments until at least one AP was evoked. The noise stimulus was generated

by simulating EPSCs at 1,000 Hz as the product of two exponentials, with amplitude +25 pA and rise / decay time constants of 0.303 / 2.0 ms (Sohal et al., 2009). IPSCs were similarly generated, but with amplitude -25 pA at 250 Hz. The noisy current stimulus was then added to a square pulse of amplitude (rheobase – 50 pA), as the mean of the noisy current stimulus was ~50 pA. Following an initial LED pulse 500 ms after the onset of the noisy-current waveform, intervals corresponding to 1, 5, 10 and 20 Hz were shuffled, generating a train of LED stimuli of varying frequency. Pairs of trials with the same noisy current waveform were interleaved with and without LED stimulation (data not shown). After collecting baseline data, D1R and $GABA_BR$ agonists were bath-applied for 10 minutes before collecting the "post-drug" data. Offline, spikes were detected reliably by crossing 0 mV and LED-triggered averages of instantaneous frequency were calculated using 3 ms bins. The change in evoked spiking quantified in Fig. 8J measured average instantaneous frequency in the 12 ms following an LED pulse. The same inclusion criteria were used for these experiments as outlined for ChR2 oEPSC experiments.

2.5.9 Quantification and Statistical Analysis

All data are shown as mean ± SEM, where "n" refers to the number of cells (for electrophysiological recording experiments) or boutons or spines (for Ca imaging experiments). Summary data and the name and results of statistical tests are interspersed with text in parentheticals in the Results section. Preliminary analysis and data visualization was performed in Igor Pro and MATLAB (MathWorks). Statistical tests used Kruskal-Wallis with Wilcoxon's rank-sum test and the Holm-Sidak correction for multiple comparisons. Significance was set to $p < 0.05$ unless otherwise stated.

2.5.10 Data and Software Availability

All code for computational models of vesicle release, and tutorials for simple simulations or replication, is available at https://github.com/kenburke/synapseModel.

2.6 FIGURES

2.6.1 Main Figures

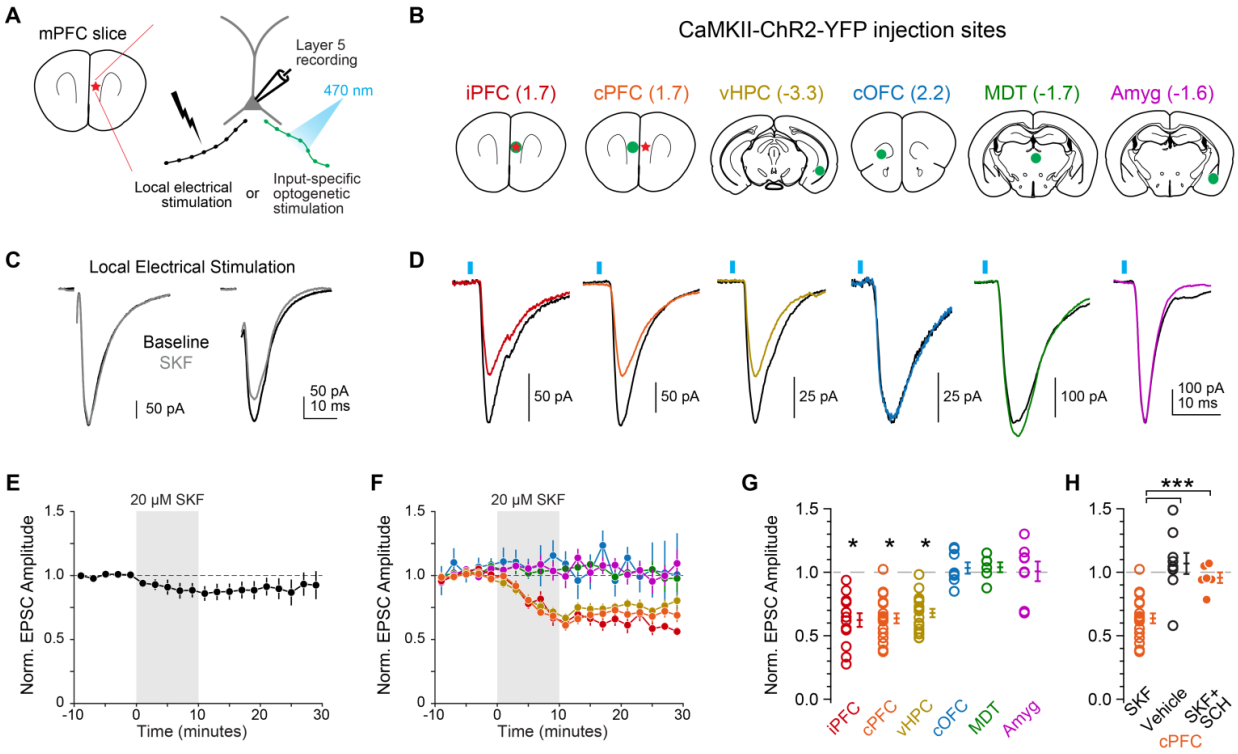

Figure 2.1: D1R Suppresses a Subset of Excitatory Synapses in PFC

A) Schematics of *in vitro* recording location in mPFC (left) and stimulation configurations (right). EPSCs currents were evoked via local theta-barrel electrode or by input-specific ChR2 stimulation.

B) ChR2-expressing virus injection locations, with injection sites shown in green and recording site in red where applicable. Numbers in parenthesis are distance from bregma (mm).

C) Representative effects of D1R activation on electrode-evoked eEPSCs. Baseline: black. Post-SKF: grey.

D) Same as C, but for oEPSCs. Baseline: black. Post SKF: other colors.

E, F) Summary of normalized EPSC amplitude over time for both eEPSC and oEPSC conditions (color coding as in B-D).

G) Summary of change in EPSC after D1R activation (same cells as in F).

H) Modulation of cPFC oEPSCs with vehicle or D1R activation in presence of D1R antagonist SCH23390.

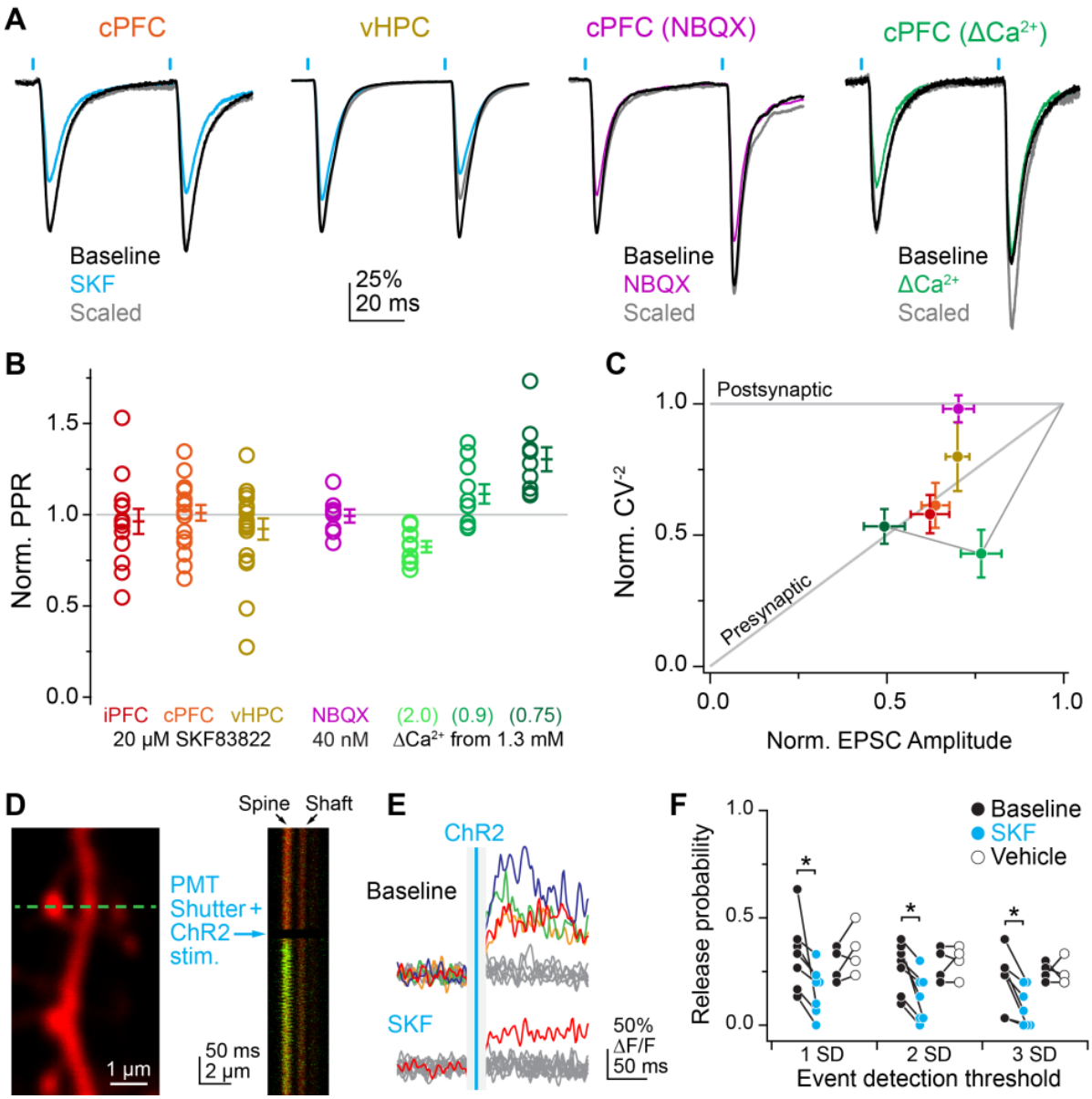

Figure 2.2: D1R Modulates oEPSC Amplitude, Coefficient of Variation and Release Probability, but not Paired-Pulse Ratio

A) Examples of D1R modulation of paired pulses. Baseline: black. Post-SKF: cyan. Post-SKF scaled: grey. From left to right: D1R activation of oEPSCs from cPFC and vHPC, subsaturating NBQX on cPFC oEPSCs (40 nM) and reduced extracellular calcium on cPFC oEPSCs. All traces scaled to baseline amplitude of first oEPSC for comparison.

B) Summary of PPR change. Colors as in A, with D1R activation of iPFC oEPSCs in red. All values normalized to pre-drug baseline, except ΔCa conditions are normalized to PPR at 1.3 mM.

C) Normalized CV plotted against change in oEPSC amplitude. Colors as in B. Line connects green ΔCa conditions in order of decreasing extracellular Ca concentration.

D) Spine imaging configuration for OQA. Left: Example of Alexa 594 fluorescence in dendritic shaft and spines, with linescan location indicated by dashed blue line. Right: Example single trial linescan of dendritic spine and shaft on left. PMTs were shuttered during LED stimulation. Note that shutter reopening resulted in a small amount of vibration, which is largely cancelled out when averaging fluorescence over the spine head area of the linescan.

E) Trials before and after bath application of SKF. Data analyzed from Fluo-5F fluorescence only ($\Delta F/F$). Grey and non-grey lines indicate failure and success trials, respectively. Blue vertical line is ChR2 timing.

F) Changes in P_R with D1R stimulation or vehicle. All P_R measures are calculated as the ratio of successful trials to total trials. Different thresholds for defining a success trial are shown along the x-axis.

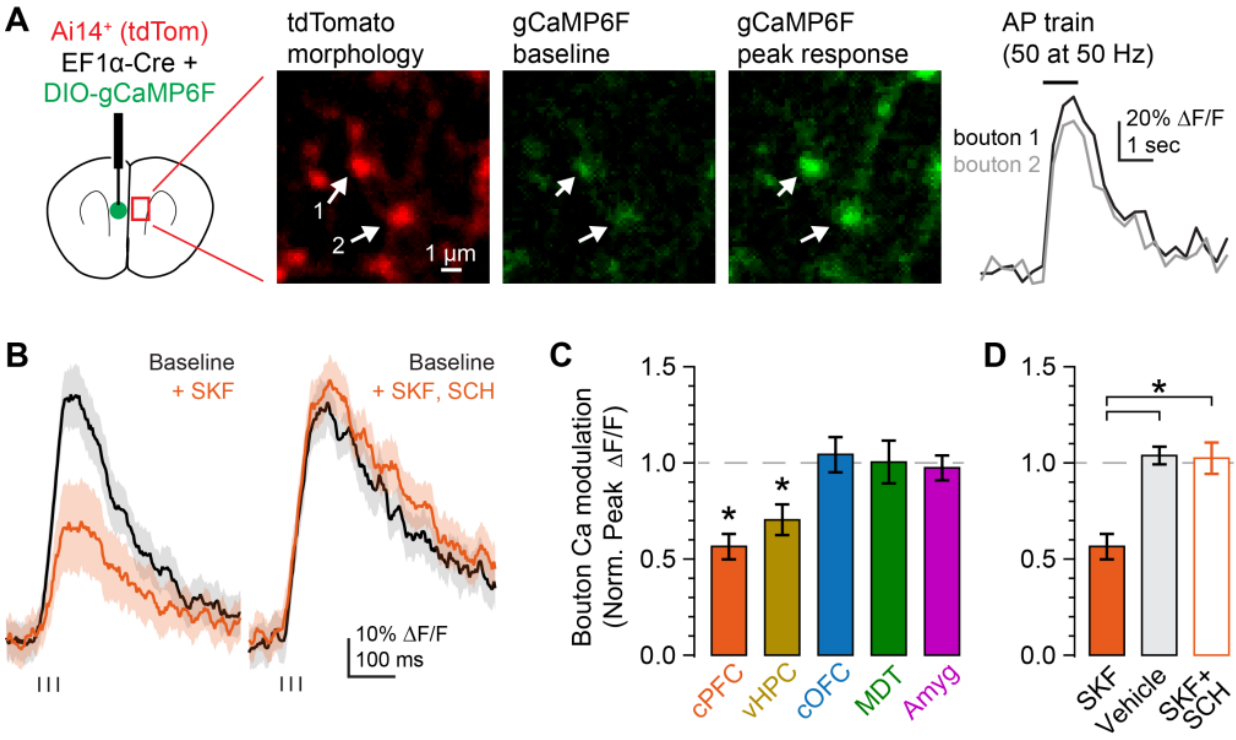

Figure 2.3: D1R Suppresses Evoked Axonal Calcium Influx in PFC

A) Long-range axon imaging configuration. Left: Schematic of recording. Injection site in green, stimulation and imaging location in red box. Middle: Example fluorescence response of axonal boutons. Red fluorescence was used to locate boutons, green fluorescence was monitored in response to electrical stimulation. Arrows highlight two boutons quantified in right panel. Right: Normalized change in fluorescence for example boutons from middle panels.

B) Evoked gCaMP6f signals in PFC boutons. SKF-mediated suppression was blocked by SCH23390.

C) Summary of change in peak ΔF/F in response to D1R activation for different long-range iputs to PFC (colors as in Figs. 1-2).

D) Summary of modulation of peak ΔF/F responses from cPFC axonal boutons with vehicle application or D1R activation in presence of D1R antagonist SCH23390.

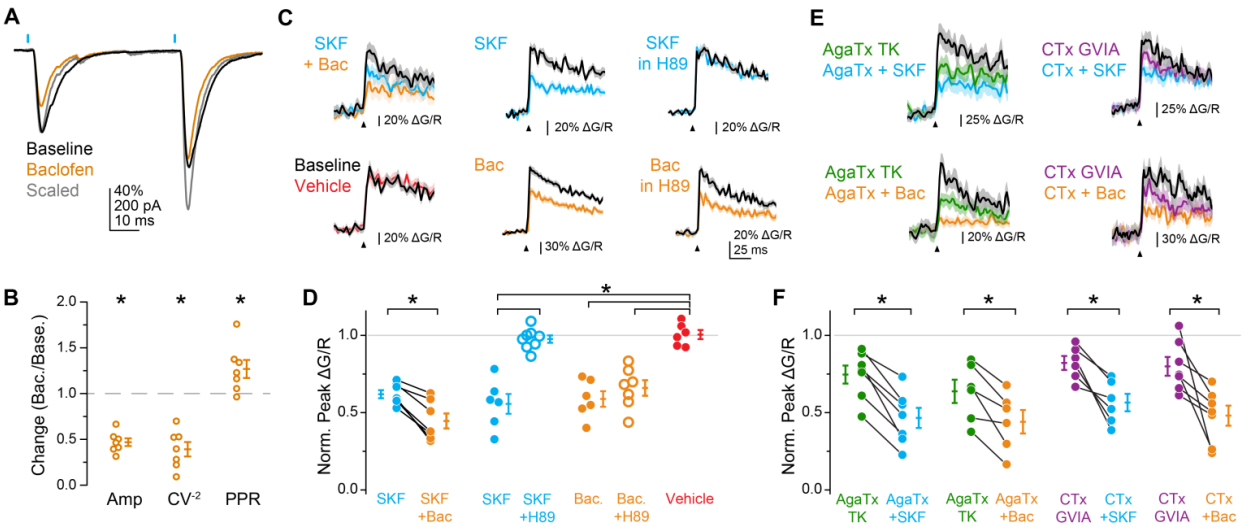

Figure 2.4: $GABA_BR$ Suppresses Presynaptic Calcium Influx with Canonical Increase in PPR

A) Example of $GABA_BR$ modulation of cPFC oEPSCs and PPR (as in Fig. 2A).

B) Summary of $GABA_BR$ modulation of oEPSC amplitude, CV^{-2} and PPR.

C) Examples of AP-evoked bouton calcium transients for D1R followed by $GABA_BR$ activation, D1R activation alone, D1R activation with 10 μM H89, vehicle application, $GABA_BR$ activation alone, or $GABA_BR$ activation with H89. Data plotted as mean ΔG/R with shaded error bars indicating within-condition SEM.

D) Summary of change in peak ΔG/R for conditions in C.

E) Example responses, as in C, for effects of D1R or GABABR activation with concurrent $Ca_V2.1$ or $Ca_V2.2$ block.

F) Summary of change in peak ΔG/R for conditions in E.

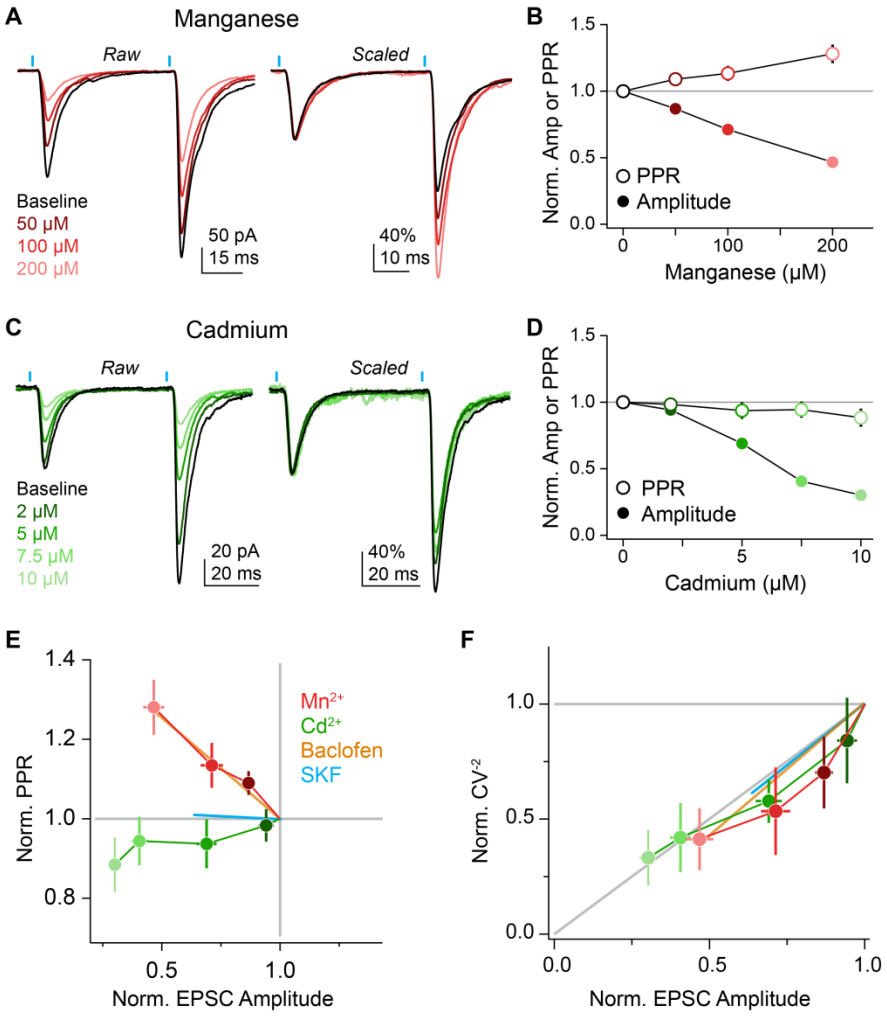

Figure 2.5: CaV Antagonists with Different Binding Kinetics Mimic D1R and $GABA_BR$

A) Example cell with increasing manganese concentrations. Left: raw oEPSCs. Right: scaled to initial oEPSC amplitude.

B) Summary for manganese effects on oEPSC amplitude and PPR.

C-D) Same as A-B, but for cadmium.

E-F) Normalized PPR and CV^{-2} for manganese and cadmium conditions vs. normalized oEPSC amplitude. D1R and $GABA_BR$ modulation shown in cyan and orange, respectively, for reference.

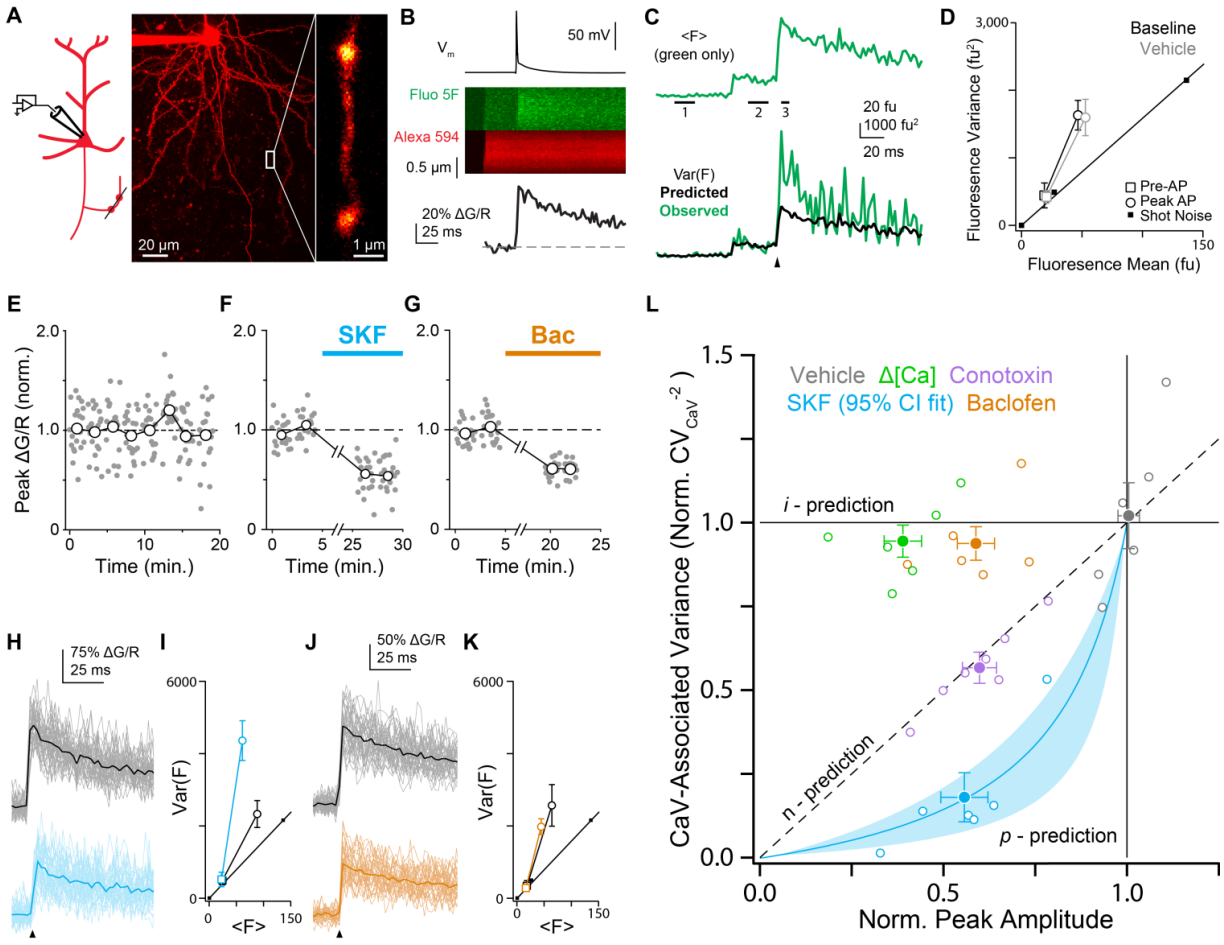

Figure 2.6: D1R and GABA$_B$R Modulate Different Biophysical Properties of Presynaptic CaVs

A) OFA recording configuration. Left: Schematic for local axonal bouton imaging. Center: Z-projection image of dendritic and axonal processes containing Alexa 594. Right: magnification of center panel highlighting two boutons in series along axon branch.

B) Bouton calcium response. Top: Mean membrane voltage (V_m) in response to short-duration somatic current injection (2-2.5 nA x 2 ms). Middle: Example mean fluorescence response of axonal bouton over 20 trials (note: 2-photon excitation begins with 50 ms delay to measure dark noise). Bottom: Mean ΔG/R response as a function of time for data in middle panel (dashed line indicates baseline fluorescence; timepoints before laser excitation excluded for clarity).

C) Top: mean response, green channel only. Numbers and black bars indicate time range for calculating 1) dark noise, 2) baseline and 3) peak mean and variance. Bottom: variance, $Var(F)$, compared to variance predicted by dark and shot noise alone (black trace). Arrowhead: AP timing.

D) Variance-Mean plot before and after vehicle application. Variance and mean fluorescence were measured at baseline (empty squares, “Pre-AP”) and peak response (empty circles, “Peak AP”) time ranges (ranges 2 and 3 from Fig. 6C,

respectively). All values corrected for dark noise. Shot noise measurements shown for reference (filled squares and linear fit). Error bars are 1 S.D. from estimates obtained from multiple timepoints per range.

E) Peak ΔG/R response of a single bouton over time. Grey points represent individual trials, open circles are average of 20 trials.

F, G) Peak ΔG/R responses of boutons before and after D1R or $GABA_BR$ activation.

H) Mean ΔG/R with individual trials for baseline (top) and post-drug (bottom) conditions with D1R activation.

I) Variance-mean plot for one cell before (black) and after (cyan) D1R activation (same cell as in Fig. 6H).

J, K) Example cell with $GABA_BR$ activation, as in H, I.

L) Normalized CaV-associated Variance versus Normalized Peak Amplitude. (Vehicle, peak ΔG/R=1.01±0.03, CV^{-2}=1.02±0.10, n=6)

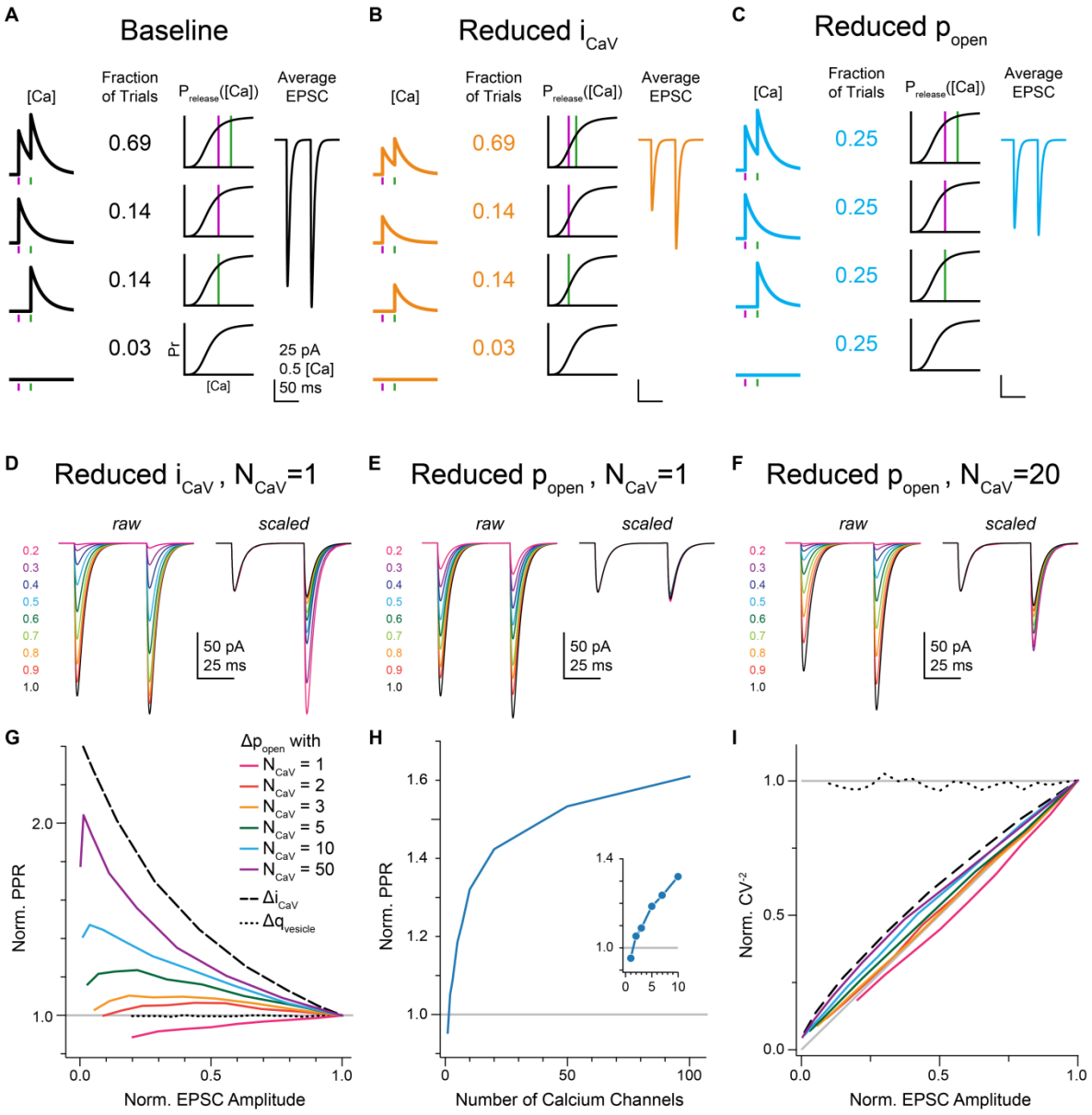

Figure 2.7: Model of Synapse Reproduces Non-Canonical Presynaptic Modulation

A) Reduced Model of Presynaptic Release. Rows are possible trial outcomes for different CaV p_{open} values for a single bouton given release mediated by one presynaptic CaV. Columns, from left to right: presynaptic calcium concentration (purple/green tick marks indicate first and second AP), fraction of trials where this occurred, P_R as a function of calcium concentration (calcium concentrations for two APs indicated by purple/green lines), total average EPSC across synapses and trials.

B, C) As in A, but with CaV single-channel current i_{CaV} or open probability p_{open} reduced to 60% of baseline to mimic OFA results for $GABA_BR$ and D1R, respectively.

D) Suppression of EPSC by graded reduction in i_{CaV} with release mediated by one presynaptic CaV. Left: Colors indicate fraction reduction in i_{CaV}. Right: scaled to first EPSC amplitude.

E) Suppression of EPSC by graded reduction in p_{open}, as in D.
F) Suppression of EPSC by graded reduction in p_{open}, with release mediated by 20 CaVs.
G) Normalized PPR vs. normalized EPSC amplitude for reductions in i_{CaV}, $q_{vesicle}$ or p_{open} under different numbers of presynaptic CaVs mediating release.
H) Normalized PPR with reduction in p_{open} to 60% of baseline, as a function of number of presynaptic CaVs mediating release. Grey line indicates no change in PPR. Inset: Expanded view of first few channel numbers.
I) Normalized CV^{-2} plotted against normalized EPSC amplitude for reductions in i_{CaV}, $q_{vesicle}$ or p_{open} under different numbers of presynaptic CaVs mediating release.

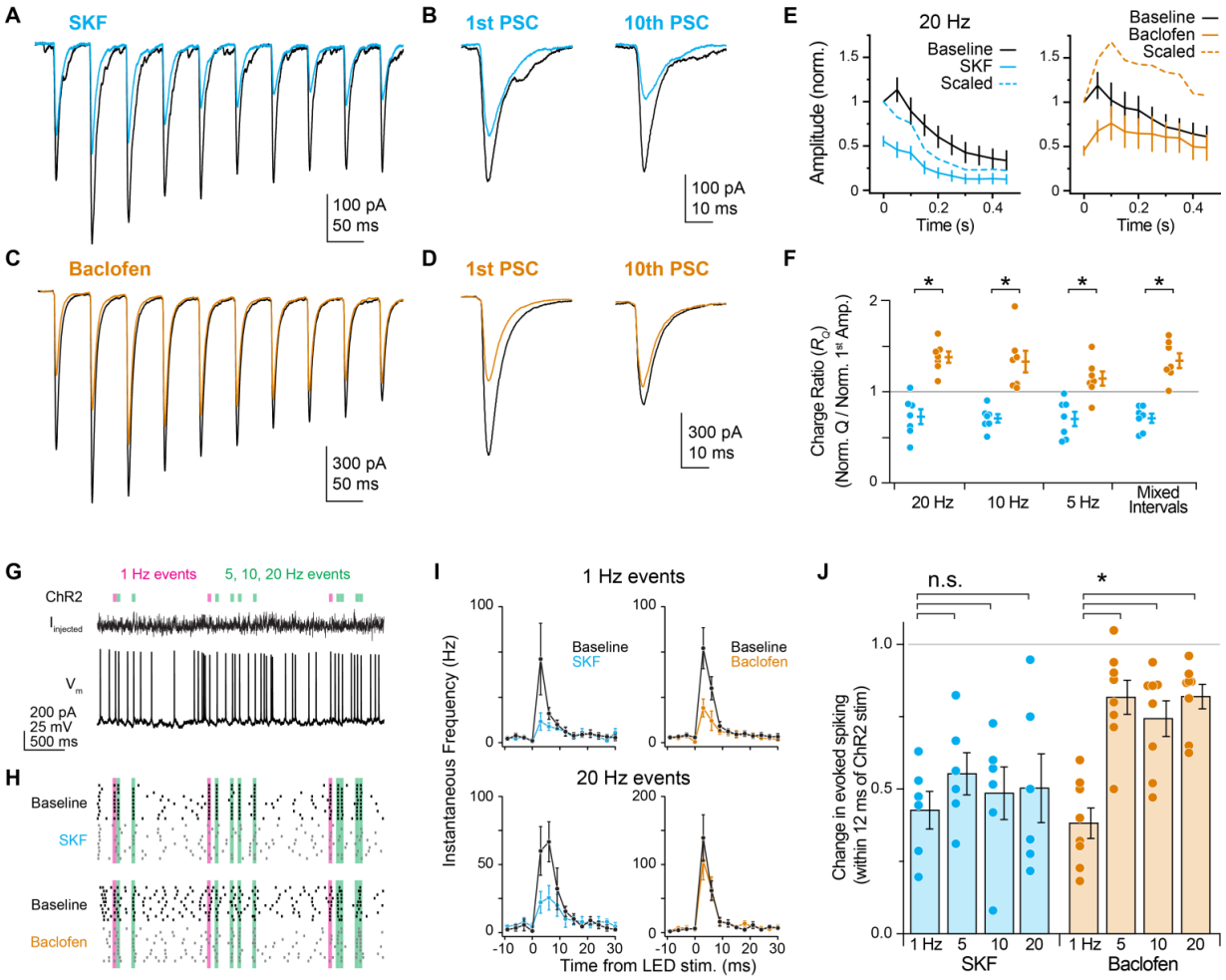

Figure 2.8: D1R and $GABA_BR$ Differentially Filter Ongoing Synaptic Activity

A) Train of ten oEPSCs at 20 Hz before and after D1R stimulation.

B) Expanded view of first and tenth oEPSC.

C-D) As in A-B but with $GABA_BR$ stimulation.

E) Modulation of ongoing activity at 20 Hz. Left: oEPSC amplitudes before and after D1R stimulation. Right: As on left, but with $GABA_BR$ activation.

F) Suppression of ongoing activity relative to first amplitude. The charge ratio was consistently larger for $GABA_BR$ activation than for D1R activation across multiple frequencies. "Mixed Intervals" was a predetermined combination of 3 inter-stimulus intervals at 5, 10 and 20 Hz, shuffled.

G) Recording configuration for current-clamp experiments. Top: Train of LED pulses to activate ChR2-positive long-range inputs from cPFC (color-coded by preceding interval being equal to or faster than 1 Hz for pink and green tic marks, respectively). Middle: Simulated PSC waveform injected into the soma through the recording electrode. Bottom: Recorded membrane voltage.

H) Modulation of spike timing. Top: Example raster plot (same cell as in G) of spike times over trials with different injected PSC waveforms before (above, "Baseline") and after (below, "SKF") D1R activation. Bottom: As above, but with $GABA_BR$

activation. Black tic marks indicate spike times, pink and green bars indicate timing of 1Hz and >1Hz LED pulses, respectively.

I) Modulation of LED-evoked spiking. Top: Instantaneous frequency of spiking aligned to 1Hz LED stimuli, averaged across cells, before and after D1R and $GABA_BR$ activation for left and right plots, respectively (n=6 and 8 for D1R and $GABA_BR$). Bottom: As above, but aligned to 20Hz LED stimuli.

J) Summary data of neuromodulation of LED-evoked spiking. Bars are mean ± SEM. Circles are single cells.

2.6.2 Supplemental Figures

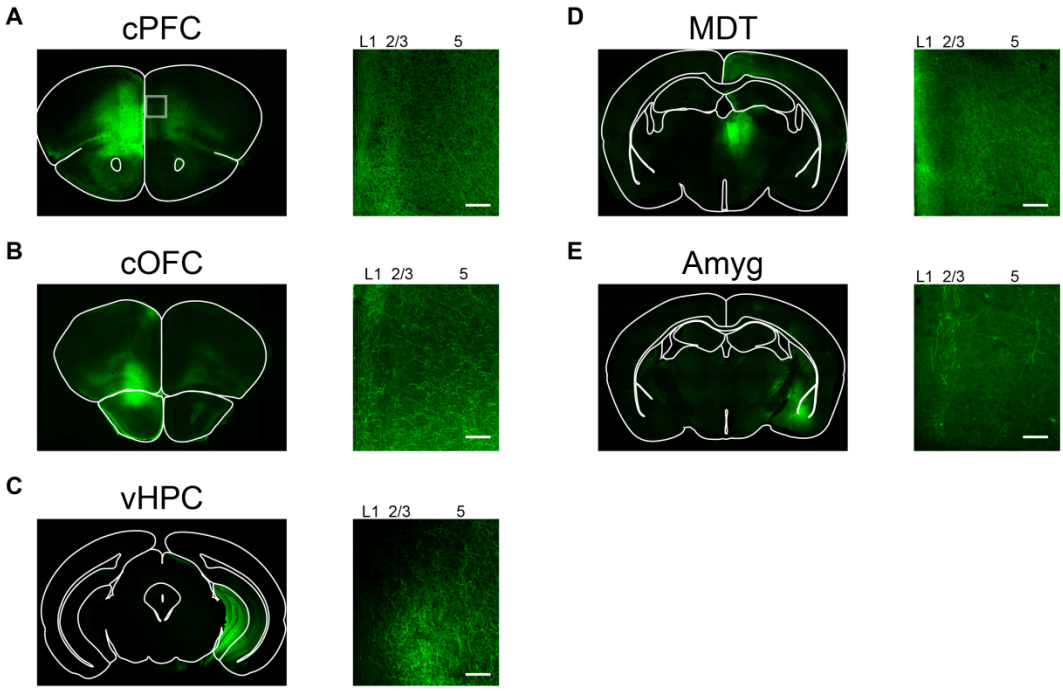

Figure 2.9 (S1, Related to Main Figure 2.1): Viral Injection Sites
(A-E) Examples of ChR2-eYFP viral expression for long-range inputs into PFC from contralateral PFC, contralateral orbitofrontal cortex, ipsilateral ventral hippocampus, ipsilateral mediodorsal thalamus and ipsilateral amygdala, respectively. *Left*: ChR2-eYFP expression in the injection site, with outline of landmarks in white. Transparent box indicates approximate location of confocal images. *Right*: Confocal image of axonal projections to PFC (left side aligned to pia, scale bar indicates 100 μm). For injection site coordinates, see Methods.

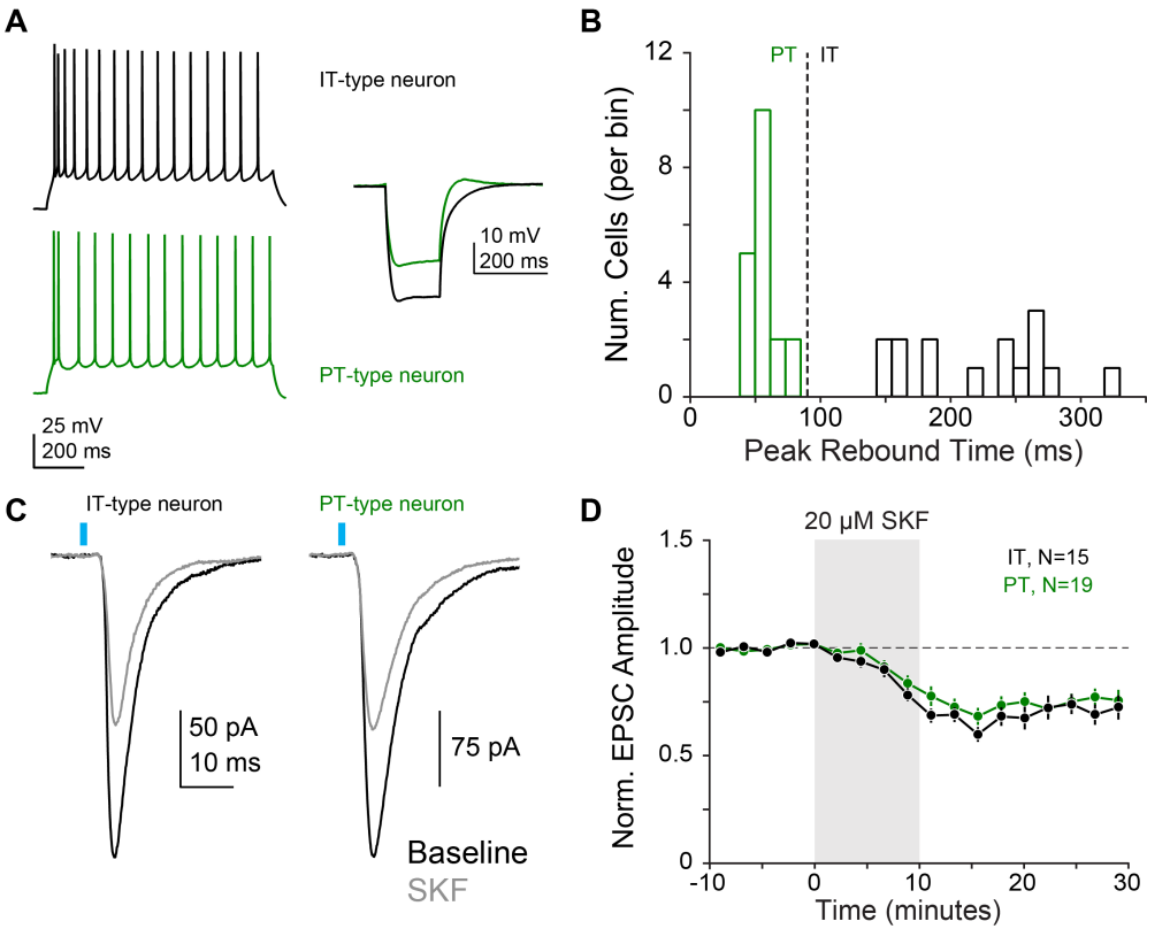

Figure 2.10 (S2, Related to Main Figure 2.2): D1R Modulation Does Not Depend on Postsynaptic Cell Subtype

(A) Example responses of intratelencephalic and pyramidal tract (IT vs PT) neurons to depolarizing and hyperpolarizing somatic current injections. Note rapid voltage rebound after hyperpolarizing current offset in PT but not IT cells.

(B) Distribution of peak voltage rebound after hyperpolarizing current offset across cells. Cutoff of 90 ms (dashed line) separating the two cell subtypes obtained from Clarkson et al., 2017.

(C) Example oEPSC responses from an IT (black/grey) and PT (black/green) before and after D1R stimulation (black vs. color; PT-like, 0.69 ± 0.04, n = 19; IT-like, 0.63 ± 0.03, n = 15; p = 0.47, rank-sum test).

(D) Summary diary plot of normalized oEPSC amplitude over time for classified IT vs PT cells. Cells with projections from either cPFC or vHPC were pooled for this analysis (see Fig. 1F).

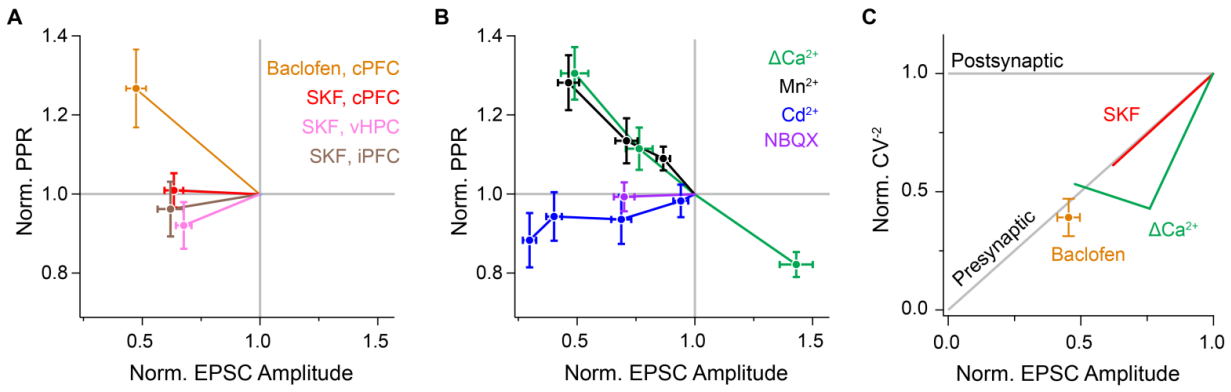

Figure 2.11 (S3, Related to Main Figure 2.2-2.5): Paired-Pulse Ratio, CV^{-2} and oEPSC Amplitude Across Experimental Conditions

(A) Normalized PPR plotted against normalized oEPSC amplitude for D1R and $GABA_BR$ activation at cPFC inputs, as well as D1R activation at vHPC and iPFC inputs.

(B) Normalized PPR plotted against normalized oEPSC amplitude for several control conditions (all at cPFC inputs): ΔCa^{2+} (2.0, 0.9, and 0.75 mM, normalized to 1.3 mM), Cd^{2+} (2, 5, 7.5, 10 μM), Mn^{2+} (50, 100, 200 μM), NBQX (40 nM).

(C) Normalized CV^{-2} plotted against normalized oEPSC amplitude for $GABA_BR$ activation at cPFC inputs. D1R activation and extracellular Ca^{2+} reduction conditions shown for reference in red and green, respectively. Expected normalized CV^{-2} functions of normalized oEPSC amplitude for postsynaptic and presynaptic modulations (y=1 and y=x) plotted as grey lines for reference.

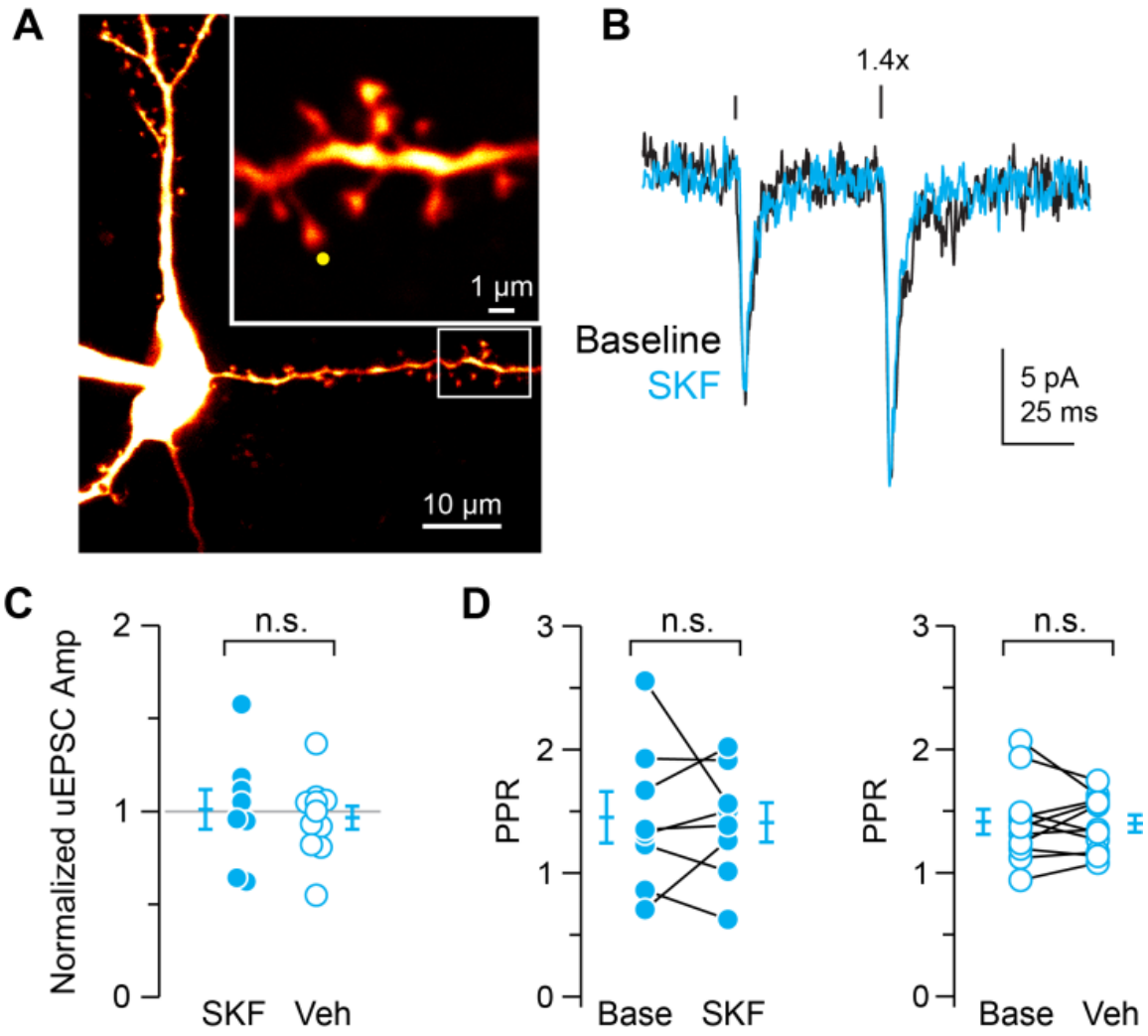

Figure 2.12 (S4, Related to Main Figure 2.2): Glutamate Uncaging-Evoked uEPSCs are Not Altered by D1R Activation.

(A) Maximum intensity 2PLSM Z-stack of layer 5 pyramidal cell visualized with AlexaFluor 488. Spine chosen for uncaging is highlighted in inset by yellow dot.

(B) A pair of uEPSCs were evoked at an interval of 50 ms. Facilitation was mimicked by increasing laser intensity on the second pulse.

(C) uEPSC amplitude following SKF or vehicle application, normalized to baseline value per spine. Circles are single spines, bars are mean ± SEM.

(D) PPR before and after SKF or vehicle application. Circles and lines connect measurements at single spines, bars are mean ± SEM.

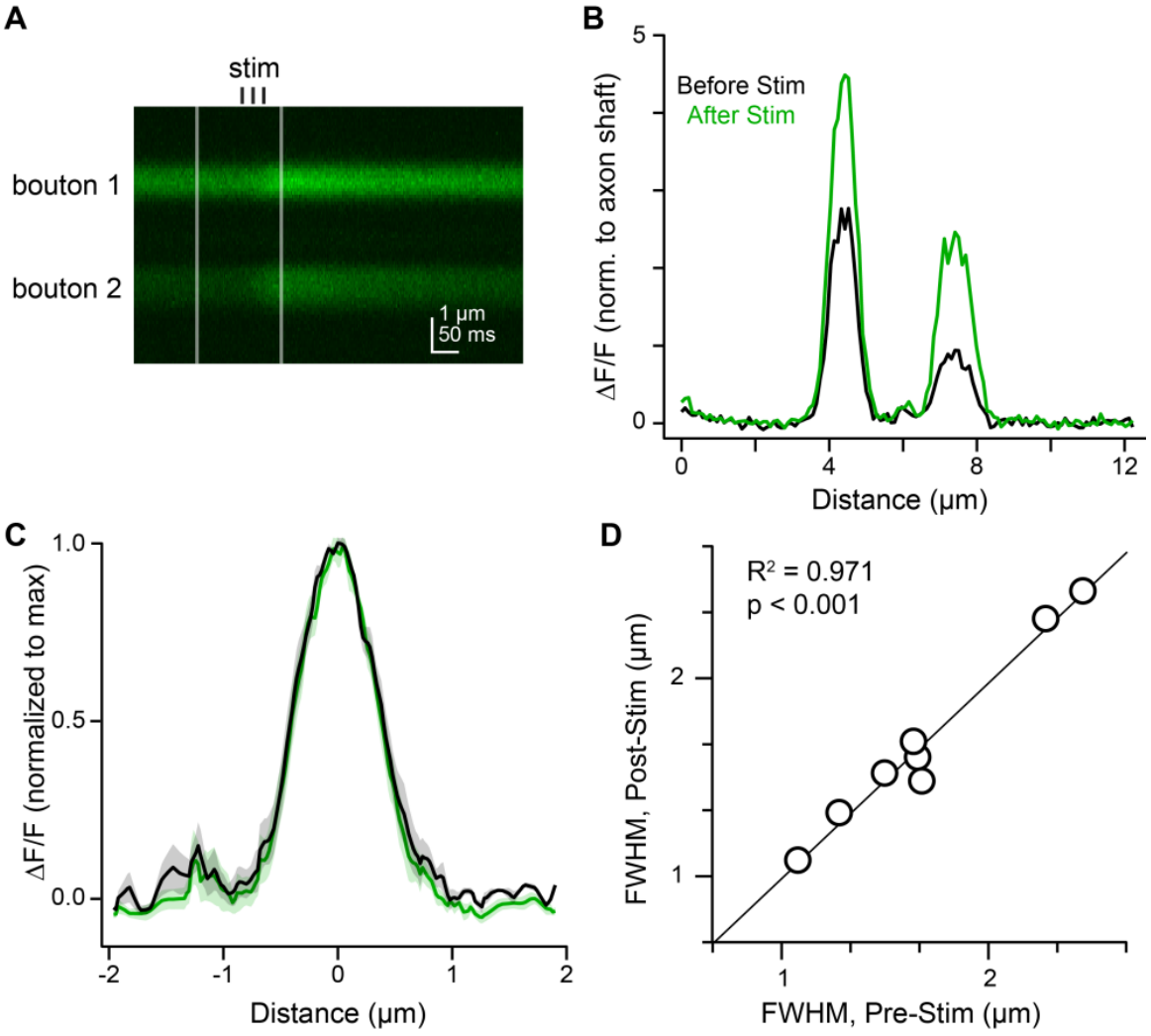

Figure 2.13 (S5, Related to Main Figure 2.3): Evoked gCaMP Responses are Restricted to the Bouton

(A) Example recording from a pair of gCaMP-expressing boutons in series in response to a train of 3x stimuli (black tic marks), with distance along the axon and time on the y-axis and x-axis, respectively. White lines indicate time of baseline and peak measurements.

(B) Mean gCaMP fluorescence as a function of distance along the axon, before (black) and after (green) extracellular stimulation. Time of measurement corresponds to vertical white lines in A. Fluorescence is reported as mean ΔF/F, normalized to axonal shaft fluorescence at baseline.

(C) As in B, but aligned and normalized to peak response across boutons (n = 8, data shown as mean ± SEM).

(D) Correlation in full-width half-max (FWHM) before and after stimulation for each bouton in C.

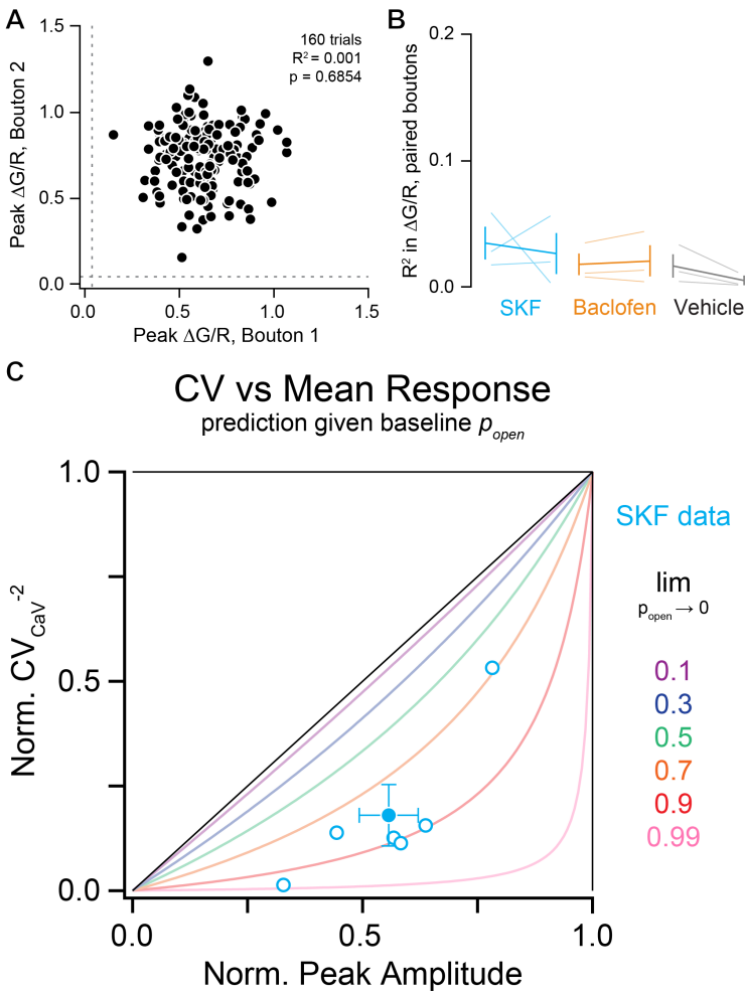

Figure 2.14 (S6, Related to Main Figure 2.6): Axonal Bouton Calcium Signals are Uncorrelated, and Predicted Variance Function for Different Values of Baseline Open Probability

(A) Example pair of boutons in time-locked control experiments with 160 trials. Similar plots and correlation statistics were generated for baseline periods for each bouton pair to detect overall correlated signals as well as single-trial correlated failures as exclusion criteria (see Experimental Procedures).

(B) Correlations between boutons did not increase after D1R, $GABA_BR$ or vehicle stimulation (pre-SKF R^2 = 0.035 ± 0.012, post-SKF R^2 = 0.026 ± 0.016 ; pre-Baclofen R^2 = 0.018 ± 0.009, post-Baclofen R^2 = 0.020 ± 0.012 ; pre-vehicle R^2 = 0.017 ± 0.009, post-vehicle R^2 = 0.004 ± 0.003)

(C) Normalized CaV-associated Variance versus Normalized Peak Amplitude (see Fig. 6L). Modulation of bouton calcium signal variance by D1R plotted against predicted changes for suppression of CaV p_{open}, given different baseline value of p_{open}. Note that the difference between model predictions for reductions in p_{open} and the number of CaVs *N* (black diagonal line) are largest for high baseline open probabilities.

Main Figure Model

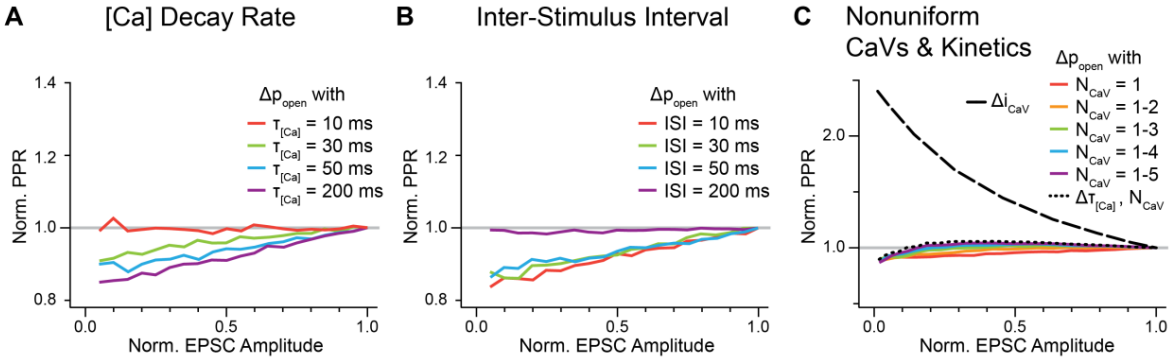

Diffusion Model

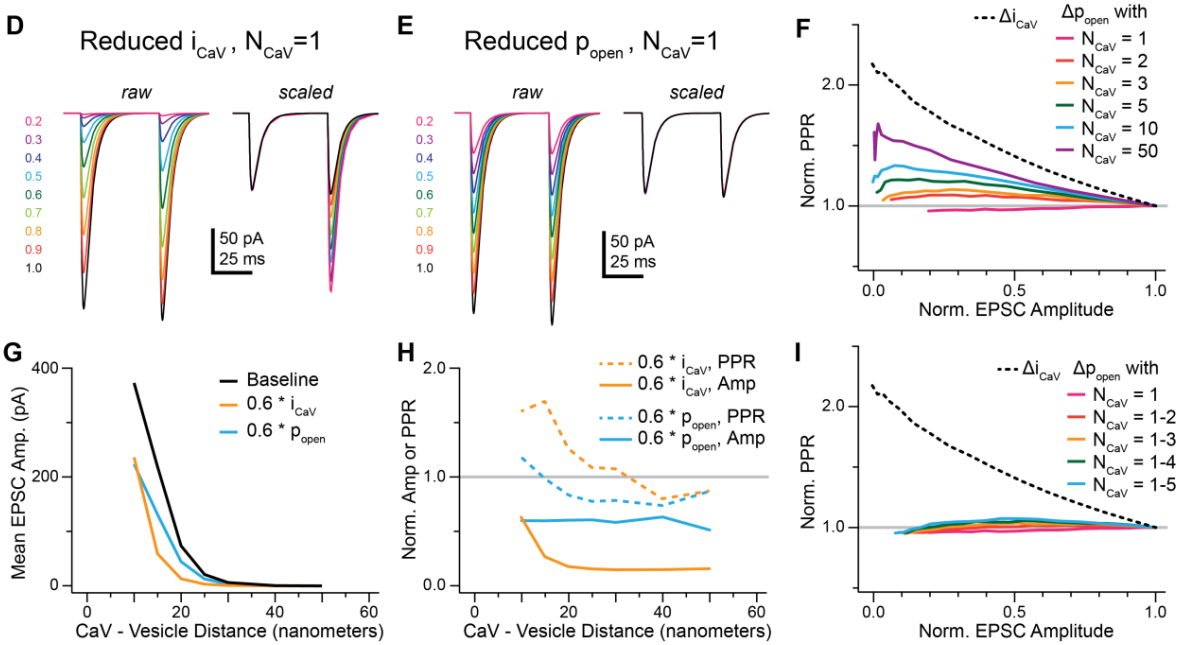

Simplified Model

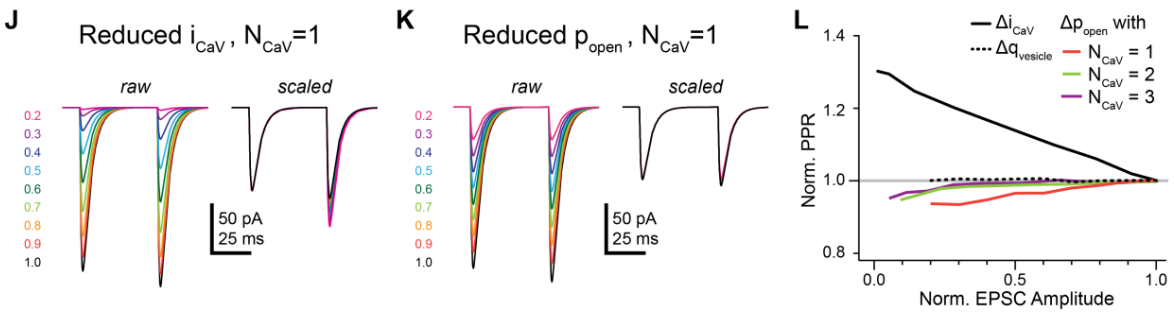

Figure 2.15 (S7, Related to Main Figure 2.7): Several Different Models of Synaptic Transmission Show Non-Canonical Modulation with Suppression of Presynaptic CaV Open Probability

(A) Suppression of EPSC by graded reduction in p_{open} with release mediated by one presynaptic CaV under varying time constants for monoexponential decay of intracellular calcium concentration.

(B) As in A, but varying inter-stimulus interval instead of calcium decay time constant.

(C) Suppression of EPSC by graded reduction in p_{open} with release mediated by a variable number of CaVs in different synapses per trial. Each synapse had an integer number of CaVs in the range listed in the figure legend (e.g. for N_{CaV} = 1-3, 33% of synapses had 1 CaV, 33% had 2 CaVs, and 33% had 3 CaVs). Dashed line indicates graded reduction of i_{CaV} with 1 CaV per synapse, for reference. Dotted line indicates uniform distribution of channel number (between 1-5) as well as calcium decay time constant (from set of 10, 30, 50, 100, or 200 ms) between synapses.

(D) Presynaptic model of release using one-dimensional linearized buffer approximation to model intracellular [Ca] dynamics (see Methods). Suppression of EPSC by graded reduction in i_{CaV} with release mediated by one presynaptic CaV. Left: Colors indicate fraction reduction in i_{CaV}, EPSCs colored correspondingly. Right: same simulations but scaled to match first EPSC amplitude. Compare to Fig. 7D.

(E) Same model as in D, but reducing p_{open}. Compare to Fig. 7E.

(F) Normalized PPR plotted against normalized EPSC amplitude for reductions in i_{CaV} or p_{open} under different numbers of presynaptic CaVs mediating release. Compare to Fig. 7G. Note: In Figure 7G, single-channel current was scaled down by the number of CaVs to maintain constant the expected calcium concentration; here we hold single-channel current constant but increase the distance between the CaVs and the vesicle calcium sensor, also to keep expected calcium concentration constant.

(G) Mean EPSC amplitude as a function of distance between CaV and vesicle. Baseline conditions and suppression of i_{CaV} or p_{open} to 60% of baseline values are plotted in black, orange and cyan, respectively.

(H) Normalized EPSC Amplitude (solid line) or normalized PPR (dashed line) after suppression of i_{CaV} (orange) or p_{open} (cyan) to 60% of baseline levels, as a function of distance between CaV and vesicle. Line indicating no change (y=1) plotted in gray for reference.

(I) Suppression of EPSC by graded reduction in p_{open} with release mediated by a variable number of CaVs in different synapses per trial (as in C, but with diffusion model). Dashed line indicates graded reduction of i_{CaV} with 1 CaV per synapse, for reference.

(J) Suppression of EPSC by graded reduction in i_{CaV} with release mediated by one presynaptic CaV and phenomenological facilitation (see Methods, compare to Fig. 7D). Left: Colors indicate fraction reduction in i_{CaV}, EPSCs colored correspondingly. Right: same simulations but scaled to match first EPSC amplitude.

(K) Suppression of EPSC by graded reduction in p_{open}, as in Fig. S6A. Compare to Fig. 7E.

(L) Change in PPR plotted against change in EPSC amplitude for reductions in i_{CaV}, $q_{vesicle}$ or p_{open} with one presynaptic CaV mediating release. Compare to Fig. 7G.

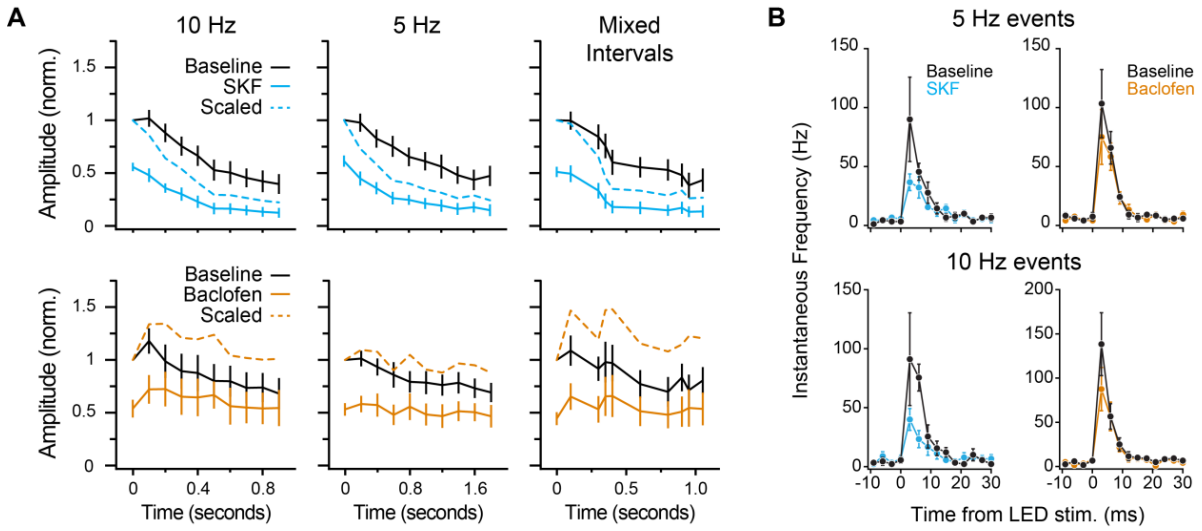

Figure 2.16 (S8, Related to Main Figure 2.8): Modulation of oEPSCs and Evoked Spiking at Intermediate Frequencies

(A) Modulation of ongoing activity at 10 Hz, 5 Hz, and a shuffled mix of intervals between 5-20Hz. Top: oEPSC amplitudes before and after D1R stimulation. Bottom: As on top, but with $GABA_BR$ activation. See Figure 8E.

(B) Neuromodulation of LED-evoked spiking. Top: Instantaneous frequency of spiking aligned to 5Hz LED stimuli, averaged across cells, before and after D1R and $GABA_BR$ activation for left and right plots, respectively (n = 6 and 8 for D1R and $GABA_BR$). Bottom: As above, but aligned to 10Hz LED stimuli. See Figure 8I.

2.7 REFERENCES

Abbott, L.F., and Regehr, W.G. (2004). Synaptic computation. Nature 431, 796–803.

Arnsten, A.F., Cai, J.X., Murphy, B.L., and Goldman-Rakic, P.S. (1994). Dopamine D1 receptor mechanisms in the cognitive performance of young adult and aged monkeys. Psychopharmacology (Berl). 116, 143–151.

Barth, A.L., and Poulet, J.F.A. (2012). Experimental evidence for sparse firing in the neocortex. Trends Neurosci. 35, 345–355.

Behr, J., Gloveli, T., Schmitz, D., and Heinemann, U. (2000). Dopamine depresses excitatory synaptic transmission onto rat subicular neurons via presynaptic D1-like dopamine receptors. J. Neurophysiol. 84, 112–119.

Bender, K.J., Ford, C.P., and Trussell, L.O. (2010). Dopaminergic modulation of axon initial segment calcium channels regulates action potential initiation. Neuron 68, 500–511.

Betz, W.J. (1970). Depression of transmitter release at the neuromuscular junction of the frog. J. Physiol. 206, 629–644.

Bolkan, S.S., Stujenske, J.M., Parnaudeau, S., Spellman, T.J., Rauffenbart, C., Abbas, A.I., Harris, A.Z., Gordon, J.A., and Kellendonk, C. (2017). Thalamic projections sustain prefrontal activity during working memory maintenance. Nat. Neurosci. 20, 987–996.

Borst, J.G.G., and Sakmann, B. (1998). Calcium current during a single action potential in a large presynaptic terminal of the rat brainstem. J. Physiol. 506, 143–157.

Boudewijns, Z.S.R.M., Groen, M.R., Lodder, B., McMaster, M.T.B., Kalogreades, L., de Haan, R., Narayanan, R.T., Meredith, R.M., Mansvelder, H.D., and de Kock, C.P.J. (2013). Layer-specific high-frequency action potential spiking in the prefrontal cortex of awake rats. Front. Cell. Neurosci. 7, 99.

Branco, T., and Staras, K. (2009). The probability of neurotransmitter release: variability and feedback control at single synapses. Nat. Rev. Neurosci. 10, 373–383.

Brozoski, T.J., Brown, R.M., Rosvold, H.E., and Goldman, P.S. (1979). Cognitive deficit caused by regional depletion of dopamine in prefrontal cortex of rhesus monkey. Science 205, 929–932.

Bucurenciu, I., Kulik, A., Schwaller, B., Frotscher, M., and Jonas, P. (2008). Nanodomain Coupling between Ca2+ Channels and Ca2+ Sensors Promotes Fast and Efficient Transmitter Release at a Cortical GABAergic Synapse. Neuron 57, 536–545.

Bucurenciu, I., Bischofberger, J., and Jonas, P. (2010). A small number of open Ca2+ channels trigger transmitter release at a central GABAergic synapse. Nat. Neurosci. 13, 19–21.

Burgos-Robles, A., Vidal-Gonzalez, I., Santini, E., and Quirk, G.J. (2007). Consolidation of Fear Extinction Requires NMDA Receptor-Dependent Bursting in the Ventromedial Prefrontal Cortex. Neuron 53, 871–880.

Carter, B.C., and Jahr, C.E. (2016). Postsynaptic, not presynaptic NMDA receptors are required for spike-timing-dependent LTD induction. Nat. Neurosci. 19, 1218–1224.

Chalifoux, J.R., and Carter, A.G. (2011). GABAB receptor modulation of synaptic function. Curr. Opin. Neurobiol. 21, 339–344.

Clarkson, R.L., Liptak, A.T., Gee, S.M., Sohal, V.S., and Bender, K.J. (2017). D3 Receptors Regulate Excitability in a Unique Class of Prefrontal Pyramidal Cells. J. Neurosci. 37, 5846–5860.
Clements, J.D. (1990). A statistical test for demonstrating a presynaptic site of action for a modulator of synaptic amplitude. J. Neurosci. Methods 31, 75–88.
Delaney, A.J., Crane, J.W., and Sah, P. (2007). Noradrenaline Modulates Transmission at a Central Synapse by a Presynaptic Mechanism. Neuron 56, 880–892.
Fedchyshyn, M.J., and Wang, L.-Y. (2005). Developmental Transformation of the Release Modality at the Calyx of Held Synapse. J. Neurosci. 25, 4131–4140.
Gao, W.-J., and Goldman-Rakic, P.S. (2002). Selective modulation of excitatory and inhibitory microcircuits by dopamine.
Gao, W.-J., Krimer, L.S., and Goldman-Rakic, P.S. (2001). Presynaptic regulation of recurrent excitation by D1 receptors in prefrontal circuits. Proc. Natl. Acad. Sci. 98, 295–300.
Gao, W.-J., Wang, Y., and Goldman-Rakic, P.S. (2003). Dopamine modulation of perisomatic and peridendritic inhibition in prefrontal cortex. J. Neurosci. 23, 1622–1630.
Gee, S., Ellwood, I., Patel, T., Luongo, F., Deisseroth, K., and Sohal, V.S. (2012). Synaptic Activity Unmasks Dopamine D2 Receptor Modulation of a Specific Class of Layer V Pyramidal Neurons in Prefrontal Cortex. J. Neurosci. 32, 4959–4971.
Goutman, J.D., and Glowatzki, E. (2007). Time course and calcium dependence of transmitter release at a single ribbon synapse. Proc. Natl. Acad. Sci. 104, 16341–16346.
Hefft, S., Kraushaar, U., R. P. Geiger, J., and Jonas, P. (2002). Presynaptic short-term depression is maintained during regulation of transmitter release at a GABAergic synapse in rat hippocampus. J. Physiol. 539, 201–208.
Hennig, M.H. (2013). Theoretical models of synaptic short term plasticity. Front. Comput. Neurosci. 7, 45.
Holmes, A., Fitzgerald, P.J., MacPherson, K.P., DeBrouse, L., Colacicco, G., Flynn, S.M., Masneuf, S., Pleil, K.E., Li, C., Marcinkiewcz, C.A., et al. (2012). Chronic alcohol remodels prefrontal neurons and disrupts NMDAR-mediated fear extinction encoding. Nat. Neurosci. 15, 1359–1361.
Holmes, N.M., Crane, J.W., Tang, M., Fam, J., Westbrook, R.F., and Delaney, A.J. (2017). α2-adrenoceptor-mediated inhibition in the central amygdala blocks fear-conditioning. Sci. Rep. 7, 11712.
Jackman, S.L., and Regehr, W.G. (2017). The Mechanisms and Functions of Synaptic Facilitation. Neuron 94, 447–464.
Jackman, S.L., Turecek, J., Belinsky, J.E., and Regehr, W.G. (2016). The calcium sensor synaptotagmin 7 is required for synaptic facilitation. Nature 529, 88–91.
Kamiya, H., and Zucker, R.S. (1994). Residual Ca2 + and short-term synaptic plasticity. Nature 371, 603–606.
Kisilevsky, A.E., Mulligan, S.J., Altier, C., Iftinca, M.C., Varela, D., Tai, C., Chen, L., Hameed, S., Hamid, J., MacVicar, B.A., et al. (2008). D1 Receptors Physically Interact with N-Type Calcium Channels to Regulate Channel Distribution and Dendritic Calcium Entry. Neuron 58, 557–570.

Lansman, J.B., Hess, P., and Tsien, R.W. (1986). Blockade of current through single calcium channels by Cd2+, Mg2+, and Ca2+. Voltage and concentration dependence of calcium entry into the pore. J. Gen. Physiol. 88, 321–347.
Laviolette, S.R., Lipski, W.J., and Grace, A.A. (2005). A Subpopulation of Neurons in the Medial Prefrontal Cortex Encodes Emotional Learning with Burst and Frequency Codes through a Dopamine D4 Receptor-Dependent Basolateral Amygdala Input. J. Neurosci. 25, 6066–6075.
Li, C., Pleil, K.E., Stamatakis, A.M., Busan, S., Vong, L., Lowell, B.B., Stuber, G.D., and Kash, T.L. (2012). Presynaptic Inhibition of Gamma-Aminobutyric Acid Release in the Bed Nucleus of the Stria Terminalis by Kappa Opioid Receptor Signaling. Biol. Psychiatry 71, 725–732.
Li, L., Bischofberger, J., and Jonas, P. (2007). Differential Gating and Recruitment of P/Q-, N-, and R-Type Ca2+ Channels in Hippocampal Mossy Fiber Boutons. J. Neurosci. 27, 13420–13429.
Markram, H., Wang, Y., and Tsodyks, M. (1998). Differential signaling via the same axon of neocortical pyramidal neurons. Proc. Natl. Acad. Sci. U. S. A. 95, 5323–5328.
McDonough, S.I., Swartz, K.J., Mintz, I.M., Boland, L.M., and Bean, B.P. (1996). Inhibition of calcium channels in rat central and peripheral neurons by omega-conotoxin MVIIC. J. Neurosci. 16, 2612–2623.
Mintz, I.M., and Bean, B.P. (1993). GABAB receptor inhibition of P-type Ca2+ channels in central neurons. Neuron 10, 889–898.
Otis, T.S., and Trussell, L.O. (1996). Inhibition of transmitter release shortens the duration of the excitatory synaptic current at a calyceal synapse. J. Neurophysiol. 76, 3584–3588.
Park, D., and Dunlap, K. (1998). Dynamic regulation of calcium influx by G-proteins, action potential waveform, and neuronal firing frequency. J. Neurosci. 18, 6757–6766.
Patil, P.G., de Leon, M., Reed, R.R., Dubel, S., Snutch, T.P., and Yue, D.T. (1996). Elementary events underlying voltage-dependent G-protein inhibition of N-type calcium channels. Biophys. J. 71, 2509–2521.
Quastel, D.M. (1997). The binomial model in fluctuation analysis of quantal neurotransmitter release. Biophys. J. 72, 728–753.
Saviane, C., and Silver, R.A. (2006). Errors in the estimation of the variance: implications for multiple-probability fluctuation analysis. J. Neurosci. Methods 153, 250–260.
Schmitt, L.I., Wimmer, R.D., Nakajima, M., Happ, M., Mofakham, S., and Halassa, M.M. (2017). Thalamic amplification of cortical connectivity sustains attentional control. Nature 545, 219–223.
Scimemi, A., and Diamond, J.S. (2012). The Number and Organization of Ca2+ Channels in the Active Zone Shapes Neurotransmitter Release from Schaffer Collateral Synapses. J. Neurosci. 32, 18157–18176.
Seamans, J.K., and Yang, C.R. (2004). The principal features and mechanisms of dopamine modulation in the prefrontal cortex. Prog. Neurobiol. 74, 1–58.
Seamans, J.K., Durstewitz, D., Christie, B.R., Stevens, C.F., and Sejnowski, T.J. (2001).

Dopamine D1/D5 receptor modulation of excitatory synaptic inputs to layer V prefrontal cortex neurons. Proc. Natl. Acad. Sci. 98, 301–306.
Seong, H.J., and Carter, A.G. (2012). D1 Receptor Modulation of Action Potential Firing in a Subpopulation of Layer 5 Pyramidal Neurons in the Prefrontal Cortex. J. Neurosci. 32, 10516–10521.
Sigworth, F.J. (1980). The variance of sodium current fluctuations at the node of Ranvier. J. Physiol. 307, 97–129.
Silver, R.A. (2010). Neuronal arithmetic. Nat. Rev. Neurosci. 11, 474–489.
Stanley, E.F. (2016). The Nanophysiology of Fast Transmitter Release. Trends Neurosci. 39, 183–197.
Südhof, T.C. (2013). A molecular machine for neurotransmitter release: synaptotagmin and beyond. Nat. Med. 19, 1227–1231.
Surmeier, D.J., Bargas, J., Hemmings, H.C., Nairn, A.C., and Greengard, P. (1995). Modulation of calcium currents by a D1 dopaminergic protein kinase/phosphatase cascade in rat neostriatal neurons. Neuron 14, 385–397.
Svoboda, K., and Sabatini, B.L. (2000). Analysis of calcium channels in single spines using optical fluctuation analysis. Nature 408, 589–593.
Takahashi, T., Kajikawa, Y., and Tsujimoto, T. (1998). G-Protein-coupled modulation of presynaptic calcium currents and transmitter release by a GABAB receptor. J. Neurosci. 18, 3138–3146.
Tejeda, H.A., Wu, J., Kornspun, A.R., Pignatelli, M., Kashtelyan, V., Krashes, M.J., Lowell, B.B., Carlezon, W.A., and Bonci, A. (2017). Pathway- and Cell-Specific Kappa-Opioid Receptor Modulation of Excitation-Inhibition Balance Differentially Gates D1 and D2 Accumbens Neuron Activity. Neuron 93, 147–163.
Tritsch, N.X., and Sabatini, B.L. (2012). Dopaminergic Modulation of Synaptic Transmission in Cortex and Striatum. Neuron 76, 33–50.
Urban, N.N., González-Burgos, G., Henze, D.A., Lewis, D.A., and Barrionuevo, G. (2002). Selective reduction by dopamine of excitatory synaptic inputs to pyramidal neurons in primate prefrontal cortex. J. Physiol. 539, 707–712.
Varela, J.A., Sen, K., Gibson, J., Fost, J., Abbott, L.F., and Nelson, S.B. (1997). A quantitative description of short-term plasticity at excitatory synapses in layer 2/3 of rat primary visual cortex. J. Neurosci. 17, 7926–7940.
Vijayraghavan, S., Wang, M., Birnbaum, S.G., Williams, G. V, and Arnsten, A.F.T. (2007). Inverted-U dopamine D1 receptor actions on prefrontal neurons engaged in working memory. Nat. Neurosci. 10, 376–384.
Vyleta, N.P., and Jonas, P. (2014). Loose Coupling Between Ca2+ Channels and Release Sensors at a Plastic Hippocampal Synapse. Science (80-.). 343, 665–670.
Wang, W., Dever, D., Lowe, J., Storey, G.P., Bhansali, A., Eck, E.K., Nitulescu, I., Weimer, J., and Bamford, N.S. (2012). Regulation of prefrontal excitatory neurotransmission by dopamine in the nucleus accumbens core. J. Physiol. 590, 3743–3769.
Yang, S., Ben-Shalom, R., Ahn, M., Liptak, A.T., van Rijn, R.M., Whistler, J.L., and Bender, K.J. (2016). β-Arrestin-Dependent Dopaminergic Regulation of Calcium Channel Activity in the Axon Initial Segment. Cell Rep. 16, 1518–1526.
Yasuda, R., Sabatini, B.L., and Svoboda, K. (2003). Plasticity of calcium channels in

dendritic spines. Nat. Neurosci. 6, 948–955.
Zhang, X.-F., Cooper, D.C., and White, F.J. (2002). Repeated cocaine treatment decreases whole-cell calcium current in rat nucleus accumbens neurons. J. Pharmacol. Exp. Ther. 301, 1119–1125.
Zucker, R.S., and Regehr, W.G. (2002). Short-Term Synaptic Plasticity. Annu. Rev. Physiol. 64, 355–405.

CHAPTER 3

Detection of Synaptic Deficits in Autism Model through Deconvolution

---

3.1 INTRODUCTION

The study of synaptic transmission in the cortical pyramidal neuron has historically been complicated by the thinness and tortuosity of its dendrites (Figure 1). These features make synapses experimentally inaccessible, both from a physical and electrical standpoint: physically, dendrites and spines are often (but not always, see Nevian *et al.*, 2007) too small to directly record with electrodes, and electrically, the diameter of dendrites is usually very small compared to their axial length, leading to a strong attenuation of electrical signals (Weiss, 1996). The cable equation (Equation 1 below) illustrates this phenomenon, known as the "space-clamp" problem, by showing how the electrotonic potential V is related to its first temporal derivative and second spatial derivative:

$$V = V_m - E_{pas} \tag{1a}$$

$$\lambda^2 \frac{\partial^2 V}{\partial x^2} = V + \tau \frac{\partial V}{\partial t} \tag{1b}$$

where

$$\lambda = \sqrt{\frac{d}{4}\frac{R_m}{R_i}} \tag{2a}$$

$$\tau = R_m C_m \tag{2b}$$

and V_m is transmembrane voltage, E_{pas} is reversal potential of the cell at rest, d is the dendrite diameter, t and x are time and distance along the length of the dendrite, R_m is

the membrane resistance, R_i is the axial resistance, and C_m is the membrane capacitance (Weiss, 1996).

We note that this equation amounts to a one-dimensional heat equation, and furthermore that if R_m and R_i are treated as constants, then the length constant λ gets shorter with decreasing axon diameters (Equation 2a). Thus, the effective electrotonic distance between the synapse and the recording electrode (and thus the attenuation of the amplitude of synaptic inputs) grows larger with smaller axon diameters (Rall, 1964). Furthermore, strong impedance along the dendrite also leads to low-pass temporal filtering (Equation 2b). In this way, the thinness and length of pyramidal cell dendrites leads to substantial signal attenuation and filtering between synapses and the recording electrode.

While the spatiotemporal filtering of synaptic inputs as they travel from the synapse to the soma is an interesting feature of synaptic integration that is worthy of study in its own right (Silver, 2010), it nevertheless can impede the functional characterization of inputs distributed across the dendritic arbor, especially in the presence of noise and voltage-clamp errors (Figure 2). Algorithms to detect synaptic events have historically relied on heuristics such as thresholding the amplitude or the temporal derivative of the membrane voltage; however, these algorithms do not leverage the stereotyped timecourse of synaptic currents. By contrast, one method that uses this stereotypy to its advantage is “deconvolution-based detection” (Pernía-Andrade et al., 2012), whereby one deconvolves the data recorded at the soma from a “template” synaptic event, thus generating a trace that in theory is a sum of Dirac delta functions located at the time of synaptic events (Figure 2b).

In this chapter, I will discuss my implementation of the algorithm designed by Pernía-Andrade et al., how it was applied to pyramidal neurons in the neocortex, and a number of improvements I made to the algorithm in order to incorporate it into a larger analytical suite and user interface for electrophysiological analysis. Finally, we will apply this new analytical system to study synaptic deficits in a mouse model of autism.

3.2 RESULTS

As discussed above, synaptic inputs generate electrical potentials that follow a characteristic timecourse (henceforth referred to as the "synaptic template") which then undergo passive filtering between the synapse and the recording electrode. Thus, in theory, if one deconvolves the recorded data with this synaptic template, the output should be the sum of a series of Dirac delta functions. However in practice, these "delta functions" are contaminated by several sources of noise: 1) different synapses have different synaptic templates due to varying synapse strength and location (and thus events with different kinetics can be missed, see yellow synapse in Figure 2), 2) nonlinear electrophysiological mechanisms exist between the synaptic receptors and the recording electrode, and 3) biological and non-biological sources of noise in the recording rig are inevitable. The end result is that the peaks in the output trace after deconvolution are shorter and wider than "true" delta functions (Figure 2B, bottom), representing uncertainty about the precise time, amplitude and template of the detected event. Throughout the rest of this section, I will first describe in greater detail the deconvolution algorithm as posed by Pernía-Andrade et al., then I will discuss how I adapted the algorithm to address some of the aforementioned limitations.

3.2.1 Detection of Synaptic Events by Deconvolution

The fundamental presumption behind the deconvolution detection strategy is that the recorded data $V_m(t)$ is the convolution of each synaptic template $V_i(t)$ arising from synapse i and the input synaptic activity $\rho_i(t)$ represented as a sum of impulse functions, plus some noise ϵ :

$$V_m(t) = \sum_i (V_i * \rho_i)(t) + \epsilon = \sum_i \int_{-\infty}^{\infty} d\tau \, V_i(t-\tau) \, \rho_i(\tau) + \epsilon \tag{3}$$

The convolution theorem (Bialek, 2012) states that convolution (and deconvolution) in the time domain are equivalent to multiplication (and division) in the frequency domain:

$$\mathcal{F}\{f * g\} = \mathcal{F}\{f\} \cdot \mathcal{F}\{g\} \tag{4a}$$

$$\mathcal{F}\{f\} = \frac{\mathcal{F}\{f*g\}}{\mathcal{F}\{g\}} \tag{4b}$$

where $\mathcal{F}$ indicates the Fourier transform. The Fourier transform $\mathcal{F}\{f\}$ and its inverse $\mathcal{F}^{-1}\{f\}$ convert a function of time $f(t)$ into a function of frequency $\tilde{f}(\omega)$ or vice-versa, respectively, according to the following equations:

$$\mathcal{F}\{f(t)\} = \tilde{f}(\omega) = \int_{-\infty}^{\infty} dt \, e^{i\omega t} f(t) \tag{5a}$$

$$\mathcal{F}^{-1}\{\tilde{f}(\omega)\} = f(t) = \int_{-\infty}^{\infty} \frac{d\omega}{2\pi} e^{-i\omega t} \tilde{f}(\omega) \tag{5b}$$

Thus, we can formalize the synaptic event detection problem as the deconvolution of $V_m(t)$ from $V_i(t)$ to estimate $\rho_i(t)$ for each synapse i, optionally returning the sum of all input synaptic activity $\rho(t)$:

$$\rho(t) = \sum_i \rho_i(t) \approx \sum_i \mathcal{F}^{-1}\{ \mathcal{F}\{V_m(t)\} / \mathcal{F}\{V_i(t)\} \} \tag{6}$$

where $\mathcal{F}^{-1}$ indicates the inverse Fourier transform.

3.2.2 Strategies and Limitations to Deconvolution-Based Detection

There are several limitations to this method, as described earlier. The first is implied by the assertion that Equation 6 is only an estimation; this is because we cannot disentangle the signal from the noise ϵ in $V_m(t)$. In practice, this leads to estimates of $\rho(t)$ that are not "pure" delta functions (Figure 2). In the context where the synaptic activity is high and many synaptic events overlap, $\rho(t)$ can be seen as a rate of activity; however, ironically, if activity is low one must determine the location of the underlying individual impulses by using one of the aforementioned (non-deconvolution based) event detection algorithms, this time on $\rho(t)$ to detect impulses rather than on $V_m(t)$ to detect synaptic events.

Fortunately, our data from cortical pyramidal neurons showed a large signal-to-noise ratio in $\rho(t)$; this allowed us to low-pass filter $\rho(t)$ and apply a thresholding algorithm that detects events that rise above N standard deviations from the noise, defined by fitting a gaussian to the 80% of points symmetrically surrounding zero (Figure 3). We found that a detection threshold of $N = 5$ standard deviations from the noise obtained similar precision and recall of detected events as compared to experimenter intuition (Figure 4).

The second limitation of this approach is that it is impossible to directly measure the synaptic templates $V_i(t)$ from each synapse i. In practice, however, a reasonable approximation can be made by using a sum of two exponentials waveform. We improved upon this approach by first detecting many events with this precomputed waveform,

then averaging the detected events to form a new template and repeating the detection algorithm with this “empirical kernel” (Figure 5).

While this approach reduces detection bias due to the arbitrary kinetics of the precomputed waveform, we note that if it is iterated multiple times the empirical kernel will approach a synaptic waveform that resembles the largest and the most frequent synaptic events that are detected. Thus, this approach does not guarantee detection of smaller or less frequent events, especially ones whose kinetics are different from the original precomputed waveform. This can be seen easily in Figure 2b, where deconvolution using the orange synaptic template as $V_i(t)$ led to strong recall of events from both the orange and blue synapses, but *not* the yellow synapse with a smaller amplitude and much slower kinetics.

The inability to detect the yellow events in Figure 2 also calls to a third limitation of deconvolution: the presence of $1/f$ noise (or “pink noise”) in electrical recordings. This noise (as compared to white noise) produces large, low frequency oscillations which have spectral characteristics that resemble heavily-filtered events such as the yellow synaptic template in Figure 2. This leads to strong contamination of slow synaptic events by $1/f$ noise when using deconvolution. The detection of biological signals in the presence of noise is the subject of significant research (Deneux et al., 2016), however one simple way to mitigate this problem is by performing linear regression on the original input signal $V_m(t)$ and performing detections on the residual trace. This “trendline correction” can adjust for slow drift (e.g. rundown) as well as very low frequency noise.

Finally, we incorporated functionality that can allow for greater experimenter control over suspected false positives. These include 1) defining a minimum event

amplitude (defined by the difference between the maximum amplitude and the smoothed value at the point of deconvolved detection), 2) defining a minimum inter-event interval (an assumption that may be reasonable for infrequent events between independent synapses), and 3) the manual exclusion of individual events due to unpredictable experimental instability. While non-algorithmic steps of this sort must be approached with caution, we found that these additional tools allowed us to include more data for analysis, for example excluding portions of experimental traces where the holding current was transiently unstable.

3.2.3 Deconvolution Reveals Synaptic Deficits in Mouse Model of Autism

We applied this deconvolution technique to study the characteristics of spontaneous and miniature synaptic events from excitatory and inhibitory synapses in mouse prefrontal cortex. We compared these results between wildtype and heterozygous knockout mice for the autism-associated gene *Scn2a*, which encodes the sodium channel NaV1.2 (Ben-Shalom et al., 2017). Because NaV1.2 is the only sodium channel expressed in the axon initial segment (AIS) of cortical glutamatergic pyramidal cells early in development (Gazina et al., 2015), we hypothesized that haploinsufficiency of *Scn2a* would lead to hypoexcitability in critical developmental stages, which could then lead to deficits in synapse maturation in adulthood.

In order to test this hypothesis, we made acute slices of prefrontal cortex from both wildtype and *Scn2a* haploinsufficient mice (*Scn2a*$^{+/+}$ and *Scn2a*$^{+/-}$, respectively) and measured miniature excitatory postsynaptic currents (mEPSC) both during and after the developmental maturation of the AIS (P6 and P27; Figure 6). Using the deconvolution-

based detection algorithm outlined in this chapter, we found that the amplitudes of mEPSC events were identical between the two genotypes at both ages; however, we found that the frequency of mEPSC events was significantly reduced in haploinsufficient mice, but only in adulthood (*Scn2a*$^{+/+}$: 9.3 ± 1.1 Hz, n = 23; *Scn2a*$^{+/-}$: 4.9 ± 0.8, n = 19; $p < 0.001$ Mann-Whitney U test).

We next tested whether inhibitory synaptic inputs were similarly affected. To achieve this, we measure miniature inhibitory postsynaptic currents (mIPSC) within the same cells (Figure 7). Interestingly, we found no difference in frequency or amplitude of mIPSCs between the wildtype and haploinsufficient mice at both ages tested. Taken together, Figures 6 and 7 suggest that haploinsufficiency of *Scn2a* leads to a selective deficit in excitatory synaptic activity, but not strength, in the prefrontal cortex of adult mice.

3.3 DISCUSSION

In this chapter, I discussed the challenges associated with detecting synaptic events, reposed the problem with the formalism of deconvolution (Pernía-Andrade et al., 2012) and adapted this approach to accommodate some of its limitations. We then applied this technique to study synaptic deficits in a mouse model of autism, discovering that in mutant mice there is a significant decrease in synaptic event frequency, but not amplitude. Furthermore, we found that this deficit is specific to excitatory (not inhibitory) synapses and is only seen in adulthood. Thus, taken together, in this chapter I have expanded the deconvolution-based detection system posed by Pernía-Andrade et al. and have shown its utility in a proof-of-concept study where unbiased detection of

synaptic activity was critical in discovering the underlying developmental synaptic deficits arising from mutation of the autism-associated gene *Scn2a*.

3.4 FIGURES

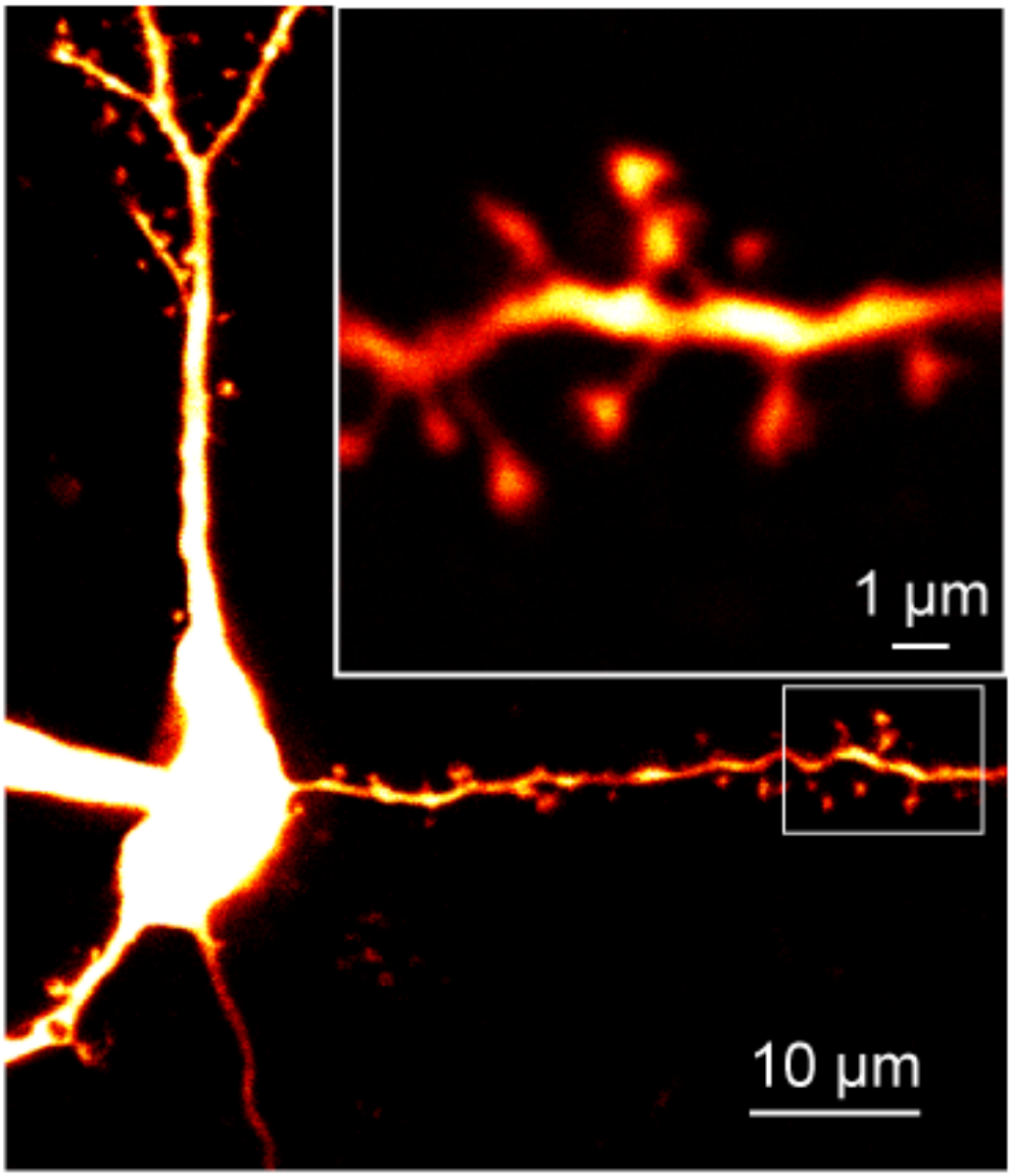

Figure 3.1: Prefrontal Pyramidal Neuron Morphology
Prefrontal pyramidal neuron filled with Alexa 594. *Inset:* expanded section of dendrite with several spines. Note the thinness of dendrites and spine necks relative to the soma.

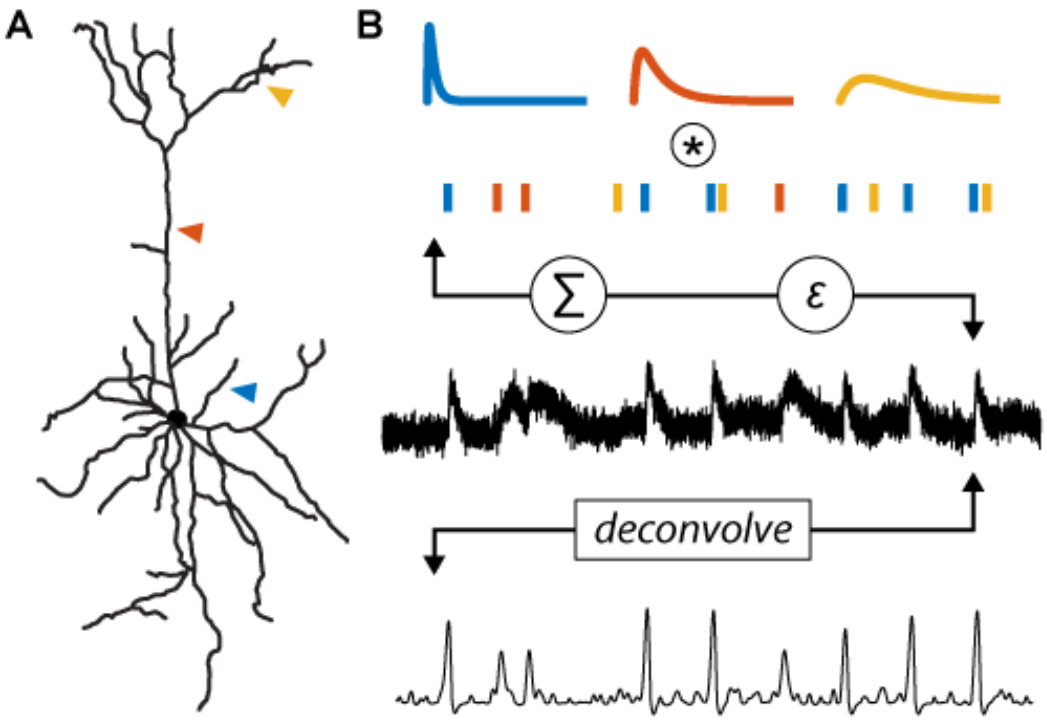

Figure 3.2: Schematic of Synaptic Event Detection

A) Pyramidal neuron morphology (borrowed with permission from Clarkson et al., 2017), with three locations of synapses indicated by arrows. Colors of synapse match B.

B) Schematic showing deconvolution algorithm. *Top*: three synaptic templates convolve with respective activity functions, indicated by colored raster plots. *Middle*: the three convolved traces are then summed, and both Gaussian and 1/f noise are added to mimic a "realistic" recorded somatic potential in black. *Bottom*: This somatic potential is then deconvolved with a synaptic template (in this case, the orange template above) to generate a noisy sum-of-impulses waveform, which then undergoes thresholding to detect event times. Note that the yellow synaptic template was *not* recovered well from this procedure, due to its low amplitude and slower kinetics.

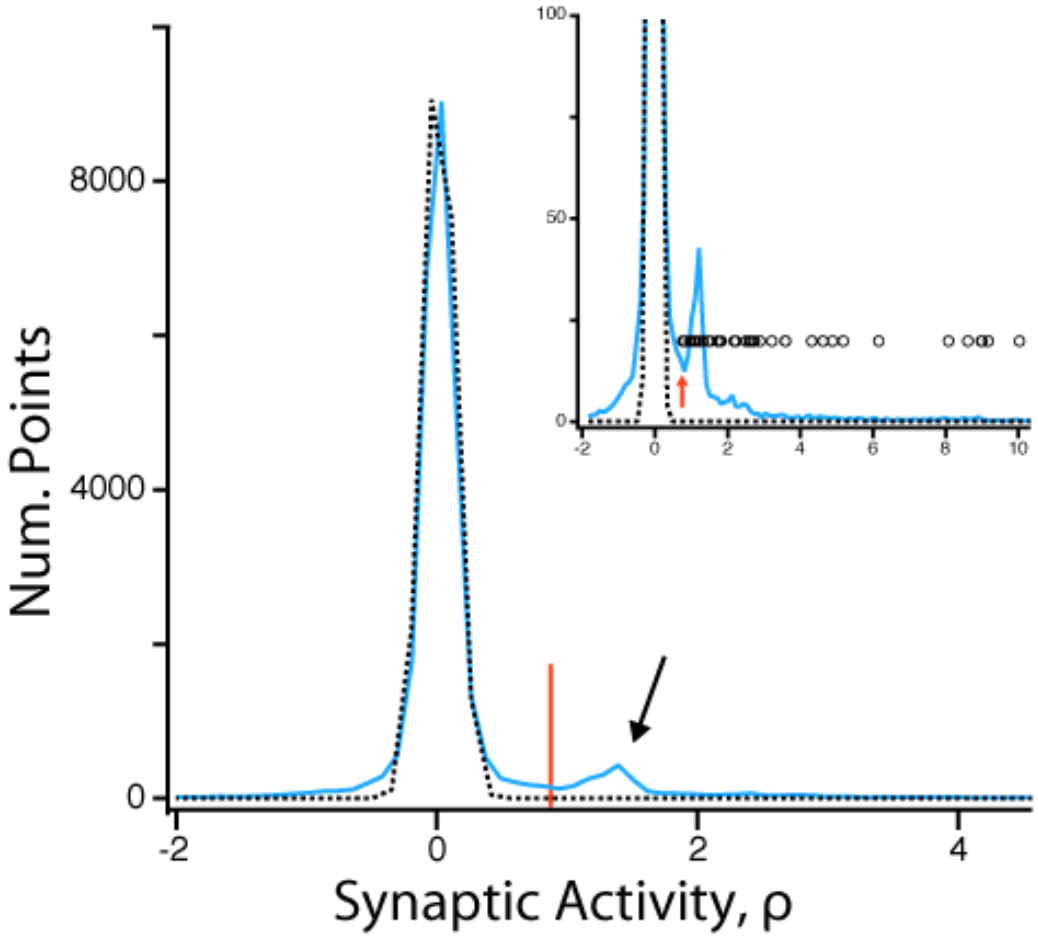

Figure 3.3: Example Histogram of Deconvolved Synaptic Activity
All-point histogram of synaptic activity $\rho(t)$ estimated by deconvolution from 2.5 seconds of data recorded from a prefrontal pyramidal neuron. Blue line is the raw histogram data, dotted black line is the Gaussian fit to the data surrounding $\rho(t) = 0$, red line indicates threshold of $N = 5$ standard deviations from 0, note that the arrow indicates significant deviation from expected Gaussian noise corresponding to detected events. *Inset:* Expanded view. Red arrow indicates threshold as in main figure. Open circles indicate detected events. Note that the location where the raw histogram deviates from the fit Gaussian is smooth, indicating a tradeoff between precision and recall in defining the detection threshold.

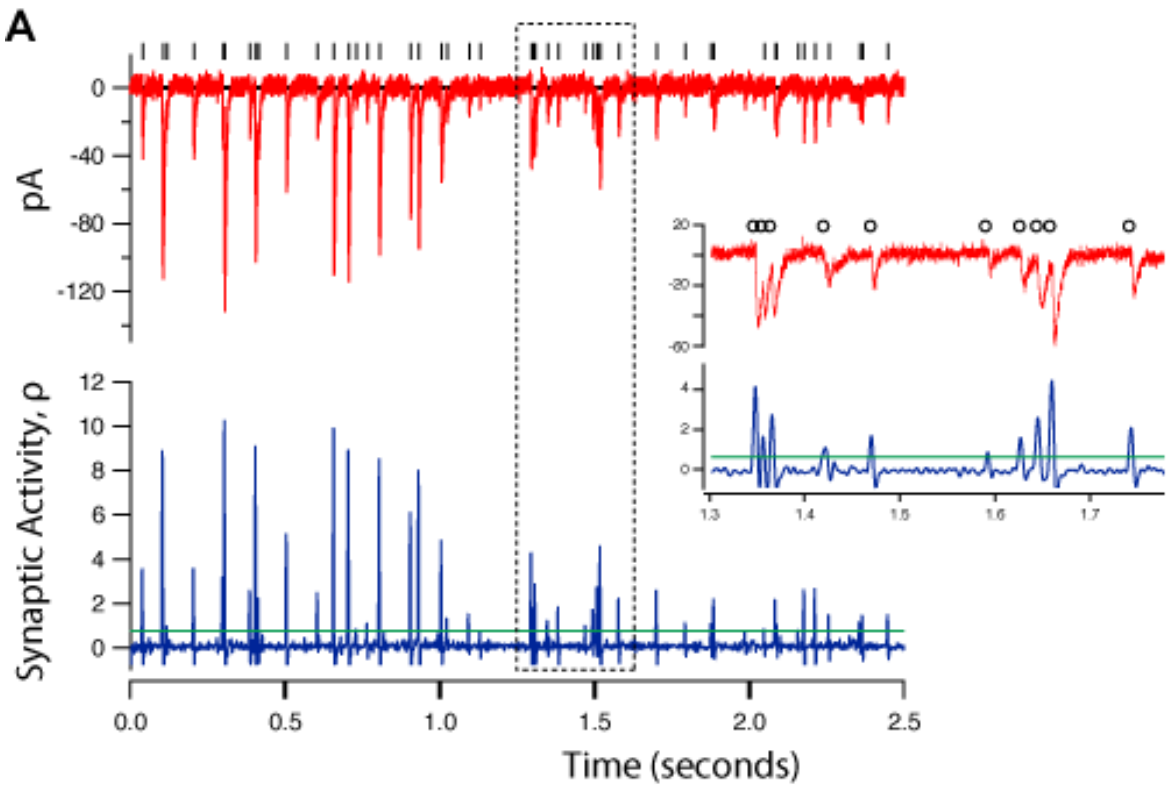

Figure 3.4: Example of Detected Synaptic Events
Example data recorded from pyramidal neuron (same trace used to generate Figure 3). *Top*: Mean-subtracted data (as $V_m(t)$ in Equation 6, but in voltage-clamp instead, using current $I_m(t)$ and template $I_i(t)$ in picoamps), with detected events indicated by black tick marks. *Bottom*: Deconvolved estimate of synaptic activity, $\rho(t)$, in blue with threshold in green (note, $\rho(t)$ is expressed in arbitrary units). Dashed box indicates timing of inset. *Inset*: Detected events now shown as open circles. Note that deconvolution can detect highly-overlapping synaptic events reliably.

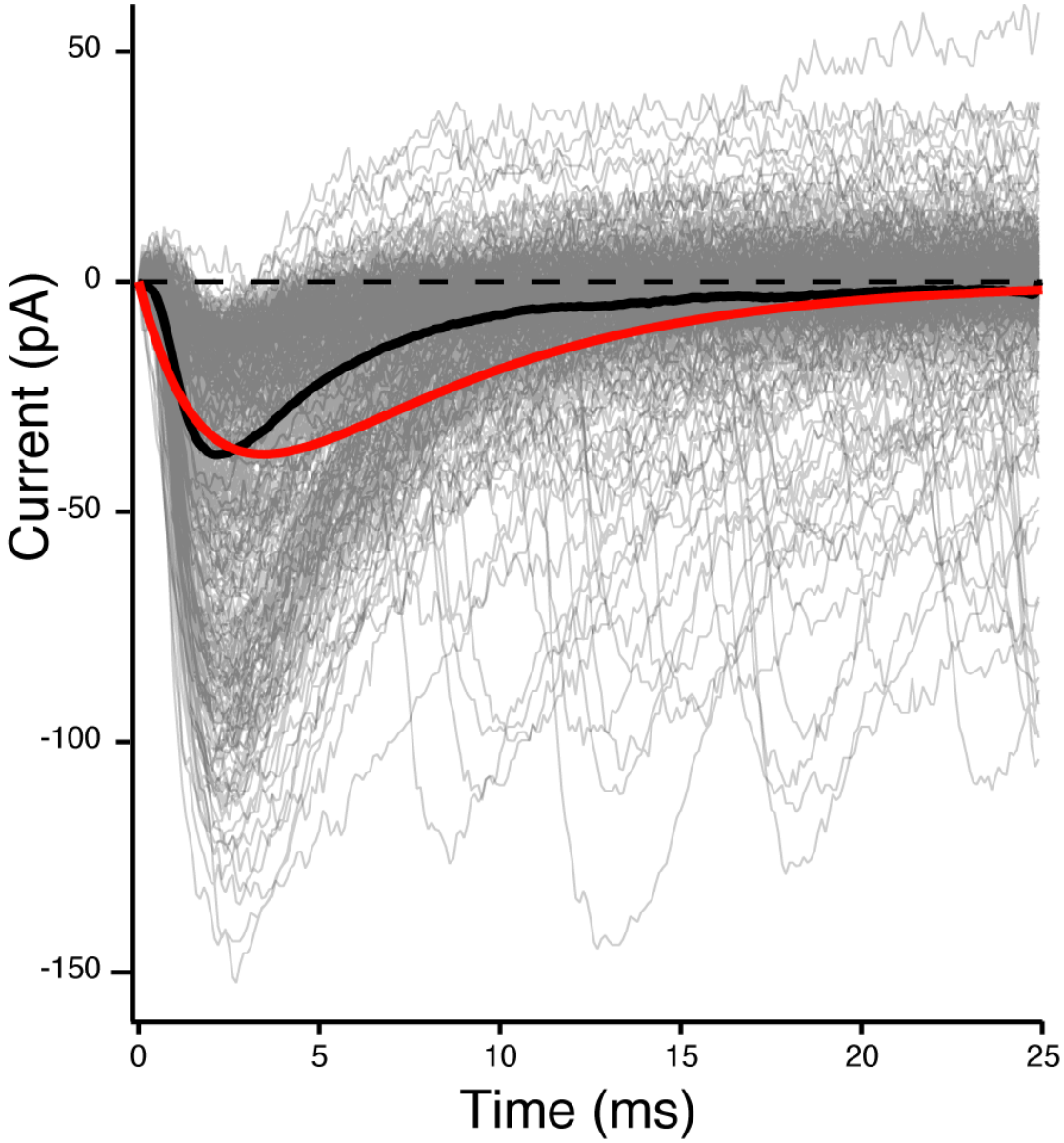

Figure 3.5: Generation of Empirical Synaptic Template
Example of generation of empirical template from precomputed synaptic template. An initial sum-of-exponentials template (red) was used to detect 495 synaptic events (grey), which were then averaged to generate and empirical template (solid black).

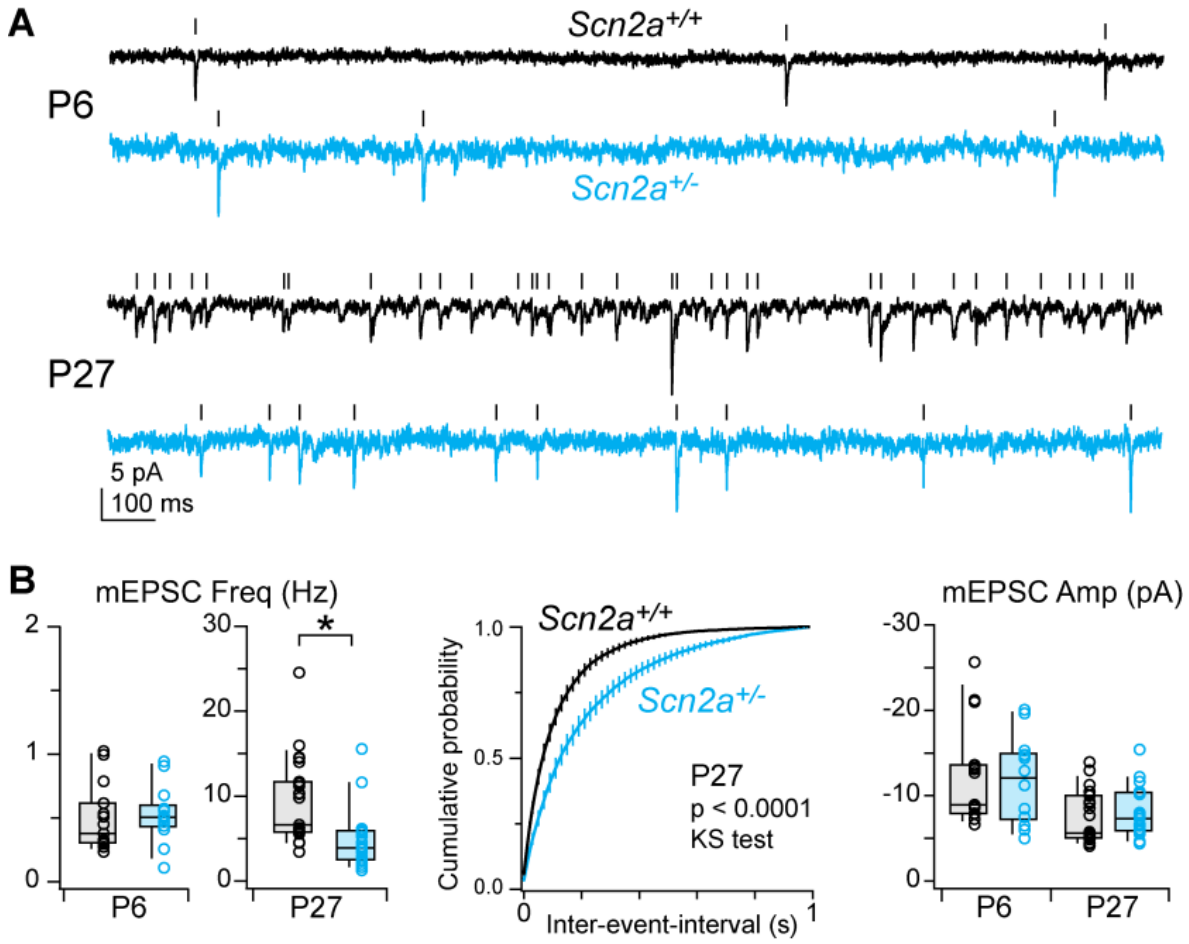

Figure 3.6: *Scn2a* haploinsufficiency disrupts excitatory synapse function
(reproduced with permission from Figure 3 of Spratt et al.)

A) mEPSCs recorded in *Scn2a*$^{+/+}$ (black) and *Scn2a*$^{+/-}$ (cyan) pyramidal cells at P6 and P27. Tick marks denote detected events.

B) Left, average mEPSC frequency per cell (open circles). Box plots are median, quartiles, and 90% tails. Note that frequency range is different for P6 and P27. Middle, cumulative probability distribution of mEPSC event intervals at P27. Distributions were generated per cell, then averaged. Bars are SEM. $P < 0.0001$, Kolmogorov-Smirnov test. Right, average mEPSC amplitude per cell.

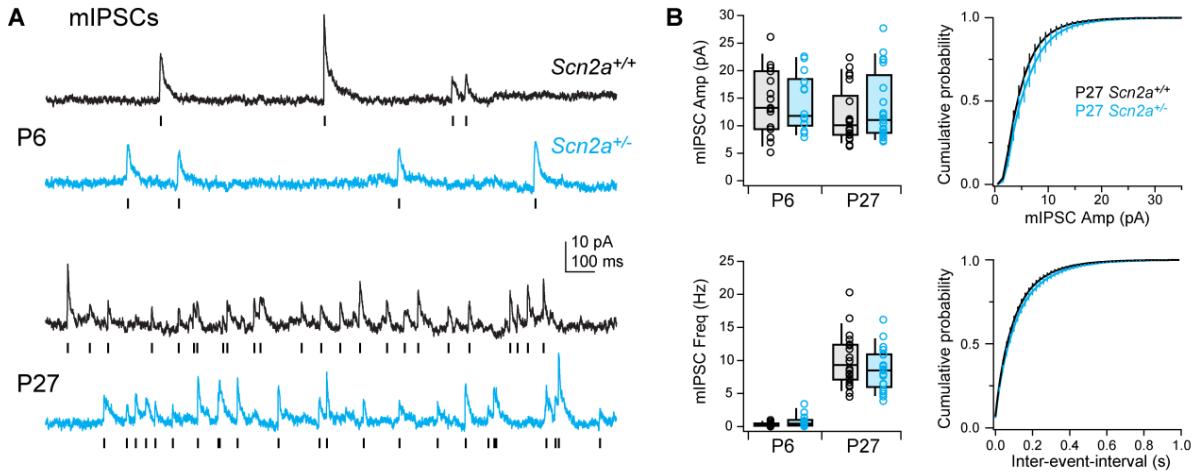

Figure 3.7: No effect of *Scn2a* haploinsufficiency on inhibitory synapse function.
(reproduced with permission from Supplemental Figure 5 of Spratt et al.)

A) Examples of mIPSCs recorded in pyramidal cells voltage-clamped to 0 mV in *Scn2a*$^{+/+}$ (black) and *Scn2a*$^{+/-}$ (cyan) cells. Tick marks denote detected events. Data obtained at P6 (top) and P27 (bottom).

B) Mean mIPSC frequency and amplitude per cell, separated by age. Open circles are single cells. Box plots are median, quartiles, and 90% tails. Cumulative probability histograms were generated per cell, then averaged across all cells. Bars are SEM per data bin. n = 15, 14, 22, 21 for P6 *Scn2a*$^{+/+}$, P6 *Scn2a*$^{+/-}$, P27 *Scn2a*$^{+/+}$, and P27 *Scn2a*$^{+/-}$ cells, respectively. No statistical differences noted.

3.5 REFERENCES

Ben-Shalom, R., Keeshen, C.M., Berrios, K.N., An, J.Y., Sanders, S.J., and Bender, K.J. (2017). Opposing Effects on Na V 1.2 Function Underlie Differences Between SCN2A Variants Observed in Individuals With Autism Spectrum Disorder or Infantile Seizures. Biol. Psychiatry 82, 224–232.

Bialek, W. (2012). Biophysics: Searching for Principles (Princeton University Press).

Clarkson, R.L., Liptak, A.T., Gee, S.M., Sohal, V.S., and Bender, K.J. (2017). D3 Receptors Regulate Excitability in a Unique Class of Prefrontal Pyramidal Cells. J. Neurosci. 37, 5846–5860.

Deneux, T., Kaszas, A., Szalay, G., Katona, G., Lakner, T., Grinvald, A., Rózsa, B., and Vanzetta, I. (2016). Accurate spike estimation from noisy calcium signals for ultrafast three-dimensional imaging of large neuronal populations in vivo. Nat. Commun. 7, 12190.

Gazina, E. V., Leaw, B.T.W., Richards, K.L., Wimmer, V.C., Kim, T.H., Aumann, T.D., Featherby, T.J., Churilov, L., Hammond, V.E., Reid, C.A., et al. (2015). 'Neonatal' Nav1.2 reduces neuronal excitability and affects seizure susceptibility and behaviour. Hum. Mol. Genet. 24, 1457–1468.

Nevian, T., Larkum, M.E., Polsky, A., and Schiller, J. (2007). Properties of basal dendrites of layer 5 pyramidal neurons: a direct patch-clamp recording study. Nat. Neurosci. 10, 206–214.

Pernía-Andrade, A.J., Goswami, S.P., Stickler, Y., Fröbe, U., Schlögl, A., and Jonas, P. (2012). A Deconvolution-Based Method with High Sensitivity and Temporal Resolution for Detection of Spontaneous Synaptic Currents In Vitro and In Vivo. Biophys. J. 103, 1429–1439.

Rall, W. (1964). Theoretical Significance of Dendritic Trees for Neuronal Input-Output Relations. In Neural Theory and Modeling, (Stanford University Press), p.

Silver, R.A. (2010). Neuronal arithmetic. Nat. Rev. Neurosci. 11, 474–489.

Weiss, T.F. (1996). Cellular Biophysics: Volume 2.

CHAPTER 4

Medial Amydalar Aromatase Neurons Regulate Aggression in Both Sexes

---

4.1 SUMMARY

Aromatase-expressing neuroendocrine neurons in the vertebrate male brain synthesize estradiol from circulating testosterone. This locally produced estradiol controls neural circuits underlying courtship vocalization, mating, aggression, and territory marking in male mice. How aromatase-expressing neuronal populations control these diverse estrogen-dependent male behaviors is poorly understood, and the function, if any, of aromatase-expressing neurons in females is unclear. Using targeted genetic approaches, we show that aromatase-expressing neurons within the male posterodorsal medial amygdala (MeApd) regulate components of aggression, but not other estrogen-dependent male-typical behaviors. Remarkably, aromatase-expressing MeApd neurons in females are specifically required for components of maternal aggression, which we show is distinct from intermale aggression in pattern and execution. Thus, aromatase-expressing MeApd neurons control distinct forms of aggression in the two sexes. Moreover, our findings indicate that complex social behaviors are separable in a modular manner at the level of genetically identified neuronal populations.

4.2 INTRODUCTION

Sexually reproducing species exhibit sex differences in social interactions such as courtship and aggression that are critical for reproductive success. Accordingly, such behaviors are developmentally programmed and can be elicited in naive animals without prior training. Within a species, each of these behaviors consists of many stereotyped components, thereby enabling sensitive detection of alterations in behavioral displays subsequent to functional manipulations. Although many brain regions are implicated in the control of sexually dimorphic behaviors in mammals, how these complex behaviors are encoded by such brain regions is poorly understood (reviewed in Yang and Shah, 2014).

Sex hormones essentially act as master regulators of the entire repertoire of sex-typical social interactions in most vertebrates (Arnold, 2009, Morris et al., 2004, Yang and Shah, 2014). Sex hormone signaling pathways therefore offer a functional entry point into neural circuits underlying these behaviors. As has been known for several decades (Ball, 1937), estrogen signaling controls sex-typical behaviors in both sexes in rodents and many other vertebrates (reviewed in McCarthy, 2008, Yang and Shah, 2014). In particular, it is critical for male-typical ultrasonic courtship vocalizations, sexual displays, aggression, and territory marking (Finney and Erpino, 1976, Kimura and Hagiwara, 1985, Matsumoto et al., 2003, Nunez et al., 1978, Ogawa et al., 2000, Wallis and Luttge, 1975, Wersinger et al., 1997). A role of estradiol in controlling male behaviors seems counterintuitive because it is essentially undetectable in the male mouse circulation. Estrogenic steroids in vivo are derived from testosterone or related androgens in a reaction catalyzed by aromatase, and aromatase+ cells in the male brain convert

circulating androgens into estrogenic derivatives (Naftolin et al., 1971). It is this locally synthesized estradiol that is thought to control male-typical behaviors (Figure 1A) (MacLusky and Naftolin, 1981).

Aromatase+ cells represent <0.05% of neurons in the adult mouse brain, and they are sparsely distributed within a few brain regions thought to be important for sexually dimorphic behaviors (Wu et al., 2009). Given the role of estradiol in diverse male-typical behaviors, aromatase+ neuronal populations exert a profound effect on such behaviors. However, the behavioral function of individual aromatase+ neuronal pools is unclear. In one scenario, each aromatase+ population globally controls social interactions in males. Alternatively, individual aromatase+ populations regulate one or a subset of male-typical behaviors. Although there is little circulating testosterone in female mice and the female brain is exposed to circulating estradiol secreted by ovaries, there is aromatase expression in the female rodent brain, albeit at lower levels than in males (Roselli, 1991, Roselli et al., 1985, Wu et al., 2009). The function, if any, of aromatase+ neurons in female mice is unknown (Figure 1A).

We utilized genetic strategies to test the function of aromatase+ posterodorsal medial amygdala (MeApd) neurons in sexually dimorphic behaviors. Aromatase+ neurons comprise ~40% of neurons within the MeApd, a region important for reproductive behaviors and responsive to pheromone sources such as urine (Baum and Bakker, 2013, Bergan et al., 2014, Choi et al., 2005, DiBenedictis et al., 2012, Sokolowski and Corbin, 2012, Swanson, 2000, Wu et al., 2009). We find that aromatase+ MeApd neurons in males regulate the display of specific features of aggression, but not mating, courtship vocalization, or territory marking. In females, these neurons regulate specific

features of maternal aggression, but not other aspects of maternal care or fertility and sexual behavior. Taken together, our findings reveal a role for aromatase+ MeApd neurons in aggression in both sexes, and furthermore, they demonstrate a surprising modularity in the neural control of sexually dimorphic behaviors.

4.3 RESULTS

4.3.1 A Genetic Strategy to Target Aromatase+ Neurons in Adult Mice

The medial amygdala (MeA) is a large structure that extends >1 mm rostrocaudally (Paxinos and Franklin, 2003) and influences diverse behaviors in rodents, including sexually dimorphic behaviors (Petrovich et al., 2001, Swanson, 2000, Swanson and Petrovich, 1998). In keeping with its size and functional diversity, the mouse MeA is molecularly heterogeneous (Carney et al., 2010, Choi et al., 2005, Keshavarzi et al., 2014, Xu et al., 2012, Yang et al., 2013). These considerations make it difficult to selectively target the small pool of aromatase+ MeApd neurons (Wu et al., 2009). In order to target these neurons, we knocked in an IRES-Cre transgene into the 3′ UTR of the aromatase locus (Figures 1B and 1C). As described before, this strategy does not disrupt function or expression of the modified locus (Yang et al., 2013), and it permits expression of Cre recombinase in aromatase+ cells. Indeed, in contrast to aromatase–/– mice (Matsumoto et al., 2003), mice bearing the aromataseCre (aroCre) allele are fertile and have wild-type (WT) levels of circulating sex hormones (Figure 1D). In situ hybridization for Cre shows this enzyme to be expressed in a pattern mirroring that of aromatase (Figure 1E). To validate functional Cre expression in aromatase+ MeApd neurons, we injected an adeno-associated virus (AAV) harboring a Cre-dependent reporter in mice doubly heterozygous

for aroCre and the previously described knockin aromataseIPIN (aroIPIN) allele that drives nuclear β-galactosidase in aromatase+ cells (Wu et al., 2009). In these animals, we observed colocalization of β-galactosidase and mCherry, confirming functional expression of Cre in aroCre mice (Figure 1F and see below). In addition, these studies confirmed the highly restricted nature of aromatase expression within the MeA (Figure 1F) (Wu et al., 2009).

4.3.2 Aromatase+ MeApd Neurons Specifically Regulate Male Aggression

We tested the requirement of aromatase+ MeApd neurons in sexually dimorphic behaviors. We first ablated these neurons in adult mice via bilateral targeted delivery to the MeA of an AAV encoding a genetically modified caspase-3 whose activation requires Cre recombinase (Figure 2A) (Yang et al., 2013). Activation of this caspase-3 triggers apoptosis exclusively in Cre+ cells without bystander toxicity to neighboring cells not expressing Cre (Morgan et al., 2014, Nelson et al., 2014, Yang et al., 2013). Only those aroCre males with a substantive loss (>50% loss bilaterally) of aromatase+ MeApd neurons were included for analysis of behavioral performance (Figures 2B–2D and S1A–S1F). AAV-injected aroCre/IPIN (experimental) and aro+/IPIN (control) males were allowed to recover for 4 weeks to ensure maximal cell loss, singly housed thereafter, and tested for behavioral performance (Figure 2A). Male mice exhibit a stereotyped routine of mating displays toward females, consisting of bouts of anogenital sniffing, mounting, and intromission (penetration) that can culminate in ejaculation (McGill, 1962). We observed no difference in these mating components between aroCre/IPIN and control males when they were presented with a sexually receptive intruder female (Figure 2B).

Male mice vocalize to females, and there was no difference between aroCre/IPIN and control males in such courtship vocalization (Figure S1A). AroCre/IPIN males also directed their courtship vocalizations preferentially to females (Figure S1A), indicative of unaltered sex discrimination (Stowers et al., 2002). Taken together, our findings show that despite the importance of the MeApd in reproductive behavior (Baum and Bakker, 2013, Bergan et al., 2014, Choi et al., 2005, DiBenedictis et al., 2012, Sokolowski and Corbin, 2012, Swanson, 2000), most aromatase+ MeApd neurons are not essential for WT levels of male sexual behavior and courtship vocalizations in mice.

We next tested these resident males for aggression toward an unfamiliar adult WT intruder male. Both aroCre/IPIN and aro+/IPIN residents chemoinvestigated, groomed, and attacked intruders, but aroCre/IPIN males took significantly longer time to initiate aggression (Figures 2C and S1A). There was a corresponding decrease in the number of attacks directed toward the intruder by aroCre/IPIN males (Figure 2C). The deficits in attacks correlated strongly with the extent of loss of aromatase+ MeApd neurons (Figure S1G). Resident males often tail rattle as a threat to intruder males, and we observed a significant increase in the latency to tail rattle in aroCre/IPIN males (Figure 2C). In addition to attacking intruder males, male mice also mark their home territory with numerous urine spots. Despite the reduced aggression toward intruders, aroCre/IPIN males marked their territory similar to controls (Figure S1C). We tested aroCre/IPIN males to determine if they exhibited pervasive deficits that could contribute to the deficits in aggression. However, these males did not exhibit deficits in finding hidden food, anxiety-type behavior on an elevated plus maze, and locomotor activity, and they maintained body weight and circulating testosterone (Figures S1D–S1F). The

anatomically restricted nature of aromatase expression (Wu et al., 2009) allows specific ablation of aromatase+ MeApd neurons (Figure 2D). It also ensures that other non-MeApd aromatase+ populations such as those in the bed nucleus of the stria terminalis (BNST) are distant from the injection site and are not infected by the stereotactically delivered virus. Indeed, the number of aromatase+ BNST neurons was unchanged (aroCre/IPIN, 660 ± 198; aro+/IPIN, 565 ± 132; $n = 5$, $p > 0.1$) following viral delivery to the MeA. Ablation of progesterone receptor-expressing neurons in the ventromedial hypothalamus reduces all aspects of aggression, including the pattern of attacks as measured by interattack interval and mean duration of an attack bout (Yang et al., 2013). Although we cannot exclude a subtle role of aromatase+ MeApd neurons in all components of aggression, our findings reveal that ablation of a majority of these neurons reduces aggression without altering the pattern of attack (Figure S1B). It is possible that aromatase+ MeApd neurons relay pheromonal information relating to aggression rather than regulating different aspects of this behavior. If so, this would represent the identification of a class of molecularly specified MeA neurons that respond to pheromonal cues relating to aggression but not other social behaviors. Regardless of the underlying mechanism, our findings show that aromatase+ MeApd neurons are required for the display of WT levels of specific components of aggression.

4.3.3 Aromatase+ MeApd Neurons Acutely Regulate Male Aggression

We used a chemogenetic approach to acutely silence aromatase+ MeApd neurons (Sternson and Roth, 2014). Most aromatase+ neuroendocrine cells in the MeApd express glutamate decarboxylase 1 (GAD1), suggesting that they are GABAergic

neurons (Figure S2A). Silencing these neurons allows us to test directly whether their neural activity is essential for social behaviors. Moreover, this approach permits testing whether the chronic loss of neurons following caspase-mediated ablation activates compensatory mechanisms that mask a role of these neurons in marking, mating, or courtship vocalization. We delivered AAVs encoding a Cre-dependent fusion protein consisting of a Gi-coupled DREADD (designer receptor exclusively activated by designer drug) and mCherry bilaterally to the MeA (Figure 3A). This DREADD-Gi is activated exclusively by the biologically inert small-molecule clozapine-N-oxide (CNO) such that CNO-bound DREADD-Gi hyperpolarizes neurons and silences them (Armbruster et al., 2007, Sternson and Roth, 2014). Only aroCre/IPIN males where a majority of aromatase+ MeApd neurons coexpressed mCherry were included for behavioral analysis (Figures 3B–3D and S2B–S2G). We singly housed males 1 week after viral injection and began behavior testing 1 week later. They were tested in behavioral assays following CNO administration (Ray et al., 2011, Sasaki et al., 2011). There was no difference between aroCre/IPIN males administered saline or CNO in assays of mating, courtship vocalization, urine marking, anxiety-type behavior, food finding, and locomotor activity (Figures 3B, S2B, S2D, and S2E); these males also maintained body weight and circulating testosterone (Figures S2F and S2G). Thus, control levels of neural activity of most aromatase+ MeApd neurons are not required for these aspects of male physiology or behaviors, including male sexual behaviors.

Comparable proportions of aroCre/IPIN males administered saline or CNO sniffed and attacked a WT male intruder (Figure 3C). AroCre/IPIN males administered CNO had a significantly longer latency to initiate attacks and tail rattle toward intruder males

(Figure 3C) without a change in the pattern of attack as measured by attack duration and interattack interval (Figure S2C). There was a strong correlation between the increased latency to attack in the presence of CNO and DREADD-Gi expression (Figure S2H). Importantly, aro+/IPIN control males injected with this AAV showed unaltered mating and aggressive behaviors even in the presence of CNO (Figures S2I and S2J), demonstrating that CNO itself does not modulate social behaviors. Our histological studies confirmed that DREADD-Gi expression was limited to the MeApd and did not spread to other aromatase-expressing locations such as the BNST (Figure S2K). Thus, acute silencing of aromatase+ MeApd neurons parallels the specific deficits in aggression observed with targeted ablation of these neurons. Importantly, activating these neurons with a Gq-coupled DREADD that increases neuronal activity (Sternson and Roth, 2014) did not alter sexual or aggressive displays at CNO doses previously shown by us and others to activate neurons and modulate behavior (Figure S3) (Anaclet et al., 2014, Sasaki et al., 2011). Indeed, CNO elicited a large increase in c-Fos+ neurons in the MeApd in vivo and depolarized and increased spike rate in aromatase+ MeApd neurons in acute brain slices (Figures S3A and S3B). The lack of behavioral modulation with activation of aromatase+ MeApd neurons may reflect that a larger subset of MeApd neurons needs to be activated to alter aggression. Alternatively, these neurons may relay chemosensory information to neurons that receive additional inputs required to drive mating or aggression. Indeed, fly sensory neurons that relay the presence of pheromones are required, but not sufficient, for WT levels of aggression (Wang et al., 2011). Regardless, our findings demonstrate that neural activity of a majority of

aromatase+ MeApd neuroendocrine neurons is required for appropriate display of male aggression, but not other sexually dimorphic behaviors.

4.3.4 Aromatase+ MeApd Neurons Specifically Regulate Maternal Aggression

We tested the function of aromatase+ MeApd neurons in female-typical displays of receptivity and parental care by ablating them via targeted delivery of AAV encoding Cre-dependent caspase-3 (Figure 4A). As with males, we only analyzed females with a substantive loss (>50%) of aromatase+ MeApd neurons (Figures 4B–4D and S4A–S4F). To test for sexual behavior, female aroCre/IPIN and aro+/IPIN mice were injected bilaterally into the MeA with virus, and their ovaries were removed to permit estrus induction on the day of testing. These mice were allowed to recover from surgery for 4 weeks, hormonally primed to be in estrus, and inserted into the home cage of sexually experienced WT males. We observed that sexual behavior of both groups of females was comparable, such that they stayed still rather than running away when the male approached and mounted them (Figure 4B). This receptive behavior permitted mounts to proceed to intromission (receptivity index) equivalently between these two sets of females (Figure 4B). WT males also appeared equally interested in aroCre/IPIN and aro+/IPIN females as they investigated, mounted, and intromitted them with comparable latency and number (Figure S4A). These females did not exhibit deficits in finding food, anxiety-type behavior, and locomotor activity, and they maintained their body weight (Figures S4B and S4C). In summary, despite the importance of the MeA in female sexual behavior (DiBenedictis et al., 2012), a majority of aromatase+ MeApd neurons are not essential for this behavior.

To test whether aromatase+ MeApd neurons regulate maternal behaviors, we ablated them in a separate cohort of females that were subsequently mated with WT males to generate litters (Figure 4A). AroCre/IPIN and aro+/IPIN females were inseminated (as determined by the presence of a vaginal plug) and generated litters at equivalent rates (Figure S4D), indicating that ablation of aromatase+ MeApd neurons does not render females infertile. Upon parturition, aroCre/IPIN as well as aro+/IPIN females ate their afterbirths, cleaned pups, and nursed them in their nest. Pups can crawl away from the nest, and dams efficiently retrieve them to the nest. Experimental removal of pups from their nest elicited pup retrieval with comparable efficiency between the two groups of females (Figure 4C). In addition, aroCre/IPIN females did not exhibit deficits in finding hidden food, anxiety-type behavior on an elevated plus maze, and locomotor activity, and they maintained their body weight (Figures S4E and S4F). Thus, most aromatase+ MeApd neurons are not essential for these behaviors, including many components of maternal care.

Nursing mice attack unfamiliar intruder mice because such intruders can be infanticidal toward pups (Gandelman, 1972, Wu et al., 2014). We tested whether aromatase+ MeApd neurons were required for such maternal aggression by inserting a WT male into the cage of experimental and control nursing females. Both groups of females investigated and attacked intruders with equivalent probability (Figure 4D). There was a significant 2.4-fold decrease in the number of attacks by aroCre/IPIN females that strongly correlated with the degree of cell loss within the MeApd (Figures 4D and S4G). Similar to males (Figure S1B), once aggression was initiated, there was no difference in the attack pattern between control and aroCre/IPIN females (Figure S4D).

Thus, ablation of aromatase+ MeApd neurons leads to a specific deficit in maternal aggression. We wished to test whether these neurons also acutely regulate maternal aggression by using DREADD-Gi mediated chemogenetic control of neural activity. However, we consistently observed only a few weakly expressing mCherry+ neurons within the MeApd of aroCre/IPIN females (data not shown), presumably reflecting the lower levels of aromatase in the female brain. Given that caspase-3 is extremely cytotoxic (Morgan et al., 2014), it is not surprising that despite the lower efficiency of Cre recombination in females, we succeeded in ablating aromatase+ MeApd neurons. In any event, our findings demonstrate that aromatase+ MeApd neurons are required for WT levels of maternal aggression. Moreover, our studies reveal that aromatase+ neurons are, in fact, functional in females.

Different forms of fighting such as intermale and maternal aggression are thought to be controlled by different neural pathways (Moyer, 1968). Indeed, there are distinct sensory, hormonal, and molecular requirements for intermale and maternal aggression (Demas et al., 1999, Finney and Erpino, 1976, Gammie and Nelson, 1999, Gammie et al., 2000, McDermott and Gandelman, 1979, Nelson et al., 1995, Svare and Gandelman, 1975, Svare and Gandelman, 1976a, Svare and Gandelman, 1976b). Previous work suggested that these two forms of aggression may be executed differently (Gandelman, 1972, Scott, 1966). Given our finding that aromatase+ MeApd neurons regulate both intermale and maternal aggression, we sought to determine the nature of the differences in these two forms of fighting. We identified many quantitative differences between intermale and maternal aggression (Figure 4E). Moreover, there were striking qualitative differences between these two forms of aggression. Males typically attack the back and

flank of the intruder, whereas dams attack the head and genital regions of the intruder and they rarely box, chase, or wrestle (Figure 4E; Movies S1 and S2). In summary, these findings show that aromatase+ MeApd neurons regulate distinct forms of aggression in the two sexes.

4.4 DISCUSSION

4.4.1 A Shared Neural Pathway for Distinct Forms of Aggression

It can be argued that intermale and maternal aggression are different forms of a common behavioral display, fighting. However, we observe dramatic differences between intermale and maternal aggression. Nevertheless, we find that aromatase+ MeApd neurons regulate both maternal and intermale aggression, demonstrating a hitherto unknown neural circuit link between different forms of aggression. More broadly, our findings suggest the possibility that a primordial neural pathway underlying aggression predates the divergent needs of the two sexes to fight in different contexts. Such a neural circuit could be modified during evolution and sexual selection such that it is activated by different stimuli and drives different motor programs in the two sexes.

4.4.2 Aromatase+ MeApd Neurons Subserve Distinct Behaviors in the Two Sexes

Most sexual dimorphisms in the vertebrate brain represent quantitative rather than qualitative differences in gene expression or neurocytological features. Indeed, there are significantly more aromatase+ MeApd neurons in males compared to females (Wu et al., 2009). It is possible that a sexually dimorphic neuronal pool is nonfunctional in one sex, drives distinct behaviors in both sexes, or functions to suppress a behavior of the

opposite sex (De Vries and Boyle, 1998). We show here that aromatase+ MeApd neurons control distinct forms of aggression in males and females. The cell number difference in aromatase+ MeApd neurons could drive distinct behaviors (such as tail rattling or boxing) in the two sexes. The MeApd also expresses many other sex hormone-dependent genes in sex-specific patterns (Xu et al., 2012), and these may also permit aromatase+ MeApd neurons to regulate distinct behaviors in the two sexes. We have previously shown that sexually dimorphic progesterone receptor-expressing neurons in the ventromedial hypothalamus control distinct behaviors in males and females (Yang et al., 2013). Such functional bivalence may therefore be a general property of sexually dimorphic neuronal populations.

4.4.3 Global versus Modular Control of Complex Social Behaviors

Sex hormones exert global control over the display of sexually dimorphic social behaviors. For example, estrogen signaling in males governs vocalization, sexual displays, aggression, and territory marking. By contrast, we find that aromatase+ MeApd neurons are only required for WT levels of aggression. At least some components of the global control of vertebrate male behavior by estradiol likely result from paracrine signaling and masculinizing neural circuits during development (Balthazart and Ball, 1998, Forlano et al., 2006, McCarthy, 2008, Wu et al., 2009). In addition, specificity in behavioral control may be a general feature of molecularly defined neuronal populations such as those in the MeApd that are close to sensory input. In this case, aromatase+ neuronal populations more distant from sensory input, such as those in the

hypothalamus, are predicted to control multiple features of different male-typical behaviors.

Our data show that it is possible to dissociate specific components of a complex social behavior such as aggression without altering other features of the behavior. In fact, the MeA itself is critical for aggressive as well as courtship displays in both sexes, whereas we find that the aromatase+ MeApd neurons regulate aggression, but not territory marking or sexual behaviors (Baum and Bakker, 2013, Bergan et al., 2014, Choi et al., 2005, DiBenedictis et al., 2012, Sokolowski and Corbin, 2012, Swanson, 2000, Wu et al., 2009). Aromatase+ MeApd neurons comprise ~40% of neurons within the MeApd and, we estimate, ~10%–20% of neurons within the MeA. Given the molecular heterogeneity within the MeA, we anticipate that other molecularly specified MeA neuronal subsets regulate other aspects of social interactions. Such exquisite modularity in behavioral control may be a general property of many similarly discrete neuronal populations in other brain regions. It will be interesting to understand how such neural modules underlying particular behavioral components are coordinated to generate apparently seamless behavioral displays. Presumably, neurons close to motor output pathways encode multiple features of a behavioral program. Indeed, neurons expressing progesterone receptor (and estrogen receptor α) in the ventromedial hypothalamus that are distant from sensory input are necessary and sufficient for multiple components of mating and aggression (Lee et al., 2014, Yang et al., 2013). Such modularity in the neuronal control of social behavior is likely to be a general mechanism whereby other complex behaviors such as feeding are regulated (Sternson, 2013). As discussed

recently (Yang et al., 2013), such modular control of behavior resembles the modularity in signaling proteins and networks and may enable rapid evolution of behaviors.

Hong et al. (2014) recently published a study describing the contribution of MeA neurons to male mating, aggression, and grooming. Our study genetically identifies the aromatase+ subset of MeA neurons as specifically underlying male aggression and further shows that these neurons also regulate maternal aggression.

4.5 EXPERIMENTAL PROCEDURES

4.5.1 Generation of Mice Bearing the aroCre Allele

The IRES-Cre transgene was inserted into the 3′ UTR of the aromatase locus via homologous recombination as described previously (Wu et al., 2009, Yang et al., 2013). All experiments involving animals were performed in accordance with institutional animal care and use committee guidelines at University of California, San Francisco.

4.5.2 Viruses and Stereotaxic Surgery

The caspase-3 and DREADD-encoding cassettes and AAV viruses we used have been described previously (Alexander et al., 2009, Anaclet et al., 2014, Armbruster et al., 2007, Ray et al., 2011, Sasaki et al., 2011, Yang et al., 2013). We used AAV serotype 1 or 10 for delivering caspase-3 and AAV serotype 10 for all DREADD studies. Stereotaxic surgery was performed as described previously, and virus was delivered bilaterally at coordinates corresponding to the MeA (rostrocaudal, −1.6 mm; mediolateral, ±2.2 mm; depth of 5.15 mm) (Paxinos and Franklin, 2003).

4.5.3 Behavior

Testing for social behaviors was performed ≥1 hr after onset of the dark cycle and recorded and analyzed as described previously (Juntti et al., 2010, Wu et al., 2009, Xu et al., 2012, Yang et al., 2013). All tests were scored by an experimenter blind to the genotype and drug treatment of the mice, using a software package we developed in MATLAB (Wu et al., 2009).

4.5.4 Electrophysiology

As described above, AAV-flex-DREADD-Gq:mCherry was injected bilaterally into the MeA of aroIPIN/Cre males 8 weeks of age. The mice were allowed to recover >10 days from surgery and then sacrificed brain slice preparation. Slices were cut in ice-cold HEPES buffer solution, incubated for 15 min at 33 ºC in NMDG recovery solution, and finally maintained for 1-5 hrs before recording at room temperature in HEPES buffer solution. HEPES solution composition (in mM): 92 NaCl, 2.5 KCl, 1.2 NaH2PO4, 30 NaHCO3, 20 HEPES, 25 Glucose, 5 Na+ Ascorbate, 2 Thiourea, 3 Na+ Pyruvate, 10 MgSO4, 0.5 CaCl2, 305 mOsm, 7.3-7.4 pH. NMDG solution was identical to HEPES, except for an equimolar replacement of NaCl for NMDG.

Neurons were visualized under differential interference contrast optics and epifluorescence and selected for recording based on mCherry expression. Whole cell current-clamp recordings were made using the following recording solutions (in mM): Internal: 9 HEPES, 113 K-Gluconate, 4.5 MgCl2, 0.1 EGTA, 14 Tris-phosphocreatine, 4 Na2ATP, 0.3 TrisGTP, 10 Sucrose, 290 mOsm, 7.2-7.25 pH ; External: 125 NaCl, 2.5 KCl, 1 MgCl2, 1.25 NaH2PO4, 25 NaHCO3, 25 Glucose, 2 CaCl2, 305 mOsm, 7.25-7.30 pH.

Synaptic transmission was maintained to allow for any potential DREADD effects on synaptic input. Spontaneously spiking cells (n = 4 of 6 cells) were held with constant negative holding current ("bias current", -18.9 ± 7.2 pA) to prevent cells from entering depolarization block with CNO application. Bias current was determined before the baseline period and was held constant throughout individual recordings. Vm were not corrected for junction potential (12 mV). All statistics were performed in MATLAB and exclusion criteria were as follows: if cells did not appear to have a stable baseline during the experiment, CNO was not applied. Linear regression was also performed on the baseline period Vm for each cell; if a statistically significant ($p < 0.05$) slope of greater than ± 0.5 mV/min was observed during this period, the cell was excluded from analysis (n = 0 cells).

4.6 FIGURES

4.6.1 Main Figures

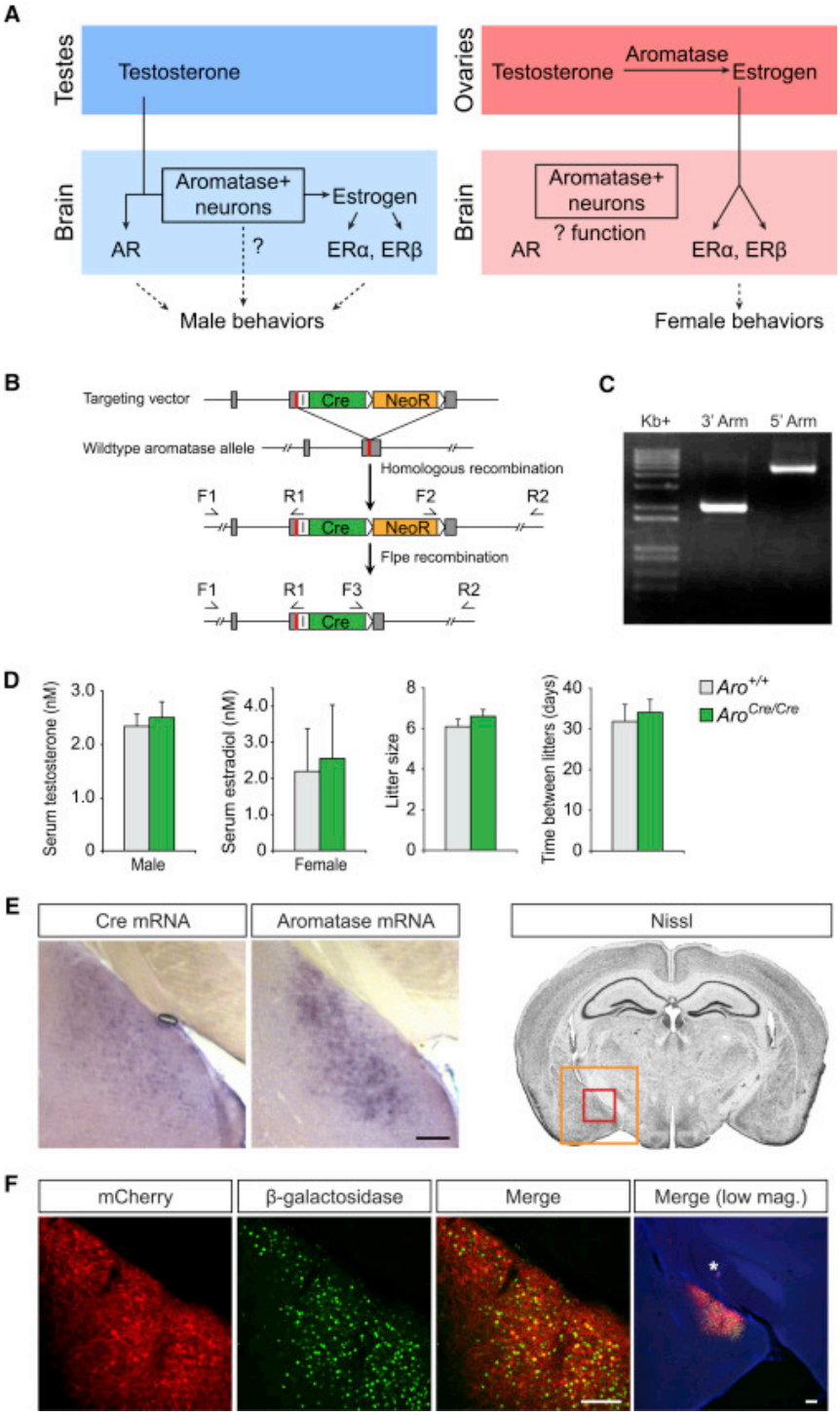

Figure 4.1. Generation and characterization of mice expressing Cre recombinase in aromatase+ cells

(A) Role of aromatase in sexually dimorphic behaviors. Aromatase+ neurons in the male brain produce estradiol that controls many male-typical behaviors, but the function of individual aromatase+ neuronal populations in these behaviors is unknown. Given that the female brain is exposed to circulating estradiol, the function, if any, of aromatase+ neurons is unclear in females.
(B) Generating the aroCre allele. Gray boxes represent last two exons of aromatase, and red line in 3' exon denotes stop codon. Primers (F1-3 and R1, 2) used for PCR-based genotyping are shown. Schematic not drawn to scale.
(C) PCR verification of homologous recombination at the aromatase locus from tail DNA of an aroCre/Cre mouse.
(D) No difference in serum hormone titers, litter size, or time between litters between WT and aroCre/Cre mice (Mean ± SEM; n = 10 WT and 6 aroCre/Cre of each sex).
(E) Cre mRNA expression mirrors that of aromatase mRNA in an adjacent section through the MeA. Boxed area in red in Nissl-stained coronal section highlights the MeApd (Paxinos and Franklin, 2003).
(F) Injection of AAV encoding a Cre-dependent mCherry into the MeA activates mCherry expression in aromatase+ neurons expressing □-galactosidase in aroCre/IPIN mice. The low magnification (mag.) merge panel is counterstained with DAPI (blue) to show that aromatase expression (and Cre-dependent reporter) is restricted to the MeApd and not to be found in neighboring regions; asterisk in the low mag. panel denotes needle track. Boxed areas in red and orange in Nissl-stained coronal section (E) highlight the areas shown at high and low mag., respectively.
Scale bars = 200 μm.

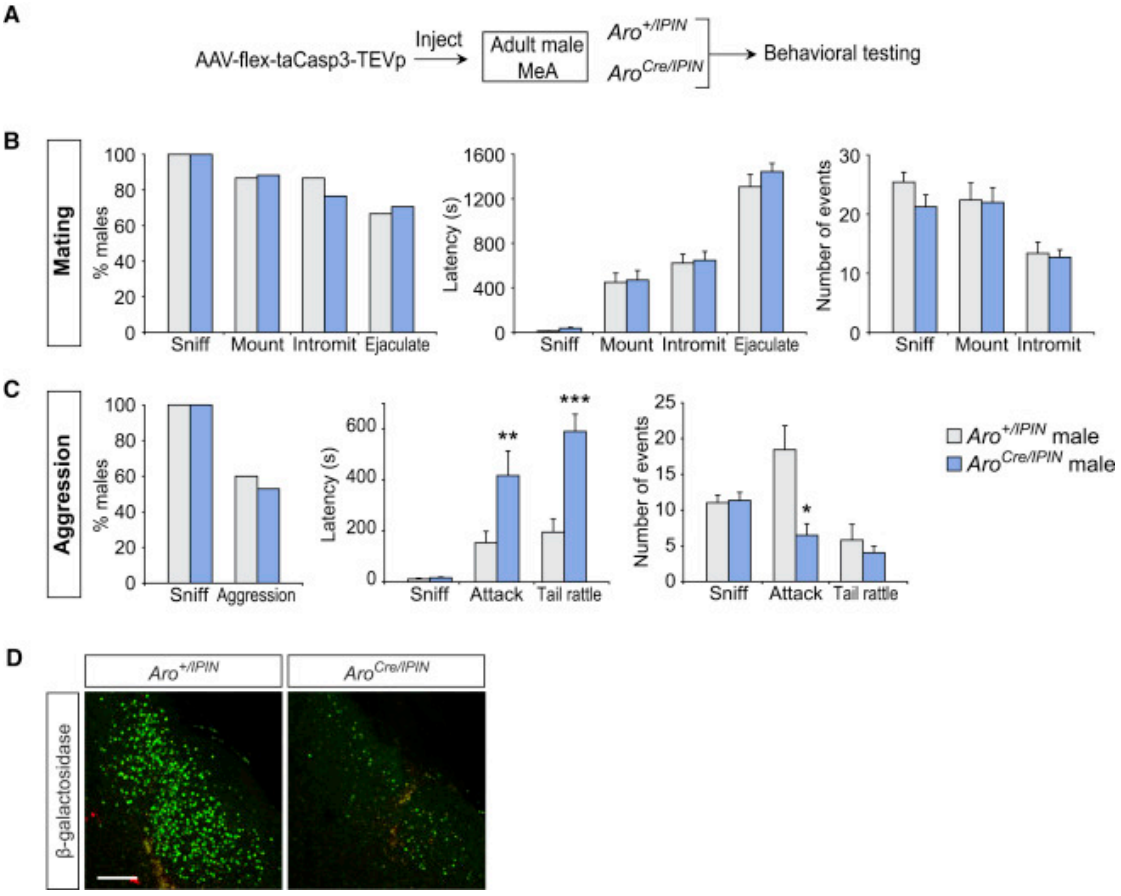

Figure 4.2. Ablation of Aromatase+ MeApd Neurons Reduces Specific Components of Male Aggression

(A) Experimental strategy to ablate Cre-expressing aromatase+ MeApd neurons and test for behavioral deficits. AAV encoding Cre-dependent caspase-3 was injected into the MeA of aroCre/IPIN and aro+/IPIN males that were subsequently tested for mating and aggression.

(B) No difference between aroCre/IPIN and control aro+/IPIN males in mating with a WT estrus female.

(C) Comparable percent of aroCre/IPIN and aro+/IPIN males sniff and attack a WT intruder male. AroCre/IPIN males take significantly longer to attack and tail rattle, and they attack the intruder less.

(D) Histological verification of ablation of aromatase+ neurons in MeApd of aroCre/IPIN males. Some autofluorescence is visible in the red channel.

Mean ± SEM; n = 14 aro+/IPIN, n = 15 aroCre/IPIN; $*p < 0.05$, $**p < 0.01$, $***p < 0.005$. Scale bar represents 200 μm. See also Figure S1.

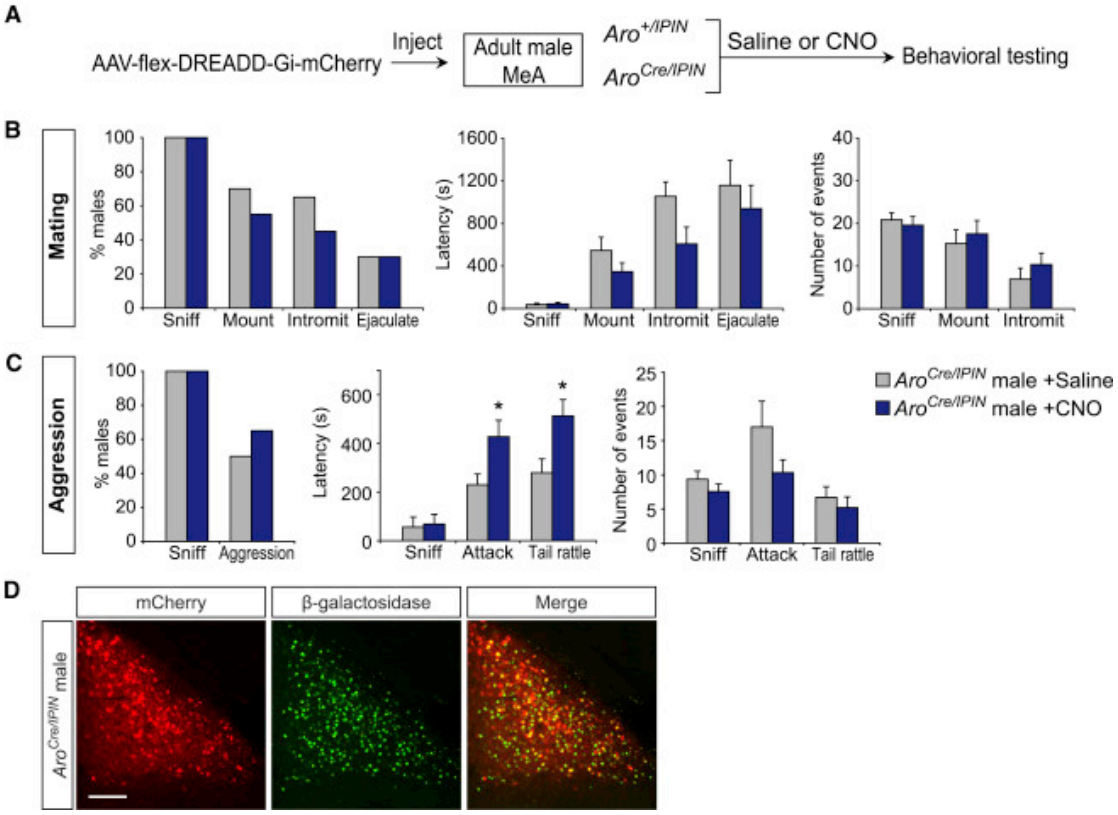

Figure 4.3. Inhibiting Aromatase+ MeApd Neurons with DREADD-Gi Reduces Specific Components of Male Aggression

(A) Experimental strategy to inhibit Cre-expressing aromatase+ MeApd neurons and test for behavioral deficits in males. AAV encoding Cre-dependent DREADD-Gi was injected into the MeA of aroCre/IPIN males that were subsequently tested for behaviors following intraperitoneal CNO or saline administration.

(B) No difference between aroCre/IPIN males administered saline or CNO in mating with a WT estrus female.

(C) No difference between percent aroCre/IPIN males given saline and CNO that sniffed or attacked a WT intruder male. AroCre/IPIN males administered CNO took significantly longer to initiate attacks or tail rattle.

(D) Histological verification of DREADD-Gi (mCherry) expression in aromatase+ neurons in MeApd of aroCre/IPIN males.

Mean ± SEM; n = 20 aroCre/IPIN; for parallel studies with aro+/IPIN, please see Figure S2; $*p < 0.05$. Scale bars represent 200 μm. See also Figures S2 and S3.

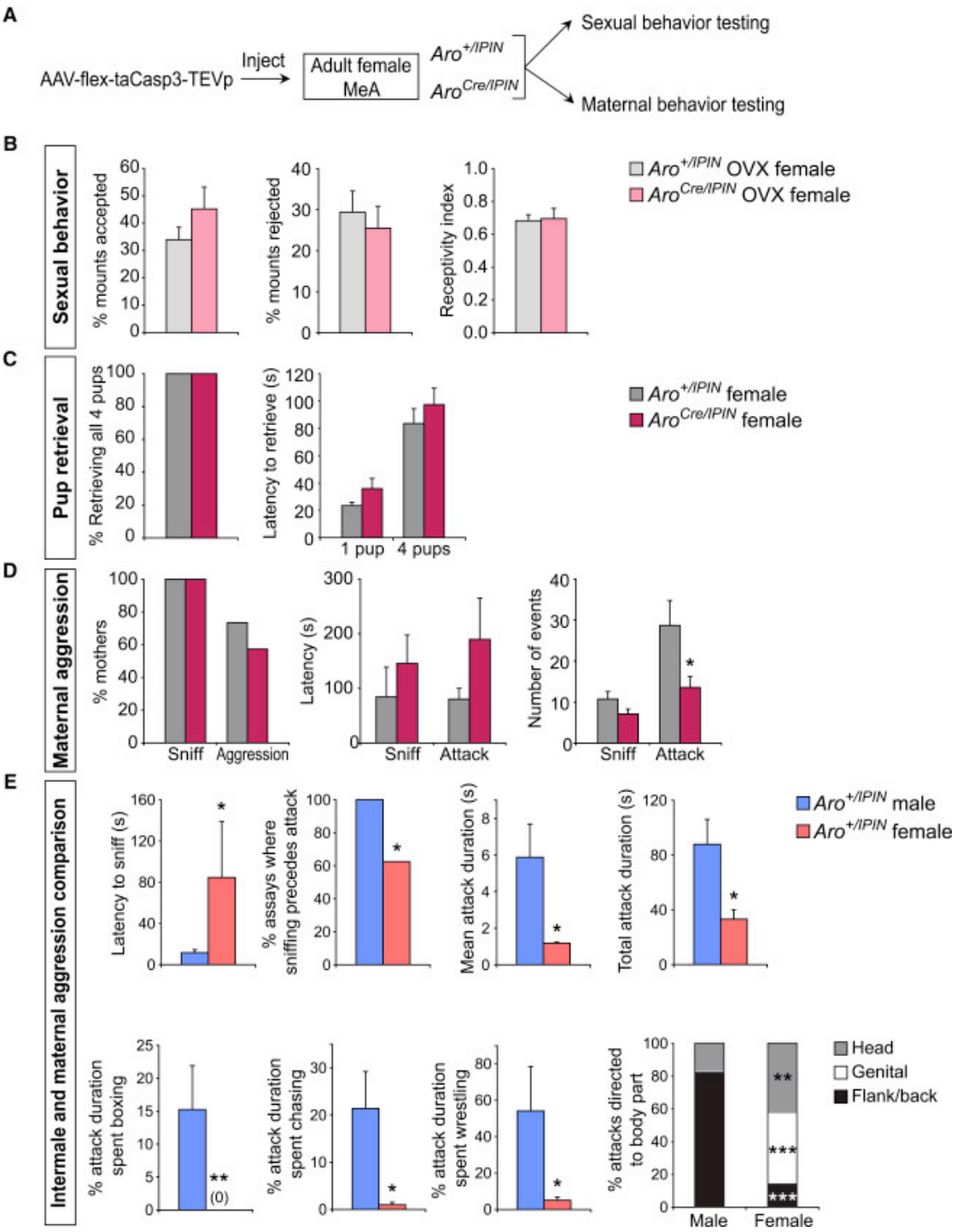

Figure 4.4. Ablation of Aromatase+ MeApd Neurons Reduces Specific Components of Maternal Aggression

(A) Experimental strategy to ablate Cre-expressing aromatase+ MeApd neurons and test for behavioral deficits. AAV encoding Cre-dependent caspase-3 was injected into the MeA of separate cohorts of aroCre/IPIN and aro+/IPIN females for testing performance in mating and maternal behaviors.

(B) No difference in fraction of mounts that were accepted or rejected and no difference in receptivity index (# intromissions/# mounts) between aroCre/IPIN and aro+/IPIN females.
(C) Vast majority of aroCre/IPIN and aro+/IPIN females retrieved all pups to the nest, and they did so with similar latencies.
(D) Comparable percent of aroCre/IPIN and aro+/IPIN females sniff and attack a WT intruder male. Significant decrease in number of attacks directed to intruder male by aroCre/IPIN females.
(E) A WT male intruder was inserted into the cage of a resident male or lactating female for 15 min. Mothers have a longer latency to sniff the intruder and, unlike resident males, can attack the intruder prior to chemoinvestigation. The duration of individual attacks as well as total duration of attacks initiated by mothers is significantly shorter. Mothers spend significantly less time chasing or wrestling with the intruder male. No boxing was observed in attacks initiated by mothers. Mothers bite the intruder significantly more on the head or anogenital region compared to resident males. Resident males bite the intruder significantly more on the back and flank compared to mothers. Data for these behavioral comparisons are taken from animals used to generate data for panels in Figures 2C, 4D, S1B, and S4D.
Mean ± SEM; $n > 14$ aro+/IPIN and $n > 7$ aroCre/IPIN for tests of sexual and maternal behaviors each (A–D); $n = 7$ aro+/IPIN males and 6 aro+/IPIN mothers (E); $*p < 0.05$, $**p < 0.01$, $***p < 0.005$; OVX, ovaries surgically removed. See also Figure S4.

4.6.2 Supplemental Figures

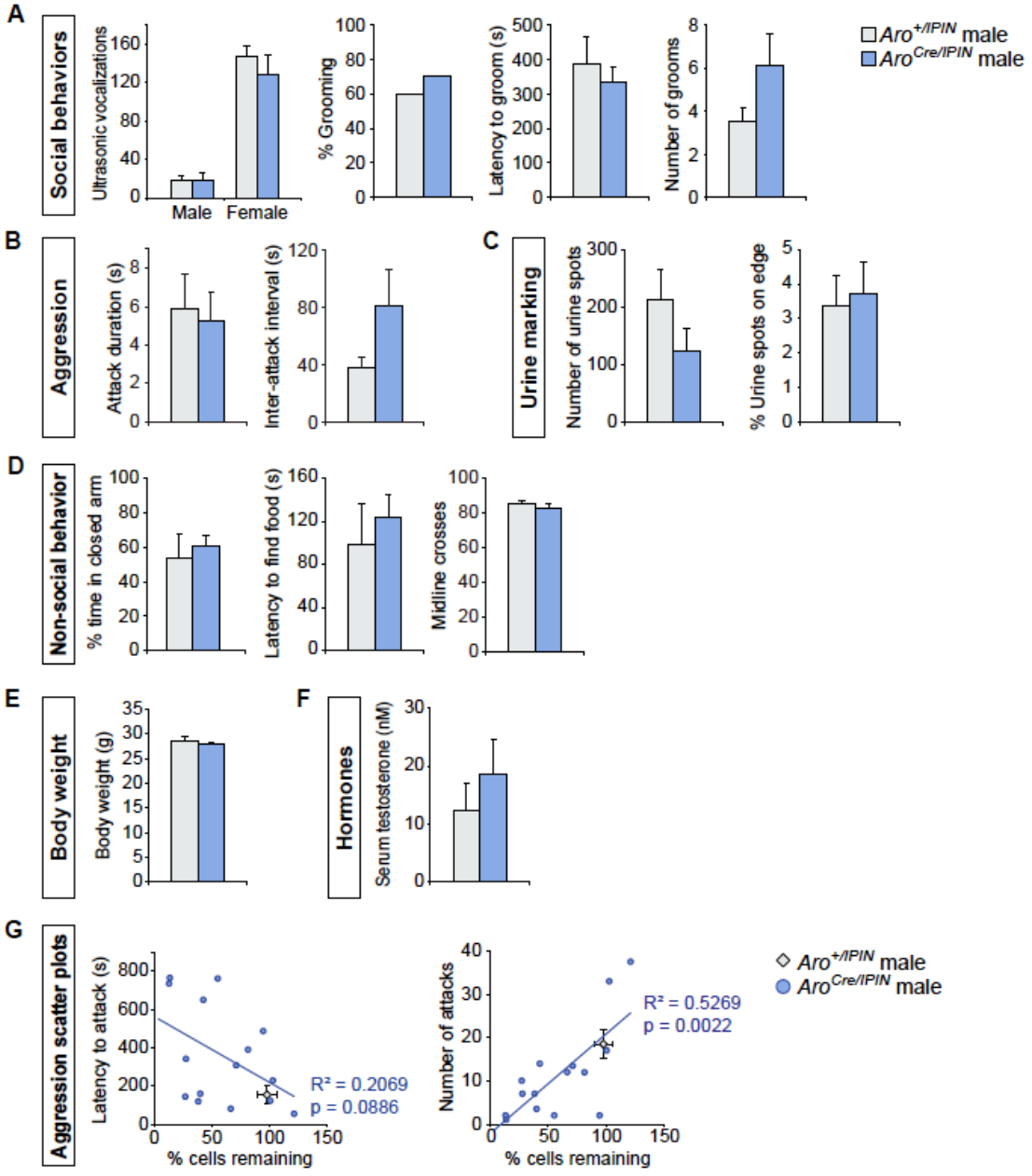

Figure 4.5 (S1). Ablation of male aromatase+ MeApd neurons reduces specific components of aggression, Related to Figure 4.2.
(A) No difference between aroCre/IPIN and aro+/IPIN males in emitting ultrasonic vocalizations toward WT male and female intruders or in grooming WT intruder males.
(B) No difference between aroCre/IPIN and aro+/IPIN males in pattern of attacks (mean attack bout duration and inter-attack interval) toward a WT intruder male.

(C) No difference between aroCre/IPIN and aro+/IPIN males in marking territory with urine.
(D) No difference between aroCre/IPIN and aro+/IPIN males in anxiety-type behavior (elevated-plus maze), finding food when starved, or locomotor activity as measured by number of midline crosses.
(E, F) No difference between aroCre/IPIN and aro+/IPIN males in body weight or serum testosterone.
(G) Significant correlation between loss of aromatase+ MeApd neurons and number of attacks toward a WT intruder male. Scatter plots include data from all aroCre/IPIN males who displayed any attacks (15/27); gray diamond in the plots depicts number of attacks by aro+/IPIN males toward WT intruder males. Mean ± SEM; n = 14 aro+/IPIN (A-G), n = 15 aroCre/IPIN (A-F), n = 27 aroCre/IPIN (G)

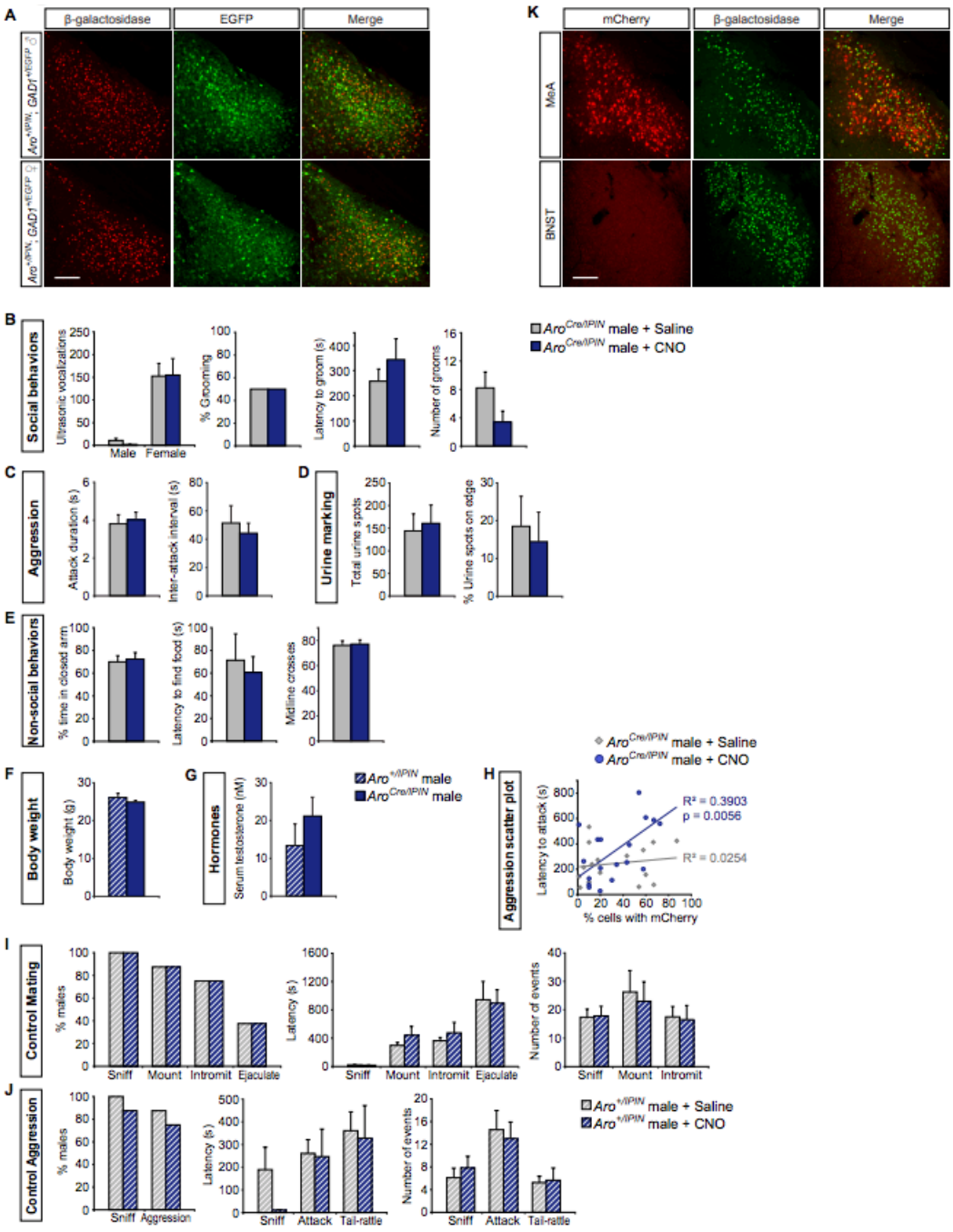

Figure 4.6 (S2). Inhibiting male aromatase+ MeApd neurons reduces specific components of aggression, Related to Figure 4.3.

(A) Most aromatase+ MeApd neurons co-express GAD1, a biosynthetic enzyme for the neurotransmitter GABA. (% aromatase+ MeApd neurons that are GAD1+: Male, 83.7% ± 3.4; Female, 90.6% ±4.8; n = 2 for each sex).

(B) No difference between aroCre/IPIN males given CNO or saline in emitting ultrasonic vocalizations toward WT male and female intruders or in grooming WT intruder males.

(C) No difference between aroCre/IPIN males given CNO or saline in pattern of attacks (mean attack bout duration and inter-attack interval) toward a WT intruder male.

(D) No difference between aroCre/IPIN males given CNO or saline in marking territory with urine.
(E) No difference between aroCre/IPIN males given CNO or saline in anxiety-type behavior (elevated-plus maze), finding food when starved, or locomotor activity as measured by number of midline crosses.
(F, G) No difference between aroCre/IPIN and aro+/IPIN males in body weight or serum testosterone.
(H) Significant correlation between more aromatase+ MeApd neurons expressing DREADD-Gi and increased latency to attack WT intruder male following CNO administration. Scatter plot includes data from all aroCre/IPIN males who displayed any attacks (18/28, CNO; 16/28, saline).
(I, J) No difference between aro+/IPIN males given CNO or saline in mating or aggression with WT female and male intruders, respectively.
(K) Injection of AAV encoding the Cre-dependent fusion protein DREADD-Gi:mCherry into the MeA results in expression of mCherry in this region but not in other aromatase+ (Cre+) regions such as the BNST. Mean ± SEM; n = 8 aro+/IPIN (F, G, I, J), n = 20 aroCre/IPIN (B-G), n = 28 aroCre/IPIN (H). Scale bars = 200 μm.

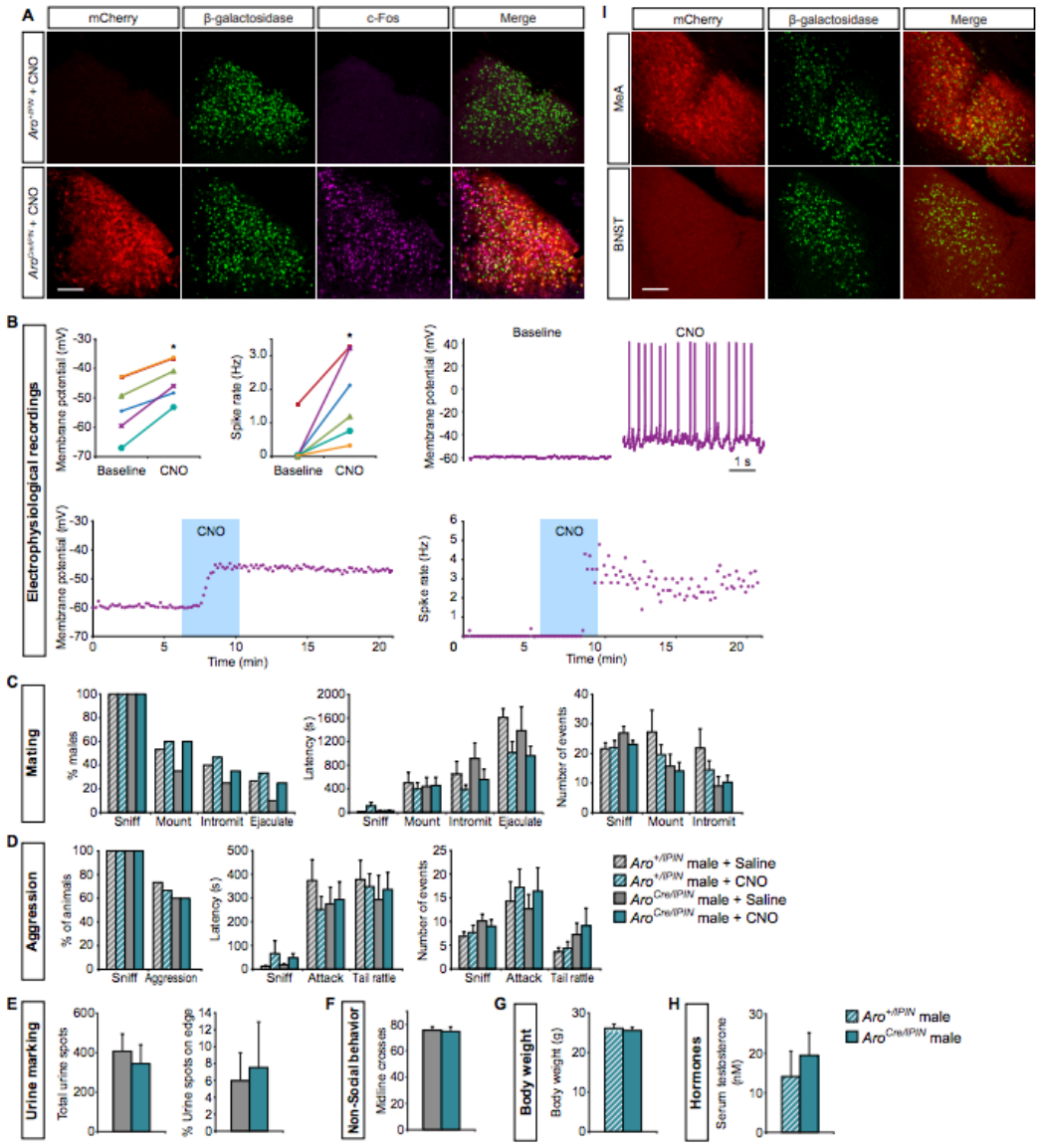

Figure 4.7 (S3). Activating male aromatase+ MeApd neurons does not modulate behavior, Related to Figure 4.3.

AAV encoding Cre-dependent DREADD-Gq:mCherry was injected bilaterally into the MeA of aroCre/IPIN and aro+/IPIN males, and animals were allowed to recover for >10 days.

(A) CNO administration leads to c-Fos activation in MeApd of aro Cre/IPIN but not aro+/IPIN males.

(B) Electrophysiological recordings were performed on coronal brain slices (225-230 μm thick) containing the MeA. Aromatase+ neurons expressing DREADD-Gq were selected for patchclamp recording based on mCherry expression. Both membrane potential and spike rate increased after the application of 1 μM CNO in aCSF for 4 min. Panels at top left show increases in membrane potential and spike rate in the presence of CNO for each of the 6 neurons (each cell represented in a different color). Other panels show

changes in membrane potential and spike rate in an example neuron; the blue box denotes time of CNO application. n = 6 cells from 4 animals. *$p < 0.05$ (sign-rank test).
(C-F) No difference between aroCre/IPIN and aro+/IPIN males given saline or CNO in displays of mating, aggression, urine marking, or locomotor behavior.
(G, H) No difference between aroCre/IPIN and aro+/IPIN males in body weight or serum testosterone.
(I) Injection of AAV encoding the Cre-dependent fusion protein DREADD-Gq:mCherry into the MeA results in expression of mCherry in this region but not in other aromatase+ (Cre+) regions such as the BNST. Mean ± SEM; n ≥ 5 for both genotypes (A), n = 5 aro +/IPIN (B-G), n = 24 aroCre/IPIN (B-G). Scale bars = 200 μm.

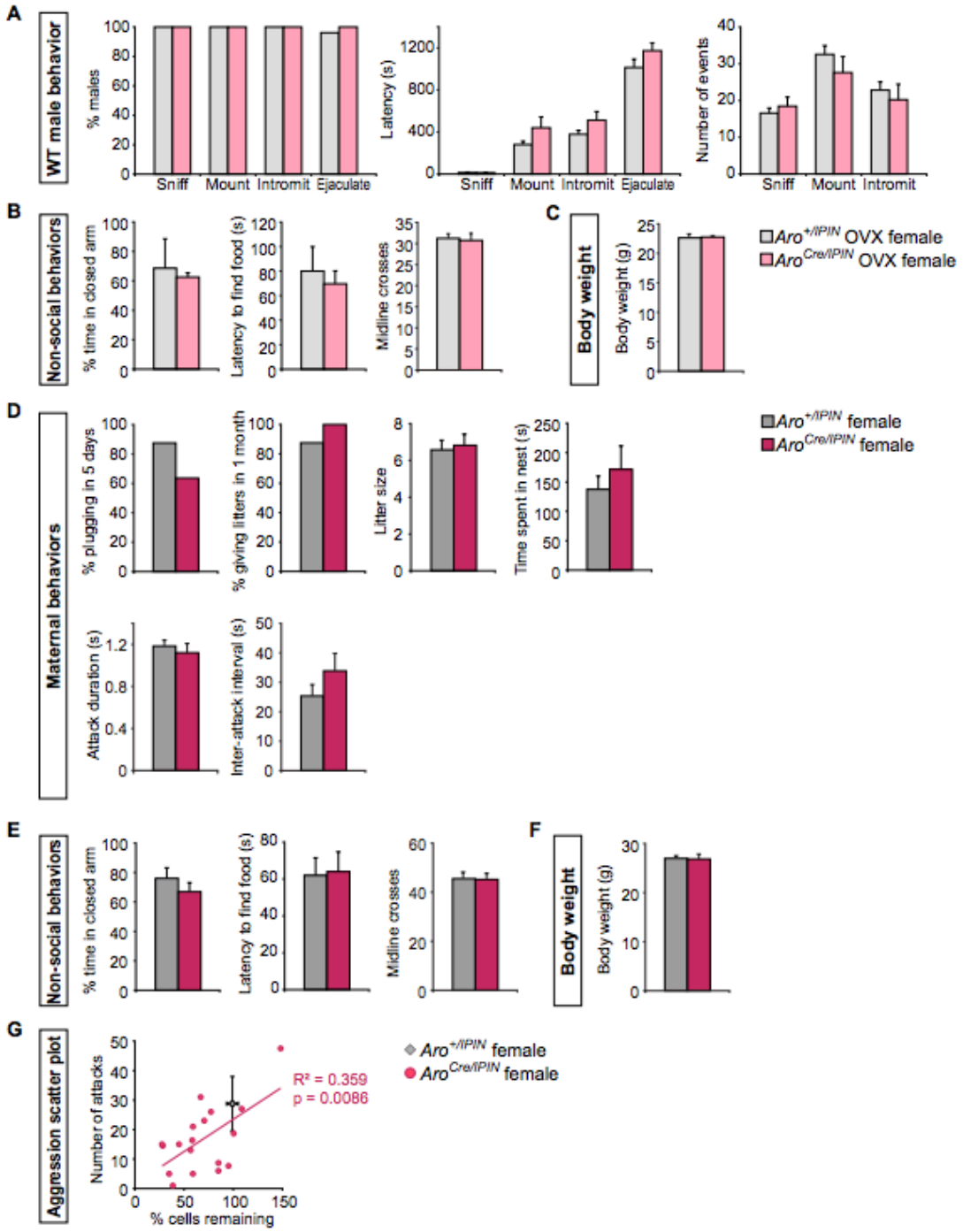

Figure 4.8 (S4). Ablation of aromatase+ MeApd neurons reduces specific components of maternal aggression, Related to Figure 4.4.

For tests of sexual behavior (A-C), aroCre/IPIN and aro+/IPIN females were ovariectomized (OVX) and estrus was hormonally induced prior to testing. For tests of maternal behavior (D-G), aroCre/IPIN and aro+/IPIN females were gonadally intact, mated with a WT male, and allowed to deliver a litter.

(A) WT males mate equivalently with aroCre/IPIN and aro+/IPIN females.

(B) No difference between aroCre/IPIN and aro+/IPIN females in anxiety-type behavior (elevated-plus maze), finding food when starved, or locomotor activity as measured by number of midline crosses.
(C) No difference between aroCre/IPIN and aro+/IPIN females in body weight.
(D) No difference between aroCre/IPIN and aro+/IPIN females in percent plugged by WT male, percent producing litters, litter size, and time spent in the nest in 15 min during pup retrieval. No difference between aroCre/IPIN and aro+/IPIN mothers in pattern of attacks (mean attack bout duration and inter-attack interval) toward a WT intruder male.
(E) No difference between aroCre/IPIN and aro+/IPIN females in anxiety-type behavior (elevated-plus maze), finding food when starved, or locomotor activity as measured by number of midline crosses.
(F) No difference between aroCre/IPIN and aro+/IPIN females in body weight.
(G) Significant correlation between extent of loss of aromatase+ MeApd neurons and reduced number of attacks toward WT intruder male. Scatter plot includes data from all aroCre/IPIN mothers who displayed any attacks; gray diamond in the plot depicts number of attacks by aro+/IPIN mothers toward WT intruder males (18/28). Mean ± SEM; $n \geq 14$ aro+/IPIN (A-G), $n = 7$ aroCre/IPIN (A-C), $n = 8$ aroCre/IPIN (D-F), $n = 28$ aroCre/IPIN (G)

4.7 REFERENCES

Alexander, G.M., Rogan, S.C., Abbas, A.I., Armbruster, B.N., Pei, Y., Allen, J.A., Nonneman, R.J., Hartmann, J., Moy, S.S., Nicolelis, M.A., et al. (2009). Remote Control of Neuronal Activity in Transgenic Mice Expressing Evolved G Protein-Coupled Receptors. Neuron 63, 27–39.

Anaclet, C., Ferrari, L., Arrigoni, E., Bass, C.E., Saper, C.B., Lu, J., and Fuller, P.M. (2014). The GABAergic parafacial zone is a medullary slow wave sleep-promoting center. Nat. Neurosci.

Armbruster, B.N., Li, X., Pausch, M.H., Herlitze, S., and Roth, B.L. (2007). Evolving the lock to fit the key to create a family of G protein-coupled receptors potently activated by an inert ligand. Proc. Natl. Acad. Sci. U. S. A. 104, 5163–5168.

Arnold, A.P. (2009). The organizational-activational hypothesis as the foundation for a unified theory of sexual differentiation of all mammalian tissues. Horm. Behav. 55, 570–578.

Ball, J. (1937). Sex activity of castrated male rats increased by estrin administration. J. Comp. Psychol. 24, 135–144.

Balthazart, J., and Ball, G.F. (1998). New insights into the regulation and function of brain estrogen synthase (aromatase). Trends Neurosci. 21, 243–249.

Baum, M.J., and Bakker, J. (2013). Roles of sex and gonadal steroids in mammalian pheromonal communication. Front. Neuroendocrinol. 34, 268–284.

Bergan, J.F., Ben-Shaul, Y., and Dulac, C. (2014). Sex-specific processing of social cues in the medial amygdala. eLife 3, e02743.

Carney, R.S.E., Mangin, J.-M., Hayes, L., Mansfield, K., Sousa, V.H., Fishell, G., Machold, R.P., Ahn, S., Gallo, V., and Corbin, J.G. (2010). Sonic hedgehog expressing and responding cells generate neuronal diversity in the medial amygdala. Neural Develop. 5, 14.

Choi, G.B., Dong, H.-W., Murphy, A.J., Valenzuela, D.M., Yancopoulos, G.D., Swanson, L.W., and Anderson, D.J. (2005). Lhx6 delineates a pathway mediating innate reproductive behaviors from the amygdala to the hypothalamus. Neuron 46, 647–660.

Demas, G.E., Kriegsfeld, L.J., Blackshaw, S., Huang, P., Gammie, S.C., Nelson, R.J., and Snyder, S.H. (1999). Elimination of aggressive behavior in male mice lacking endothelial nitric oxide synthase. J. Neurosci. Off. J. Soc. Neurosci. 19, RC30.

DiBenedictis, B.T., Ingraham, K.L., Baum, M.J., and Cherry, J.A. (2012). Disruption of urinary odor preference and lordosis behavior in female mice given lesions of the medial amygdala. Physiol. Behav. 105, 554–559.

Finney, H.C., and Erpino, M.J. (1976). Synergistic effect of estradiol benzoate and dihydrotestosterone on aggression in mice. Horm. Behav. 7, 391–400.

Forlano, P.M., Schlinger, B.A., and Bass, A.H. (2006). Brain aromatase: new lessons from nonmammalian model systems. Front. Neuroendocrinol. 27, 247–274.

Gammie, S.C., and Nelson, R.J. (1999). Maternal aggression is reduced in neuronal nitric oxide synthase-deficient mice. J. Neurosci. Off. J. Soc. Neurosci. 19, 8027–8035.

Gammie, S.C., Huang, P.L., and Nelson, R.J. (2000). Maternal aggression in endothelial nitric oxide synthase-deficient mice. Horm. Behav. 38, 13–20.

Gandelman, R. (1972). Mice: postpartum aggression elicited by the presence of an intruder. Horm. Behav. 3, 23–28.
Hong, W., Kim, D.-W., and Anderson, D.J. (2014). Antagonistic control of social versus repetitive self-grooming behaviors by separable amygdala neuronal subsets. Cell 158, 1348–1361.
Juntti, S.A., Tollkuhn, J., Wu, M.V., Fraser, E.J., Soderborg, T., Tan, S., Honda, S.-I., Harada, N., and Shah, N.M. (2010). The androgen receptor governs the execution, but not programming, of male sexual and territorial behaviors. Neuron 66, 260–272.
Keshavarzi, S., Sullivan, R.K.P., Ianno, D.J., and Sah, P. (2014). Functional Properties and Projections of Neurons in the Medial Amygdala. J. Neurosci. 34, 8699–8715.
Kimura, T., and Hagiwara, Y. (1985). Regulation of urine marking in male and female mice: effects of sex steroids. Horm. Behav. 19, 64–70.
Lee, H., Kim, D.-W., Remedios, R., Anthony, T.E., Chang, A., Madisen, L., Zeng, H., and Anderson, D.J. (2014). Scalable control of mounting and attack by Esr1+ neurons in the ventromedial hypothalamus. Nature 509, 627–632.
MacLusky, N.J., and Naftolin, F. (1981). Sexual differentiation of the central nervous system. Science 211, 1294–1302.
Matsumoto, T., Honda, S., and Harada, N. (2003). Alteration in sex-specific behaviors in male mice lacking the aromatase gene. Neuroendocrinology 77, 416–424.
McCarthy, M.M. (2008). Estradiol and the developing brain. Physiol. Rev. 88, 91–124.
McDermott, N.J., and Gandelman, R. (1979). Exposure to young induces postpartum-like fighting in virgin female mice. Physiol. Behav. 23, 445–448.
McGill, T.E. (1962). Sexual behavior in three inbred strains of mice. Behavior 19, 341–350.
Morgan, C.W., Julien, O., Unger, E.K., Shah, N.M., and Wells, J.A. (2014). Turning on caspases with genetics and small molecules. Methods Enzymol. 544, 179–213.
Morris, J.A., Jordan, C.L., and Breedlove, S.M. (2004). Sexual differentiation of the vertebrate nervous system. Nat. Neurosci. 7, 1034–1039.
Moyer, K. (1968). Kinds of aggression and their physiological basis. Commun. Behav. Biol. Part A 2, 65–87.
Naftolin, F., Ryan, K.J., and Petro, Z. (1971). Aromatization of androstenedione by the diencephalon. J. Clin. Endocrinol. Metab. 33, 368–370.
Nelson, A.B., Hammack, N., Yang, C.F., Shah, N.M., Seal, R.P., and Kreitzer, A.C. (2014). Striatal cholinergic interneurons Drive GABA release from dopamine terminals. Neuron 82, 63–70.
Nelson, R.J., Demas, G.E., Huang, P.L., Fishman, M.C., Dawson, V.L., Dawson, T.M., and Snyder, S.H. (1995). Behavioural abnormalities in male mice lacking neuronal nitric oxide synthase. Nature 378, 383–386.
Nunez, A.A., Nyby, J., and Whitney, G. (1978). The effects of testosterone, estradiol, and dihydrotestosterone on male mouse (Mus musculus) ultrasonic vocalizations. Horm. Behav. 11, 264–272.
Ogawa, S., Chester, A.E., Hewitt, S.C., Walker, V.R., Gustafsson, J.A., Smithies, O., Korach, K.S., and Pfaff, D.W. (2000). Abolition of male sexual behaviors in mice lacking estrogen receptors alpha and beta (alpha beta ERKO). Proc. Natl. Acad. Sci. U. S. A. 97, 14737–14741.

Paxinos, G., and Franklin, K.B.J. (2003). The Mouse Brain in Stereotaxic Coordinates: Compact Second Edition, Second Edition (Academic Press).
Petrovich, G.D., Canteras, N.S., and Swanson, L.W. (2001). Combinatorial amygdalar inputs to hippocampal domains and hypothalamic behavior systems. Brain Res. Rev. 38, 247–289.
Ray, R.S., Corcoran, A.E., Brust, R.D., Kim, J.C., Richerson, G.B., Nattie, E., and Dymecki, S.M. (2011). Impaired respiratory and body temperature control upon acute serotonergic neuron inhibition. Science 333, 637–642.
Roselli, C.E. (1991). Sex differences in androgen receptors and aromatase activity in microdissected regions of the rat brain. Endocrinology 128, 1310–1316.
Roselli, C.E., Horton, L.E., and Resko, J.A. (1985). Distribution and regulation of aromatase activity in the rat hypothalamus and limbic system. Endocrinology 117, 2471–2477.
Sasaki, K., Suzuki, M., Mieda, M., Tsujino, N., Roth, B., and Sakurai, T. (2011). Pharmacogenetic modulation of orexin neurons alters sleep/wakefulness states in mice. PloS One 6, e20360.
Scott, J.P. (1966). Agonistic behavior of mice and rats: a review. Am. Zool. 6, 683–701.
Sokolowski, K., and Corbin, J.G. (2012). Wired for behaviors: from development to function of innate limbic system circuitry. Front. Mol. Neurosci. 5, 55.
Sternson, S.M. (2013). Hypothalamic survival circuits: blueprints for purposive behaviors. Neuron 77, 810–824.
Sternson, S.M., and Roth, B.L. (2014). Chemogenetic tools to interrogate brain functions. Annu. Rev. Neurosci. 37, 387–407.
Stowers, L., Holy, T.E., Meister, M., Dulac, C., and Koentges, G. (2002). Loss of sex discrimination and male-male aggression in mice deficient for TRP2. Science 295, 1493–1500.
Svare, B., and Gandelman, R. (1975). Postpartum aggression in mice: inhibitory effect of estrogen. Physiol. Behav. 14, 31–35.
Svare, B., and Gandelman, R. (1976a). Postpartum aggression in mice: the influence of suckling stimulation. Horm. Behav. 7, 407–416.
Svare, B., and Gandelman, R. (1976b). Suckling stimulation induces aggression in virgin female mice. Nature 260, 606–608.
Swanson, L.W. (2000). Cerebral hemisphere regulation of motivated behavior. Brain Res. 886, 113–164.
Swanson, L.W., and Petrovich, G.D. (1998). What is the amygdala? Trends Neurosci. 21, 323–331.
De Vries, G.J., and Boyle, P.A. (1998). Double duty for sex differences in the brain. Behav. Brain Res. 92, 205–213.
Wallis, C.J., and Luttge, W.G. (1975). Maintenance of male sexual behavior by combined treatment with oestrogen and dihydrotestosterone in CD-1 mice. J. Endocrinol. 66, 257–262.
Wang, L., Han, X., Mehren, J., Hiroi, M., Billeter, J.-C., Miyamoto, T., Amrein, H., Levine, J.D., and Anderson, D.J. (2011). Hierarchical chemosensory regulation of male-male social interactions in Drosophila. Nat. Neurosci. 14, 757–762.

Wersinger, S.R., Sannen, K., Villalba, C., Lubahn, D.B., Rissman, E.F., and De Vries, G.J. (1997). Masculine sexual behavior is disrupted in male and female mice lacking a functional estrogen receptor alpha gene. Horm. Behav. 32, 176–183.

Wu, M.V., Manoli, D.S., Fraser, E.J., Coats, J.K., Tollkuhn, J., Honda, S.-I., Harada, N., and Shah, N.M. (2009). Estrogen masculinizes neural pathways and sex-specific behaviors. Cell 139, 61–72.

Wu, Z., Autry, A.E., Bergan, J.F., Watabe-Uchida, M., and Dulac, C.G. (2014). Galanin neurons in the medial preoptic area govern parental behaviour. Nature 509, 325–330.

Xu, X., Coats, J.K., Yang, C.F., Wang, A., Ahmed, O.M., Alvarado, M., Izumi, T., and Shah, N.M. (2012). Modular genetic control of sexually dimorphic behaviors. Cell 148, 596–607.

Yang, C.F., and Shah, N.M. (2014). Representing sex in the brain, one module at a time. Neuron 82, 261–278.

Yang, C.F., Chiang, M.C., Gray, D.C., Prabhakaran, M., Alvarado, M., Juntti, S.A., Unger, E.K., Wells, J.A., and Shah, N.M. (2013). Sexually dimorphic neurons in the ventromedial hypothalamus govern mating in both sexes and aggression in males. Cell 153, 896–909.

CHAPTER 5

Social Control of Hypothalamus-Mediated Male Aggression

5.1 SUMMARY

How environmental and physiological signals interact to influence neural circuits underlying developmentally programmed social interactions such as male territorial aggression is poorly understood. We have tested the influence of sensory cues, social context, and sex hormones on progesterone receptor (PR)-expressing neurons in the ventromedial hypothalamus (VMH) that are critical for male territorial aggression. We find that these neurons can drive aggressive displays in solitary males independent of pheromonal input, gonadal hormones, opponents, or social context. By contrast, these neurons cannot elicit aggression in socially housed males that intrude in another male's territory unless their pheromone-sensing is disabled. This modulation of aggression cannot be accounted for by linear integration of environmental and physiological signals. Together, our studies suggest that fundamentally non-linear computations enable social context to exert a dominant influence on developmentally hard-wired hypothalamus-mediated male territorial aggression.

5.2 INTRODUCTION

Social behaviors are essential for reproductive success and for success in other domains across diverse human societies. Many forms of social interactions are acquired traits that depend on learning. However, behaviors such as mating and aggression are

primal, sexually dimorphic social interactions that are innate in the sense that they can be displayed without prior training, suggesting that the underlying neural circuits are developmentally programmed. Indeed, previous work shows that, in mice and many other vertebrates, sex hormones produced by the gonads during a critical developmental window control the organization of neural pathways underlying these behaviors in a sexually dimorphic manner (Arnold, 2009, Bronson and Desjardins, 1968, McCarthy, 2008, Peters et al., 1972, Phoenix et al., 1959, Wu et al., 2009, Yang and Shah, 2014). The extent to which social cues and internal signals modulate behavioral output elicited by such developmentally wired neural circuits in adult animals is poorly characterized (Fernald, 2015, Insel and Fernald, 2004, Wallen, 1996). In addition, how cues relating to social setting and prior experience are conveyed to neural circuits that control these innate behaviors is not well understood.

It can be difficult to tease apart the relative roles of social cues and internal physiological signals in shaping neural decisions underlying even innate behaviors. This is because salient sensory cues, ethological relevance of social setting, and molecularly defined neural pathways remain to be clearly determined for most behaviors, even in a laboratory setting. Hypothalamus-dependent male aggression in mice provides a suitable platform to study the relative contributions of environment and genetic hard-wiring. Wild male mice are naturally territorial across diverse settings; they attack other males even in the presence of abundant resources and without competition for mates (Berry and Bronson, 1992, Crowcroft, 1955, Crowcroft, 1966, Crowcroft and Rowe, 1963, Quadagno, 1968). A successful territorial male will often drive other males into social cohabitation in small areas from which these males rarely attack the territorial male

(Crowcroft, 1955, Crowcroft, 1966, Crowcroft and Rowe, 1963). Male lab mice are also aggressive, and, as with wild mice, this aggression is purposive and flexible. It is purposive in the sense that a male attacks a male but not a female. Male aggression is flexible in the sense that a resident male attacks a male intruding in his homecage (Crowcroft, 1966, Miczek et al., 2001), whereas an intruder male who is cohoused with other males prior to being inserted into the resident's cage does not initiate attacks toward the resident male. Resident male aggression is triggered by intruder male pheromones such that residents disabled for pheromone sensing do not attack other males (Chamero et al., 2007, Leypold et al., 2002, Liberles, 2014, Mandiyan et al., 2005, Stowers et al., 2002, Yoon et al., 2005). However, the mechanisms that inhibit socially cohoused males from initiating attacks on residents are poorly understood. In addition to these external cues, resident male aggression in mice, as in many other vertebrates, also requires testosterone or its metabolites such that castration essentially abrogates fighting (Beeman, 1947). Finally, many studies have localized a hypothalamic center in or around the functionally heterogeneous ventromedial hypothalamus (VMH) of diverse vertebrates, including mice, that controls aggressive displays (Cheung et al., 2015, Lin et al., 2011, Silva et al., 2013, Yang and Shah, 2014). Indeed, optogenetic stimulation of the VMH elicits aggression by a resident male (Lin et al., 2011). We recently demonstrated that this center consists of a cluster of progesterone receptor (PR+) neurons in the ventrolateral subdivision of the mouse VMH (VMHvl) that is essential for resident male aggression (Yang et al., 2013). However, the functional relevance of PR+ VMHvl neurons in socially housed males that are not normally aggressive is unknown.

We set out to determine the relative influence of physiological signals and social context, defined here as the setting of the behavioral assay as well as prior experience, on PR+ VMHvl-modulated male aggression. We find that experimental activation of PR+ VMHvl neurons in solitary males elicits aggressive displays independent of social context, pheromone sensing, opponents, or circulating testosterone. By contrast, social housing with other males suppresses initiation of aggression by PR+ VMHvl neurons in intruder males. Genetic disabling of pheromone sensing in socially housed males enables PR+ VMHvl neurons to drive aggression in these males in this setting. Our functional network modeling studies show that, rather than linearly accumulating evidence from sensory modalities, physiological state, and social context, the neural circuit underlying aggression appears to utilize a fundamentally non-linear computation to generate behavioral output. In summary, we demonstrate that it is social setting and housing conditions rather than just the activation of a neural pathway necessary and sufficient for fighting that determine whether a male will initiate aggression.

5.3 RESULTS

5.3.1 PR+ VMHvl Neurons Acutely Regulate Male Aggression

We sought to define the role of PR+ VMHvl neurons in aggression by determining whether these neurons can drive this behavior independent of external sensory cues or internal physiological signals required for aggression in wild-type (WT) males. Accordingly, we sought to activate PR+ VMHvl neurons in an inducible manner. We had previously generated a PR-IRES-Cre (PRCre) knockin allele to drive the desired virally encoded transgenes in these neurons in a Cre-dependent manner (Yang et al., 2013). To

activate PR+ VMHvl neurons, we expressed a Cre-dependent designer receptor exclusively activated by a designer drug (DREADD), which couples with the Gα protein Gq in these neurons, using an adeno-associated virus (AAV-flex-hM3DGq:mCherry) (Alexander et al., 2009, Ray et al., 2011, Sternson and Roth, 2014). Delivery of this virus into the VMH of PRCre mice results in reliable expression of the DREADD, as visualized by mCherry, which is fused to hM3DGq (Figures 1A and 1B). Importantly, there was no detectable expression of mCherry when the virus was injected in WT mice (Figure S1A). We sought to further define the specificity of DREADD expression in PR+ neurons. PR is expressed at very low levels in vivo, making it difficult to perform co-labeling studies with PR mRNA or protein. To visualize PR+ cells, we had previously generated a PRPL knockin allele that drives expression of nuclear β-galactosidase (nβ–gal) in PR+ cells (Yang et al., 2013). Nuclear localization of β-gal enables detection of PR+ cells and co-expression studies. Upon injecting the virus into PRCre/PL mice, we found that most mCherry+ cells were nβ–gal+ (91.7% ± 1.8; n = 331 mCherry+ neurons from 5 PRCre/PL males); the ~8% mCherry+, nβ-gal– cells likely reflect the greater sensitivity in detection of functional Cre expression, which can recombine multiple copies of the virally encoded, flexed transgene, compared with single-copy expression of nβ-gal.

hM3DGq leads to membrane depolarization and increased spiking in neurons in the presence of its cognate ligand, CNO (clozapine N-oxide). We tested the functional expression of hM3DGq in the VMHvl of PRCre mice in acute brain slices through this region. We observed membrane depolarization as well as an increase in spike frequency in DREADD+ neurons exposed to CNO (Figures 1C and 1D; hM3DGq spike rate: 2.7 ± 1.1 Hz [baseline] and 5.5 ± 1.6 Hz [CNO], $p < 0.01$; mCherry spike rate: 2.7 ± 1.3 Hz

[baseline] and 2.3 ± 1.1 Hz [CNO], p = 0.1; hM3DGq membrane potential [Vm]: –59 ± 1.8 mV [baseline] and –53 ± 2.3 mV [CNO], p < 0.01; mCherry Vm: –62 ± 2.7 mV [baseline] and –63 ± 3.8 mV [CNO], p = 0.7; hM3DGq, n = 14 cells from 6 males; mCherry, n = 8 cells from 4 males). Expression of DREADD did not alter the baseline properties of PR+ VMHvl cells because these were comparable in neurons expressing hM3DGq:mCherry or mCherry (spike rate, p = 0.99; Vm, p = 0.35). Consistent with excitation of PR+, hM3DGq+ VMHvl neurons by CNO in slices, we observed >10-fold induction of Fos, a surrogate of neural activity (Morgan and Curran, 1991), in these neurons when mice were given CNO (Figure 1E). Taken together with our findings that DREADD expression is Cre-dependent (Figure S1A) and that most mCherry+ cells are nβ-gal+ (a PR reporter in PRCre/PL mice), these results indicate that CNO activates PR+, hM3DGq+ VMHvl neurons.

We next tested whether activating PR+, hM3DGq+ VMHvl neurons triggered aggression in PRCre males. Solitary (singly housed) male mice attack intruder males in their homecage without prior training; in these assays, the intruder male, who is from a group of socially housed males, does not initiate attacks (Miczek et al., 2001). CNO increased the probability of a solitary male initiating aggression toward a male intruder, and it also increased the intensity of the ensuing attacks (Figure 1F; Figure S1B). Male mice rattle their tail, presumably as a threatening display, in aggressive encounters (Scott, 1966). There is no 1:1 relation between individual episodes of tail rattling and physical attacks such as biting or wrestling, but most assays containing attacks also feature tail rattling (Figure 1F). Correspondingly, males given CNO also tail-rattled with a shorter latency (saline, 238.8 ± 51.4 s; CNO, 38.1 ± 22.1 s; n = 25 each; p < 0.01) and more

frequently (saline, 6.5 ± 1.8; CNO, 20.9 ± 3.4; n = 25 each; $p < 0.01$). The majority (>92%) of PR+ VMHvl neurons express estrogen receptor alpha (ERα or Esr1) (Yang et al., 2013), and optogenetic activation of Esr1+ neurons also triggers attacks toward an intruder (Lee et al., 2014). Our findings extend this initial observation significantly because we assayed for aggression in a more naturalistic setting where resident solitary males were unencumbered and freely interacting with an intruder, thereby allowing us to rigorously assess the patterns of attack and effectively vary social housing conditions as described below.

This increase in aggression in solitary males complements our previous study showing that ablation of PR+ VMHvl neurons reduces fighting in male mice (Yang et al., 2013). We also confirmed behavioral deficits following chronic ablation of the neurons by acutely inhibiting their activity via bilateral delivery of AAV-flex-hM4DGi and administering CNO to a separate cohort of males. Binding of CNO to hM4DGi leads to membrane hyperpolarization and a reduction in neuronal activity (Sternson and Roth, 2014). Consistent with such inhibition of neuronal activity, intermale fighting was dramatically reduced in solitary males given CNO (Figure S1D). Ablation of PR+ VMHvl neurons also reduced male sexual behavior toward WT females, with a significant decrease in intromission (penetration) displays (Yang et al., 2013). We observed that males expressing hM4DGi and treated with CNO also reduced the number and duration of intromission events toward WT females (Figure S1F), demonstrating that these neurons acutely regulate both male mating and aggression. A previous study using optogenetic inhibition of Esr1+ VMHvl neurons did not observe deficits in male sexual behavior, and this could reflect ineffective silencing of these neurons (Lee et al., 2014).

By contrast, our findings with chemogenetics here are in accord with those from chronic ablation of PR(Esr1)+ VMHvl neurons (Yang et al., 2013) and show that these neurons are required acutely as well as chronically for WT levels of male sexual behavior and aggression.

We next sought to test whether activating PR+ VMHvl neurons in males would alter sexual behavior. We found that males expressing hM3DGq in PR+ VMHvl neurons attacked females when given CNO, whereas they never did so when given saline (Figure 1G; Figure S1C). Increasing optogenetic stimulation of Esr1+ VMHvl neurons in male mice altered their behavior from mating to aggression (Lee et al., 2014). Given that PR+ VMHvl neurons also express Esr1, we wondered whether changing the dose of CNO would lead to a similar switch. Indeed, we observed that males administered lower doses of CNO mated with females or mated and attacked females, whereas they exclusively attacked females at higher doses (Figures S1E and S1G). Importantly, experimental triggering of aggression required expression of hM3DGq in PR+ VMHvl neurons because injection of AAV-flex-hM3DGq:mCherry into WT males did not lead to detectable mCherry expression or aggression (Figure S1A). Because we wished to study the influence of social context and internal physiological conditions on male aggression, we utilized CNO at a dose that reliably elicited this behavior (Figures 1F and 1G; Figure S1G). Indeed, we did not observe sexual behavior with this dose of CNO (0.3 mg/kg) in other behavioral assays unless otherwise mentioned. Moreover, this dose of CNO is within the range used in vivo to modulate neuronal activity in diverse brain regions (Ray et al., 2011, Sasaki et al., 2011, Unger et al., 2015).

Taken together with prior studies showing that PR+/Esr1+ VMHvl neurons, but not other neighboring neurons, are critical for triggering aggression in males (Lee et al., 2014, Yang et al., 2013), our results demonstrate that acute activation of PR+ VMHvl neurons is necessary and sufficient to elicit aggression from solitary males. We wondered whether this chemogenetically induced aggression resembles the aggression displayed by WT males or leads to novel patterns of fighting. We found that the patterns of CNO-elicited aggression were comparable with those shown by control males (Figure S1H). Consistent with this observation, CNO-elicited male aggression was also distinct from maternal aggression displayed by females defending their pups. These females do not tail-rattle, and they direct their bites largely to the neck and genital region (Unger et al., 2015); by contrast, males given CNO tail-rattled and largely directed bites to the flanks. Prior optogenetic studies employed arbitrary stimulation to elicit aggression during various phases of social interactions (Lee et al., 2014), thereby precluding analysis of patterns of aggression between freely interacting males. By contrast, our chemogenetic approach demonstrates that activation of PR+ VMHvl neurons in males elicits aggression that appears comparable with WT patterns of male-typical territorial aggression.

5.3.2 PR+ VMHvl Neurons Trigger Aggression in Singly Housed Males Independent of Pheromone Signaling

The observation that activation of PR+ VMHvl male neurons elicits aggression toward females suggests that such activation overrides the pheromonal input that would normally direct sexual displays toward females. If this is true, then it should be possible

to drive aggression in solitary males genetically disabled for pheromone sensing. Alternatively, pheromonal input to other neuronal populations may be essential to drive aggression even when PR+ VMHvl neurons have been experimentally activated (Figure 2A). In the latter scenario, genetic disabling of pheromone sensing should abrogate aggressive displays. To distinguish between these possibilities, we activated PR+ VMHvl neurons in singly housed males genetically disabled for the major pheromone-sensing pathways, the vomeronasal organ (VNO) and the main olfactory epithelium (MOE). The cation channels Trpc2 and Cnga2 are essential for normal odor-evoked activity in VNO and MOE sensory neurons (Brunet et al., 1996, Leypold et al., 2002, Stowers et al., 2002), respectively, and for male aggression (Leypold et al., 2002, Mandiyan et al., 2005, Stowers et al., 2002). The deficit in male aggression in mice mutant for Trpc2 or Cnga2 likely reflects a requirement for Trpc2 or Cnga2 in VNO and MOE neurons rather than cells elsewhere because this phenotype is also observed in male mice mutant for other channels that are expressed in the VNO or MOE and essential for normal odor-evoked activity (Kim et al., 2012, Wang et al., 2006). As expected, few males disabled for pheromone sensing via the VNO (PRCre;Trpc2–/–) or MOE (PRCre;Cnga2–/Y) and expressing hM3DGq in the VMHvl were aggressive when given saline; the majority of these males, however, initiated aggression toward male or female intruders when given CNO (Figure 2B; Figures S2A and S2B). Moreover, we did not observe any sexual behavior by PRCre;Trpc2–/– or PRCre;Cnga2–/Y males given CNO, except that one male of each of these genotypes mated with a female intruder (compared to 7 of 12 PRCre;Trpc2–/– males given saline, $p < 0.01$, and 1 of 8 PRCre;Cnga2–/Y males given saline, $p = 1$, respectively). In summary, PR+ VMHvl neurons can elicit aggression in

males genetically disabled for pheromone-sensing pathways that are otherwise essential for this behavior.

The foregoing results do not exclude the possibility that activation of PR+ VMHvl neurons elicits aggression as long as either the VNO or MOE is functional. Cnga2 mutant pups have severe nursing defects, and adult mutants have difficulty mating and providing parental care (Brunet et al., 1996, Fraser and Shah, 2014, Mandiyan et al., 2005, Yoon et al., 2005), making it difficult to obtain males of the genotype PRCre;Trpc2–/–;Cnga2–/Y. However, the VNO and MOE are required non-redundantly for sex discrimination and sniffing (anogenital chemoinvestigation), which presumably enable access to aggression-eliciting pheromones in exocrine secretions, respectively (Chamero et al., 2007, Leypold et al., 2002, Mandiyan et al., 2005, Stowers et al., 2002, Yoon et al., 2005). Our findings show that PR+ VMHvl neurons can drive male aggression independent of these aspects of pheromone sensing.

Both the VNO and MOE sense conspecific pheromones and chemosensory cues emanating from other species, and recognition of conspecifics via either pathway may be sufficient for subsequent species-typical interactions such as aggression (Isogai et al., 2011, Kobayakawa et al., 2007, Li et al., 2012, Papes et al., 2010). Accordingly, we tested whether activation of PR+ VMHvl neurons in PRCre males WT for Trpc2 and Cnga2 can elicit aggression toward Peromyscus. Peromyscus is a rodent genus that last shared an ancestor with lab mice (Mus) ~25 million years ago (Ramsdell et al., 2008). Consistent with the notion that conspecific recognition is critical for meaningful social interactions (Fan et al., 2013), we observed that PRCre males rarely attacked Peromyscus eremicus in the presence of saline (Figure 2C; Figures S2C and S2D). By

contrast, a majority of PRCre males attacked P. eremicus males and females when given CNO (Figure 2C; Figures S2C and S2D). Thus, activation of PR+ VMHvl neurons bypasses pheromone-mediated sex discrimination or conspecific recognition and elicits aggression.

5.3.3 PR+ VMHvl Neurons Can Elicit Limited Forms of Aggression-Related Responses

We next tested whether activating PR+ VMHvl neurons would provoke aggressive displays in the absence of a stimulus animal or animal-like object by inserting a mirror in the homecage. The use of a mirror was prompted by previous work showing that fish show aggressive displays to a mirror image (Desjardins and Fernald, 2010, Oliveira et al., 2016, Tinbergen, 1951). Strikingly, males given CNO did not physically attack the mirror, but they reliably tail-rattled to it (Figure 2D; Movies S1 and S2). Activation of PR+ VMHvl neurons also elicited tail rattling when males encountered the non-reflective surface of a mirror, although this was less effective than the reflective side (Figure 2D; Movies S3 and S4). CNO did not elicit tail rattling in the absence of a mirror, indicating that even this limited aggression-related display requires sensory input (Figure 2D). Males occasionally bit an inflated glove inserted into their homecage upon activation of PR+ VMHvl neurons (data not shown), but, as reported previously, this did not reach statistical significance (Lin et al., 2011). Nevertheless, a significant number of males tail-rattled to the glove when administered CNO (Figure 2D; Movies S5 and S6). These findings are in agreement with our observations that PR+ VMHvl neurons can elicit behavioral responses in a chemosensation-independent manner. Tail rattling (and, in the case of a glove, even

biting) under these conditions upon stimulation of these neurons might result from a stress response. This is unlikely because optogenetic stimulation of VMHvl elicits time-locked biting of gloves, suggesting that this is not a result of elevated stress hormones (Lin et al., 2011); moreover, we have previously shown that ablation of PR+ VMHvl neurons does not affect anxiety-type behavioral responses (Yang et al., 2013). Consistent with this notion, chemogenetic stimulation of PR+ VMHvl neurons did not alter behavior in an elevated plus maze (Figure S2E). In summary, our findings demonstrate that mice can use visual cues to assess whether to initiate tail rattling, a display that usually accompanies aggressive behavior (Scott, 1966, Stowers et al., 2002). Moreover, our results demonstrate that activation of PR+ VMHvl neurons can elicit graded displays of aggression or related behaviors: none in the absence of a novel stimulus, some tail rattling to an object, increased tail rattling to a reflective surface, and tail rattling as well as physical attacks to intruders.

5.3.4 Gonadal Hormones Are Not Required for PR+ VMHvl-Activated Male Aggression

In addition to chemosensory cues, testicular hormones are required for aggression in standard male lab mice (Figure 3A) such that solitary males castrated as adults do not attack other males (Beeman, 1947). This behavioral deficit can be corrected if the male is administered testosterone or its bioactive metabolites (Finney and Erpino, 1976, Yang and Shah, 2014). We tested whether chemogenetic stimulation of PR+ VMHvl neurons would bypass the need for testicular hormones in fighting. Accordingly, we infected PR+ VMHvl neurons in PRCre males with AAV-flex-hM3DGq

as before, castrated them, and waited 3 weeks to allow the circulating testosterone to subside to undetectable levels. We then tested these males for aggression after administering saline or CNO. Castrated solitary males administered saline rarely showed aggression, consistent with undetectable levels of testosterone in their circulation (Figure 3B; Figures S3A–S3C; Movie S7). However, when given CNO, they attacked male or female intruders (Figure 3B; Figures S3A and S3B; Movie S8). The aggression elicited in the presence of CNO was comparable with that observed in sham-castrated control solitary males, demonstrating that PR+ VMHvl neuronal activation elicits male aggression in a gonadal hormone-independent manner.

These findings raise the possibility that stimulation of PR+ VMHvl neurons in females may also trigger aggression. Optogenetic stimulation of female Esr1+ VMHvl neurons does not elicit aggression, but it is unclear whether the females were singly housed in a manner similar to males (Lee et al., 2014). In acute brain slices through the female VMH, we found that bath application of CNO depolarized the membrane and increased spiking activity in PR+ VMHvl neurons (Figure S3D). We next delivered AAV-flex-hM3DGq:mCherry to the VMHvl of adult PRCre females, ovariectomized them, and housed them singly. None of these female residents attacked a male or female intruder in the presence of CNO (Figure S3E), indicating that stimulation of PR+ VMHvl neurons is not sufficient to trigger territorial aggression in females under these conditions. Our findings are in agreement with prior studies showing that the neural pathways underlying male territorial aggression are developmentally wired during a critical perinatal period (McCarthy, 2008, Wu et al., 2009, Yang and Shah, 2014). Such sexual differentiation could subsequently preclude the ability of PR+ VMHvl neurons to trigger territorial

aggression in females. In contrast to these findings in females, our results show that stimulation of PR+ VMHvl neurons in male residents is sufficient to trigger aggression independent of circulating gonadal hormones. Testosterone-sensitive neurons are found all along the neuraxis, from the olfactory bulb to the spinal cord, including in the VMH (Shah et al., 2004, Simerly et al., 1990), and testosterone or its metabolites can elicit dramatic changes in neuronal morphology (Morris et al., 2004). Nevertheless, activation of PR+ VMHvl neurons bypasses these powerful effects of gonadal sex hormones and elicits aggression in castrate males.

5.3.5 Social Context and Housing Regulate the Ability of Males to Initiate Aggression

Given that stimulation of PR+ VMHvl neurons triggers aggression in solitary males under conditions that typically do not trigger fighting, we wondered whether such stimulation would enable socially housed males to initiate attacks. Socially housed males are, in fact, used as intruders into cages of singly housed males because they elicit but do not display aggression (Miczek et al., 2001). We injected socially housed PRCre males with AAV-flex-hM3DGq into the VMH and tested them as intruders. We found that few socially housed intruders tail-rattled or initiated attacks on the resident even when given CNO (Figures 4A; Figure S4A). Thus, stimulation of PR+ VMHvl neurons is insufficient to initiate aggressive displays in most socially housed male intruders. However, when the WT solitary male resident started attacking, more socially housed male intruders given CNO defended themselves aggressively (saline, 5.3%; CNO, 61.9%; $n = 19, 21$, respectively; $p < 0.001$). We wondered whether the inability of socially housed male

intruders to initiate aggression was dependent on social housing or being an intruder. Accordingly, we tested whether solitary males would initiate aggression in the context of being an intruder in a WT solitary resident male's cage. We injected PRCre males with AAV-flex-hM3DGq into the VMH, housed them singly, and then tested them as intruders. Few solitary male intruders given saline tail-rattled or attacked the resident male (Figure 4B; Figure S4B). By contrast, a majority of these intruders tail-rattled and initiated attacks when given CNO prior to being inserted into another resident male's cage (Figure 4B; Figure S4B). Importantly, although the latency to initiate attacks after CNO injection was comparable between socially housed and solitary male intruders (Figure 4; latency to initiate attack toward resident: socially housed intruder, 104.2 ± 52.8 s; solitary intruder, 179.7 ± 70.1 s; $p = 0.36$), significantly fewer socially housed intruders attacked the male resident (Figure 4; percentage of intruders that initiated attack toward resident: socially housed intruder, 23.8%; solitary male, 85.7%; $p < 0.001$). In summary, social housing suppresses initiation of male aggression otherwise triggered by PR+ VMHvl neurons.

The inability of socially housed intruders to initiate aggression contrasts with the performance of solitary intruders who attack and suggests the possibility that social housing abrogates initiation of aggression. We first tested whether CNO could activate PR+ VMHvl neurons in socially housed males, using Fos induction (Figure 1E) as a measure of neural activity. A similar percentage of hM3DGq/PR+ VMHvl neurons in PRCre males expressed Fos following CNO in solitary (43.6% ± 2.7%, $n = 7$) and social (44.0% ± 5.4%, $n = 7$; $p = 0.94$ for the comparison between these groups) housing conditions. These results do not exclude the possibility that CNO activates different subsets of PR+ VMHvl neurons in solitary and socially housed males, but they show that

the inability of socially housed male intruders to initiate attacks is not due to a complete failure of CNO to activate these neurons. Consistent with the fact that CNO activates PR+ VMHvl neurons in socially housed males, we show below that CNO can elicit aggression in these males in specific social settings.

We tested whether socially housed males can initiate attacks in two paradigms in which solitary males initiate aggression without experimental activation of PR+ VMHvl neurons, as residents of their homecage (Figure 1F; Figure S1B) and as intruders in a clean cage (neutral arena) (Figure S5A). We tested separate cohorts of socially housed PRCre males in these two settings following injection of AAV-flex-hM3DGq into the VMH (Figure 5). For testing as a resident, a socially housed male was injected with saline or CNO and his cagemates were removed, and 30 min later, a WT solitary male intruder was inserted into the homecage. For testing in a neutral arena, a socially housed male was given saline or CNO and inserted 30 min later with an unfamiliar WT socially housed male into a clean cage with fresh bedding. In both settings, socially housed males given CNO initiated attacks and tail-rattled significantly more than males injected with saline, who displayed little aggression (Figure 5; Figures S5B and S5C). These findings show that there may be distinct modes of inhibiting aggression in socially housed males. In the absence of experimental activation of PR+ VMHvl neurons, these males do not initiate aggression in settings (as a resident or in a neutral arena) in which solitary males attack (Figure 5; Figures S5B and S5C). Such inhibition of aggression in socially housed males can be overcome by activating PR+ VMHvl neurons. By contrast, insertion as an intruder in a resident male's cage exerts a stronger inhibition on aggression. In this latter situation, most socially housed intruders do not initiate aggression even when PR+

VMHvl neurons have been stimulated (Figure 4A). Together, our findings show that suppression of attack in social housing is functionally upstream or downstream of PR+ VMHvl neurons in a social context-dependent manner.

5.3.6 Pheromone Sensing Inhibits Aggression by Socially Housed Males

We next sought to understand why socially housed male intruders did not initiate aggression. Social housing enables the emergence of an aggressive interaction-based hierarchy (Miczek et al., 2001), and we reasoned that a social hierarchy could suppress aggression in socially housed intruder males (Wang et al., 2011). In fact, the experimental solitary males we used had been housed socially prior to viral delivery of DREADDs and then housed singly after the injection for 10–12 days before being tested for aggression. In this situation, 10–12 days of solitary housing were clearly sufficient to erase any potential effects of a hierarchy within social housing. We wondered whether eliminating such aggression-based aspects of hierarchy in socially housed males would permit attacks when they were used as intruders. To eliminate aggressive interactions, we castrated all adult, co-housed males 1–2 days after injecting AAV-flex-hM3DGq into the VMH and then kept them socially housed for an additional 3 weeks to allow testosterone levels to subside. However, the majority of castrated, socially housed male intruders did not attack male residents even when given CNO (Figure 6A; Figures S6A and S6B). Thus, gonadal hormone-dependent aggressive interactions are not required to inhibit aggression in socially housed males. Castration also eliminates aggression-eliciting pheromones such as major urinary proteins (MUPs) (Chamero et al., 2007), and our

findings therefore suggest that such pheromones are not required to suppress aggression in socially housed males.

We next tested whether pheromones secreted by residents inhibit aggression by socially housed intruders. We tested whether chemogenetic activation of PR+ VMHvl neurons in socially housed cohorts of PRCre males mutant for Cnga2 or Trpc2 would enable them to attack a male resident in his homecage. Indeed, we found that the majority of male intruders mutant for Cnga2 or Trpc2 tail-rattled and initiated attacks against resident males when given CNO (Figure 6B; Figure S6C). These findings support our hypothesis that pheromones secreted by resident mice inhibit aggression by intruder males; moreover, both the VNO and MOE are non-redundantly required to detect such inhibitory pheromones. We wondered whether pheromones secreted by either male or female residents can inhibit aggression by socially housed male intruders. We therefore tested whether activating PR+ VMHvl neurons in socially housed PRCre male intruders WT for Cnga2 and Trpc2 would enable aggression toward a female resident. We found that, upon administration of CNO, socially housed male intruders both tail-rattled and initiated attacks on female residents (Figure 6C; Figure S6D). This is in contrast to the lack of aggression toward male residents (Figure 4A) and in agreement with the notion that intruder males are inhibited from initiating attacks by pheromones produced by the resident male.

5.3.7 Modeling Male Aggression with Logic Circuits and Neural Networks

Our findings demonstrate that many features of the external world and internal state modulate male territorial aggression. We wished to capture these variables

succinctly within a logic circuit model that represented various paths leading to aggression toward conspecifics. We therefore first collected these features and their influence on aggression in a truth table (Table 1) and then set about building a model that incorporated studies involving Mus opponents. This resulted in a binary output variable (attack) for all remaining experiments and allowed us to assemble a logic circuit that includes every binary input variable (social experience, social setting, opponent, pheromone sensing, circulating sex hormones, and VMHvl stimulation) we tested (Figure 7A). This schematic utilizes basic logic gates (and, or, not) to represent our findings in a concise manner. Starting from the output variable, our Boolean model shows two paths to aggression so that if either pathway is active, then the male will attack. In the absence of experimental stimulation of VMHvl activity (bottom pathway, Figure 7A), all other input variables need to be active or switched on; that is, the male needs to be solitary, in his homecage or neutral arena, have circulating testosterone, sense pheromones, and face a male opponent. By contrast, when the VMHvl is stimulated (top pathway, Figure 7A), any one of four conditions is needed to make the male fight; that is, the male needs to be solitary, or in his homecage or neutral arena, or have pheromone sensing disabled, or face a female opponent. This logic circuit highlights our finding that VMHvl neurons are not command neurons and that stimulation-elicited aggression is independent of circulating testosterone.

We next wondered how our Boolean logic circuit could be recapitulated within the modeling framework of a neuron-like network. Such modeling should potentially provide insights into the underlying mechanisms at the algorithmic (Marr, 1982) but not necessarily the physical implementation level of the neural circuit underlying aggression.

Moreover, neural networks can provide a biologically plausible implementation of logic circuits as well as insights into the complexity of the underlying Boolean function. We first tested whether a single-layer network could model the developmentally hard-wired nature of male territorial aggression, as schematized in the logic circuit (Figure 7A). Strikingly, we find that there is no such single-layer network (Figure 7B). This finding rules out a mechanism whereby a single integrator network generates aggression by linearly combining evidence from neuronal populations representing the different input variables shown in the logic circuit (Figure 7A). Although not all Boolean functions are realizable by single-layer networks (Minsky and Papert, 1969), adding additional layers or non-linear features to a single-layer network can fit any such function (Bishop, 1995, Hornik, 1991), given enough neurons or features. Indeed, we find that adding only two units in an additional (hidden) layer is sufficient to train the network to capture all responses (Figure 7B). Our neural network modeling shows that our experimental findings are not well modeled by a linear classifier. Rather, a cascaded or nonlinear classifier has to be invoked to model the modulation of male aggression by features of the external world and internal state. This cascading or nonlinear classifier is required to model aggression because of our finding that male pheromones inhibit aggression in socially housed intruder males (Figures 6B, 6C, and 7B; Table 1). The antagonistic functions of pheromones in promoting and inhibiting aggression could be implemented within the VMHvl itself or elsewhere within the neural circuit underlying aggression.

5.4 DISCUSSION

We have varied external sensory and internal physiological signals to delineate their influence on the role of PR+ VMHvl neurons in intermale aggression. Given that we have identified a genetically defined neural center that is necessary and sufficient for aggression in solitary male residents, one might expect that these neurons can elicit unbridled aggression in all other contexts. In contrast to this expectation, our studies show that social context can override a developmentally hard-wired neural pathway that is necessary and sufficient for aggression in solitary males. Moreover, our studies have uncovered inordinate richness in the rules of social engagement between male mice, rules that inhibit aggressive displays in most social contexts in WT males and that are different for solitary and socially housed males.

5.4.1 Function of PR+ VMHvl Neurons in Male Aggression

We previously showed that genetically targeted ablation of PR+ VMHvl neurons reduces male aggression (Yang et al., 2013). Our current findings reveal that activation of PR+ VMHvl neurons is acutely necessary and sufficient for this behavior and, moreover, that these neurons can trigger the full complement of male-typical aggression. VMHvl PR+ neurons co-express Esr1, and these Esr1+ cells are also necessary and sufficient for male aggression (Lee et al., 2014, Yang et al., 2013). Moreover, knockdown of Esr1 in the VMH reduces male aggression (Sano et al., 2013), indicative of a signaling role of this receptor in this behavior. In addition, PR (Esr1)+ neurons constitute the functionally relevant population for male aggression in this region, and VMHvl neurons are active during fighting (Falkner et al., 2014, Lee et al., 2014, Lin et al., 2011, Yang et

al., 2013). Together, these findings from complementary approaches demonstrate a physiological role for PR (Esr1)+ VMHvl neurons in male territorial fighting. Chemogenetic (our study) or optogenetic stimulation that reliably triggers male aggression induces Fos in more VMHvl neurons than observed in unmanipulated males that attack (Lee et al., 2014). However, unmanipulated males do not always show aggression (see Figure 1F for example). We speculate that experimental activation of more PR/Esr1+ VMHvl neurons reliably triggers male aggression because it may elicit network dynamics that ensure aggression or stimulate a subset of PR/Esr1+ VMHvl neurons whose activation always drives aggression. Regardless of these considerations, these observations regarding male aggression were made in singly housed resident males. As we show here, activation of these neurons is not sufficient to elicit aggression in socially housed intruders, providing a fundamentally new perspective into their function in ethologically relevant settings.

What might be the function of PR+ VMHvl neurons in male territorial aggression? These cells are not command neurons (Kupfermann and Weiss, 1978) for aggression because their ability to trigger behavior is contingent on sensory input or social context. These neurons also do not encode or relay a complete motor plan for aggression because their activation elicits tail rattling but not attacks to a mirror. It is possible that PR+ VMHvl neurons are part of a decision network (Gold and Shadlen, 2007, Newsome, 1997) that accumulates evidence in a non-linear manner from various sensory modalities, physiological state, and social experience prior to relaying signals to downstream centers about whether the animal should fight. In this scenario, our results are in contrast to the classic “diffusion to bound” model in which decision dynamics are well

approximated by a circuit that linearly integrates evidence from a sensory modality (Gold and Shadlen, 2002). Our findings also do not exclude the possibility that PR+ VMHvl neurons constitute one of several more or less independent neural pathways that feed on to a downstream command-type neural center whose activation state is obligatorily linked to aggression. In this instance, non-linear integration of particular input variables could occur within the VMHvl or other pathways, including a command-type center, that modulate aggression. Our modeling efforts in this study make simplifying assumptions in that we excluded findings from encounters with gloves, mirrors, and Peromyscus and focused on interactions with conspecifics. Such simplifying assumptions in other models (e.g., Hopfield, 1982) have nevertheless yielded important insights in the past and, in our case, reveal a non-linearity in the network that modulates innate male territorial aggression. In future studies, it will be interesting to incorporate other features into the model that enable the animal to respond to inanimate objects or other species.

5.4.2 Social Context Controls Territorial Aggression

In keeping with the notion that male aggression is developmentally hard-wired, many genetic loci controlling male aggression have been identified (Miczek et al., 2001, Nelson and Trainor, 2007). This hard-wiring of territorial aggression is also evident from studies showing that, barring particular strains, wild or lab female mice typically do not display such aggression, including upon stimulation of VMHvl neurons (Figure S3E; Crowcroft, 1966, Ferrari et al., 1996, Lee et al., 2014, Miczek et al., 2001, Scott, 1966). Nevertheless, male territorial aggression is sensitive to social cues and experience so that males intruding in another male's territory do not initiate fights. Despite decades of

studies in mice, the mechanisms underlying these dichotomous male territorial behaviors have remained poorly understood.

Solitary males are aggressive in their homecage or a neutral arena but not when inserted in another male's cage. These observations suggest that pheromones from a male's cage inhibit attacks by an intruding solitary male. A test of this hypothesis will require molecular identification of such pheromones and their cognate receptors because disabling all pheromone sensing by the MOE or VNO also abrogates male aggression (Leypold et al., 2002, Mandiyan et al., 2005, Stowers et al., 2002, Yoon et al., 2005). We find that activating PR+ VMHvl neurons enables solitary males to attack even as intruders, thereby placing these neurons functionally downstream of potential pheromones that inhibit their aggression. Activation of PR+ VMHvl neurons also enables solitary males to show aggressive displays in every situation we have tested. Under these conditions, therefore, activation of PR+ VMHvl neurons in solitary males appears to correspond with a decision to fight.

The control of aggression in socially housed males is more complex. Absent activation of PR+ VMHvl neurons, these males do not attack. Chemogenetic activation of these neurons elicits aggression in the homecage, in a neutral arena, and to female residents. This inhibition of aggression by social housing that can be chemogenetically bypassed may be controlled by pheromones or other sensory cues present in social housing. In flies, exposure to pheromones in social housing over the course of a few days inhibits aggression elicited by presence of a desirable resource, such as food, in a neutral chamber (Liu et al., 2011). Whether such pheromonal inhibition regulates aggression in flies in other ethologically relevant settings is unknown. More importantly,

it is unclear whether manipulating the activity of central neural pathways underlying aggression in flies can override the suppression of aggression mediated by pheromones in social housing. Regardless, our findings place PR+ VMHvl neurons functionally downstream of any aggression-suppressing cues or social interactions in social housing when the male is tested as a resident or in a neutral arena or encounters a female resident. By contrast, activation of these neurons in socially housed intruders does not trigger attacks to male residents unless pheromone sensing is disabled. Thus, PR+ VMHvl neurons are effectively upstream of pheromone sensing in this particular social context. It will be interesting to determine the mechanisms whereby MOE and VNO pathways inhibit aggression in socially housed male intruders.

5.4.3 Nature and Nurture in the Display of Male Aggression

How nature and nurture—in the form of genetic underpinnings and social context—influence neural pathways underlying the instinctual display of male territorial aggression is an important question (Stowers and Liberles, 2016). We find that social context can effectively veto a neural pathway whose activation is otherwise necessary and sufficient for male territorial aggression. Social housing reduces aggression in many animals, indicating that it may be a general strategy to enable otherwise aggressive animals to cohabit. Distinct sensory modalities may underlie social housing-mediated changes in aggression in different species, and this reduced aggression can also be accompanied by changes in gene expression (Korzan et al., 2014, Maruska and Fernald, 2011, Maruska et al., 2013, Wang et al., 2008). In the naturally territorial male mouse, we have identified a neural locus in PR+ VMHvl neurons whose ability to drive aggression is

dictated by the social setting of the encounter and prior experience. Intriguingly, the logic circuit summarizing our data shows that an elevated level of activity in PR+ VMHvl neurons is sufficient to unmask aggression when even one of the several variables normally restricting aggression is modified. It is possible that heightened activity in these neural pathways contributes to violent outbursts seen in animals with rage syndrome or humans with intermittent explosive disorder in situations that do not typically provoke aggression (Dodman et al., 1992, Rosell and Siever, 2015, Scott et al., 2016).

More generally, our study shows the importance of exploring ethologically meaningful social settings and prior experience of test animals to understand the behavioral relevance of a population of neurons. Previous work on VMH neurons had deemed them necessary and sufficient for aggression without exploring their role in different social contexts. Our study shows that, in fact, the social context in which aggression is assayed can override the sufficiency of these neurons in triggering aggression, thereby forcing a re-evaluation of their role in male aggression. We intuit that territorial aggression in animals of other species, inhabiting distinct ecological niches, is responsive to social setting and prior experience in a species-specific manner. It will be interesting to understand how sensitivity to social context is genetically selected for during evolution.

5.5 EXPERIMENTAL PROCEDURES

5.5.1 Experimental Model and Subject Details

Mice were bred in a barrier facility at UCSF and Stanford University (PRCre, PRPL, Trpc2−/+, Cnga2−/+, P. eremicus) or purchased from Jackson (C57BL/6J for WT female

stimulus animals) and Taconic (129/SvEvTac for WT socially housed male stimulus animals). All animals were housed under a reversed 12:12 hr light:dark cycle and controlled temperature and humidity, and water and food were available ad libitum. All animal studies were performed following Institutional Animal Care and Use Committee guidelines and protocols at UCSF and Stanford.

5.5.2 Viruses

AAV2/1-EF1α-flex-hM3DGq:mCherry, AAV2/1-EF1α-flex-hM4DGi:mCherry, and AAV2/1-EF1α-flex-mCherry were purchased from the UNC Vector Core or custom packaged by the UNC Vector Core with maxi-prepped plasmid DNA that was originally purchased from Addgene. Virus titers were 1.5-2.5 × 1012 genomic copies/mL.

5.5.3 Stereotaxic Surgery

Viruses were stereotaxically delivered to the brain of male or female mice at 2-6 months of age exactly as described previously (Yang et al., 2013). Mice were allowed to recover in a clean cage on a heated pad, closely monitored, and returned to their home cage when ambulatory. Animals were allowed at least 10 days of recovery following surgery prior to being tested in behavioral assays.

5.5.4 Histology

We validated viral delivery by confirming that virally delivered DREADDs (mCherry+) were expressed within the VMHvl in all experimental animals using standard histological procedures (Yang et al., 2013). We had previously established the

stereotaxic coordinates and viral serotype (AAV2/1) for reliable infection of PR+ VMHvl neurons such that we observed very little infection of other PR+ neurons elsewhere in the hypothalamus (Yang et al., 2013). Using these stereotaxic coordinates and the identical serotype for our DREADD-encoding AAVs, we once again reliably achieved bilateral infection of VMHvl neurons in our PRCre animals. The specificity of this infection was demonstrated by lack of DREADD (mCherry) expression in WT animals following injection of these viruses (Figure S1A). In rare cases (< 5%), some animals were found dead in their cage and we could not histologically verify DREADD expression in the VMHvl; in these instances, behavioral data from these animals was not included for further analysis. For histological analysis following termination of behavioral studies, animals were perfused with 4% paraformaldehyde, and the brains were dissected and post-fixed for at least 2 hr in 4% paraformaldehyde. Brains were sectioned at 65 μm thickness using a vibrating microtome (Leica) and immunostaining was performed as described previously (Yang et al., 2013). The primary antisera used are rat anti-RFP (Chromotek; 1:2,000), rabbit anti-Fos (Calbiochem; 1:2,000), and chicken anti-β-galactosidase (Abcam; 1:3,000). The secondary antisera used are: Cy3 donkey anti-rat (Jackson ImmunoResearch; 1:800), Alexa Fluor 488 donkey anti-rabbit (Invitrogen; 1:300), and Alexa Fluor 488 donkey anti-chicken (Jackson ImmunoResearch; 1:300). The sections were also counterstained with DAPI (0.2 μg/mL). To examine Fos induction by hM3DGq, a subset of animals was perfused 1 hr after intraperitoneal (IP) administration of saline or 0.3 mg/kg of CNO. This Fos induction paradigm closely mirrors the procedure we followed for behavioral studies in which we tested the behavior of animals 30 min after CNO injection; these behavioral studies were conducted for 15 min, and unless

otherwise mentioned, we also used 0.3 mg/kg of CNO. Sections were imaged via confocal microscopy (LSM780 or LSM880, Zeiss). Neurons expressing hM3DGq, Fos, or nβgal were imaged using confocal microscopy and quantified using NIH ImageJ software as described previously (Unger et al., 2015, Yang et al., 2013).

5.5.5 Electrophysiology

Electrophysiological response of PRCre neurons to CNO was determined as described previously (Unger et al., 2015). Briefly, AAV2-EF1α-flex-hM3DGq:mCherry or AAV2-EF1α-flex-mCherry was injected bilaterally into the VMH of PRCre males or females 8 weeks of age. The mice were allowed to recover > 10 days from surgery and then sacrificed for brain slice preparation. 225 μm-thick coronal slices were cut in ice-cold HEPES buffer solution, incubated for 15 min at 33°C in NMDG recovery solution, and maintained for 1-5 hr at room temperature in HEPES buffer solution. HEPES solution composition (in mM): 92 NaCl, 2.5 KCl, 1.2 NaH2PO4, 30 NaHCO3, 20 HEPES, 25 Glucose, 5 Na+ Ascorbate, 2 Thiourea, 3 Na+ Pyruvate, 10 MgSO4, 0.5 CaCl2, 305 mOsm, 7.3-7.4 pH. NMDG solution was identical to HEPES, with an equimolar replacement of NaCl for NMDG. Neurons were then selected for recording based on mCherry expression visualized with 2-photon or conventional fluorescent microscopy. Whole cell current-clamp recordings were made using the following recording solutions (in mM): Internal: 9 HEPES, 113 K-Gluconate, 4.5 MgCl2, 0.1 EGTA, 14 Tris-phosphocreatine, 4 Na2ATP, 0.3 Tris-GTP, 10 Sucrose, 290 mOsm, 7.2-7.25 pH; External: 125 NaCl, 2.5 KCl, 1 MgCl2, 1.25 NaH2PO4, 25 NaHCO3, 25 Glucose, 2 CaCl2, 305 mOsm, 7.25-7.30 pH. Reported Vm was not corrected for junction potential (12 mV).

Cells with an unstable baseline membrane potential, defined as a significant ($p < 0.05$) linear regression in Vm > ± 0.5 mV/min, were excluded from analyses.

5.5.6 CNO

CNO stock solution was prepared by dissolving CNO (Enzo) in sterile saline at 5 mg/mL, kept as frozen aliquots, and freshly diluted with sterile saline prior to intraperitoneal (IP) administration. The final dose of CNO for hM3DGq and hM4DGi studies was 0.3 mg/kg and 3 mg/kg, respectively, unless mentioned otherwise. Saline (vehicle) or CNO were administered in a randomized manner to each animal during successive trials. Assays were initiated 30 min after IP injection of CNO or saline.

5.5.7 Behavioral Assays

Behavioral assays were performed in the dark cycle (≥1 hr after lights out), recorded using camcorders (Sony) under infrared illumination, and analyzed as previously described (Yang et al., 2013). All experimental males were group housed by sex after weaning until they were to be injected with virus. Thus, solitary males were singly housed for > 10 days prior to behavioral testing. These males had been socially housed prior to stereotaxic viral injections and were subsequently singly housed. They were tested for mating for 15 min with a WT socially housed stimulus female that was hormonally primed to be in estrus as described previously (Wu et al., 2009). Solitary males were tested for aggression with WT socially housed stimulus males for 15 min as described previously (Yang et al., 2013). Solitary males to be tested as intruders in another solitary male's homecage were injected with saline or CNO and, 30 min later,

were inserted into the resident's homecage for 15 min. Tests of aggression toward inanimate objects lasted 10 min with the object in the homecage; a custom sized mirror that fit against the short wall of the cage or partially inflated glove was inserted into the cage of a solitary male that had been administered saline or CNO. Solitary mice were tested once each with saline and CNO in a randomized manner, with the assays separated by 2-3 days. CNO or saline was administered to the solitary male in his homecage 30 min prior to the beginning of the assay.

Socially housed males had never been housed singly and, after recovery from surgery, continued to cohabit in same sex groups of 4-5 mice/cage. Prior to testing these males in behavioral assays, they were injected with saline or CNO, immediately moved to a clean cage for 30 min to preclude any social interactions with cagemates, and then inserted into a solitary male's cage (as an intruder in resident-intruder test) or clean cage (neutral arena) or returned to their homecage after removing the other cagemates (as a resident in resident-intruder test). Solitary males who received an experimental intruder male (PRCre) in their homecage were experienced fighters. Tests of aggression lasted 15 min. Socially housed males were tested once each with saline or CNO in a randomized manner.

Females used as stimulus animals in mating assays were ovariectomized as described previously (Wu et al., 2009) and estrus was induced via subcutaneous administration of 10 μg of 17 β-estradiol benzoate (Sigma) in 100 μL of sesame oil on day –2, 5 μg of 17 β-estradiol benzoate in 50 μL of sesame oil on day –1, and 50 μg of progesterone (Sigma) in 50 μL of sesame oil on day 0, the day of behavioral testing.

In some cases, PRCre males were surgically castrated and allowed to recover for ≥ 3 weeks to eliminate gonadal hormones from the circulation. These males had been previously injected with virus into the VMH. Some males were singly housed following castration whereas others continued to be socially housed; these males were used as solitary residents or socially housed intruders as described in the main text.

In experiments where we used PRCre females as residents, these females had been socially housed with other females post-weaning. During stereotaxic delivery of the virus into the VMH, these females were ovariectomized and allowed to recover in social housing for 2 weeks. They were subsequently singly housed for 10-12 days and then tested for behavioral responses for 15 min to male or female intruders 30 min after intraperitoneal injection of saline or CNO.

Behavior in elevated-plus maze was tested as described previously (Unger et al., 2015). In brief, 30 min following saline or CNO administration, a solitary male was placed in the common center area of the elevated plus maze. His behavior was recorded for 5 min and analyzed subsequently as described before (Unger et al., 2015).

5.5.8 Hormone Assays

Serum testosterone level was measured using an ELISA kit (EIA1559, DRG International) following the manufacture's instruction. Cardiac blood from castrated and control males were collected at the time of perfusion and serum was obtained as described previously (Wu et al., 2009).

5.5.9 Building Logic Circuits and Neural Network Models for Male Aggression

To model the experimental results, each feature (experience, environment, VMHvl stimulation, opponent, pheromone sensing, and circulation of hormones) and the response (attack behavior) was treated as a binary variable ('0' or '1'). The Boolean circuit was designed by manual inspection of the truth table, ensuring that it satisfied each of the rows (experiments). Other Boolean circuit configurations could presumably also account for our findings.

The single layer network was trained as a logistic regression model, where the model prediction consisted of a weighted sum of the binary features, passed through a sigmoidal threshold. The multi-layer network consisted of two cascaded layers of the single layer architecture. To train each model, we minimized the model prediction error plus a small penalty to constrain the weight scale (all results did not depend on the choice of this penalty). This minimization was done via batch gradient descent using the scikit-learn software package. To identify the experiment(s) that precludes linear classification from explaining the data, we iteratively removed each experiment from the table and re-trained the single layer model to determine if removing a particular example would allow the rest to be linearly classified. For neural network modeling, we treated each input variable (such as pheromone sensing or opponent) as a single categorical entity. However, we note that even splitting up pheromone sensing into two, one inhibiting aggression and the other promoting it, during modeling did not yield a single layer network capable of capturing all the findings in the truth table.

5.5.10 Quantification and Statistical Analysis

Recorded videos and histological samples were analyzed blind to relevant variables, including administrated solution, genotype, sex, prior housing condition, surgical procedure, and virus injected. Videos were played at 30 frames per second and manually annotated using custom software as previously described (Wu et al., 2009). In particular, anogenital investigation (sniff), mounting, repeated pelvic thrust (intromission), and ejaculation were scored for male sexual behaviors. Aggression was scored when a physical attack (episodes of biting, wrestling, or chasing) was observed, and various parameters of attack (latency, number, inter-attack interval, and duration) were subsequently calculated. Importantly, tail rattling was always scored as a distinct event such that a tail rattle was not considered as an episode of physical attack. Similarly, we only included physical attacks for analysis in our modeling studies. Distinct events during physical attacks such as biting the neck, biting the flank, chasing, or wrestling were also annotated separately for a subset of animals to analyze specific patterns of attack for Figure S1H.

Statistical analysis was performed using MATLAB or GraphPad PRISM (GraphPad Software). To compare categorical data, including percentage of males initiating attack and percentage of males tail rattling, Fisher's exact test was performed from a 2x2 contingency table. For non-categorical data, behavioral parameters such as number of attack, latency to first attack, mean duration of attack, total duration of attack, and inter-attack interval were analyzed only from animals who displayed behaviors. We first determined if the data values came from a normal distribution with D'Agostino-Pearson omnibus normality test. In experiments with paired samples, we used a paired

t test and Wilcoxon matched-pairs signed rank test for parametric and non-parametric data, respectively. In all other experiments, we used a t test, t test with Welch's correction for unequal standard deviation, or ANOVA for parametric data and a Mann-Whitney or Kruskal-Wallis test for non-parametric data.

5.6 FIGURES

5.6.1 Main Figures

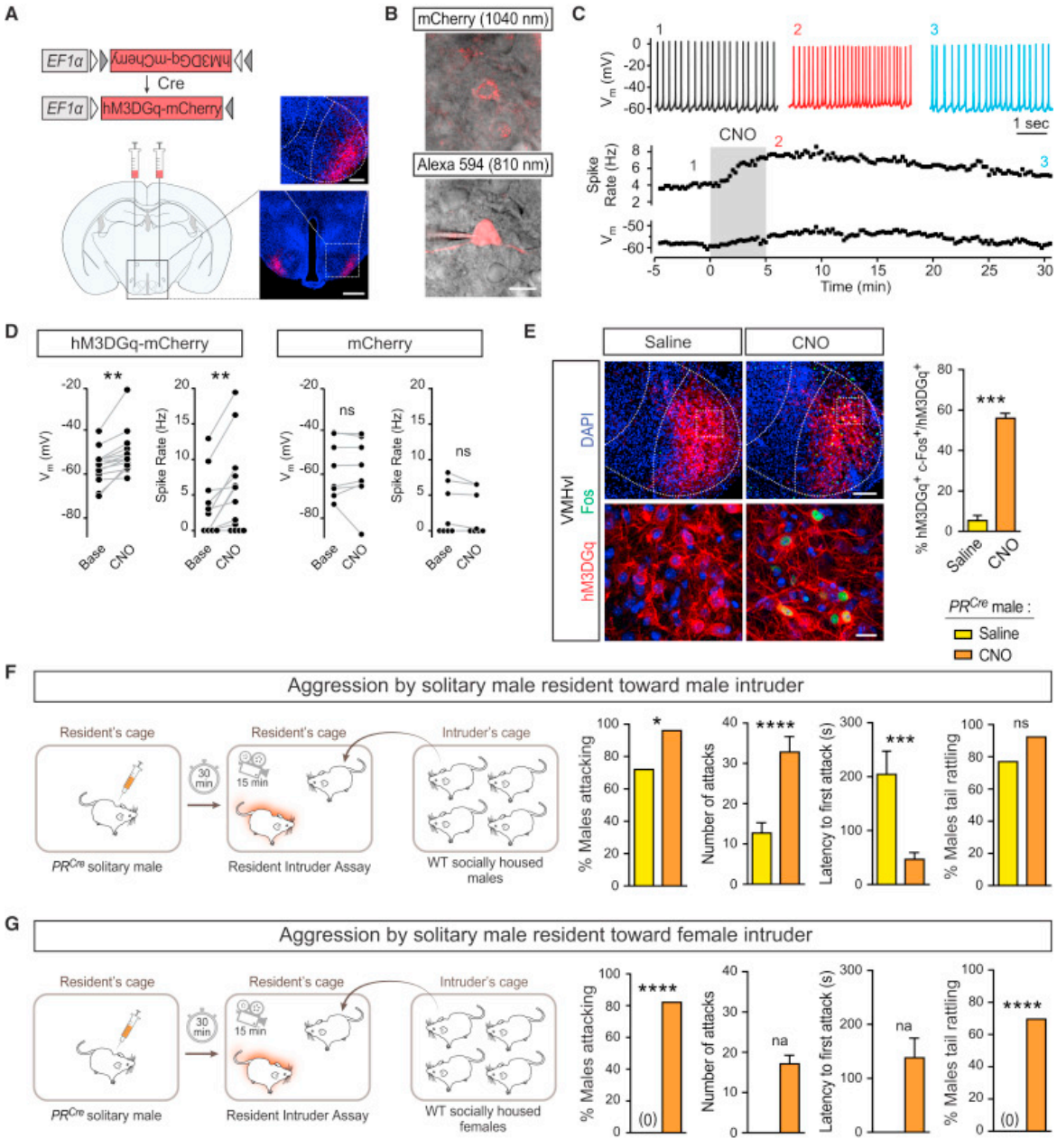

Figure 5.1. Chemogenetic Activation of PR+ VMHvl Neurons Triggers Aggression
(A–G) All mice were injected with an AAV encoding Cre-dependent hM3DGq-mCherry (A–G) or mCherry (D) into the VMHvl of adult PRCre males.
(A) Schematic showing bilateral stereotaxic delivery of the AAV to the VMHvl of PRCre mice. The inset shows mCherry+ cells in the VMHvl 10 days following injection.
(B) Top: mCherry+ (PR+, hM3DGq+) neuron in VMHvl targeted for patch-clamp recording using a 1,040-nm, two-photon excitation source. Bottom: a target neuron filled

with Alexa 594 was visualized with 810-nm, two-photon excitation to confirm neuronal identity. Scanning differential interference contrast was visualized in both imaging configurations to guide recording.
(C) Example of such a patched mCherry+ neuron, where 5 min of CNO (1 μM, gray shading) depolarized the neuron and increased spiking activity. Numbers (1–3) highlight spiking during baseline, immediately after CNO, and 25 min following washout.
(D) Summary of electrophysiological studies on PR+ VMHvl neurons expressing hM3DGq-mCherry (left) or control mCherry (right). Each dot represents a single neuron, and lines connect baseline and CNO conditions within recordings. Data are from six hM3DGq-mCherry and four mCherry injected males.
(E) CNO injection increases Fos expression in PR+ VMHvl neurons expressing hM3DGq-mCherry. Top and bottom: histological images captured at 10× and 63× objectives, respectively. Quantification shows the percentage of hM3DGq-mCherry VMHvl neurons that express Fos following CNO or saline (control) injection. n = 3/condition.
(F) Resident solitary PRCre males attack WT socially housed intruder males with increased probability and intensity when injected with CNO. There is no difference in the percentage of resident males tail-rattling to an intruder when given CNO or saline. n = 25/condition.
(G) Resident solitary PRCre males tail-rattle to and attack WT socially housed intruder females primed to be in estrus only when given CNO. n = 28/condition.

na, not applicable. Only mice showing attack behavior were included in the analysis of non-categorical data, such as number of attacks and latency to first attack, in this and all other figures. If no or too few males given saline displayed attacks, it precluded statistical analysis of these attack parameters. See also Table S1 for this and all other figures where we have analyzed these non-categorical data following inclusion of all animals regardless of whether they displayed attacks. ns, not significant. Mean ± SEM. $*p < 0.05$, $**p < 0.01$, $***p < 0.001$, $****p < 0.0001$. Scale bars, 100 μm and 500 μm for the top and bottom insets, respectively (A), 10 μm (B), and 100 μm and 20 μm for the top and bottom insets, respectively (E).

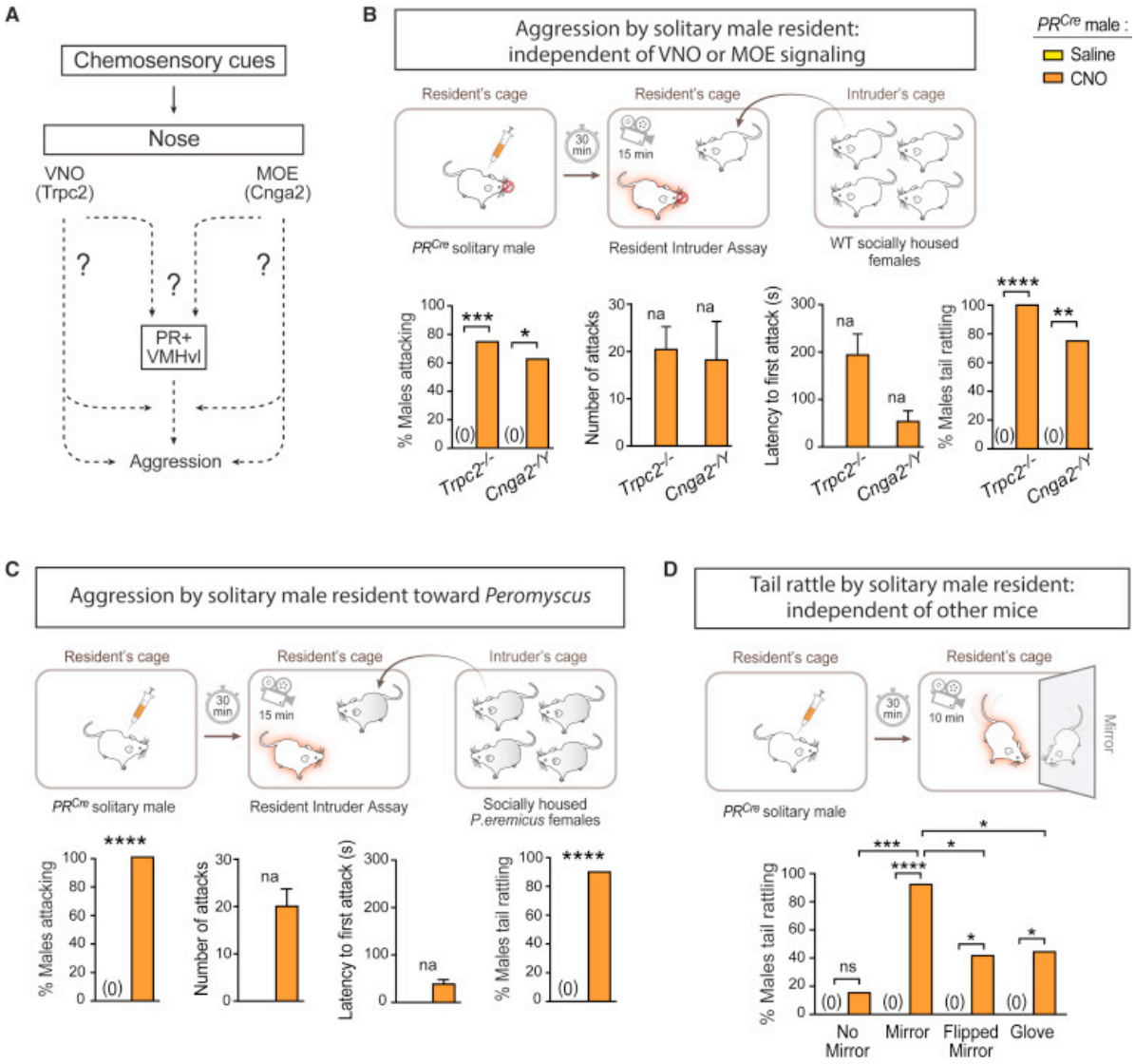

Figure 5.2. PR+ VMHvl Neurons Elicit Aggressive Displays Independent of Chemosensory Signaling

(A) Schematic showing that chemosensory cues detected by MOE or VNO neurons may elicit aggression by functioning in pathways upstream, downstream, or parallel to PR+ VMHvl neurons.

(B–D) An AAV encoding Cre-dependent hM3DGq-mCherry was delivered to VMHvl of PRCre;Trpc2–/– (B), PRCre;Cnga2–/Y (B), or PRCre (C and D) adult males.

(B) Solitary male residents null for Trpc2 or Cnga2 tail-rattled to and attacked socially housed female intruders only after being administered CNO. n = 12/condition (Trpc2–/–) and 8/condition (Cnga2–/Y).

(C) Solitary male residents tail-rattled to and attacked socially housed P. eremicus female intruders only after CNO injection. n = 10/condition.

(D) Solitary male residents tail-rattled more to inanimate objects after CNO administration. They also tail-rattled more to the reflective side of the mirror compared

with its non-reflective side or to a partially inflated glove. n = 13/condition (no mirror, mirror), 12/condition (flipped mirror), and 13 (saline) and 9 (CNO) (glove).
Mean ± SEM. $*p < 0.05$, $**p < 0.01$, $***p < 0.001$, $****p < 0.0001$.

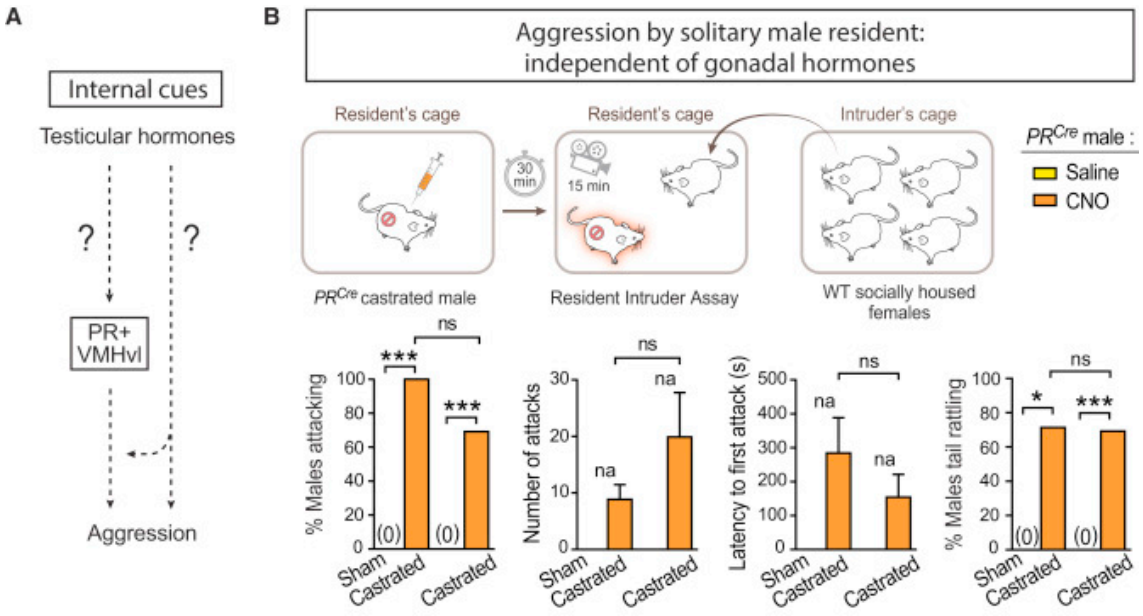

Figure 5.3. PR+ VMHvl Neurons Elicit Aggressive Displays Independent of Male Gonadal Hormones

(A) Schematic showing that testicular hormones may influence aggression by activating the physiological function of PR+ VMHvl neurons directly or that of the neural pathways upstream, downstream, or parallel to PR+ VMHvl neurons.

(B) An AAV encoding Cre-dependent hM3DGq-mCherry was delivered to VMHvl of PRCre adult males who were subsequently castrated or subjected to sham castration surgery. There were no differences between castrated and sham control males tail rattling to and attacking WT socially housed female intruders when injected with CNO. Mean ± SEM, n = 7/condition (sham-castrated) and 13/condition (castrated). $*p < 0.05$, $***p < 0.001$.

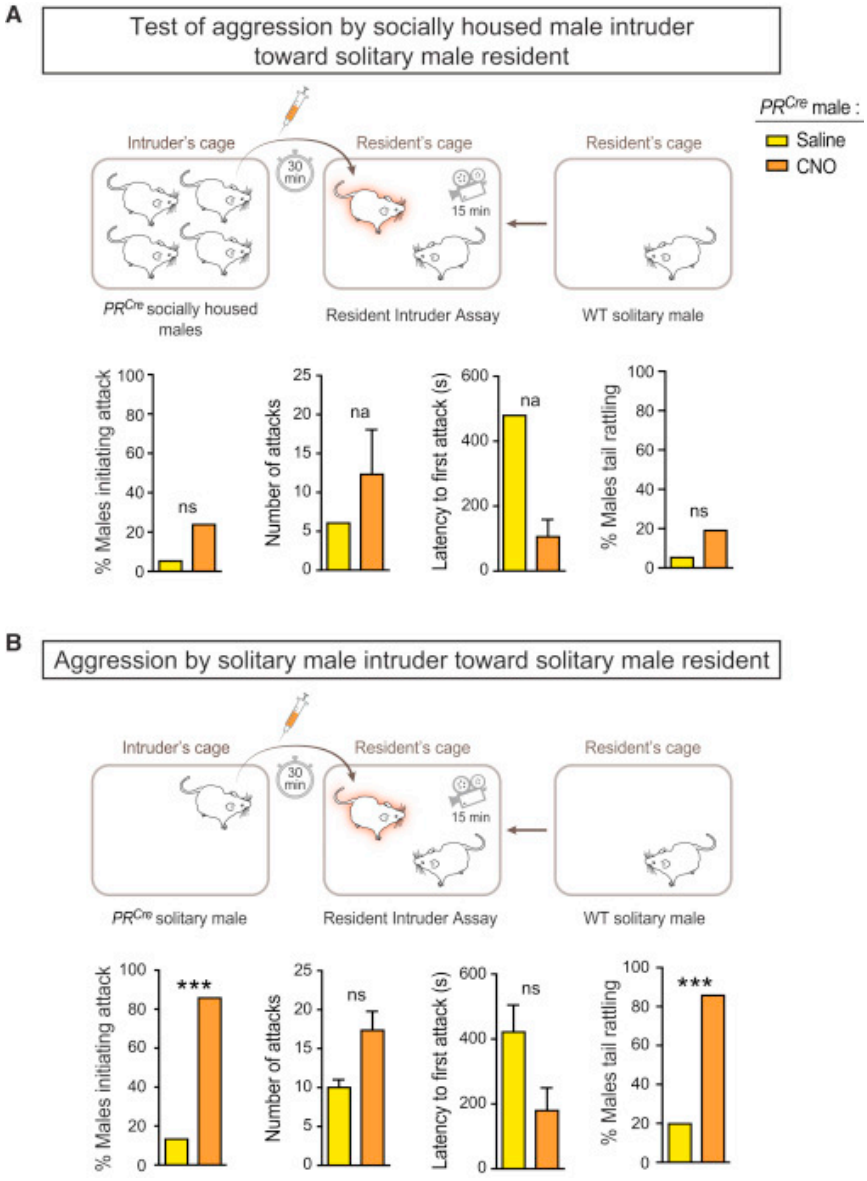

Figure 5.4. PR+ VMHvl Neuron-Elicited Aggression Is Dependent on Social Context

(A and B) An AAV encoding Cre-dependent hM3DGq-mCherry was delivered to VMHvl of PRCre adult males who were socially housed with other males (A) or housed singly (B) and used as intruders. Singly but not socially housed male intruders given CNO routinely tail-rattled to and initiated attacks toward a WT solitary male resident. Too few socially housed (n = 1) or solitary (n = 2) male intruders given saline attacked the resident, thereby precluding meaningful statistical analysis for non-categorical data. Mean ± SEM; n = 19 (saline) and 21 (CNO) (A); n = 15 (saline) and 14 (CNO) (B). ***p < 0.001.

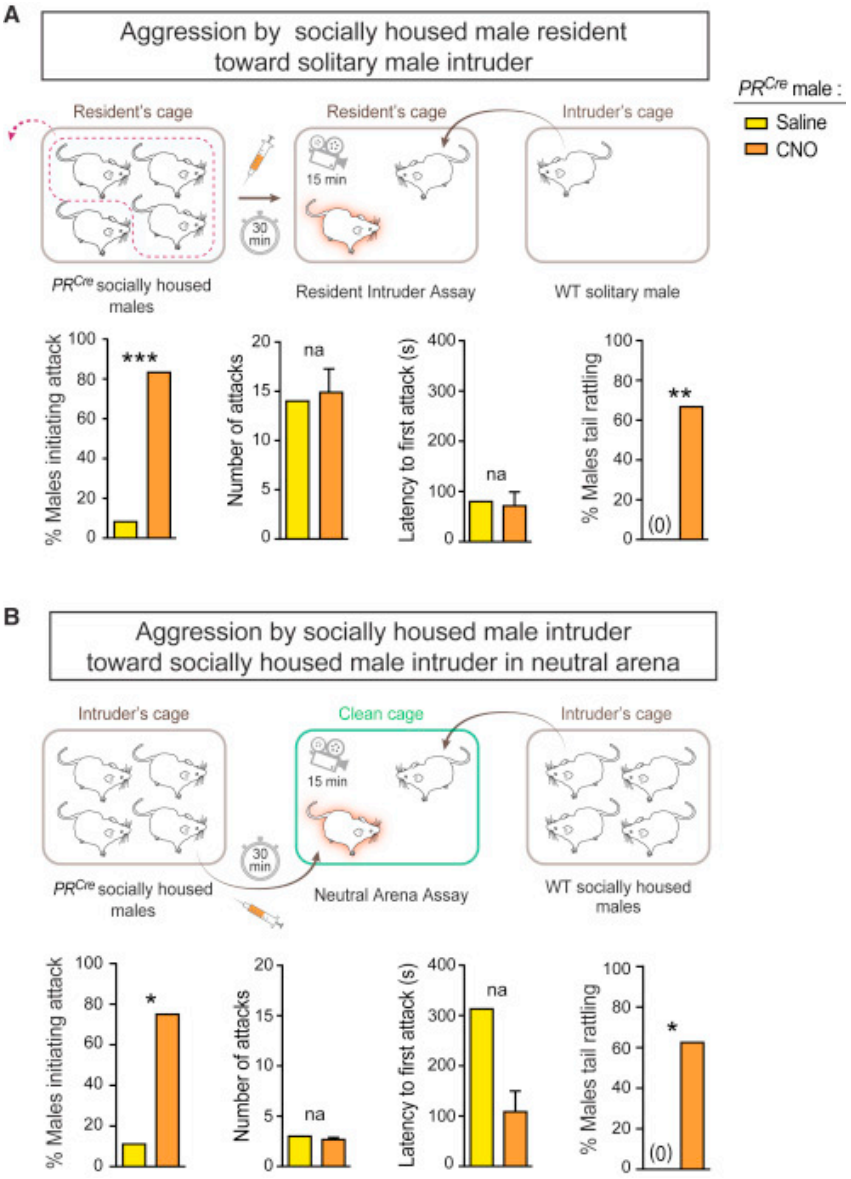

Figure 5.5. PR+ VMHvl Neurons Can Trigger Aggression in Socially Housed Males
(A and B) An AAV encoding Cre-dependent hM3DGq-mCherry was delivered to VMHvl of PRCre adult males who were socially housed with other males and used as residents (A) or intruders (B).
(A) Socially housed resident males were injected with CNO or saline, their cage mates were removed from the homecage, and a WT intruder male was inserted into the cage. Such socially housed residents tail-rattled to and attacked intruders significantly more with CNO compared with saline. n = 12/condition.
(B) Socially housed males injected with CNO or saline were inserted into a clean cage (neutral arena) along with a WT socially housed male. CNO-administered males tail-rattled to and attacked the WT male more than males injected with saline. n = 8/condition.

Too few socially housed males given saline initiated attacks in their homecage or a neutral arena (n = 1 each), thereby precluding meaningful statistical analysis for non-categorical data. Mean ± SEM. $*p < 0.05$, $**p < 0.01$, $***p < 0.001$.

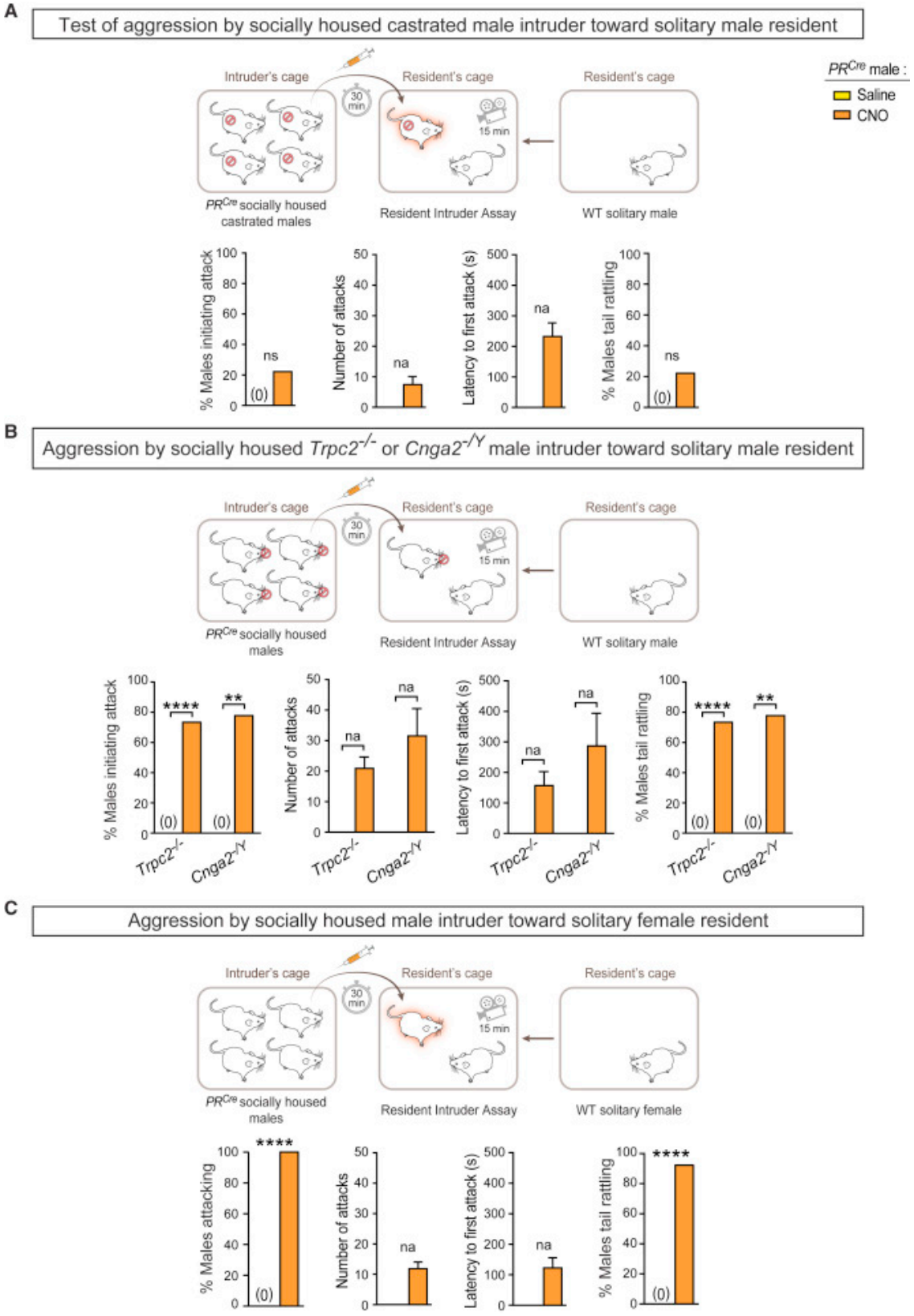

Figure 5.6. Male Pheromones Inhibit Aggression Elicited by PR+ VMHvl Neurons

An AAV encoding Cre-dependent hM3DGq-mCherry was delivered to VMHvl of PRCre adult males who were socially housed with other males and used as intruders.
(A) Castrated male intruders injected with CNO did not tail-rattle to or initiate attacks toward WT solitary resident males significantly more than when they were injected with saline. n = 15/condition.
(B) Male intruders genetically disabled for chemosensory signaling via the VNO or MOE (PRCre; Trpc2–/– or PRCre;Cnga2–/Y), injected with CNO but not saline, tail-rattled to and attacked WT solitary resident males. n = 15/condition (Trpc2–/–) and 8/condition (Cnga2–/Y).
(C) Male intruders injected with CNO but not saline tail-rattled to and attacked WT solitary resident females. n = 13/condition.
Mean ± SEM. $^{**}p < 0.01$, $^{****}p < 0.0001$.

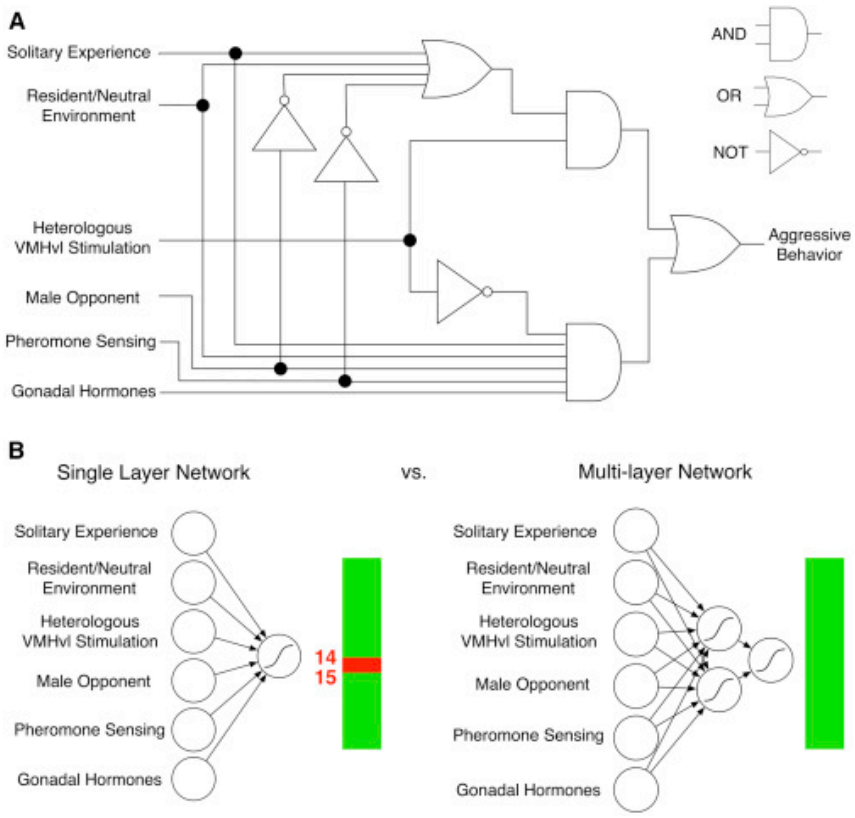

Figure 5.7. Modeling Male Aggression with Logic Circuits and Neural Networks
(A) Schematic of a logic circuit that summarizes results in which the output variable is attack and the opponent is a lab mouse.
(B) A two-layer but not a single-layer network adequately captures the findings summarized in the logic circuit outlined in (A) and Table 1. We determined the fewest experiments that need to be excluded for the logic circuit to be implementable by a single-layer network. This search showed that removal of only one experiment, outlined in rows 14 and 15 (Table 1), is sufficient for the logic circuit to be realized by a linear classifier. The experiment outlined in these two rows demonstrates that socially housed intruder males do not initiate attacks toward resident males even upon stimulation of PR+ VMHvl neurons. The green bars indicate findings from rows in Table 1 that can be implemented by the neural network, whereas findings from numbered rows (red) cannot be implemented by the network.

5.6.2 Supplemental Figures

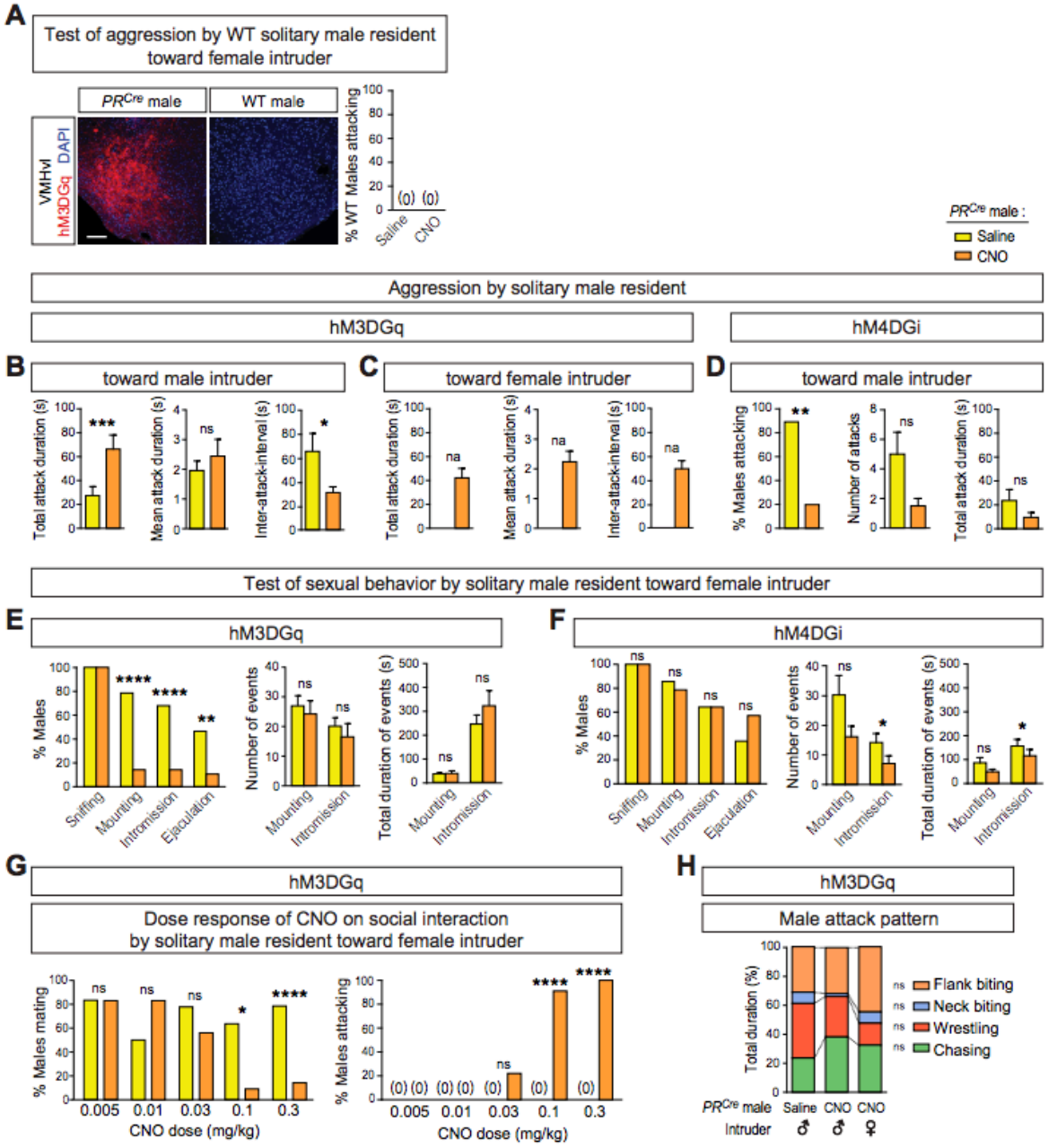

Figure 5.8 (S1): Further characterization of the role of PR+ VMHvl neurons in adult males. Related to Figure 5.1.

AAV encoding Cre-dependent hM3DGq-mCherry (A, B, C, E, G, H) or hM4DGi-mCherry (D,F) was delivered to VMHvl of WT (A) or PRCre (B-H) adult males.

(A) mCherry is not detectable in WT males, and these males did not attack females when given saline or CNO (bar graph; n = 3/condition). By contrast, hM3DGq-mCherry is expressed in VMHvl of PRCre male.

(B) Males given CNO attacked a WT socially housed intruder male for longer duration in the assay and more frequently compared to males given saline. n = 25/condition.
(C) Males given CNO but not saline attacked a WT socially housed female intruder in estrus. N = 28/condition.
(D) Fewer males expressing hM4DGi-mCherry in PR+ VMHvl neurons attacked a WT socially housed intruder male when injected with CNO compared to saline. Of the males that attacked the intruder, there was a non-significant decrease in the intensity of attacks. n = 10/condition.
(E) Fewer males mated (mounted, intromitted, or ejaculated) with WT female intruders primed to be in estrus when given CNO compared to saline. Of the males that mated following CNO administration, there was no difference in parameters of mounting or intromission compared to males who mated after being given saline. n = 28/condition.
(F) There was a decrease in number and duration of intromission in males given CNO compared to saline when mating with WT female intruders primed to be in estrus. n = 14/condition.
(G) Increasing dose of CNO led to switch from mating to aggression by solitary male residents toward WT female intruders primed to be in estrus. n = 6-11 for all doses except 0.3 mg/kg for which n = 28 (same animals as in panels B, D).
(H) No difference in attack pattern by solitary resident PRCre males expressing hM3DGqmCherry in VMHvl neurons when faced with a WT socially housed male or female intruder. n = 8/condition; these animals represent a randomly chosen subset of the animals used for studies in panels A, B, and D.
Mean ± SEM. *$p < 0.05$, **$p < 0.01$, ****$p < 0.0001$. Scale bars = 100 μm (A).

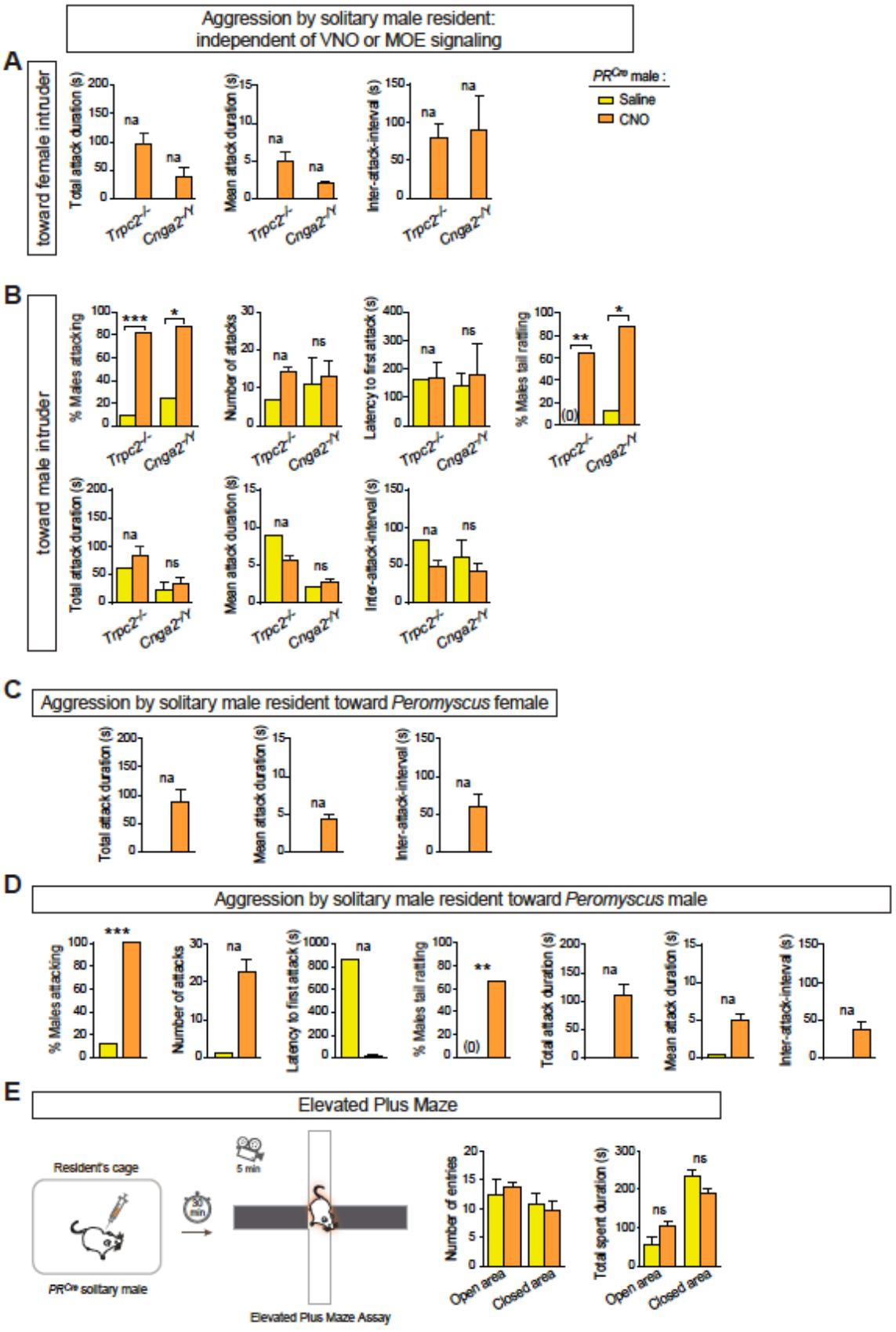
Aggression by solitary male resident:
independent of VNO or MOE signaling
A
toward female intruder
Total attack duration (s)
Mean attack duration (s)
Inter-attack-interval (s)
PRCre male :
Saline
CNO
na
Trpc2-/-
Cnga2-/-
B
toward male intruder
% Males attacking
Number of attacks
Latency to first attack (s)
% Males tail rattling
Total attack duration (s)
Mean attack duration (s)
Inter-attack-interval (s)
***
*
**
ns
(0)
C
Aggression by solitary male resident toward Peromyscus female
D
Aggression by solitary male resident toward Peromyscus male
E
Elevated Plus Maze
Resident's cage
PRCre solitary male
30 min
5 min
Elevated Plus Maze Assay
Number of entries
Total spent duration (s)
Open area
Closed area

Figure 5.9 (S2): PR+ VMHvl neurons elicit aggressive displays independent of chemosensory signaling. Related to Figure 5.2.

AAV encoding Cre-dependent hM3DGq-mCherry was delivered to VMHvl of PRCre adult males that were Trpc2–/– or Cnga2–/Y (A, B) or WT for these channels (C-E).

(A) Trpc2–/– or Cnga2–/Y males given CNO but not saline attacked WT female intruders primed to be in estrus. n = 12/condition (Trpc2–/–) and 8/condition (Cnga2–/Y).

(B) More Trpc2–/– or Cnga2–/Y males tail rattled to and attacked WT socially housed male intruders when given CNO compared to saline. No difference in other parameters of aggression in CNO or saline injected resident males that attacked. n = 12/condition (Trpc2–/–) and 8/condition (Cnga2–/Y). Too few Trpc2 (n = 1) or Cnga2 (n = 2) mutant male residents given saline attacked a male intruder to permit meaningful statistical analysis of non-categorical data.

(C) Males given CNO but not saline attacked Peromyscus female intruders. n = 10/condition.

(D) More males given CNO attacked Peromyscus male intruders. n = 10/condition.

(E) No difference in entries or time spent in open and closed arms of elevated-plus maze between solitary resident males given saline (n = 6) or CNO (n = 7).

Mean ± SEM. *$p < 0.05$, **$p < 0.01$, ***$p < 0.001$.

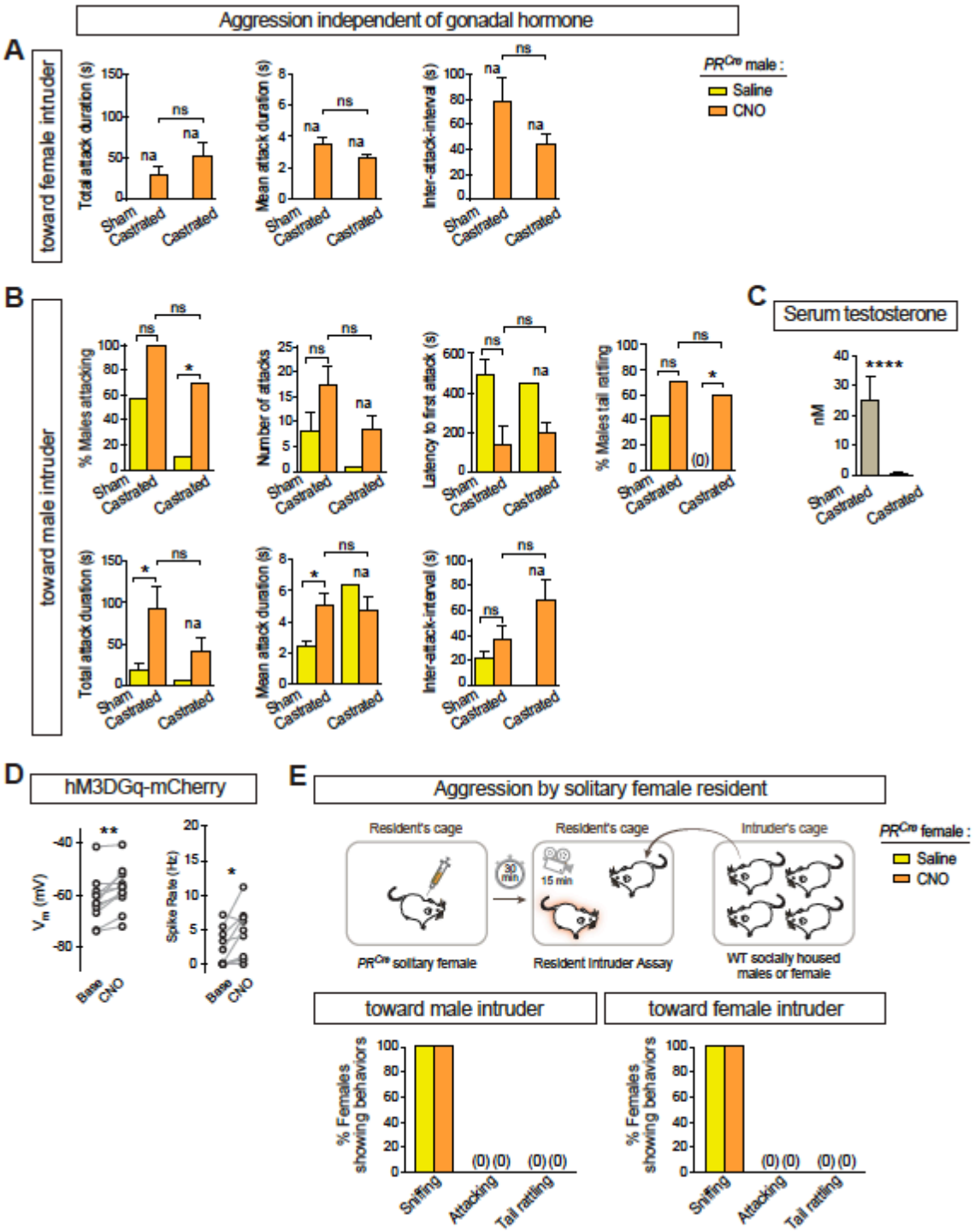

Figure 5.10 (S3): PR+ VMHvl male neurons elicit aggressive displays independent of gonadal hormones. Related to Figure 5.3.

AAV encoding Cre-dependent hM3DGq-mCherry was delivered to VMHvl of PRCre adult males that were castrated or underwent sham surgery (A-C) or PRCre adult, gonad-intact females (D, E).

(A) Castrate and sham castrate males attacked WT female intruders primed to be in estrus in a comparable manner when given CNO. Neither group of males attacked females when given saline.
(B) More castrate males tail rattled to and attacked WT socially housed male intruders when given CNO compared to saline. Castrate males given CNO attacked such intruders in a manner comparable to sham castrate males.
(C) Testosterone was essentially undetectable in serum of castrate males, and profoundly reduced compared to sham castrate males.
Mean ± SEM. n = 7/condition (Sham castrated) and 13/condition (Castrated). *$p < 0.05$, ****$p < 0.0001$.
(D) Summary of electrophysiological studies on female PR+ VMHvl neurons expressing hM3DGq-mCherry. Each dot represents a single neuron, and lines connect baseline and CNO conditions within recordings. Data from 3 AAV-flex-hM3DGq:mCherry injected females. Significant changes in electrophysiological properties were observed with CNO (Vm: -62 ± 2.9 mV (baseline) and -57.5 ± 2.8 mV (CNO), n = 10 cells, $p < 0.01$; spike rate: 1.7 ± 0.8 Hz (baseline) and 3.2 ± 0.9 Hz (CNO), n = 10 cells, $p < 0.05$). No significant difference in Vm and spike rate between male and female PR+ VMHvl neurons expressing hM3DGq:mCherry (Vm: $p = 0.38$ (baseline) and $p = 0.22$ (CNO); spike rate: $p = 0.52$ (baseline) and $p = 0.27$ (CNO)).
(E) Solitary ovariectomized female residents were injected with CNO or saline, and a WT socially housed male or WT female hormonally primed to be in estrus was inserted into the cage 30 min later. The female residents sniffed the intruders but did not tail-rattle or attacked them. n = 15/condition.

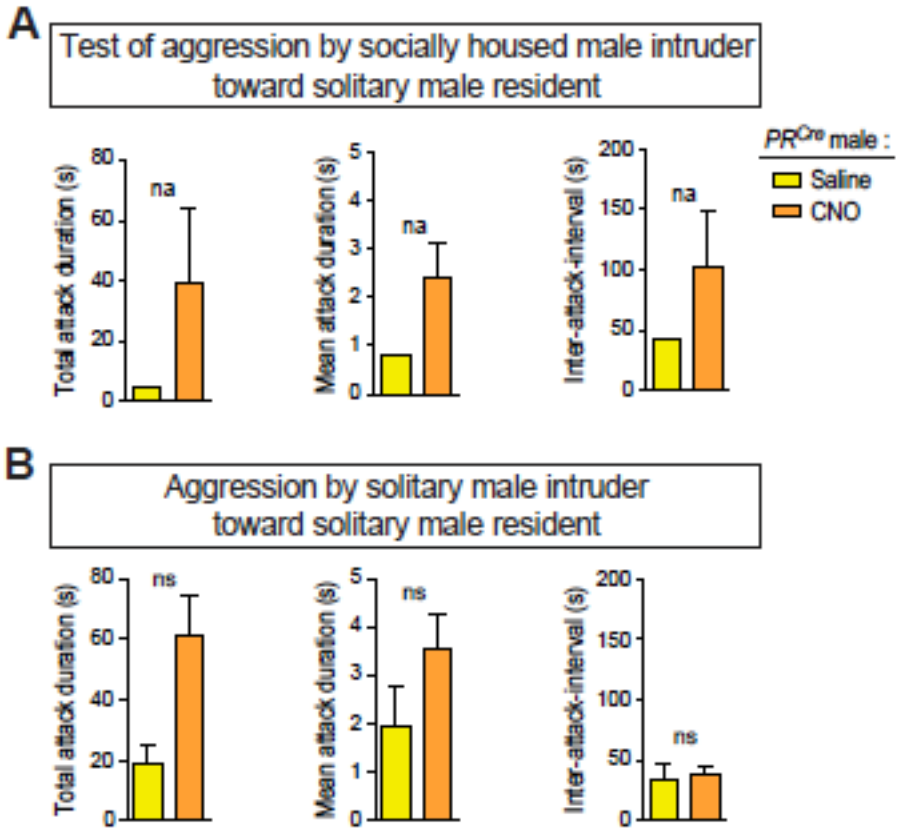

Figure 5.11 (S4): Singly but not socially housed male intruders attack male resident upon activation of PR+ VMHvl neurons. Related to Figure 5.4.
AAV encoding Cre-dependent hM3DGq-mCherry was delivered to VMHvl of PRCre socially housed (A) or solitary resident (B) adult males.
(A) Few socially housed male intruders attacked a male resident even in presence of CNO (Figure 4A), and too few intruders given saline attacked to permit statistical comparison.
(B) More singly housed male intruders attacked a male resident in presence of CNO (Figure 4B), but there was no difference in attack parameters between CNO and saline administration. Mean ± SEM. n = 19 (saline) and 21 (CNO) (A); n = 15 (saline) and 14 (CNO) (B).

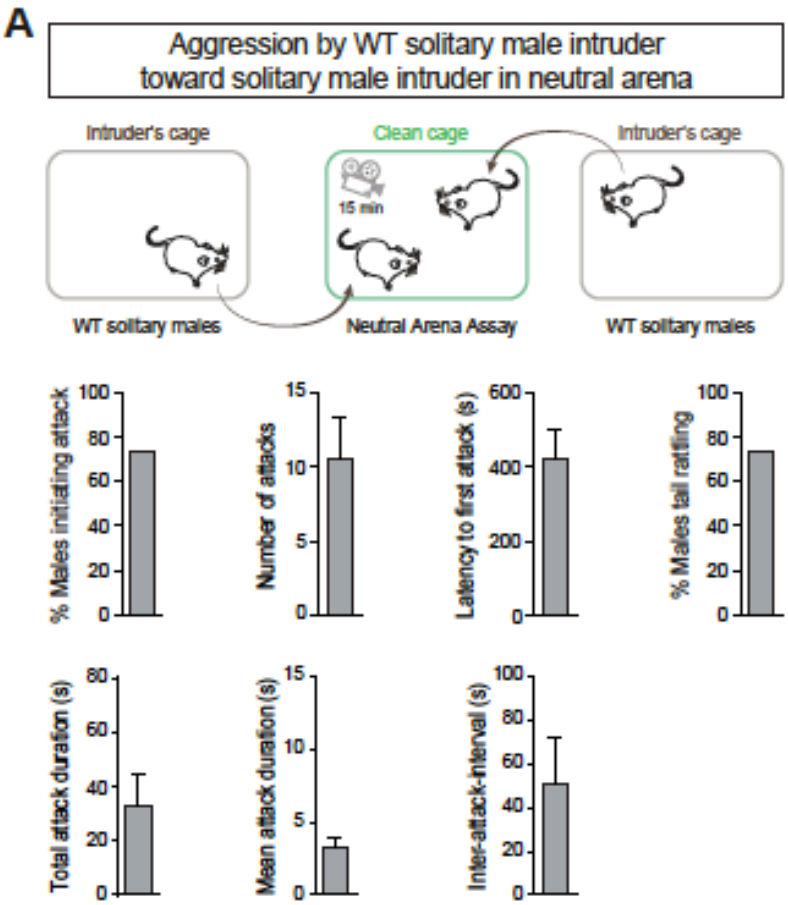
A
Aggression by WT solitary male intruder
toward solitary male intruder in neutral arena
Intruder's cage
Clean cage
Intruder's cage
15 min
WT solitary males
Neutral Arena Assay
WT solitary males
% Males initiating attack
Number of attacks
Latency to first attack (s)
% Males tail rattling
Total attack duration (s)
Mean attack duration (s)
Inter-attack-interval (s)

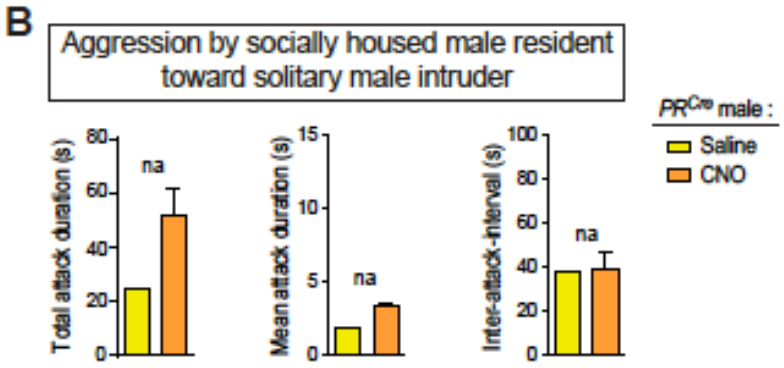
B
Aggression by socially housed male resident
toward solitary male intruder
PRCre male :
Saline
CNO
Total attack duration (s)
Mean attack duration (s)
Inter-attack-interval (s)
na
na
na

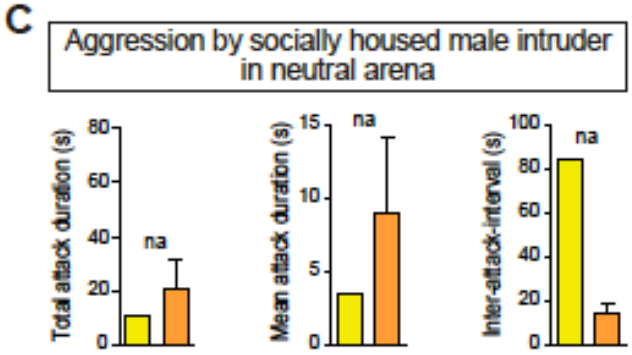
C
Aggression by socially housed male intruder
in neutral arena
Total attack duration (s)
Mean attack duration (s)
Inter-attack-interval (s)
na
na
na

Figure 5.12 (S5): Socially housed males can attack as residents or in a neutral arena. Related to Figure 5.5.

(A) WT solitary males inserted into a neutral arena tail rattled to and attacked the other male that was simultaneously introduced into the cage. Shown are parameters for the male that initiated attack. n = 15. AAV encoding Cre-dependent hM3DGq-mCherry was delivered to VMHvl of PRCre socially housed adult males (B, C).

(B) Parameters of attack by socially housed male residents toward solitary male intruder. Too few socially housed male residents given saline attacked to permit statistical comparison with such males given CNO. n =12/condition.

(C) Parameters of attack by socially housed males in a neutral arena. Too few socially housed males given saline attacked to permit statistical comparison with such males given CNO. n = 8/condition. Mean ± SEM.

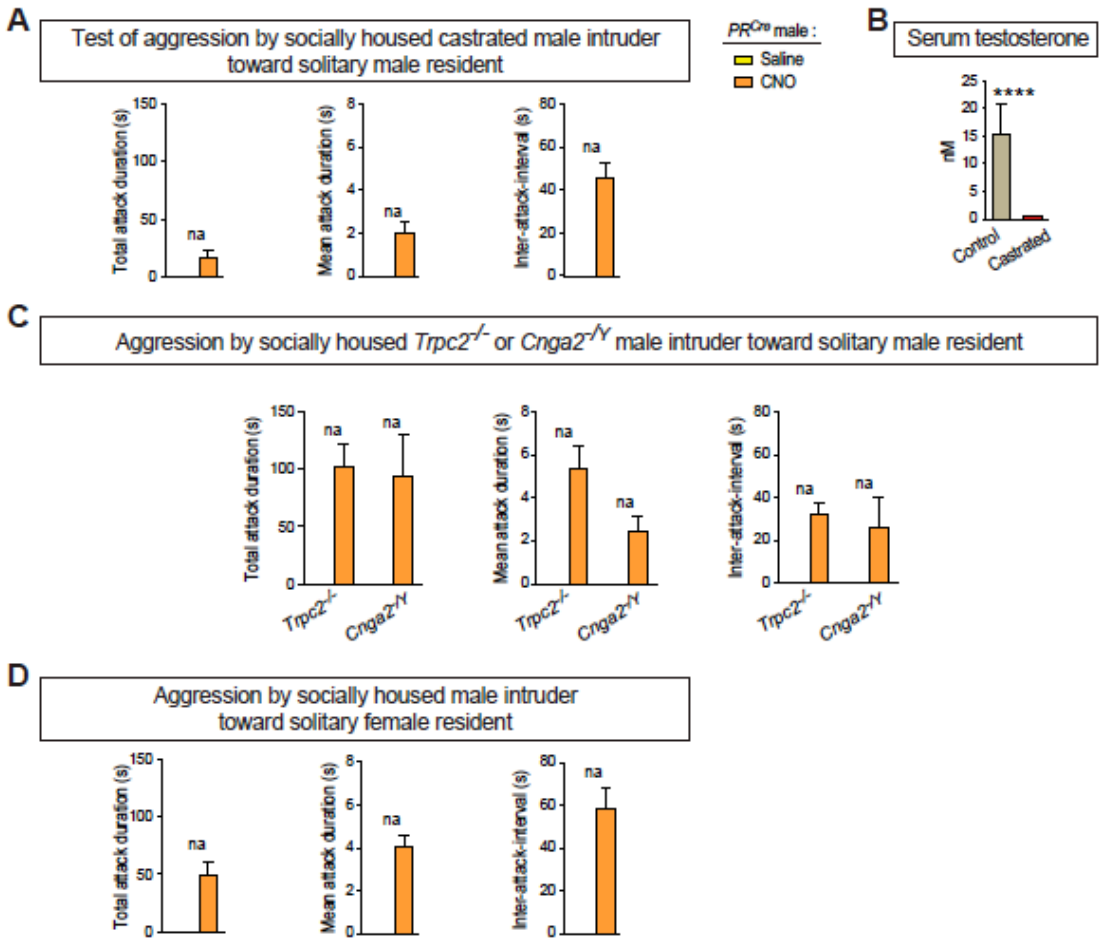

Figure 5.13 (S6): Male pheromones but not gonadal hormones inhibit aggression of socially housed intruders elicited by PR+ VMHvl neurons. Related to Figure 5.6.
AAV encoding Cre-dependent hM3DGq-mCherry was delivered to VMHvl of PRCre socially housed adult males (A-D) that were castrated (A, B) or mutant for Trpc2–/– or Cnga2–/Y (C).
(A) Few castrated male intruders (Figure 6A) given CNO attacked solitary resident males, and no intruders given saline attacked, thereby precluding statistical comparison. n = 15/condition.
(B) Testosterone was essentially undetectable in serum of castrate males, and significantly less compared to gonadally intact males. n = 9 (control) and 15 (castrated).
(C) Trpc2–/– or Cnga2–/Y male intruders given CNO but not saline attacked solitary male residents (Figure 6B), and parameters of these attacks are shown here. n = 15/condition (Trpc2-/-) and 8/condition (Cnga2–/Y).
(D) Male intruders given CNO but not saline attacked solitary female residents (Figure 6C), and parameters of these attacks are shown here. n = 13/condition. Mean ± SEM.

Figure	Aggression Parameter	p value
1G	Number of attacks	<0.0001
1G	Latency to first attack	<0.0001
2B	Number of attacks (*Trpc2*$^{-/-}$)	<0.001
2B	Number of attacks (*Cnga2*$^{-/-}$)	<0.05
2B	Latency to first attack (*Trpc2*$^{-/-}$)	<0.01
2B	Latency to first attack (*Cnga2*$^{-/-}$)	<0.05
2C	Number of attacks	<0.0001
2C	Latency to first attack	<0.0001
3B	Number of attacks (Sham castrated)	<0.001
3B	Number of attacks (Castrated)	<0.001
3B	Latency to first attack (Sham castrated)	<0.001
3B	Latency to first attack (Castrated)	<0.05
4A	Number of attacks	0.14
4A	Latency to first attack	0.1
5A	Number of attacks	<0.001
5A	Latency to first attack	<0.001
5B	Number of attacks	<0.05
5B	Latency to first attack	<0.01
6A	Number of attacks	0.1
6A	Latency to first attack	0.05
6B	Number of attacks (*Trpc2*$^{-/-}$)	<0.0001
6B	Number of attacks (*Cnga2*$^{-/-}$)	<0.01
6B	Latency to first attack (*Trpc2*$^{-/-}$)	<0.0001
6B	Latency to first attack (*Cnga2*$^{-/-}$)	<0.01
6C	Number of attacks	<0.0001
6C	Latency to first attack	<0.0001
S1B	Total attack duration	<0.0001
S1B	Mean attack duration	<0.0001
S1B	Inter-attack interval	<0.0001
S2A	Total attack duration (*Trpc2*$^{-/-}$)	<0.001
S2A	Total attack duration (*Cnga2*$^{-/-}$)	<0.05
S2A	Mean attack duration (*Trpc2*$^{-/-}$)	<0.001
S2A	Mean attack duration (*Cnga2*$^{-/-}$)	<0.05
S2A	Inter-attack interval (*Trpc2*$^{-/-}$)	<0.01
S2A	Inter-attack interval (*Cnga2*$^{-/-}$)	<0.05
S2B	Number of attacks (*Trpc2*$^{-/-}$)	<0.05
S2B	Latency to first attack (*Trpc2*$^{-/-}$)	<0.01
S2B	Total attack duration (*Trpc2*$^{-/-}$)	<0.01
S2B	Mean attack duration (*Trpc2*$^{-/-}$)	<0.01
S2B	Inter-attack interval (*Trpc2*$^{-/-}$)	<0.01
S2C	Total attack duration	<0.0001
S2C	Mean attack duration	<0.0001

Figure	Aggression Parameter	p value
S2C	Inter-attack interval	<0.01
S2D	Number of attacks	<0.0001
S2D	Latency to first attack	<0.001
S2D	Total attack duration	<0.0001
S2D	Mean attack duration	<0.0001
S2D	Inter-attack interval	<0.0001
S3A	Total attack duration (Sham castrated)	<0.001
S3A	Total attack duration (Castrated)	<0.001
S3A	Mean attack duration (Sham castrated)	<0.001
S3A	Mean attack duration (Castrated)	<0.001
S3A	Inter-attack interval (Sham castrated)	<0.01
S3A	Inter-attack-interval (Castrated)	<0.01
S3B	Number of attack (Castrated)	<0.01
S3B	Latency to first attack (Castrated)	<0.01
S3B	Total attack duration (Castrated)	<0.01
S3B	Mean attack duration (Castrated)	<0.05
S3B	Inter-attack interval (Castrated)	<0.05
S4A	Total attack duration	0.14
S4A	Mean attack duration	0.12
S4A	Inter-attack interval	0.24
S5B	Total attack duration	<0.001
S5B	Mean attack duration	<0.0001
S5B	Inter-attack interval	<0.001
S5C	Total attack duration	<0.05
S5C	Mean attack duration	<0.05
S5C	Inter-attack interval	0.05
S6A	Total attack duration	0.1
S6A	Mean attack duration	0.1
S6A	Inter-attack interval	0.1
S6C	Total attack duration (*Trpc2*$^{-/-}$)	<0.0001
S6C	Total attack duration (*Cnga2*$^{-/-}$)	<0.0001
S6C	Mean attack duration (*Trpc2*$^{-/-}$)	<0.0001
S6C	Mean attack duration (*Cnga2*$^{-/-}$)	<0.001
S6C	Inter-attack interval (*Trpc2*$^{-/-}$)	<0.001
S6C	Inter-attack interval (*Cnga2*$^{-/-}$)	<0.001
S6C	Total attack duration	<0.0001
S6C	Mean attack duration	<0.0001
S6C	Inter-attack interval	<0.0001

Table 5.1: Analysis of non-categorical parameters of aggression. Related to Figures 5.1-5.6 and 5.8-5.13.

In main and supplemental figures, we have analyzed non-categorical aggression parameters (such as latency to attack, number of attacks, mean and total attack

duration) only for animals that exhibited aggression. This Table presents analysis of these parameters for all animals that were tested, regardless of whether or not they exhibited aggression. To calculate latency of attack in tests where no aggression occurred, we assumed a latency of 900 s, which corresponds to the maximum duration of the behavioral assay.

5.7 REFERENCES

Alexander, G.M., Rogan, S.C., Abbas, A.I., Armbruster, B.N., Pei, Y., Allen,J.A., Nonneman, R.J., Hartmann, J., Moy, S.S., Nicolelis, M.A., et al. (2009). Remote control of neuronal activity in transgenic mice expressing evolved G protein-coupled receptors. Neuron 63, 27–39.

Arnold, A.P. (2009). The organizational- activational hypothesis as the foundation for a unified theory of sexual differentiation of all mammalian tissues. Horm. Behav. 55, 570–578.

Beeman, E.A. (1947). The effect of male hormone on aggressive behavior in mice. Physiol. Zool. 20, 373–405.

Berry, R.J., and Bronson, F.H. (1992). Life history and bioeconomy of the house mouse. Biol. Rev. Camb. Philos. Soc. 67, 519–550.

Bishop, C.M. (1995). Neural Networks for Pattern Recognition (Oxford University Press).

Bronson, F.H., and Desjardins, C. (1968). Aggression in adult mice: modification by neonatal injections of gonadal hormones. Science 161, 705–706.

Brunet, L.J., Gold, G.H., and Ngai, J. (1996). General anosmia caused by a targeted disruption of the mouse olfactory cyclic nucleotide-gated cation channel. Neuron 17, 681–693.

Chamero, P., Marton, T.F., Logan, D.W., Flanagan, K., Cruz, J.R., Saghatelian, A., Cravatt, B.F., and Stowers, L. (2007). Identification of protein pheromones that promote aggressive behaviour. Nature 450, 899–902.

Cheung, C.C., Krause, W.C., Edward s, R.H., Yang, C.F., Shah, N.M., Hnasko,T.S., and Ingraham, H.A. (2015). Sex-dependent changes in metabolism and behavior, as well as reduced anxiety after eliminating ventromedial hypothalamus excitatory output. Mol. Metab. 4, 857–866.

Crowcroft, P. (1955). Territoriality in wild house mice, Mus musculus L.J. Mammal. 36, 299–301.

Crowcroft, P. (1966). Mice All Over (G.T. Foulis & Co.).

Crowcroft, P., and Rowe, F.P. (1963). Social organization and territorial behaviour in the wild house mouse (Mus musculus L.). Proc. Zool. Soc. Lond. 140,517–531.

Desjardins, J.K., and Fernald, R.D. (2010). What do fish make of mirror images? Biol. Lett. 6, 744–747.

Dodman, N.H., Miczek, K.A., Knowles, K., Thalhammer, J.G., and Shuster, L.(1992). Phenobarbital-responsive episodic dyscontrol (rage) in dogs. J. Am.Vet. Med. Assoc. 201, 1580–1583.

Falkner, A.L., Dollar, P., Perona, P., Anderson, D.J., and Lin, D. (2014). Decoding ventromedial hypothalamic neural activity during male mouse aggression. J. Neurosci. 34, 5971–5984.

Fan, P., Manoli, D.S., Ahmed, O.M., Chen, Y., Agarwal, N., Kwong, S., Cai, A.G., Neitz, J., Renslo, A., Baker, B.S., and Shah, N.M. (2013). Genetic and neural mechanisms that inhibit Drosophila from mating with other species. Cell 154, 89–102.

Fernald, R.D. (2015). Social behaviour: can it change the brain? Anim. Behav.103, 259–265.

Ferrari, P.F., Palanza, P., Rodgers, R.J., Mainardi, M., and Parmigiani, S. (1996). Comparing different forms of male and female aggression in wild and laboratory mice: an ethopharmacological study. Physiol. Behav. 60, 549–553.
Finney, H.C., and Erpino, M.J. (1976). Synergistic effect of estradiol benzoate and dihydrotestosterone on aggression in mice. Horm. Behav. 7, 391–400.
Fraser, E.J., and Shah, N.M. (2014). Complex chemosensory control of female reproductive behaviors. PLoS ONE 9, e90368.
Gold, J.I., and Shadlen, M.N. (2002). Banburismus and the brain: decoding the relationship between sensory stimuli, decisions, and reward. Neuron 36,299–308.
Gold, J.I., and Shadlen, M.N. (2007). The neural basis of decision making. Annu. Rev. Neurosci. 30, 535–574.
Hopfield, J.J. (1982). Neural networks and physical systems with emergent collective computational abilities. Proc. Natl. Acad. Sci. USA 79, 2554–2558.
Hornik, K. (1991). Approximation capabilities of multilayer feedforward networks. Neural Netw. 4, 251–257.
Insel, T.R., and Fernald, R.D. (2004). How the brain processes social information: searching for the social brain. Annu. Rev. Neurosci. 27, 697–722.
Isogai, Y., Si, S., Pont-Lezica, L., Tan, T., Kapoor, V., Murthy, V.N., and Dulac,C. (2011). Molecular organization of vomeronasal chemoreception. Nature 478, 241–245.
Kim, S., Ma, L., Jensen, K.L., Kim, M.M., Bond, C.T., Adelman, J.P., and Yu,C.R. (2012). Paradoxical contribution of SK3 and GIRK channels to the activation of mouse vomeronasal organ. Nat. Neurosci. 15, 1236–1244.
Kobayakawa, K., Kobayakawa, R., Matsumoto, H., Oka, Y., Imai, T., Ikawa, M.,Okabe, M., Ikeda, T., Itohara, S., Kikusui, T., et al. (2007). Innate versus learned odour processing in the mouse olfactory bulb. Nature 450, 503–508.
Korzan, W.J., Grone, B.P., and Fernald, R.D. (2014). Social regulation of cortisol receptor gene expression. J. Exp. Biol. 217, 3221–3228.
Kupfermann, I., and Weiss, K.R. (1978). The command neuron concept. Behav. Brain Sci. 1, 3–10.
Lee, H., Kim, D.-W., Remedios, R., Anthony, T.E., Chang, A., Madisen, L.,Zeng, H., and Anderson, D.J. (2014). Scalable control of mounting and attack by Esr1+ neurons in the ventromedial hypothalamus. Nature 509, 627–632.
Leypold, B.G., Yu, C.R., Leinders-Zufall, T., Kim, M.M., Zufall, F., and Axel, R. (2002). Altered sexual and social behaviors in trp2 mutant mice. Proc. Natl. Acad. Sci. USA 99, 6376–6381.
Li, Q., Korzan, W.J., Ferrero, D.M., Chang, R.B., Roy, D.S., Buchi, M., Lemon, J.K., Kaur, A.W., Stowers, L., Fendt, M., et al. (2012). Synchronous evolution of an odor biosynthesis pathway and behavioral response. Curr. Biol. 23, 11–20.
Liberles, S.D. (2014). Mammalian pheromones. Annu. Rev. Physiol. 76,151–175.
Lin, D., Boyle, M.P., Dollar, P., Lee, H., Lein, E.S., Perona, P., and Anderson, D.J. (2011). Functional identification of an aggression locus in the mouse hypothalamus. Nature 470, 221–226.
Liu, W., Liang, X., Gong, J., Yang, Z., Zhang, Y.-H., Zhang, J.-X., and Rao, Y. (2011). Social regulation of aggression by pheromonal activation of Or65aolfactory neurons in Drosophila. Nat. Neurosci. 14, 896–902.

Mandiyan, V.S., Coats, J.K., and Shah, N.M. (2005). Deficits in sexual and aggressive behaviors in Cnga2 mutant mice. Nat. Neurosci. 8, 1660–1662.
Marr, D. (1982). Vision: A Computational Investigation into the Human Representation and Processing of Visual Information (W.H. Freeman & Co.).
Maruska, K.P., and Fernald, R.D. (2011). Social regulation of gene expression in the hypothalamic-pituitary-gonadal axis. Physiology 26, 412–423.
Maruska, K.P., Zhang, A., Neboori, A., and Fernald, R.D. (2013). Social opportunity causes rapid transcriptional changes in the social behaviour network of the brain in an African cichlid fish. J. Neuroendocrinol. 25, 145–157.
McCarthy, M.M. (2008). Estradiol and the developing brain. Physiol. Rev.88, 91–124.
Miczek, K.A., Maxson, S.C., Fish, E.W., and Faccidomo, S. (2001). Aggressive behavioral phenotypes in mice. Behav. Brain Res. 125, 167–181.
Minsky, M., and Papert, S. (1969). Perceptrons (MIT Press).
Morgan, J.I., and Curran, T. (1991). Stimulus-transcription coupling in the nervous system: involvement of the inducible proto-oncogenes fos and jun. Annu. Rev. Neurosci. 14, 421–451.
Morris, J.A., Jordan, C.L., and Breedlove, S.M. (2004). Sexual differentiation of the vertebrate nervous system. Nat. Neurosci. 7, 1034–1039.
Nelson, R.J., and Trainor, B.C. (2007). Neural mechanisms of aggression. Nat.Rev. Neurosci. 8, 536–546.
Newsome, W.T. (1997). The King Solomon Lectures in Neuroethology. Deciding about motion: linking perception to action. J. Comp. Physiol. A Neuroethol. Sens. Neural Behav. Physiol. 181, 5–12.
Oliveira, R.F., Simoes, J.M., Teles, M.C., Oliveira, C.R., Becker, J.D., and Lopes, J.S. (2016). Assessment of fight outcome is needed to activate socially driven transcriptional changes in the zebrafish brain. Proc. Natl. Acad. Sci. USA 113, E654–E661.
Papes, F., Logan, D.W., and Stowers, L. (2010). The vomeronasal organ mediates interspecies defensive behaviors through detection of protein pheromone homologs. Cell 141, 692–703.
Pedregosa, F., Varoquaux, G., Gramfort, A., Michel, V., Thirion, B., Grisel, O.,Blondel, M., Prettenhofer, P., Weiss, R., and Dubourg, V. (2011). Scikit-learn: machine learning in Python. J. Mach. Learn. Res. 12, 2825–2830.
Peters, P.J., Bronson, F.H., and Whitsett, J.M. (1972). Neonatal castration and intermale aggression in mice. Physiol. Behav. 8, 265–268.
Phoenix, C.H., Goy, R.W., Gerall, A.A., and Young, W.C. (1959). Organizing action of prenatally administered testosterone propionate on the tissues mediating mating behavior in the female guinea pig. Endocrinology 65, 369–382.
Quadagno, D.M. (1968). Home range size in feral house mice. J. Mammal. 49,149–151.
Ramsdell, C.M., Lewandowski, A.A., Glen n, J.L.W., Vrana, P.B., O'Neill, R.J.,and Dewey, M.J. (2008). Comparative genome mapping of the deer mouse (Peromyscus maniculatus) reveals greater similarity to rat (Rattus norvegicus) than to the lab mouse (Mus musculus). BMC Evol. Biol. 8,65.

Ray, R.S., Corcoran, A.E., Brust, R.D., Kim, J.C., Richerson, G.B., Nattie, E.,and Dymecki, S.M. (2011). Impaired respiratory and body temperature control upon acute serotonergic neuron inhibition. Science 333, 637–642.

Rosell, D.R., and Siever, L.J. (2015). The neurobiology of aggression and violence. CNS Spectr. 20, 254–279.

Sano, K., Tsuda, M.C., Musatov, S., Sakamoto, T., and Ogawa, S. (2013). Differential effects of site-specific knockdown of estrogen receptor a in the medial amygdala, medial pre-optic area, and ventromedial nucleus of the hypothalamus on sexual and aggressive behavior of male mice. Eur. J. Neurosci.37, 1308–1319.

Sasaki, K., Suzuki, M., Mieda, M., Tsujino, N., Roth, B., and Sakurai, T. (2011). Pharmacogenetic modulation of orexin neurons alters sleep/wakefulness states in mice. PLoS ONE 6, e20360.

Scott, J.P. (1966). Agonistic behavior of mice and rats: a review. Am. Zool. 6,683–701.

Scott, K.M., Lim, C.C.W., Hwang, I., Adamowski, T., Al-Hamzawi, A., Bromet,E., Bunting, B., Ferrand, M.P., Florescu, S., Gureje, O., et al. (2016). The cross-national epidemiology of DSM-IV intermittent explosive disorder. Psychol.Med. 46, 3161–3172.

Shah, N.M., Pisapia, D.J., Maniatis, S., Mende lsohn, M.M., Nemes, A., and Axel, R. (2004). Visualizing sexual dimorphism in the brain. Neuron 43,313–319.

Silva, B.A., Mattucci, C., Krzywkowski, P., Murana, E., Illarionova, A.,Grinevich, V., Can teras, N.S., Ragozzino, D., and Gross, C.T. (2013). Independent hypothalamic circuits for social and predator fear. Nat.Neurosci. 16, 1731–1733.

Simerly, R.B., Chang, C., Muramatsu, M., and Swanson, L.W. (1990). Distribution of androgen and estrogen receptor mRNA-containing cells inthe rat brain: an in situ hybridization study. J. Comp. Neurol. 294, 76–95.

Sternson, S.M., and Roth, B.L. (2014) . Chemogenetic tools to interrogate brain functions. Annu. Rev. Neurosci. 37, 387–407.

Stowers, L., and Liberles, S.D. (2016). State-dependent responses to sex pheromones in mouse. Curr. Opin. Neurobiol. 38, 74–79.

Stowers, L., Holy, T.E., Meister, M., Dulac, C., and Koentges, G. (2002). Loss of sex discrimination and male-male aggression in mice deficient for TRP2.Science 295 , 1493–1500.Tinbergen, N. (1951). The Study of Instinct (Clarendon Press).

Unger, E.K., Burke, K.J., Jr., Yang, C.F., Bender, K.J., Fuller, P.M., and Shah,N.M. (2015). Medial amygdalar aromatase neurons regulate aggression in both sexes. Cell Rep. 10, 453–462 .

Wallen, K. (1996). Nature needs nurture: the interaction of hormonal and social influences on the development of behavioral sex differences in rhesus monkeys. Horm. Behav. 30, 36 4–378.

Wang, Z., Balet Sindreu, C., Li, V., Nudelman, A., Chan, G.C.-K., and Storm,D.R. (2006). Pheromone detection in male mice depends on signaling through the type 3 adenylyl cyclase in the main olfactory epithelium. J. Neurosci. 26,7375–7379.

Wang, L., Dankert, H., Perona, P., and Anderson, D.J. (2008). A common genetic target for environmental and heritable influences on aggressiveness in Drosophila . Proc. Natl. Acad. Sci. USA 105, 5657–5663.

Wang, F., Zhu, J., Zhu, H., Zhang, Q., Lin, Z., and Hu, H. (2011). Bidirectional control of social hierarchy by synaptic efficacy in medial prefrontal cortex. Science 334 , 693–697.

Wu, M.V., Manoli, D.S., Fraser, E.J., Coats, J.K., Tollkuhn, J., Honda, S.,Harada, N., and Shah, N.M. (2009). Estrogen masculinizes neural pathways and sex-specific behaviors. Cell 139, 61–72.

Yang, C.F., and Shah, N.M. (2014). Representing sex in the brain, one module at a time. Neuron 82, 261–278.

Yang, C.F., Chiang, M.C., Gray, D.C., Prabhakaran, M., Alvarado, M., Juntti,S.A., Unger, E.K., Wells, J.A., and Shah, N.M. (2013). Sexually dimorphic neurons in the ventromedial hypothalamus govern mating in both sexes and aggression in males. Cell 153, 896–909.

Yoon, H., Enquist, L.W., and Dulac, C. (2005). Olfactory inputs to hypothalamic neurons controlling reproduction and fertility. Cell 123, 669–682.

CHAPTER 6

Concluding Remarks

The individual chapters of this dissertation each contain significant discussions of suggested future research directions, so they will not be repeated here. Instead, this chapter will provide a larger context to the disparate projects presented in this dissertation, alongside concluding remarks on anticipated future directions for the field of neuroscience writ large.

Taken together, the work presented in this dissertation represents several distinct and significant advances in neuroscience. In Chapter 2 we advanced a theoretical understanding of the neuromodulation of transmitter release, as well as applying cutting-edge experimental and computational techniques to provide evidence for this theory. In Chapter 3, we advanced an analytical technique for the detection of synaptic activity in the presence of noise, including substantial improvements in its technical flexibility for multiple experimenter use cases. And in Chapters 4 and 5, we show how cutting-edge experimental techniques allow for the genetic dissection of neural circuits contributing to innate social behaviors *in vivo*. These research endeavors span multiple levels of analysis in the pursuit of understanding how the physiology of the brain generates adaptive behaviors.

Over the course of the last century, the field of neuroscience has been converging from the top-down and the bottom-up. Significant progress in understanding the biology of single neurons and synapses has complemented the dissection of neural circuits and

their relation to animal behavior with increasingly fine detail. However, a strong theoretical backbone for neuroscience has proved elusive. The natural point of union for these two approaches, as well as a strong potential foundation for theoretical neuroscience, will undoubtedly be at the level of neuronal circuits and computation. Thus, our understanding of how groups of neurons generate behaviorally-relevant computations will only be complete when it matches the theoretical and mathematical rigor of well-established models like that of cable theory. As McCulloch and Pitts argued 75 years ago:

> *"Thus, both the formal and the final aspects of that activity which we are wont to call mental are rigorously deduceable from present neurophysiology… [the psychiatrist's] observables are explicable only in terms of nervous activities which, until recently, have been beyond his ken."*

Publishing Agreement

It is the policy of the University to encourage the distribution of all theses, dissertations, and manuscripts. Copies of all UCSF theses, dissertations, and manuscripts will be routed to the library via the Graduate Division. The library will make all theses, dissertations, and manuscripts accessible to the public and will preserve these to the best of their abilities, in perpetuity.

Please sign the following statement:

I hereby grant permission to the Graduate Division of the University of California, San Francisco to release copies of my thesis, dissertation, or manuscript to the Campus Library to provide access and preservation, in whole or in part, in perpetuity.

Author Signature

10/5/2018

Date